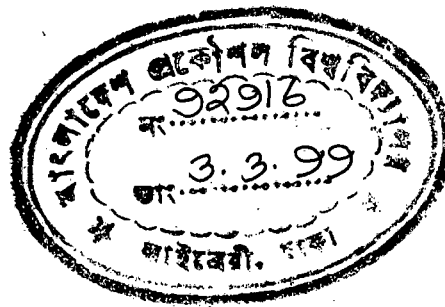# EFFECT OF INTERFACE ELEMENT TYPE ON SOIL-STRUCTURE INTERACTION

NUR SADEQUE

DEPARTMENT OF CIVIL ENGINEERING

BANGLADESH UNIVERSITY OF ENGINEERING AND TECHNOLOGY
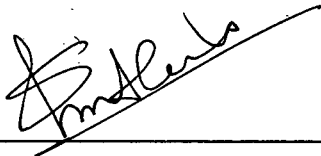
DHAKA, BANGLADESH

1999

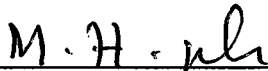# EFFECT OF INTERFACE ELEMENT TYPE ON

SOIL-STRUCTURE INTERACTION

BY

NUR SADEQUE

A thesis approved as to the style and content by:

Dr. Md. Saiful Alam Siddiquee   : Chairman
Associate Professor   (Supervisor)
Department of Civil Engineering
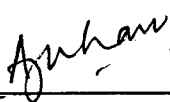BUET, Dhaka 1000

Dr. Md. Hossain Ali   : Member
Professor and Head
Department of Civil Engineering
BUET, Dhaka 1000

Dr. Abdul Muqtadir   : Member·
Professor
Department of Civil Engineering
BUET, Dhaka 1000

Dr. A. J. Khan   : Member
Director and Geotechnical   (External)
Construction and Development Corporation
44, Dhanmondi, Road No. 4A
Dhaka.

DECLARATION

I hereby certify that the research work reported in this thesis has been performed by me and that this work has not been submitted elsewhere for any other purpose (except for publication).

February, 1999

(NUR SADEQUE)

ACKNOWLEDGEMENT

ABSTRACT

A comprehensive literature survey and review of all interface elements so far developed and implemented within their limited scope of applications have been carried out in this study. From the literature survey, three major types of interface elements such as, Goodman (1968) Type, Katona (1983) Type and Desai (1984) Type have been selected for further study depending on their successful application to physical problems. These three most important interface elements are judged in an existing nonlinear incremental-itrative generalized elasto-plastic Finite Element Method (FEM) program.

The parameters controlling the main features of each interface elements have been identified. These parameters are examined critically in a typical problem setting of direct-shear box simulation. In order to investigate the evolution of different internal variables like deformation, strain or stresses, various types of figures have been drawn. Each case of analysis resulted in outputs of: (a) deformed mesh; (b) force-deformation and stress-strain relationship inside the interface; (c) shear strain contours; and (d) displacement fields. As most of the figures were drawn at different load steps in order to trace the progress of the variables, it was rather easy to identify the trouble spots for a particular type of interface.

The contrast between an analysis in direct-shear box without an interface element and with an interface element is very clear. Goodman (1968) type of interface performed well in direct shear simulation. The performance of this interface depends on the relative stiffness of the interface compared to the surrounding soil. Its behavior also depends on the thickness of the interface and load eccentricity from the interface. It shows distinct sign of mesh penetration at higher shear deformation. Katona (1983) type interface element is the simplest interface in terms of number of parameters required. It does not have any penetration or separation problem. The performance in slip mode is ideal although not realistic. The performance of Desai (1984) type interface element seems to be the most realistic although it showed tendency of mesh penetration. It also showed better convergence

properties. Reduction in the thickness of the element improves the performance of the Desai type element.

Finally, it can be concluded that among the three interfaces studied in this research, Katona and Desai type of interface element are much better in accuracy and although, practically Goodman type of interface is easy to formulate and to implement.

TABLE OF CONTENTS

CHAPTER 4

4 FORMULATION OF THE DIFFERENT INTERFACES AND PARAMETRIC STUDY

CHAPTER 5

CHAPTER 6

LIST OF TABLES

LIST OF FIGURES

LIST OF FIGURES (CONTD.)

LIST OF FIGURES (CONTD.)

LIST OF FIGURES (CONTD.)

LIST OF FIGURES (CONTD.)

LIST OF FIGURES (CONTD.)

LIST OF FIGURES (CONTD.)

LIST OF FIGURES (CONTD.)

LIST OF FIGURES (CONTD.)

LIST OF FIGURES (CONTD.)

LIST OF FIGURES (CONTD.)

LIST OF FIGURES (CONTD.)

LIST OF FIGURES (CONTD.)

LIST OF FIGURES (CONTD.)

LIST OF FIGURES (CONTD.)

LIST OF FIGURES (CONTD.)

CHAPTER 1

1.1   GENERAL

Engineering problems employing geomaterials typically involve interaction between dissimilar materials. The importance of correctly simulating the behavior of dissimilar materials along common interface is well established. In finite element analysis of geomaterials consisting of different material along their common interfaces, it is practical to use suitable interface element to simulate model for predicting their correct behavior. Such element will account for relative motion along interfaces, will prevent penetration of one material into the other, and will accurately predict stresses along and across the interface.

In geotechnical engineering distinction can be made between soil-soil interface problems and soil-structure interface problems. Road embankments, river embankments and free excavations are examples of soil-soil interface problems. Shallow foundations, deep (pile, caisson/well) foundations, tunnels and earth retaining structures are examples of soil-structure interface problems. Finite element analysis is being carried out for both types of problems. It is not a very common method of analysis in geotechnical engineering yet, but its application is continuously increasing. By far, most applications are in the field of soil-structure interaction problems, where prediction of displacements are often more important than that for soil-soil interface problems (Boulon, 1990).

The numerical modeling of soil-structure interaction in the static range of loading is highly dependent on the type of constitutive law used to simulate the contact between the surrounding deformable bodies, irrespective of numerical method (e.g., the finite element method, the boundary integral method and the distinct element method. In the early numerical analyses related to metal forming,

1

behavior of rock masses, behavior of piles and other structures embedded in soil, the constitutive equation for unilateral (no tension) frictional contact was mainly rigid perfectly plastic Coulomb's law, and the penalty function technique was considered as an excellent tool for applying these contact (constraint) conditions. But the comparison between experience and modeling has often proved to be disappointing, especially, for problems involving low stress levels (Boulon, 1990).

Geomechanics has pointed out that the contact zone (interface) frequently undergoes a complete change in structure during shearing load. This change is more or less due to granular nature of the soil, which allows for localized dilatancy or contraction (according to the density and local stress level) after small shearing movements, and for degradation of the friction at large tangential relative movements. The framework of elasto-plasticity has been usually used for representing the mechanical behavior of interfaces. Relative movements between bodies in contact are described either by a local high velocity gradient (thin layer) or by a kinematic discontinuity. In both cases, the development of a non-linear behavior within the interface is drastically rapid compared with that which can develop in the bodies in contact, inducing a very slow rate of convergence of the global solution. Except for models of thin layers, the well known joint elements, incorporating the interface constitutive equations, are different in nature from volume elements since the best sampling points for stresses are the nodes (instead of intermediate Gauss points for volume elements). This difference induces some numerical integration within joint elements. Since full plasticity frequently occurs in interfaces, and since the degradation mentioned above (partially due to grain crushing) acts as a local softening, sophisticated methods of resolution of the resulting non-linear system of algebraic equations are required at the structural level (Boulon, 1990).

Distinct interface element of zero thickness is widely used in finite element analysis of geologic structures. Goodman et al. (1968) proposed the first element of this type applied to geologic media. Several other zero thickness elements have also been developed based on the original formulation. The zero thickness interface elements possess some fundamental deficiencies which are: spurious stress oscillations attributed to inappropriate quadrature schemes; lack of accuracy due to excessively large stiffness parameters; and inaccurate interface stress predictions due to insufficient mesh fineness have been cited in the past. A kinematic inconsistency is associated with the displacement of this element proposed by Goodman et al (1968).

In spite of the kinematic deficiencies associated with tangential response, Goodman type element has been rather widely used due to its simple formulation, ease of numerical implementation and robust normal response. A higher order (six-node) version of this element has also been developed. But when integrated analytically, it possesses kinematic deficiencies similar to the original Goodman (1968) type element.

The second zero thickness interface element proposed by L.R. Herrmann (1978) is a **Link** element. The element is referred to as LRH element. It employs a desirable method for assessing response modes and exhibits acceptable tangential response which was shown to be unreliable in predicting normal response. This deficiency was attributed to the uncoupled form of the element equations.

Katona (1983) developed another type of robust interface element directly from the principle of virtual work. It avoids any numerical round-off problems inherent in the stiffness approach and controls directly interface forces and relative movements.

Desai et al. (1984) developed a new class of interface elements having very small thickness. It is mainly ordinary isoparametric thin element but having a different constitutive relationship. The constitutive relationship dictates the general behavior of the interface element.

Although the ever-popular finite element method (FEM) has been used extensively for the structural analysis and design as well as soil-structure interaction problems, it is, of course, simply a numerical solution methodology. The real challenge is to construct mechanistic models that behave something like the real world, while striking a balance between rigorous mechanics and engineering simplicity (Katona, 1983). Typically, for a buried culvert problem, this challenge extends to almost every aspect of the soil-structure system, e.g. soil constitutive model, structure constitutive model, simulation of incremental soil layers, boundary conditions, geometrical non-linearities, etc. In this case the area of particular interest is the treatment of the culvert-soil interface and the FEM models assume the soil is bonded to the culvert during deformation.

In Bangladesh major civil engineering constructions are dependent on pile foundation. Design of a complete structure with its foundation by soil-structure interaction makes the design cost effective and safe. But any reliable soil-structure interaction analysis needs better interface element. And there have been no specific studies on the relative merits and demerits of the aforementioned three major interface elements with respect to the soil condition of Bangladesh. Moreover, in some of the previous research on pile load test simulation, behavior of the interface, as shown from the numerical analysis, was not satisfactory.

1.2 SCOPE OF THE RESEARCH

The research has a broader perspective in the field of geomechanical work. A typical working field is soil-structure interaction using interface elements for various types of loading systems. However, this research is intended to carry out the following activities:

a) to study on the interface elements so far developed and implemented to physical problems;

b) to identify widely used interface element for a comprehensive parametric study and to implement of these elements in a nonlinear incremental iterative generalized elasto-plastic finite element program (ONSOLA);

c) to examine critical parameters for different material properties and loading conditions and to identify problems associated with the interfaces with respect to their original formulation, difficulties in implementing in FEM code and deviation from acceptable realistic behavior;

d) finally, to modify the original formulation of the interfaces and/or to apply appropriate numerical techniques for the highly nonlinear equations to simulate correct behavior of the interfaces.

1.3 OBJECTIVES

The primary objectives of this research are to:

- carryout sensitivity analysis of the major types of interface elements in the context of the soil condition of Bangladesh;

- modify the original formulation of the selected interface elements and/or apply appropriate solution techniques for making the interfaces compatible and ease in application to FEM Code;

- compare performance of these interface elements and recommend the best interface element for soil-structure problems.

CHAPTER 2

2   LITERATURE REVIEW

2.1   GENERAL

In any interface between structural and geological media and at joints in rock masses a situation of relative movement (translation and/or rotation) takes place under static and dynamic loading. In finite element analysis of geomaterials consisting of dissimilar materials along their common interfaces, it is practical to use suitable interface element to simulate model for predicting their correct behavior. Such elements will account for relative motion along interfaces, will prevent penetration of one material into the other, and will accurately predict stresses along and across the interface.

The use of 2D elements with compatibility in a finite element analysis of dissimilar continuum interfaces usually prohibit relative movement. Typically, nodal compatibility of finite element method constrains the adjacent structural and soil elements to move together. As such, interface or joint elements can be applied to model the soil-structure boundary such as the sides of a wall or pile, or the underside of a footing. Particular advantages being the ability to vary the constitutive behavior of the soil-structure interface (e.g., the maximum wall friction angle) and to allow differential movement of the soil and the structure, i.e., slip and separation.

Interface elements are numerical entities used in the finite element technique for modeling kinematic discontinuties that are present in some boundary value problems. In numerical practice, two types of interface elements are used: a) a reduction from a classical volume finite element (thin layer interface elements) and b) a surface element which is a zero thickness joint element. For the first type of element (Ghaboussi et al., 1973 and Desai et al., 1984) the soil-structure interface is considered as a thin continuum and the thickness

of the interface should be specified. This may cause some problem since the real thickness is often unknown and is also very small compared to the other dimensions of the region. It is even unclear which type of test should be performed to determine the constitutive law of the material within those elements: the soil should in fact be subjected to very large deformations for modeling this interface behavior.

Many methods have been proposed to model discontinuous behavior at the soil-structure interface. These include: a) use of thin 2D finite elements with standard constitutive law; b) linkage elements in which only the connections between opposite nodes are considered (usually opposite nodes are connected by discrete springs); c) special interface or joint elements of either zero or finite thickness; and d) hybrid methods where the soil and structure are modeled separately and linked through constraint equations to maintain compatibility of force and displacement at the interface.

Wilson (1977) has demonstrated that ill-conditioning of the interface element stiffness matrix due to large off-diagonal terms causes loss of accuracy. Ghaboussi et al. (1973) and Wilson (1977), therefore advocate the use of relative displacement as independent degrees of freedom for interface elements. The use of this relative degree of freedom formulation requires modification of the adjacent 2D elements only on one side of the interface, so that they use the same relative degrees of freedom. Thus, incorporation into a finite element program is complex. This formulation also causes problems at joint intersections.

The benefit of the relative degree of freedom formulation is uncertain. Pande and Sharma (1979) compared a series of analyses using the relative degrees of freedom formulation with similar analyses using the absolute degree of freedom formulation. They found that little ill-conditioning is experienced with the use of very thin 2D elements. The additional effort involved in the use of the relative displacement element may not be worthwhile.

Griffiths (1985) recommends the use of special interface elements instead of thin standard 2D elements for more accurate modeling of the interface when slippage is of prime concern.

Desai et al. (1984) propose a thin 2D joint/interface element called a thin-layer element for soil-structure interaction. A special constitutive law is used to model the principle deformation modes of shear and opening. Their report states that with the use of zero thickness elements it is often difficult to obtain constant and stable stress in the interface elements themselves, and therefore the stress in the adjacent 2D elements is often adopted rather than the interface element stress itself. It is argued that the thin-layer element is computationally more reliable than the zero thickness element. The choice of element thickness is however important, and can effect the behavior of the interface given the same constitutive parameters. An extensive parametric study has recently resulted in guidelines and empirical criteria for the determination of element thickness of the thin-layer element.

Zero thickness elements however have been used by many others without reporting similar problems. The element used has been based on that proposed by Goodman et al. (1968). The essential modifications to this original element are the extension to four and six node isoparametric formulations to make the interface element compatible with isoparametric quadrilateral 2D elements.

Numerical problems such as ill-conditioning, poor convergence of solution and unstable integration point stresses have been experienced by R.A. Day and D.M. Potts (1986) when using the zero thickness interface element to simply supported split beam, simple pull-out test and overturning of an elastic block.

Both ill-conditioning of the stiffness matrix and high stress gradients were found to cause numerical instability. Ill-conditioning can be reduced by careful selection of the size of the 2D elements adjacent to the interface. The problem of steep stress gradients is entirely one of inadequate mesh design.

Analyses of retaining wall using interface elements confirm the analytical values of active and passive earth pressure coefficients which are commonly used in analysis and design of retaining wall.

2.2 INTERFACE ELEMENT OF ZERO THICKNESS

Distinct interface element of zero thickness is widely used in finite element analysis of geologic structures. Goodman et al. (1968) proposed the first element of this type applied to geologic media. Several other zero thickness elements have also been developed based on the original formulation. The zero thickness interface elements possess some fundamental deficiencies which are: spurious stress oscillations attributed to inappropriate quadrature schemes; lack of accuracy due to excessively large stiffness parameters; and inaccurate interface stress predictions due to insufficient mesh fineness have been cited in the past. A kinematic inconsistency is associated with the displacement of this element proposed by Goodman et al (1968).

2.2.1 INTERFACE ELEMENT PROPOSED BY GOODMAN ET AL.

For simplicity in the subsequent discussion, the zero thickness interface element proposed by Goodman et al. (1968) in simulating the behavior of jointed rock masses, shall be referred to here-in-after as the "GTB" element. This rectangular element posses four nodes and eight displacement degrees of freedom (Refer to Figure 4-1). When using GTB element in the analysis of geologic media, at each node point along the interface a pair of nodes is placed at the same initial geometric location; the thickness of the element is thus initially zero. The element equations are derived on the basis of nodal relative displacement components of the continuum elements on either side of the interface. The relative displacements are then related to absolute displacements. Since they are prerequisite for understanding the subsequent discussion, some details concerning the GTB element are presented.

The vector of absolute nodal displacement degrees of freedom with respect to the local coordinate system (x'-y') is given by:

$$\{u'\} = \{u'_{1x} \ u'_{1y} \ u'_{2x} \ u'_{2y} \ u'_{3x} \ u'_{3y} \ u'_{4x} \ u'_{4y}\}^T \tag{2-1}$$

Where, the superscript T denotes the of matrix transposition. Associated with the above displacement components is a corresponding vector of nodal forces:

$$\{f^e\} = (f'_{1x} \ f'_{1y} \ f'_{2x} \ f'_{2y} \ f'_{3x} \ f'_{3y} \ f'_{4x} \ f'_{4y})^T \tag{2-2}$$

The vector of relative displacements is defined as

$$\{w\} = \begin{Bmatrix} w_t \\ w_n \end{Bmatrix} = [N^*]\{u'\} \tag{2-3}$$

Where, w_t and w_n represent tangential and normal relative displacement respectively, along the interface. The matrix relating relative and absolute displacements is given by

$$[N^*] = \begin{bmatrix} -N_1 & 0 & -N_2 & 0 & N_2 & 0 & N_1 & 0 \\ 0 & -N_1 & 0 & -N_2 & 0 & N_2 & 0 & N_1 \end{bmatrix} \tag{2-4}$$

where,

$$N_1 = 1/2 - x'/L \tag{2-5}$$

$$N_2 = 1/2 + x'/L \tag{2-6}$$

represent standard linear functions.

The tangential and normal forces per unit length of interface, σ_t and σ_n respectively, are related to the relative displacements through a suitable constitutive relation. Since the aim is to address on the deficiencies associated with zero-thickness interface elements and not on the constitutive relations used, the following simple relation shall be employed herein,

$$\begin{Bmatrix} \sigma_t \\ \sigma_n \end{Bmatrix} = \begin{bmatrix} d_{11} & 0 \\ 0 & d22 \end{bmatrix} \begin{Bmatrix} w_t \\ w_n \end{Bmatrix} = [D]\{w\} = [D][N^*]\{u'\} \tag{2-7}$$

More complex constitutive relations for such elements have been presented by various researchers.

The constitutive parameters d_{11} and d_{22} appearing in equation (2-7) represent the tangential and normal stiffness per unit length respectively, along the interface. Alternately, d_{11} and d_{22} can be thought of as tangential and normal penalty numbers.

Considering $\{w\}$ as a generalized "strain", the element stiffness matrix is computed from

$$\left[K^{e}\right]= \int_{x} \left[N^{*}\right]^{T}[D]\left[N^{*}\right]dx' = \int_{\xi} \left[N^{*}\right]^{T}[D]\left[N^{*}\right]\det[J]d\xi \qquad (2\text{-}8)$$

Since the element is rectangular, the Jacobian [J] is constant, allowing the above integrations to be performed analytically (similar results could of course be realized using standard two-point Gauss-Legendre quadrature). The resulting element stiffness matrix with respect to local element coordinates, is thus:

$$\left[K^{e}\right]=\frac{L}{6}\begin{bmatrix} 2d_{11} & 0 & d_{11} & 0 & -d_{11} & 0 & -2d_{11} & 0 \\ & 2d_{22} & 0 & d_{22} & 0 & -d_{22} & 0 & -d_{22} \\ & & 2d_{11} & 0 & -2d_{11} & 0 & -d_{11} & 0 \\ & & & 2d_{22} & 0 & -2d_{22} & 0 & -d_{22} \\ & & & & 2d_{11} & 0 & d_{11} & 0 \\ & \text{sym.} & & & & 2d_{22} & 0 & d_{22} \\ & & & & & & 2d_{11} & 0 \\ & & & & & & & 2d_{22} \end{bmatrix} \qquad (2\text{-}9)$$

The element equations must next be transformed to system coordinates (x-y). Noting that the local and system coordinates are related through

$$\begin{Bmatrix} x' \\ y' \end{Bmatrix} = \begin{bmatrix} \cos\theta & \sin\theta \\ -\sin\theta & \cos\theta \end{bmatrix}\begin{Bmatrix} x \\ y \end{Bmatrix} = [R]\begin{Bmatrix} x \\ y \end{Bmatrix} \qquad (2\text{-}10)$$

It follows that the element stiffness matrix and force vector, with respect to system coordinates, are computed in the usual manner; that is,

$$\left[K^{e}\right]=\left[R^{*}\right]^{T}\left[K^{e}\right]\left[R^{*}\right] \qquad (2\text{-}11)$$

Where,

$$\{f^e\}=[R^*]^T\{f^{e'}\}$$

(2-12)

$$[R^*]=\begin{bmatrix}[R] & 0 & 0 & 0 \\ 0 & [R] & 0 & 0 \\ 0 & 0 & [R] & 0 \\ 0 & 0 & 0 & [R]\end{bmatrix}$$

(2-13)

2.2.2 INTERFACE ELEMENT PROPOSED BY HERRMANN

The second zero thickness interface element proposed by L.R. Herrmann (1978) is a Link element. The element is referred to as LRH element.

According to Harrmann's approach, the bond behavior is modeled through fictitious springs – one normal and one tangential to the interface – at each pair of mating nodes. For each pair of nodes along the interface there are thus four global unknowns: two absolute displacements and the relative displacements δ_t and δ_n in the tangential and normal directions, respectively. The relative displacements δ_t and δ_n between a pair of mating nodes 1 and 2 are related to the absolute displacements u'_{1x} u'_{1y} u'_{2x} u'_{2y} in the following manner

$$\begin{Bmatrix}\delta_t \\ \delta_n\end{Bmatrix} = \begin{bmatrix}-1 & 0 & 1 & 0 \\ 0 & -1 & 0 & 1\end{bmatrix}\begin{Bmatrix}u'_{1x} \\ u'_{1y} \\ u'_{2x} \\ u'_{2y}\end{Bmatrix}$$

(2-14)

where primed subscripts again refer to the local (x' - y') coordinate system.

The relationship between nodal element forces and relative displacements is given by:

$$\frac{L}{2}\begin{bmatrix} -P_t & 0 \\ 0 & -P_n \\ P_t & 0 \\ 0 & P_n \end{bmatrix}\begin{Bmatrix} \delta_t \\ \delta_n \end{Bmatrix} = \begin{Bmatrix} f'_{1x} \\ f'_{1y} \\ f'_{2x} \\ f'_{2y} \end{Bmatrix} \qquad (2\text{-}15)$$

Where L represents the length of the interface element, P_t and P_n denote the tengential and normal link spring stiffness per unit length, respectively; they may likewise be thought of as penalty numbers.

Substituting equation (2-14) into (2-15) gives the element equations for a single pair of mating nodes along an interface, that is

$$\frac{L}{2}\begin{bmatrix} P_t & 0 & -P_t & 0 \\ 0 & P_n & 0 & -P_n \\ -P_t & 0 & P_t & 0 \\ 0 & -P_n & 0 & P_n \end{bmatrix}\begin{Bmatrix} u'_{1x} \\ u'_{1y} \\ u'_{2x} \\ u'_{2y} \end{Bmatrix} = \begin{Bmatrix} f'_{1x} \\ f'_{1y} \\ f'_{2x} \\ f'_{2y} \end{Bmatrix} \qquad (2\text{-}16)$$

Next consider an interface to be modeled using an element of length L with two links, one associated with nodes 1 and 2, the other with nodes 3 and 4 (Figure 2-1). Assuming that the two links are independent of each other but have the same normal and tengential stiffness per unit length, the element stiffness matrix, in local coordinates, is given by:

$$[K^e] = \frac{L}{2}\begin{bmatrix} P_t & 0 & -P_t & 0 & 0 & 0 & 0 & 0 \\ & P_n & 0 & -P_n & 0 & 0 & 0 & 0 \\ & & P_t & 0 & 0 & 0 & 0 & 0 \\ & & & P_n & 0 & 0 & 0 & 0 \\ & & & & P_t & 0 & -P_t & 0 \\ & & \text{sym.} & & & P_n & 0 & -P_n \\ & & & & & & P_t & 0 \\ & & & & & & & P_n \end{bmatrix} \qquad (2\text{-}17)$$

13

where the uncoupling between links is readily apparent. The associated vectors of nodal displacements and nodal forces are given by equations (2-1) and (2-2) respectively.
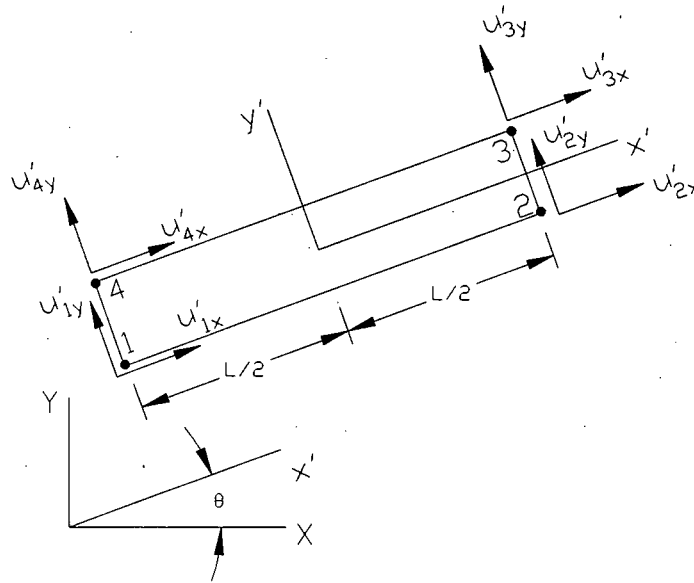
Figure 2-1: Four-Node Zero-Thickness Interface Link Element of Herrmann

2.2.3 IMPROVED FOUR-NODED INTERFACE ELEMENT (MACRO-ELEMENT)

In light of the deficiencies in the above mentioned interface elements, it is evident that an improved family of zero-thickness interface elements is desirable. Such elements should: (a) determine response modes based on the logic of the LRH elements; (b) possess the normal response characteristics of the GTB element; and (c) eliminate the kinematic deficiencies associated with the GTB element by employing tangential response similar to the LRH element. The development of the simplest member of such an element family is presented below:

Consider a macro-element composed of two rectangular GTB elements of equal length (Figure 2-2) and for brevity this has been referred to as LK1 element. The thickness of both elements is initially zero prior to deformation, the pairs of nodes 1-4, 5-6 and 2-3 are coincident. The nodal lines 1-5-2 and 4-6-3 represents straight lines of length L.
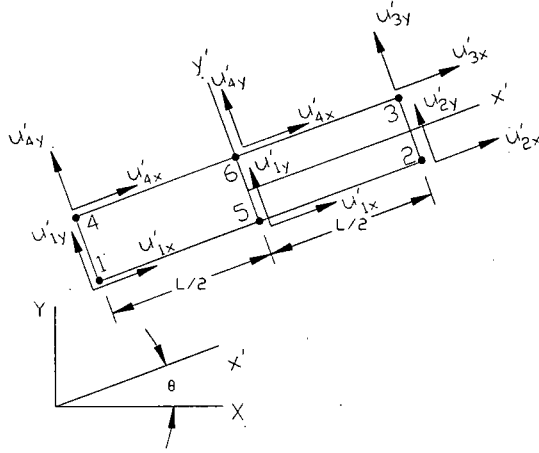
Figure 2-2: Macro-Element Consisting of Two GTB Elements

Since both GTB elements are rectangular, the integrations associated with the element stiffness matrices are performed analytically. For each element, the resulting stiffness with respect to local element coordinates, is thus given by equation (2-9) multiplied by a factor of 0.50.

Using a standard assembly procedure, the two element stiffness matrices are next combined to give

$$\left[K^{e'} \right] \left\{ u^{e'} \right\}^* = \left\{ f^{e'} \right\}^* \tag{2-18}$$

Where,

$$\left[K^{e'} \right]^* = \frac{L}{12} \begin{bmatrix} K_{11} & K_{12} \\ K^T_{12} & K_{22} \end{bmatrix} \tag{2-19}$$

$$[K_{11}] = \begin{bmatrix} 2d_{11} & 0 & 0 & 0 & 0 & 0 \\ & 2d_{22} & 0 & 0 & 0 & 0 \\ & & 2d_{11} & 0 & -2d_{11} & 0 \\ & & & 2d_{22} & 0 & -2d_{22} \\ & \text{sym} & & & 2d_{11} & 0 \\ & & & & & 2d_{22} \end{bmatrix} \qquad (2\text{-}20)$$

$$[K_{12}] = \begin{bmatrix} -2d_{11} & 0 & d_{11} & 0 & -d_{11} & 0 \\ 0 & -2d_{22} & 0 & d_{22} & 0 & -d_{22} \\ 0 & 0 & d_{11} & 0 & -d_{11} & 0 \\ 0 & 0 & 0 & d_{22} & 0 & -d_{22} \\ 0 & 0 & -d_{11} & 0 & d_{11} & 0 \\ 0 & 0 & 0 & -d_{22} & 0 & d_{22} \end{bmatrix} \qquad (2\text{-}21)$$

$$[K_{22}] = \begin{bmatrix} 2d_{11} & 0 & -d_{11} & 0 & d_{11} & 0 \\ & 2d_{22} & 0 & -d_{22} & 0 & d_{22} \\ & & 4d_{11} & 0 & -4d_{11} & 0 \\ & & & 4d_{22} & 0 & -4d_{22} \\ & \text{sym.} & & & 4d_{11} & 0 \\ & & & & & 4d_{22} \end{bmatrix} \qquad (2\text{-}22)$$

$$\{u^e\}^* = \{u'_{1x} \quad u'_{1y} \quad u'_{2x} \quad u'_{2y} \quad u'_{3x} \quad u'_{3y} \quad u'_{4x} \quad u'_{4y} \quad u'_{5x} \quad u'_{5y} \quad u'_{6x} \quad u'_{6y}\}^T \qquad (2\text{-}23)$$

$$\{f^e\}^* = \{f'_{1x} \quad f'_{1y} \quad f'_{2x} \quad f'_{2y} \quad f'_{3x} \quad f'_{3y} \quad f'_{4x} \quad f'_{4y} \quad f'_{5x} \quad f'_{5y} \quad f'_{6x} \quad f'_{6y}\}^T \qquad (2\text{-}24)$$

Using standard procedures associated with the finite element method, the degrees of freedom associated with nodes 5 and 6 are next **condensed out** from equation (2-18), resulting in the element equations

$$[K^e]^{**} \{u^e\}^{**} = \{f^e\}^{**} \qquad (2\text{-}25)$$

16

Where,

$$[K^{e'}]^{\bullet\bullet} = \frac{L}{48}\begin{bmatrix} 7d_{11} & 0 & -d_{11} & 0 & d_{11} & 0 & -7d_{11} & 0 \\ & 7d_{22} & 0 & -d_{22} & 0 & d_{22} & 0 & -7d_{22} \\ & & 7d_{11} & 0 & -7d_{11} & 0 & d_{11} & 0 \\ & & & 7d_{22} & 0 & -7d_{22} & 0 & d_{22} \\ & & & & 7d_{11} & 0 & -d_{11} & 0 \\ & \text{sym} & & & & 7d_{22} & 0 & -d_{22} \\ & & & & & & 7d_{11} & 0 \\ & & & & & & & 7d_{22} \end{bmatrix} \qquad (2\text{-}26)$$

and the vectors $\{u^e\}^{**}$ and $\{f^e\}^{**}$ are given by equations (2-1) and (2-2), respectively.

Comparing equation (2-26) with the stiffeness matrix associated with the GTB element (equation (2-9)), it is evident that although the structure of the two matrices is similar, the numerical coefficients and more importantly the signs of certain off-diagonal terms differ.

The transformation of element equations to system coordinates (x-y) is realized in the manner described by equations (2-11) to (2-13).

The interface tangential and normal forces per unit length are defined in the following manner

$$\sigma_t = \frac{f'_{3x} + f'_{4x}}{L} = \frac{d_{11}}{8}\left(-u'_{1x} - u'_{2x} + u'_{3x} + u'_{4x}\right) \qquad (2\text{-}27)$$

$$\sigma_n = \frac{f'_{3y} + f'_{4y}}{L} = \frac{d_{22}}{8}\left(-u'_{1y} - u'_{2y} + u'_{3y} + u'_{4y}\right) \qquad (2\text{-}28)$$

Where equation (2-25) has been used to substitute for f'_{3x}, f'_{4x}, f'_{3y} and f'_{4y}

2.3 CONTACT-FRICTION INTERFACE ELEMENT

The specific objective of this element formulation is to: (a) present a simple friction-contact interface element readily adaptable to standard FEM programs; (b) illustrate the implementation and validity of the interface element; and (c) demonstrate the importance and need of interface elements for modeling certain buried culvert problems.

The proposed interface element is capable of responding to a general step-by-step loading history, such that tensile separation, friction sliding, or complete bonding (or rebonding) is possible during any load step. Two nodes, one on either side of the interface, along with the interface angle φ are used to define the interface element. By selectively applying the constraint equations to the interface nodes in an incremental iterative solution procedure, the behavior of a contact-friction interface is simulated.

The formulation is limited to static and two dimensional geometry; however, the inclusion of inertia and three dimensional geometry is straightforward. Further it is assumed that deformations are small so that changes in the interface angle are negligible, and there is no thermal coupling.

Two computational advantages are inherent in the proposed interface element. Frist, the constraint equations along with the associated normal and tangential interface forces are incorporated into an incremental virtual work statement, as opposed to the more common technique of introducing constraint equations with LaGrange multipliers in a minimization principle (e.g. minimum potential energy). Thus, the formulation based on virtual work is not restricted to conservative systems. Secondly, the interface element produces an element **constraint matrix** and element **load vector** analogous to a typical element stiffness matrix and load vector. Thus, the interface element can be assembled into the global equations by standard techniques.

a)   Virtual work and constraint equations

A standard finite element displacement formulation (without constraints) based on incremental virtual work, i.e. internal virtual work is equal to external virtual work, or:

$$\delta\,u^T\{Ku - P\} = 0 \qquad\qquad (2\text{-}29)$$

where

> u = incremental displacement vector
> K = tangent global stiffness matrix
> P = incremental load vector

Here δu^T is an arbitrary virtual displacement, so that satisfaction of equation (2-29) requires that $Ku = P$ (usually solved iteratively).

If equation (2-29) represented a finite element assembly of two bodies initially in contact at node pairs as suggested in (Refer to Figure 4-2), then, of course, the two bodies can deform independently resulting in overlapping and/or separation along the interface. On the other extreme, if the node pairs at the interface are constrained to move together, a completely bonded response is obtained. Between these two extremes, a slipping response can be obtained by constraining only the displacements normal to the interface at each node pair.

The particular forms of the constraint equations and the treatment of interface friction are discussed in the next section. For now, the objective is to incorporate and arbitrary set of constraint equations into a global virtual statement. Formally, any set of linear nodal point constraint equations can be expressed as:

$$Cu - \hat{a} = 0 \qquad\qquad (2\text{-}30)$$

Where,

> C = constraint coefficient matrix
>
> $\hat{a}$ = specified constraints (e.g. displacement gaps)

19

Associated with each constraint equation in equation (2-30) there exists an unknown internal constraint force λ enforcing constraint. For convenience, equation (2-30) can be expressed in a scalar (work) form as:

$$\delta \lambda^T \{Cu - a\} = 0 \qquad (2\text{-}31)$$

where $\delta\lambda$ is an arbitrary variation of the constraint forces so that satisfaction of equation (231) implies equation (2-30).

To this end, the virtual work of the constraint forces have not been accounted and the internal constraint forces produce internal virtual work when the constraint is given a virtual movement (variation), i.e., $\delta\{Cu-a\}^T \lambda$. Since C and a are constants, this becomes:

$$\text{Constraint virtual work} = \delta u^T C^T \lambda \qquad (2\text{-}32)$$

Physically this is analogous to imposing constraints with stiff springs between node pairs wherein the internal spring force corresponds to the constraint force. However, in this case the constraint forces are primary unknowns.

To complete the formulation, we add the internal virtual work given by equation (2-32) to the virtual work statement in equation (2-29) and append the constraint requirement in equation (2-31) to get the general virtual work statement including constraints:

$$\delta \begin{Bmatrix} u \\ \lambda \end{Bmatrix}^T \left\{ \begin{bmatrix} K & C^T \\ C & 0 \end{bmatrix} \begin{Bmatrix} u \\ \lambda \end{Bmatrix} - \begin{Bmatrix} P \\ a \end{Bmatrix} \right\} = 0 \qquad (2\text{-}33)$$

Thus, the coupled matrix equations above from the global system to be solved for u and λ. Note that the separate partitioning of the global system into u and λ is a mere formality and not required in the actual assembly. Indeed, the constraint equations may be treated at the element level by forming an element constraint matrix, C^* and vector f as:

$$C^* = \begin{matrix} \quad u \quad\quad \lambda \\ \begin{Bmatrix} O & C^T \\ C & O \end{Bmatrix} \end{matrix} \qquad (2\text{-}34)$$

20

Here, The matrix and vector quantities associated with **u** pertain to only those

$$\mathbf{f} = \begin{Bmatrix} \mathbf{0} \\ \mathbf{a} \end{Bmatrix} \tag{2-35}$$

degrees of freedom affected by the constraints. Since $\mathbf{C}^*$ is symmetric it can be assembled like any stiffness element as can the element load vector **f** . Global storage locations for λ can be easily established by defining **dummy** nodes in the finite element mesh. However, to maintain narrow bandedness of the assembled matrix (equation (2-33)), the dummy nodes should be numbered as closely as possible to the nodes being constrained.

b)   Interface element constraint matrix and load vector

To separate the foregoing to friction-contact interfaces, we assume that any interface can be modeled as a sequence of node pairs (Refer Figure 4-2), so that attention can be focused on a single node pair (interface element) as shown in Figure 4-3. Here, the interface element is defined in x′, y′ coordinates which are rotated ϕ degrees from the global x, y coordinate system. At the end of any load step k, the interface responses are characterized by interface forces λ^k_n and λ^k_s and/or relative movements Δ^k_n and Δ^k_s where subscripts n and s refer to normal and tangent directions, and the superscript identifies the load step. No superscript implies and increment, e.g., $\lambda_n = \lambda^k_n - \lambda^{k-1}_n$.

Assuming both nodes of the element (nodes 1 and 2 in Figure 4-3) are initially in the same location prior to loading, the relative movements are given by the nodal displacements in the x′, y′ system as normal.

$$\Delta^k_n = (u'_2 - u'_1)^k \tag{2-36}$$

$$\Delta^k_s = (v'_2 - v'_1)^k \tag{2-37}$$

We can now identify three **interface states** impose them during a load step: fixed, slip and free.

(1)   Fixed state: for this case the relative normal and tangential movement between the nodes is specified by two constraint equations:

$$\begin{bmatrix} -\cos\varphi & -\sin\varphi & \cos\varphi & \sin\varphi \\ \sin\varphi & -\cos\varphi & -\sin\varphi & \cos\varphi \end{bmatrix} \begin{Bmatrix} u_1 \\ v_1 \\ u_2 \\ v_2 \end{Bmatrix} = \begin{Bmatrix} a \\ b \end{Bmatrix} \tag{2-38}$$

where,

a = specified normal separation (increment)
b = specified relative slip (increment)

In the above, the local u' and v' displacement increments have been replaced by global u, v displacement increments so that equation (2-38) can be used to define element constraint matrix $\mathbf{C}^*$ and load vector $\mathbf{f}$ in global displacement coordinates as implied in the equation (2-34 and (2-35). The top portion of Table 4-1 explicitly defines $\mathbf{C}^*$ and $\mathbf{f}$ and may be assembled like any stiffness element.

If a and b are both specified zero, the normal gap and relative slip do not change during the load step, i.e., both nodes experience identical displacement increments. If on the other hand, we wish to return the nodes to their initial position (no gaps), we set $a = -\Delta_n^{k-1}$, b $= -\Delta_s^{k-1}$.

(2)   Slip State: The slipping state is characterised by constraining the normal displacement increments and specifying the tangential interface force increment, i.e.;

$$(-\cos\varphi \quad -\sin\varphi \quad \cos\varphi \quad \sin\varphi) \begin{Bmatrix} u_1 \\ v_1 \\ u_2 \\ v_2 \end{Bmatrix} = a \tag{2-39}$$

$$\lambda_s = T \tag{2-40}$$

Since, λ_s is specified, the element constraint matrix and load vector can be put in the form shown in the center portion of Table 4-1 wherein the matrix size remains 6x6 for computational convenience.

To simulate a friction-contact interface, the specified values (i.e. T and a in the above equations) are generally determined iteratively dependent on the previous state of the interface (fix, slip or free) and the frictional model. For this case, simple Coulomb friction is assumed, thus the maximum possible interface tangent force at end of load step k is:

$$F^k = \mu \left| \lambda_n^{\ k} \right| sgn\left(\lambda_s^{\ k} \right)$$

(2-41)

Where:

F^k = maximum frictional tangent force

μ = coefficient of friction

$$sgn\left(\lambda_s^{\ k} \right) = \begin{cases} +1, \text{ for } \lambda_s^{\ k} > 0 \\ -1, \text{ for } \lambda_s^{\ k} < 0 \end{cases}$$

Accordingly, the specified incremental tangent force is $T = F^k - \lambda_s^{k-1}$

(3)   Free State: The free state requires suppressing both constraint equations and specifying the normal and tangent interface force increments, i.e.,

$$\lambda_n = N$$
$$\lambda_s = T$$

The corresponding interface element matrix and load vector are shown in the bottom portion of the Table 4-1 where, again, the element matrix size is maintained as 6x6 for computational convenience in global assembly.

Iterative procedures for determining the correct interface state and load vector parameters (a, b, N and/or T) are discussed next. In passing, however, it is observed that a fourth interface state characterizes by tangential displacement constraints and specified normal forces could be easily established as, for example, in simulating a gear-tooth interface.

c)   **Interface iterative procedure**

The problem is posed as follows. Given the interface solution at load step k-1, denoted by Δ_n^{k-1}, Δ_s^{k-1}, λ_n^{k-1} and λ_s^{k-1}, we seek to determine the solution increments Δ_n, Δ_s, λ_n and λ_s so that the solution at the end of load step k, denoted by $\alpha^k = \alpha + \alpha^{k-1}$ ($\alpha^k = \Delta_n^{\ k}$, $\Delta_s^{\ k}$, $\lambda_n^{\ k}$ or $\lambda_s^{\ k}$), is properly determined at the end of load step k. By a proper solution we

mean the physical compatibility and equilibrium conditions of the contact – friction interface are satisfied.

In general the solution must be determined iteratively wherein a particular state (fix, slip or free) is assumed and solved to obtain a trial solution. The trial solution is used to determine if the assumed state is correct, and if not, what state is more likely to be correct. At the same time, the trial solution is used to estimate new load vector parameters a, b or a, T or N , T depending on whether the new state is assumed fix, slip or free, respectively.

Table 4-2 offers an exhaustive set physical criteria to test the validity of an assumed state. The table may be viewed as a 3x3 decision matrix wherein the previously assumed state forms rows and the new candidate states form columns. For example, if the previously assumed state was fixed, row1 of the decision matrix is queried to determine if the net normal interface force λ_n^k is compressive and if the net tangent interface force λ_s^k is less than the maximum frictional value F^k.

If not, the fixed assumption is incorrect (at least this iteration) and the new candidate state is slip or free depending on whether λ_n^k is tensile or compressive.

In a similar manner rows 2 and 3 of Table 4-2 test the validity of assumed slip and free states. In row 2 an assumed slip is correct if λ_n^k is compressive and the relative slip increment Δ_s has the same sign as the maximum frictional value F^k. However, if Δ_s is in opposition to F^k relative slip movement cannot reverse its direction until passive frictional frictional force reverses direction, so that a fixed state for the next iteration is assumed. Lastly for row 3, an assumed free state is correct if the normal gap Δ_n^k is greater than zero, otherwise, the new state is assumed fixed. This does not imply a slip state cannot be reached from a free state; it simply implies a slip state must be reached by and iterative path; free to fix to slip.

For each iteration within the load step, Table 4-2 provides the choice for the next assumed state. However, prior to assembling the stiffness elements and constraint elements (Table 4-1) for the next trial solution, the constraint load vector parameters a, b or a, T or N, T (corresponding to fixed, slip or free) must be specified (estimated). These incremental values are dependent on the known solution at step k-1 and the current trial solution for step k. Table 4-2 gives these values located in a 3x3 matrix. For example, if a known slip state existed at load step k-1 and the next iteration for step k is to be assumed free, we set $N = -\lambda_n^{k-1}$ and $T = -\lambda_s^{k-1}$ so that the resulting trial solution will give $\lambda_n^k = \lambda_s^k = 0$, i.e. no net interface forces.

Other entries in Table 4-3 are generally self explanatory except, perhaps, for the free-to-fix case (matrix position 3, 1). Here the implication is that interface penetration ($\Delta_n^k < 0$) was observed in Table 4-2, so that we wish to assume a fixed state for the next iteration.

Accordingly, the normal gap is closed by specifying $a = -\Delta_n^{k-1}$. With regard to specifying the slip gap increment, we first observe that the ratio a/Δ_n is that portion of the normal gap increment which does not cause penetration. Thus, it is reasonable to assume that slip gap increment can be specified in this proportion, i.e., $b = \Delta_s \left| a/\Delta_n \right|$.

In brief summary, the incremental iterative algorithm is started for each load step by assuming the interface state remains as in the step just completed. For the very first load step we assume the node pairs are fixed and reside in the same geometric location. For all subsequent iterations, Table 4-1 provides the logic for determining the validity of the solution; Table 4-3 gives the corresponding load vector parameters; and Table 4-1 gives the form for the corresponding constraint matrix and load vector to be assembled. Convergence is witnessed by satisfying the criterion on the main diagonal of Table 4-2 as well as obtaining converged values for the frictional force F^k.

2.4   INTERFACE ELEMENT PROPOSED BY DESAI ET AL.

The distinguished features in the development and use of a thin solid element are to simulate interface behavior that lie in the special treatment of the constitutive laws for the thin-layer element, choice of its thickness, incorporation of various modes of deformation (Refer to Figure 4-4) and implementation for a number of problems with displacement, mixed and hybrid finite element procedures.

Schematic diagrams of the thin-layer element for two and three dimensional idealizations are shown in Figure 4-5. The element is treated essentially like any other solid (soil, rock or structural) element. However, its constitutive matrix $[C]_i$ is expressed as

$$\{d\sigma\} = [C]_i \{d\varepsilon\} \qquad (2\text{-}41)$$

Where, $\{d\sigma\}$ = vector of increments of stresses,
              $\{d\varepsilon\}$ = vector of increments of strain

and the constitutive matrix $[C]_i$ is given by

$$[C]_i = \begin{bmatrix} [C_{nn}]_i & [C_{ns}]_i \\ [C_{sn}]_i & [C_{ss}]_i \end{bmatrix} \qquad (2\text{-}43)$$

where $[C_{nn}]$ = normal component, $[C_{ss}]$ = shear component and $[C_{ns}]$, $[C_{sn}]$ represent coupling effects. Since it is difficult to determine the coupling terms from laboratory tests, at this time, they are not included.

A basic assumption made is that the behavior near the interface involves a finite thin zone (Refer to Figure 4-5) rather than a zero thickness as assumed in previous formulations. As stated earlier, it may not be appropriate to assign an arbitrary high value for the normal stiffness. Since the interface is surrounded by the structural and geological materials, normal properties during the deformation process must be dependent upon the characteristics of the thin interface zone as well as the state of stress and properties of the surrounding elements. Based on these considerations, it was proposed to express the normal stiffness as :

$$[C_n]_i = \left[C_n \left(\alpha\,^i{}_m,\ \beta\,^g{}_m,\ \gamma\,^{st}{}_m\right)\right] \qquad\qquad (2\text{-}44)$$

Where, $\alpha_m{}^i$, $\beta_m{}^g$, $\gamma_m{}^{st}$ (m = 1,2, ...) denotes the properties of the interface, geological and structural elements, respectively. From here onwards the second subscript in $[C_{nn}]$ etc. is dropped. Equation (2-44) can be written as

$$\left[\overline{C}_n\right]_i = \lambda_1 [C_n]_i + \lambda_2 \left[C_n{}^g\right] + \lambda_3 \left[C_n{}^{st}\right] \qquad\qquad (2\text{-}45)$$

Where, $[C_n]_i$ denotes normal behavior of the thin interface element, and $\lambda_1,\ \lambda_2$ and λ_3 are the participation factors varying from 0 to 1. Equation (2-45) is expressed as an addition of various components. However, it is possible to define it by using a different (polynomial) expression. One of the simplifications would be to assume $\lambda_2 = \lambda_3 = 0$ and $\lambda_1 = 1$, implying that the normal component is based on the normal behavior of the thin-layer element evaluated just as the adjacent soil element. It is possible to arrive at appropriate values for λ_1 based on a trial and error procedure in which numerical solutions are compared with laboratory or field observations. Often, it was found that satisfactory results can be obtained by assigning the interface normal component the same properties as the geological material.

For most application presented herein, $\lambda_1 = 1$ and $\lambda_2 = \lambda_3 = 0$ were adopted. As long as the significant deformation mode is stick, these values provide satisfactory results. The contribution of the participation factors becomes important when opening or debonding initiates. Preliminary work towards determination of the participation factors for normal stiffness in cyclic loading has shown $\lambda_1 = 0.75$, $\lambda_2 = 0.25$ and $\lambda_3 = 0$. Now, work towards derivation of these factors by comparison with laboratory data is in progress.

The shear component $[C_s]_i$ is obtained from direct shear or other interface shear testing devices (Refer to Figure 4-6(a)). In this study $[C_s]_i$ is assumed to be composed of a shear modulus G_i for the interface. The expression used for tangent G_i is given by:

27

$$G_T(\sigma_n, \tau, u_r) = \frac{\delta[\tau(\sigma_n u_r)]}{\delta u_r} \times t \Big|_{\sigma_n} \qquad (2\text{-}46)$$

where t = thickness of the element (Refer Figure 4-6(b) and u_r = relative displacement

a) **Constitutive Modeling**

The thin layer interface element can be formulated by assuming it to be a linear elastic, non-linear elatic or elastic-plastic. The development of its stiffness characteristic follows essentially the same procedure as solid elements, that is the stiffness matrix, $[k]_i$ is written as:

$$[k]_i = \int_V [B]^T [C^{ep}]_i [B] dV \qquad (2\text{-}47)$$

Where, [B] = transformation matrix, V = volume and $[C^{ep}]_i$ is the constitutive matrix. Then the element equations are written as:

$$[K]_i \{q\} = \{Q\} \qquad (2\text{-}48)$$

where, $\{q\}$ = vector of nodal displacements and $\{Q\}$ = vector of nodal forces.

For linear elastic behavior, $[C^e]_i$ can be expressed as

$$[C^e]_i = \begin{bmatrix} C_1 & C_2 & C_2 & 0 & 0 & 0 \\ C_2 & C_1 & C_2 & 0 & 0 & 0 \\ C_2 & C_2 & C_1 & 0 & 0 & 0 \\ 0 & 0 & 0 & G_{i2} & 0 & 0 \\ 0 & 0 & 0 & 0 & G_{i2} & 0 \\ 0 & 0 & 0 & 0 & 0 & G_{i2} \end{bmatrix} = \begin{bmatrix} [C_n]_i & 0 \\ 0 & [C_s]_i \end{bmatrix} \qquad (2\text{-}49)$$

where,

$$C_1 = \frac{E(1-\nu)}{(1+\nu)(1-2\nu)}$$

$$C_2 = \frac{E\nu}{(1+\nu)(1-2\nu)}$$

$$[C^e]_i = \begin{bmatrix} C_1 & C_2 & 0 \\ C_2 & C_1 & 0 \\ 0 & 0 & G_i \end{bmatrix}$$

(2-50)

E is the elastic (Young's) modulus, ν is Poisson's ratio and G_{ii} (I = 1,2,3) are the shear moduli defined in equation (2-46). If the shear behavior is assumed to be isotropic, G_{i1} = G_{i2} = G_{i3} . Here it is assumed that the shear response is uncoupled from the normal response represented by $[C_n]$. For two dimensional idealization, the special form of $[C^e]_i$ and its inverse form, $[D^e]_i$ are given as:

$$[D^e]_i = \begin{bmatrix} \dfrac{1-\nu^2}{E} & \dfrac{-\nu(1+\nu)}{E} & 0 \\ \dfrac{-\nu(1+\nu)}{E} & \dfrac{1-\nu^2}{E} & 0 \\ 0 & 0 & \dfrac{1}{G_i} \end{bmatrix}$$

(2-51)

For non-linear elastic behavior such as hyperbolic simulation, E, ν and G can be defined as variable moduli based on triaxial and direct shear tests. For example G_i can be written as:

$$G_i = K\gamma_w \left(\frac{\sigma_n}{p_a}\right)^n \left(1 - \frac{R_{ft}}{c_a + \sigma_n \tan\varphi}\right)^2$$

(2-52)

29

Where, K, n and R_f are material parameters, γ_w = unit weight of water, p_a = atmospheric pressure, c_a = cohesion and ϕ = angle of friction. Alternatively, the shear modulus can be obtained by expressing the τ vs u_r relation in a polynominal form described subsequently.

In addition to the foregoing linear and non-linear elastic models, the proposed formulation also allows for elastic-plastic behavior. Then the constitutive matrix for the interface is written as:

$$[C]_i^{ep} = [C^e (k_s, k_n \{du_r^p\})]_i \tag{2-53}$$

where, $\{du_r^p\}$ = vector of incremental relative displacements. The second part of equation (2-53) is found on the basis of yield and flow criteria of the theory of plasticity. Here conventional criteria such as Mohr-Coulomb can be used with yield function, f, and plastic potential function, Q; for associated plasticity f = Q. To allow for dilatancy in the case of rock joints different f and Q can be used in the context of non-associative plasticity.

b)   **Stick, slip, debonding and rebound modes**

Depending upon the material model used, criteria such as Mohr-Coulomb and Drucker-Prager are used to define the initiation of slip at the interface; before the slip, the interface is assumed to be in the stick or no slip mode (Refer to Figure 4-4(a)). The stick mode and the slip mode can occur such that the normal stress is compressive. During debonding, the computed normal stress can be tensile, but physically, it is zero at the interface. In subsequent loading or unloading, an interface that has experienced opening or debonding may close or rebond. This is identified when the normal stress in the interface becomes compressive. In soil-structure interaction problems, penetration nodes is not permitted during closing. In a non-linear incremental analysis, the (excess) tensile stress is redistributed in the surrounding zones during the iterations at each load increment. Thus the stick, slip, debonding and rebonding are accounted for.

c) Testing for interface modelling

For the static and cyclic behavior of interfaces and a new piece of equipment called a cyclic multi–degrees of freedom device has been developed. It can permit testing for interfaces and joints under stress and strain controlled loading and for translational, rocking modes.

2.5.1 SIMULATION OF INTERFACE MODES

The quality of simulation of the interface behavior depends upon a number of factors such as physical and geometrical properties of the surrounding media, non-linear material behavior and the thickness of the thin-layer element. If the thickness is too large in comparison with the average contact dimension (Refer to Figure 4-5) or the surrounding elements, the thin layer element will behave essentially as a solid element. If it is too small, computational difficulties may arise. Desai, et al. (1984) have proposed that for satisfactory simulation of the interface behavior, the ratio of thickness to the average contact dimension (t/b) should lie between 0.01 and 0.10.

Various deformation modes that an interface can experience are incorporated in the thin layered element. It is assumed that before the application of load the interface elements are in stick or non-slip mode. Mohr-Coulomb yield criterion is used to identify the various modes of deformation. For a given increment of load, the normal stress σ_n and the total shear τ on the plane of interface element are calculated. The modes of deformation are then checked and if the element is found to be in separation or slip mode, appropriate redistribution of stresses is performed. Details of the adopted procedure are given as follows:

- The normal stress σ_n and shearing stress τ due to the loading in a particular increment is calculated for the interface plane. Then the sign of normal stress σ_n is checked. If the sign is positive (compressive stress) the element can be either in stick mode or in slip mode. If σ_n is negative (tensile stress) the element is considered to be in separation mode.

31

- For value of σ_n is positive, the stick or slip mode is determined using the limiting shear stress of the interface. The limiting shear stress τ_L in the shear plane is calculated based on Mohr-Coulomb criteria which is:

$$\tau_L = c_a + \sigma_n \tan \varphi_a$$

Where, c_a is the adhesion and ϕ_a is the angle of friction between structure and soil.

- If $\tau \leq \tau_L$ then, the element is in non-slip or stick mode and there will be no redistribution of stresses and no change in the stiffness parameters E and G_i.

- If $\tau > \tau_L$ then the element is in slip mode and the shear stress τ would be made equal to the limiting shear stress τ_L. Thus, the unbalanced load due to the excess shear stress $(\tau - \tau_L)$ would be applied at all nodes of the interface elements as self-equilibrating load in the next increment. The equivalent nodal loads due to stresses in an element is calculated by:

$$\{F\} = \int [B]^T \{\sigma\} dV$$

- For negative value of σ_n, i.e. separation mode, both the shear stress, τ and normal stress, σ_n are made to be almost zero. But with a negative sign (say, -2.7×10^{-30}). As a result, the unbalanced nodal loads, calculated using the above equation is applied at nodes of interface elements as self-equilibrating load in the next load increment. The E and G_i values at this stage are actually zero. In order to avoid any numerical difficulties, a very low value of E and G_i are assigned for the next step of analysis.

- To check the possibility of rebonding, the sign of normal stress for each individual loading increment is checked. If it is positive, the total normal stress which was negative previously is made to be equal to zero. As a result, it is no longer negative and falls into the category of stick or slip mode. Then the element would undergo the same steps as experienced by a normal interface element with positive normal stress.

TEST PROBLEMS

2.6.1 Direct Shear Test

Figure 2-3(a) shows a schematic diagram of a direct shear test device in which the bottom half is concrete and the top half contains soil. A series of tests were performed with concrete-sand interface under different normal loads. Figure 2-4 shows two typical test results for the sand with a relative density around 80 per cent for two normal loads.

(a) Direct Shear Test for Concrete-soil Interface

(c) integration points

(b) Idealization of Direct Shear Test for Concrete-soil Interface
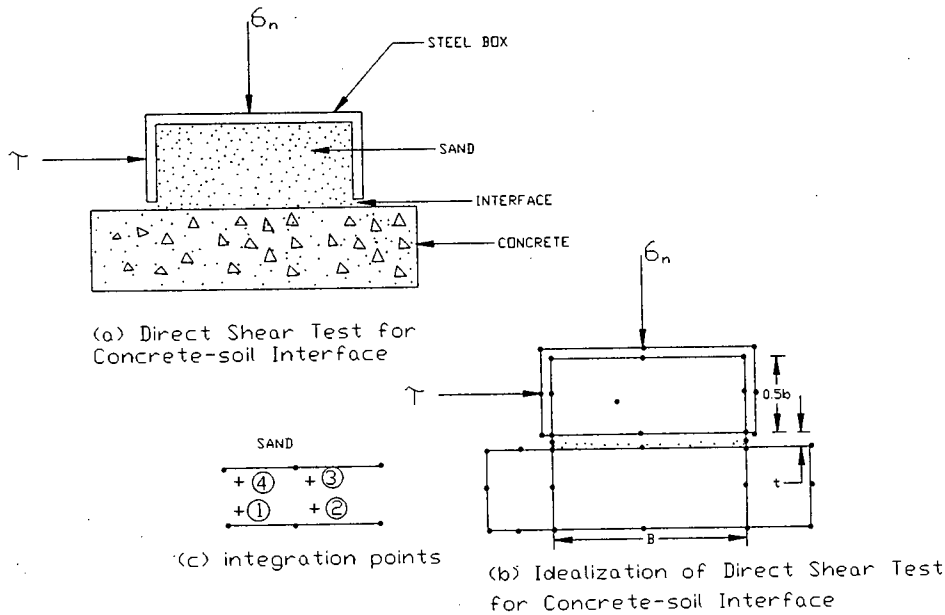
Figure 2-3: Analysis for Direct Shear Test For Choice of Thickness (Desai, C.S, Zaman, M.M., Lightner, J.G. and Siriwardane, H.J., 1984)

The direct shear test data for the normal stress of σ_n=4.89 t/ft^2 (4.77 kg/cm^2) and σ_n=9.79 t/ft^2 (4.77 kg/cm^2) were analysed by using a two-dimensional plane strain finite element procedure. The shear stress vs. relative displacement curve was simulated by using a polynomial function:

$$\tau = \alpha_1 u_\tau + \alpha_2 \sigma_n u_\tau + \alpha_4 \sigma_n^2 u_\tau^2 \tag{2-54}$$

Where α_i (i = 1,2,....,4) are constants. Here the values of α_i were found to be α_1=53 kg/cm^3, α_2=8.2 kg/cm^{-1}, α_3=8.2 kg/cm^4, α_4=7.0 kg^{-1}. The tangent stiffness k_s in equation 2-54 was evaluated as the derivative of τ with respect to u_r at a point during the incremental loading.

The finite element mesh using eight-node isoparametric elements is shown in Figure 2-3(b). The outside metallic box was also discritised and the shear load was applied at the mid-node on its vertical side. The material properties used are given below:

Soil:

Initial modulus:	E_s=1,000 kg/cm^2
Poisson's ratio	v_s=0.375

Concrete:

E_c=1.5x10^5 kg/cm^2

v_c=0.375

Interface:

Adhesion	$c_a = 0.0$
Angle of friction	$\phi = 38^0$, tan$\phi = 0.7813$
Initial modulus	$E_I = 10^3$ kg/cm^2
	v_i=0.375
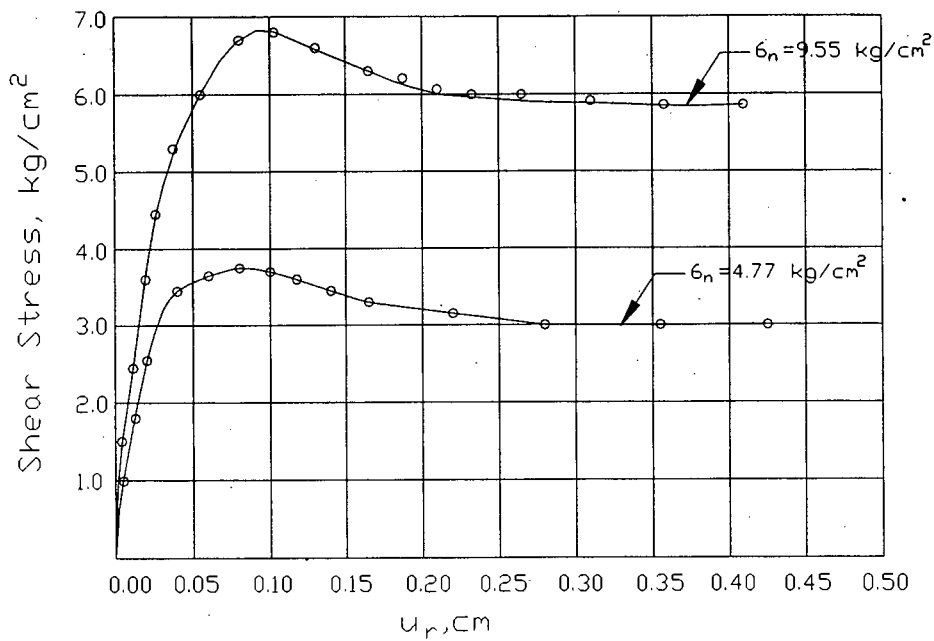
Figure 2-4: Typical Direct Shear Test Results, D_r = 80 Per Cent(Desai, C.S, Zaman, M.M., Lightner, J.G. and Siriwardane, H.J., 1984)
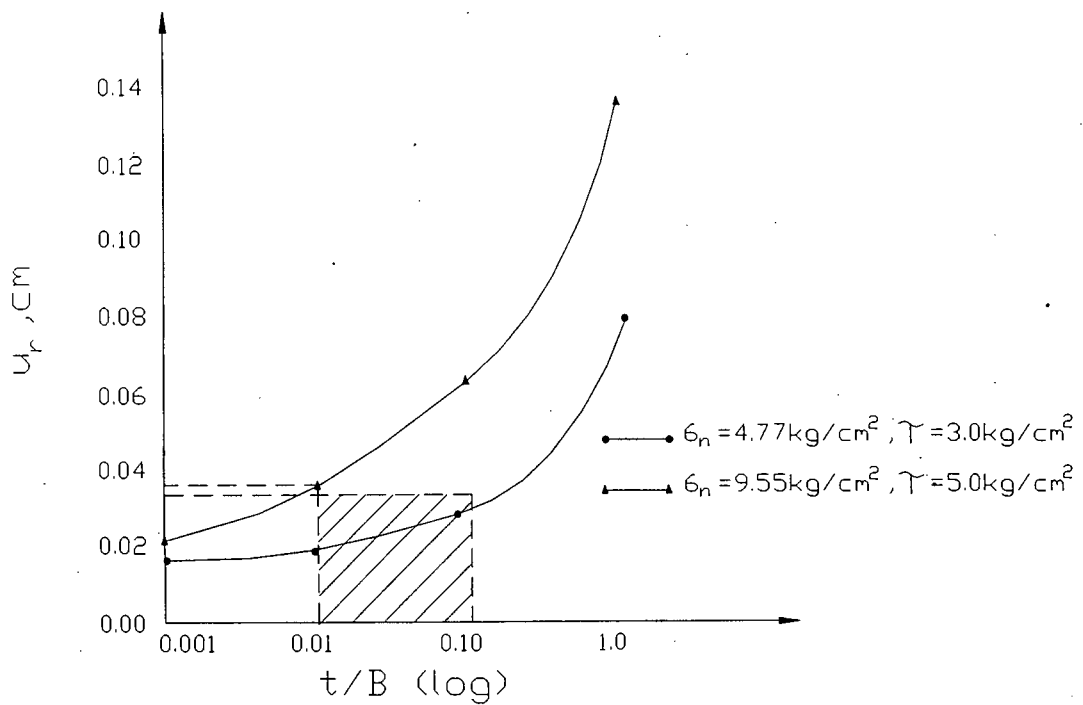
Figure 2-5: Effect of Thickness of Interface Element(Desai, C.S, Zaman, M.M., Lightner, J.G. and Siriwardane, H.J., 1984)

The thickness t, of the element was varied such that the ratio t/B was 0.001, 0.010, 0.100 and 1.00. Since the shear modulus G_i is a function of the thickness, its value also varied with the thickness.

The computed results in terms of (relative) displacement, u_r, and the ratio t/B for applied shear stress τ = 3.0 kg/cm^2, σ_n = 4.77 kg/cm^2, and τ = 5.0 kg/cm^2, σ_n = 9.55 kg/cm^2 are plotted in Figure 2-5. The computed displacements show a wide variation as the thickness is changed. However, the results in the range of 0.01 to 0.10 of t/B show satisfactory agreement with the observed values of 0.032 cm for the test and 0.034 cm for the tests with σ_n = 4.77 kg/cm^2 and 9.55kg/cm^2 respectively (Figure 2-4). Note that for higher and lower values of t/B than this range, the computed displacements are much different from the measured values.

Table 2-1:   Distribution of Shear Stress in Interface Element at Integration Points
(Figure 2-3(c)) (Desai, C.S, Zaman, M.M., Lightner, J.G. and Siriwardane, H.J., 1984)

σ_n=4.77kg/cm^2	Integration points				
t/B	1	2	3	4	Average
1	2.3939	3.6034	2.1203	3.8771	2.9987
0.1	2.7390	3.2602	2.7049	3.2940	2.9996
0.01	3.0022	2.9975	2.9975	3.0022	2.9999
0.001	2.9967	3.0021	2.9964	3.0025	2.9994
σ_n=9.55kg/cm^2					
1	3.7868	6.2084	3.239	6.7562	4.9976
0.1	4.4778	5.5210	4.4093	5.5895	4.9994
0.01	5.0044	4.9950	4.9950	5.0044	4.9997
0.001	4.9914	5.0065	4.9950	5.0075	4.9990

Table 2-1 shows computed values of shear stresses at the four integration points (Figure 2-3(c)) of the interface element. It can be seen that the best correlation between computations and the applied stresses of τ = 3.0 kg/cm^2, σ_n = 5.0 kg/cm^2 is obtained for a t/B ratios smaller than 0.10. Although the average values of the computed stresses are not significantly different for the ratios considered, the uniformity of computed stresses is greater for t/B ratios smaller than 0.01.

Based on the foregoing results, it can be concluded that satisfactory simulation of interface behavior can be obtained for t/B ratios in the range from 0.01 to 0.10. This conclusion may need (small) modifications if the non-linear behavior of soils and interfaces were simulated by using other or advanced constitutive models.

Pande and Sharma (1979) reported that thin element provided satisfactory results for much lower ratios of t/B. From the view points of both the displacements and stresses, use the ratio t/B in the range 0.01 to 0.10 can be appropriate. The ratio can vary during mesh refinement; however, if it remains within this range, the thin layer element can provide satisfactory simulation of the interface behavior.

2.6.2 Pull-Out Test
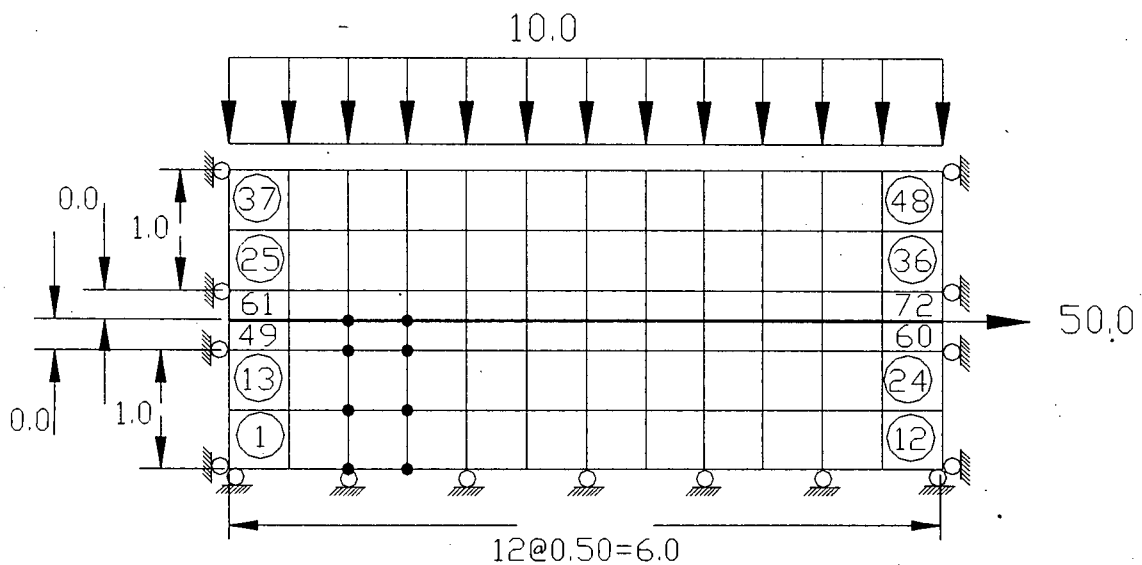
Figure 2-6:   Simulated Pull-Out Involving Zero Thickness Interface Element
(Kaliakin, V. N. and Li, J, 1995)

The finite element mesh shown in Figure 2-6 represents a simulated pull-out from a surrounding continuum. The continnum is modeled by four-node quadrilateral elements numbered 1 to 48. Element 49 to 72 are interface elements, and the inclusion of zero thickness interface element is represented by twelve two-node bar elements (for clarity, these

are not numbered in Figure 2-6). In order to better focus attention on the interface, both the continnum and the inclusion are indealised as isotropic, linear elastic materials. The elastic modulus and Poisson's ratio for the continnum are 2.0×10^3 and 0.25 respectively. The self – weight of the continnum material is considered to be negligible, and a state of plane strain is assumed. For the inclusion, the elastic modulus and cross-sectional area are taken equal to 2×10^4 and 0.10 respectively. The shear strength of the interface is assumed to be governed by a Mohr-Coulomb criterion with a friction co-efficient equal to 0.50 and cohesion intercept equal to zero. A normal distributed compressive load equal to 10.0 is applied in the first solution step and is maintained constant throughout the remainder of the loading history. The horizontal load is applied monotonically from a value of zero at the solution step to a value of 50.0 at the twenty-first step.

The normal response of the interface elements is first assessed. In elements such as the GTB, LRH and LK1 (Refer to Section 2.2) that employ a penalty type formulation, momentum is exactly conserved while compatibility is approximated. Since in the first solution step only the uniform normal distributed load is applied to the mesh, the normal response can easily be assessed from just this one step. The results of such analyses, for different values of d_{22} and for different interface elements, are summarized in Table 2-2. In order to realize comparable vertical (normal) displacements, the values of d_{22} used for the LK1 elements are three times those used for the GTB and LRH element

TABLE 2-2:   Summary of Results for Response Normal to Interface
             (Kaliakin, V. N. and Li, J, 1995)

Element (d$_{22}$)	Average Vertical Stress in Elements 1-12	Average Vertical Stress in Elements 13-24	Average Vertical Stress in Elements 25-36	Average Vertical Stress in Elements 37-48	Relative Vertical Displacement Along Interface
GTB (10^8)	-10.00	-10.00	-10.00	-10.00	2.0x10^{-7}
LRH (10^8)	-10.00	-10.00	-10.35	-19.35	2.0x10^{-7}
LK1 (3x10^8)	-10.00	-10.00	-10.00	-10.00	2.0x10^{-7}
GTB (10^{12})	-10.00	-10.00	-10.00	-10.00	2.0x10^{-11}
LRH (10^{12}	No Convergence	n/a	n/a	n/a	n/a
LK1 (3x10^{12})	-10.00	-10.00	-10.00	-10.00	2.0x10^{-11}
GTB (10^{16})	-10.00	-10.00	-10.00	-10.00	2.0x10^{-15}
LRH (10^{16})	No Convergence	n/a	n/a	n/a	n/a
LK1 (3x10^{16})	-10.00	-10.00	-10.00	-10.00	2.0x10^{-15}

From Table 2-2 it is evident that even for values of d$_{22}$ equal to 10^{16}, the normal stress associated with the GTB and LK1 elements are exactly transmitted across the interface. Furthermore, the use of large values of d$_{22}$ yields relative normal displacements across the interface that are effectively zero. In comparison, the normal response of the LRH element was obviously unacceptable. In particular, for large values of d$_{22}$ convergence could not be realised. This performance characteristic, which has also been found to mesh-specific, further supports previous observations concerning the lack of robustness of this element in simulating response normal to the interface. For this reason, the LRH element could not be included in the subsequent pull-out simulations.

The combined normal and tangential response of the GTB and LK1 elements is considered next. In particular, the simulated pullout test shown in Figure 2-6 is analysed. For the GTB elements the values $d_{11} = 1.0 \times 10^6$ and $d_{22} = 1.0 \times 10^{10}$ are assumed, for the LK1 element $d_{11} = 1.0 \times 10^6$ and $d_{22} = 4.0 \times 10^{10}$.
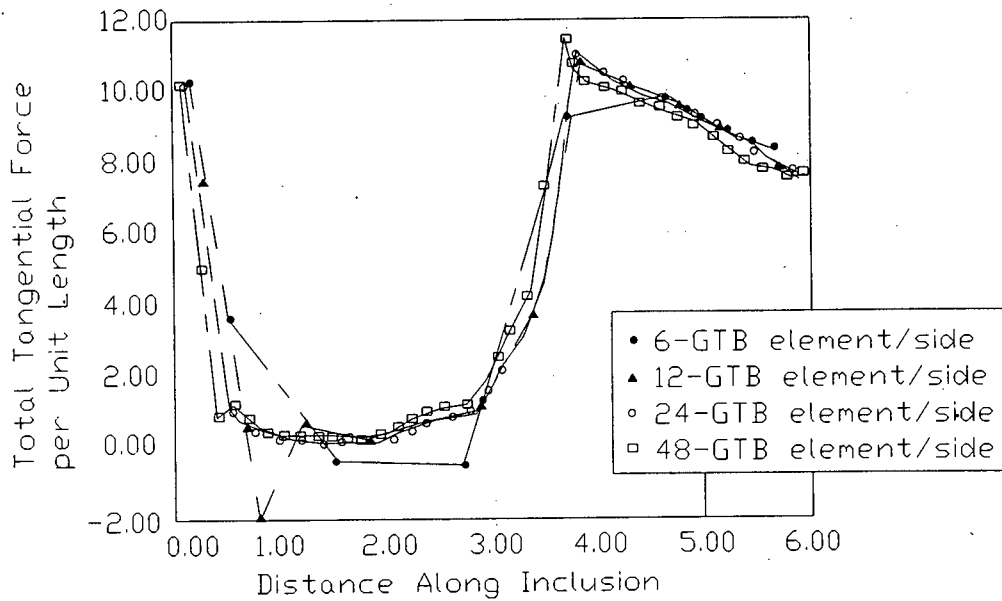
Figure 2-7:   Distribution of Total Tangential Force Along Inclusion at Load of 30.0: GTB elements (Kaliakin, V. N. and Li, J, 1995)

The response of the GTB element is first analysed. In order to verify the convergence of this element, three other mesh were created in addition to that shown in Figure 2-7. In these meshes the number of interface elements along each side of the inclusion was equal to six, twenty-four and forty-eight. For each of the four meshes, the distribution of total tangential force along the inclusion at a pull-out force equal to 30 is shown in Figure 2-7. From this figure it is evident that : (a) convergence is realized, but with some oscillations in the sign of the tangential force for the two coarsest meshes; and (b) mesh refinement eventually removes the oscillations, through acceptable results require a mesh containing 24 elements per side.
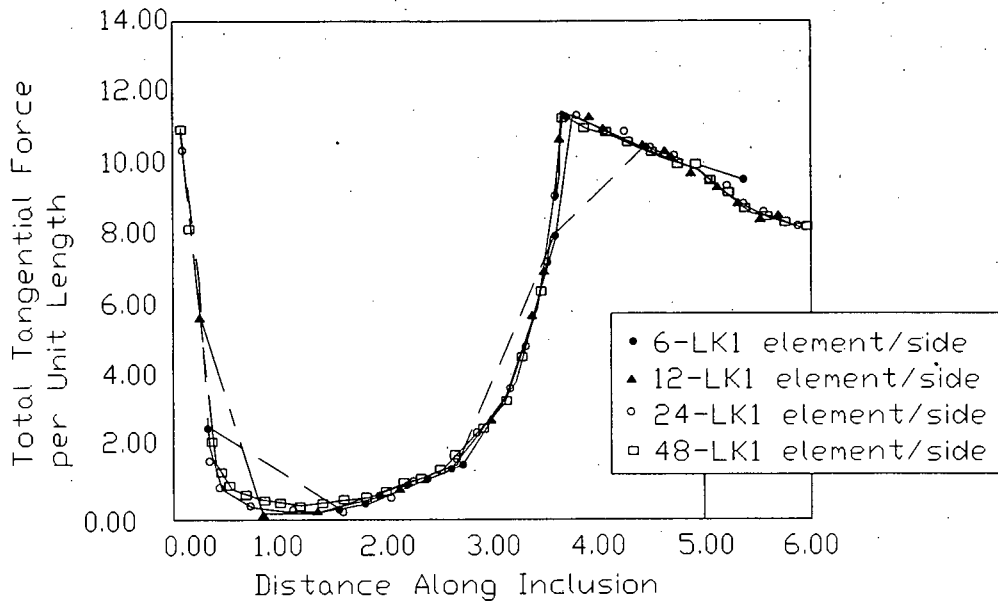
Figure 2-8:   Distribution of Total Tangential Force Along Inclusion at Load of 30.0: GTB elements (Kaliakin, V. N. and Li, J, 1995)

The results of a similar convergence study for the LK1 element are presented in Figure 2-8. From this figure it is evident that: (a) monotonic convergence is realized; and, (b) the result associated with the mesh containing twelve elements on either side of the inclusion are practically identical to those associated with the finer meshes. As such, the mesh shown in Figure 2-6 and used in the previous portions of this example is deemed sufficiently fine.

In summary, it has been shown that the normal response of the LK1 element to be associated with the LRH element. The combined normal and tangential response of the LK1 element was found to be superior to that of the GTB element. More precisely, the force oscillations associated with the latter element have been removed from the response of the former. With respect to the tangential force distributions, the convergence of the LK1 element was found to be superior to the GTB element. Finally, it is pertinent to note that the capabilities of the LK1 element for simulating actual laboratory pull-out experiments have recently been assessed. The agreement between numerical results and experimental measurements was found to be quite good.

CHAPTER 3

3 SOLUTION TECHNIQUES

3.1 GENERAL

In Dynamic relaxation (DR) a system undergoes damped vibration excited by a momentum constrained force which ultimately comes to at rest in the displaced position of static equilibrium of the system under the action of the stationary force. As it attains a static solution through a dynamic process, it is sometime called 'pseudo-transient' or 'fictitious dynamic' process. This solution method was initially developed as an alternative to linear solution techniques. It has got high ability to solve nonlinear geometric and material behavior. It is a very suitable method for computation of since it treats all quantities as vectors which results in easy programmable method. The implementation of force-level DR solvers has undergone a significant success in treating problems with strong, sharp nonlinearities like non-associated flow in plasticity with large non-normality and very high friction angle.

3.2 DYNAMIC RELAXATION SOLUTION STRATEGY

3.2.1 Dynamic Relaxation Equations

The governing equations for nonlinear geometry and material behavior are given by the following:

$$P - P^{init} = F$$
$$\text{and } P = \sum_N \int_{ve} B\sigma \, dv$$

(3-1)

Where,

P is the vector of internal forces.

$\mathbf{P}^{\text{init}}$ is the vector of nodal forces due to initial stresses.

$\mathbf{F}$ is the vector of external forces.

$\mathbf{B}$ is the displacement-strain transformation matrix.

N is the number of elements in the FEM discretization.

σ is the vector of stresses in each element.

ve is the volume of each element.

The solution to the above governing equations are obtained from the steady state response of a dynamic equation of motion;

$$\mathbf{m\ddot{u}} + \mathbf{c\dot{u}} + \mathbf{P} - \mathbf{P}^{init} = \mathbf{F} \tag{3-2}$$

Where,

$\mathbf{m}$ is the mass matrix.

$\mathbf{c}$ is the damping matrix.

$\ddot{u}$ is the acceleration vector.

and $\dot{u}$ is the velocity vector.

Applying the central difference technique to Equation 3-2, we get;

$$\dot{\mathbf{u}} = \frac{\mathbf{u}^{t+\Delta t} - \mathbf{u}^{t-\Delta t}}{2\Delta t} \tag{3-3}$$

$$\ddot{\mathbf{u}} = \frac{\mathbf{u}^{t+\Delta t} - 2\mathbf{u}^{t} + \mathbf{u}^{t-\Delta t}}{(\Delta t)^2} \tag{3-4}$$

where, Δt is the time increment.

Using a diagonal mass matrix $\mathbf{m}$, the damping matrix is determined as:

$$\mathbf{c} = \alpha\mathbf{m} \tag{3-5}$$

where, α is the damping ratio.

Substituting Equations 3-3, 3-4 and 3-5 into Equation 3-2), we get,

$$\mathbf{u}^{t+\Delta t} = \frac{1}{(1+0.5\alpha\Delta t)} \left[\frac{\Delta t^2}{\mathbf{m}} \left(\mathbf{F} - \mathbf{P} + \mathbf{P}^{init} \right)^t + 2\mathbf{u}^t - (1 - 0.5\alpha\Delta t)\mathbf{u}^{t-\Delta t} \right] \qquad \cdot(3\text{-}6)$$

The above equation is a time marching equation, which has to be solved explicitly. Hence a limitation of the critical time step is imposed on this equation, which will be discussed in the latter subsequent sections.

3.2.2 Damping Parameter Determination

The determination of the damping value is the most critical one in the dynamic relaxation method. For a given arbitrary damping factor much larger amount of computer time is required to get the damped static value. So, many researchers suggested several methods to determine the critical damping factor. Those methods are listed below:

♦ Method 1: This method (Alwar et al., 1984) does not need to calculate nearly critical damping factors. Rather this method uses the decaying exponential envelope of the damped oscillations as the basis for determining the converged static solution.

♦ Method 2: The variation of kinetic energy of an undamped free vibration for a system is monitored (Rushton, 1968, Pica et al., 1980, Bicanic, 1979). By observing the first peak in kinetic energy variation, critical viscous damping factor, $\mathbf{c} = \omega$ is calculated as:

$$\omega = \frac{2\pi}{T}$$
$$T = 4T_1$$
$$\qquad \cdot(3\text{-}4)$$

Where T_1 is the time to obtain the first peak in kinetic energy.

♦ Method 3: This method suggests that the kinetic energy of the structure be constantly monitored and when the energy peak is detected, all the current velocities be set to zero (Papadrakakis, 1981a, Cundall, 1976). Using this approach, the viscous damping coefficient of Equation 3-2) is neglected and the equation of motion becomes,

$$\mathbf{m\ddot{u}} + \mathbf{Ku} = \mathbf{F} \qquad (3\text{-}5)$$

44

♦ Method 4: In this method critical damping parameter is estimated by Rayleigh's quotient (Bunce, 1972) as follows:

$$c = 2\sqrt{\frac{\mathbf{x}^T \mathbf{K} \mathbf{x}}{\mathbf{x}^T \mathbf{m} \mathbf{x}}} \qquad (3\text{-}6)$$

Where,

x is the eigenvectors (incremental displacement is also acceptable for approximate damping factor)

K is the full or diagonal (approximate) stiffness matrix.

m is the diagonal mass matrix.

♦ Method 5: The fifth approach is by Papadrakakis (1981). He calculated a series of approximation to the dominant eigenvalue λ_{DR} from,

$$\lambda_{DR} = \frac{\left\| x^{n+1} - x^n \right\|}{\left\| x^n - x^{n+1} \right\|} \qquad (3\text{-}7)$$

When λ_{DR} converged to almost a constant value, then this is the minimum eigenvalue needed to determine 'c' for the optimum iteration parameter.

All the methods except Method 4 need some fruitless iterations only to determine the damping parameter or achieve kinetic damping. So, in this formulation Method 4 is used. The Rayleigh's norm shown in Method 4 is proposed mainly for linear analysis. For nonlinear problem, the same expression as Equation 3-6) can be used, selecting the nodal displacement vector u and the local tangent stiffness matrix K. The tangent stiffness matrix K is approximated by the diagonal form as:

$$\mathbf{K} = \frac{{}^t\mathbf{P} - {}^{t-\Delta t}\mathbf{P}}{\Delta t \cdot {}^t\dot{\mathbf{u}}} \qquad (3\text{-}8)$$

where,

${}^t\mathbf{P}$ and ${}^{t-\Delta t}\mathbf{P}$ are components of the internal force vector at time t and $t - \Delta t$, respectively, and ${}^t\dot{\mathbf{u}}$ is a component of the velocity vector at time t.

3.2.3 Stabilization and optimization

The dynamic relaxation scheme is an explicit formulation, and all the explicit time-wise integration procedure which uses the central difference formula is only conditionally stable. In many cases this restricts the choice of the time interval to very small values if numerical instability is to be avoided. It has a definite limit of time step length beyond which the solution method becomes unstable. This is governed by the well-known Courant-Friedrichs-Levy condition. Actually it says that $\Box t$ cannot be larger than the time taken by the two adjacent nodes of the mesh to transfer the information of deformation. This instability arises mainly from the mismatch of integration speed and deformation wave speed. Mathematically this condition can be expressed as:

$$\Delta t \le \beta \frac{l}{V_c}$$ (3-9)

where β is a factor to control the stability and speed of computation($\beta \le 1.0$). l is the minimum distance between the adjacent nodal points for an element. For constant strain elements, the value of β can be near 1.0, but for higher order elements it reduces very fast. V_c is the constrained compression wave velocity of the medium, since the pseudo-densities are calculated separately in each of the x and y directions. From Equation 3-9) we get the following expression:

$$\Delta t = \beta l \sqrt{\frac{\rho(1+v)(1-2v)}{E(1-v)}}$$ (3-10)

Following the above equation, the stability of the integration of the equation of motion can be assured but the critical time for stability may be too short, thus too conservative. So various forms of fictitious mass are introduced in order to increase the convergence rate towards the static solution. In the literature the following methods proposed to estimate the fictitious density:

◆ A unit mass matrix (Rushton and Laing,1968a).

◆ A real mass matrix computed from different densities corresponding to the u,v and w directions (Rushton, 1968, Alwar et al., 1974) .

46

- A diagonal mass matrix obtained from the stiffness matrix K, in which the ith component is given by $m_{ii} = \sum_{j=1}^{r} K_{ij}$ where r is the order of K_{ij} (Brew and Brotton, 1971).

- A diagonal mass matrix obtained from the stiffness matrix K, in which the ith component is given by $m_{ii} = K_{ii}$ (Brew and Brotton, 1971).

- The most effective method for determining the elements of **m** is to choose m_{ii} in such that the transit time for deformation wave for the degree of freedom 'i' to the adjacent and similar degrees of freedoms is a constant. Usually this constant is linked to the time step, $\Delta t = 1$. So m_{ii} is determined in such a way that Δt is always equal to 1 according to the stiffness of the medium through which deformation wave is proceeding (Cassel and Hobbs, 1976).

Among these methods, essentially the fifth one is employed here to have the optimum speed of convergence. Based on Equation 3-10) a scaling method can be introduced, which is essentially a mesh homogenization. Namely, an artificial mass density ρ is calculated from Equation 3-10) on the element-by-element basis so as to give the same transit time across each element for any element size. In this way, deformation information (unbalance forces) travels uniformly over the whole mesh irrespective of different size elements. In this way, the computational speed can be maximized by minimizing the ratio of maximum to minimum eigenvalues of the system. So, from Equation 3-10), taking $\Delta t = 1$, we can have the fictitious density for the pseudo-mass matrix: as:

$$\rho = \frac{E(1-v)}{\beta^2 l^2 (1+v)(1-2v)} \qquad (3\text{-}11)$$

where, E is the Young's modulus of elasticity, v is the Poisson's ratio. l is the minimum distance between the adjacent nodes of an element in the FEM mesh. ρ is the fictitious density varying from element to element in the FEM mesh. It is already said that β is a factor ($0 < \beta < 1$) controlling the stability and speed of convergence. $\beta = 1$ means that the integration scheme will have maximum speed and $\beta \approx 0.0$ means that it will have the lowest speed. In all of the numerical tests described in later chapter, the only adjustable DR parameter was β, which was set equal to 0.6 to achieve the stability of the explicit DR

47

computation. All the other parameters were adapted and adjusted automatically throughout the equilibrium iterations.

3.3 TRACING THE EQUILIBRIUM PATH

In this section, the DR method is evaluated from the view point of its ability in tracing the whole equilibrium curve in the load-displacement (stress-strain) space exhibiting post-peak softening. In the case of material non-linearity, usually there is a snap-through. This problem has been handled in three ways: (a) load control with a real time dynamic solution at post-peak, (b) direct displacement control and (c) arc-length control. Three types of DR solution strategy were employed to solve this type of material non-linear problem. A new way of tracing the whole equilibrium curve with DR has been derived using an arc-length from the origin (Ramesh and C. S. Krishnamoorthy, 1993) and an adaptive DR technique (Underwood, 1983). The arc-length method of solution, which was originally developed by Riks (Riks, 1979) and Wempner (Wempner, 1971), and later developed and applied by Crisfield (Crisfield, 1981) and others to some boundary-value problems, was used in this study. Further, the load control method was augmented by a real-mass dynamic solution to capture the post-peak part of the equilibrium path. The direct displacement control method (Batoz and Dhatt, 1979) was also applied to trace the whole equilibrium curve.

3.3.1 Load Control Strategy

Using the following substitutions in Equation (3-6),

$$\xi = 0.5\alpha\Delta t, \delta_1 = \frac{1}{1+\xi}, \delta_2 = 1-\xi$$

$$\mathbf{m}' = \frac{\Delta t^2}{\mathbf{m}}, \mathbf{R}' = \left(\mathbf{F} - \mathbf{P} + \mathbf{P}^{init}\right)'$$

(3-12)

48

Equation (3-6) can be rewritten in the following concise form;

$$\mathbf{u}^{t+\Delta t} = \delta_1 \left(\mathbf{m}^t \mathbf{R}^t + 2\mathbf{u}^t - \delta_2 \mathbf{u}^{t-\Delta t} \right) \tag{3-13}$$

In the load control solution method, Equation 3-13) is followed strictly up to the peak state until the residual grows to a predetermined threshold value. After that moment the solution in the post-peak is sought by following a dynamic solution with a realistic damping ratio. This is shown schematically in Figure 3-3.

3.3.2 Displacement Control Strategy

In the displacement control solution, some of the displacement components are fixed during one load step while the others are solved. Equations for fixed displacement components are as follows:

$$\mathbf{u}^{t+\Delta t} = \delta_1 \left(\mathbf{m}^t \mathbf{R}^t + 2\mathbf{u}^t - \delta_2 \mathbf{u}^{t-\Delta t} \right)$$
$$\mathbf{R}^{t-\Delta t} = 0, \delta_1 = \delta_2 = 1.0, \mathbf{u}^t = \mathbf{u}^{t-\Delta t} \tag{3-14}$$

The other degrees of freedom are solved by Equation 3-13) as usual, which is shown in Figure 3-4.

3.4 CONVERGENCE CRITERION

In this analysis, convergence was checked by checking the global residual force norm as follows:

$$\frac{\left(\left\| F - P + P^{init} \right\| \right)^2}{\left(\left\| F \right\| \right)^2} \leq \varepsilon_1 \tag{3-15}$$

and the differential residual force norm between two successive iterations,

$$^{n}\left(\left\| F - P + P^{init} \right\| \right)^2 - ^{n+1}\left(\left\| F - P + P^{init} \right\| \right)^2 \leq \varepsilon_2 \tag{3-16}$$

In this analysis, most of the computations were made, based on $\varepsilon_1 = \varepsilon_2 = 10^{-6}$. Differential tolerance is necessary to make the solutions independent of number, size of finite elements. Some analysis done with other tolerance values will be described where needed. This specific value was chosen considering a compromise between the computation time and desired accuracy. It has been checked that for one order reduction in that tolerance, the computation time doubles although results did not change significantly.

3.5   REDUCED INTEGRATION

The use of reduced integration technique in the development of FEM analysis can be traced through the references to Zienkiewicz and his colleagues, Nagtegaal et al. (1974), Sandhu and Singh (1978) and Bicanic and Hinton (1979) and Pica and Hinton (1980). Reduced integration uses the quadrature rule which doesn't integrate exactly all the terms contributing to the governing coefficient matrix. Often the stresses obtained from models based on reduced integration are more accurate than those obtained from models based on integration orders sufficient to integrate exactly all contributions to the governing coefficient matrix.

The improvement of accuracy by using reduced integration can be explained according to Kelly (1980). According to Kelly, there are two basic way of FEM formulation. One is based on displacement formulation and the other is the assumed stress method. The former model is mostly used. In this analysis, also this kind of FEM approximation is used. They are based on parametric displacement fields ensuring compatibility of deformations both internal of the elements and across the boundaries. Displacement field is usually approximated within an element by applying some polynomial and constraints in terms of known displacements. This model usually produces too stiff responses as it always underestimates the internal strain energy. So it gives an upper bound solution. The second type of models are based on the assumed parametric stress fields maintaining the internal equilibrium and assuring continuous stress transmission between element boundaries. Here,

the whole stress field is in equilibrium. This model is too flexible as the physical constraint of compatibility is not enforced. It always overestimate the internal strain energy and giving a lower bound solution. Uniformly reduced integration gives result in-between the upper and lower bound solution, thus improving the accuracy of solution.

However, the use of low order integration for all terms in the coefficient matrix can lead to a hourglass mode or a zero energy (Irons and Ahmads, 1980) displacement pattern in the model. These modes produce rigid body motion and the mesh starts self-straining, consequently the solution is destroyed. Flanagan et al. (1981) showed that elastic and viscous resistance can stabilize hourglass mode. Kelly (1980) showed that proper constraintment can eliminate any redundant load path (zero energy mode) also. In this analysis, an anti-hourglass scheme (Flanagan et al.,1981) of elastic resistance (0.05% of the elastic shear modulus of material) is used to prevent the hourglass model. This fractional value is decided after some trial and error runs with the objective that it should be kept at the minimum level while preventing the zero-energy mode. Otherwise it stiffens the solution.

3.6   STRESS UPDATING

In the way of the solution of the non-linear incremental equilibrium equations, the elasto-plastic incremental stress-strain relations are integrated. This integration is based on either incremental or iterative strains. Based on the type of strain increments, stress and other state variables are updated either incrementally or iteratively as shown in Figure 3-1.
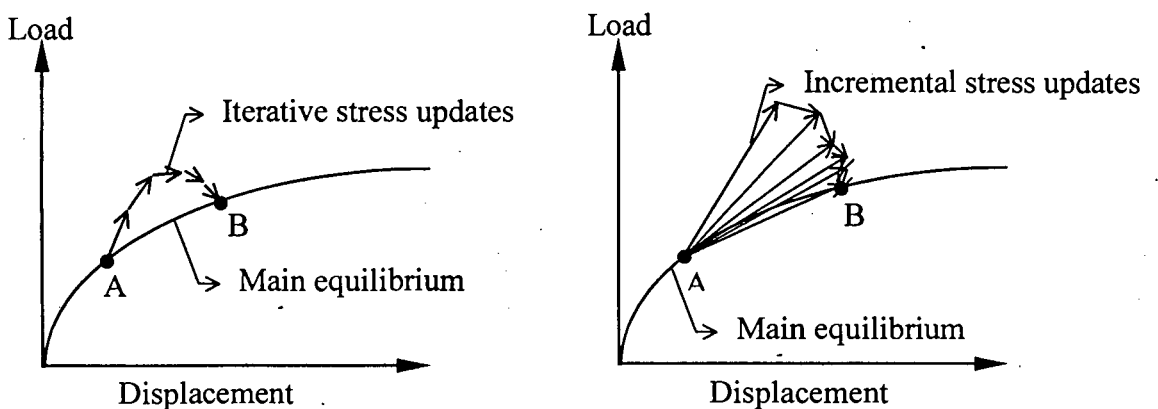

Figure 3-1:   It shows the iterative and incremental solution strategy.

3.6.1 Iterative Stress Update

Iterative stress update is based on the iterative strain updated. The solution method used here is a Dynamic Relaxation (DR) method consisting of time marching scheme, therefore, at any point of equilibrium iteration it is possible to compute the iterative strains and hence the iterative stress, which can further be integrated and updated. The drawback of this method is the 'spurious unloading' due to the iterative nature of the strain increment and the iterative strain produced by DR is most likely to oscillate initially due to the nature of any dynamic solution scheme.

3.6.2 Incremental Stress Update

Incremental stress update is on the incremental strain update. Due to solution procedure (DR), incremental strain has to be calculated from the last equilibrium position as shown in Figure 3-2. Obviously, in incremental stress update more CPU is used due to the larger incremental strain (stress). But with a good elasto-plastic incremental stress-strain integrating tool, it produces more accurate results. Best of it is that it reduces the 'spurious unloading', which can be significantly high in case of DR as it is based on explicit dynamic time marching scheme.

```
┌─────────────┐
│ Equilibrated│
│displacements│
│     D_0     │
└─────────────┘
      │ DR equilibrium iteration
      ▼
┌─────────────┐
│ Intermediate│
│ displacement│
│   D^{n=1}   │
└─────────────┘
      │
DR equilibrium iteration
      ▼
┌─────────────┐
│ Intermediate│
│ displacement│
│   D^{n=2}   │
└─────────────┘
```

$$\varepsilon^{iter}=\mathbf{B}(D^{n=1}-D^{n=2})$$ Iterative strain,

$$\varepsilon^{iter}=\mathbf{B}(D_0-D^{n=2})$$ Incremental strain,

Iterative stress update

Incremental stress update

DR Solution Scheme
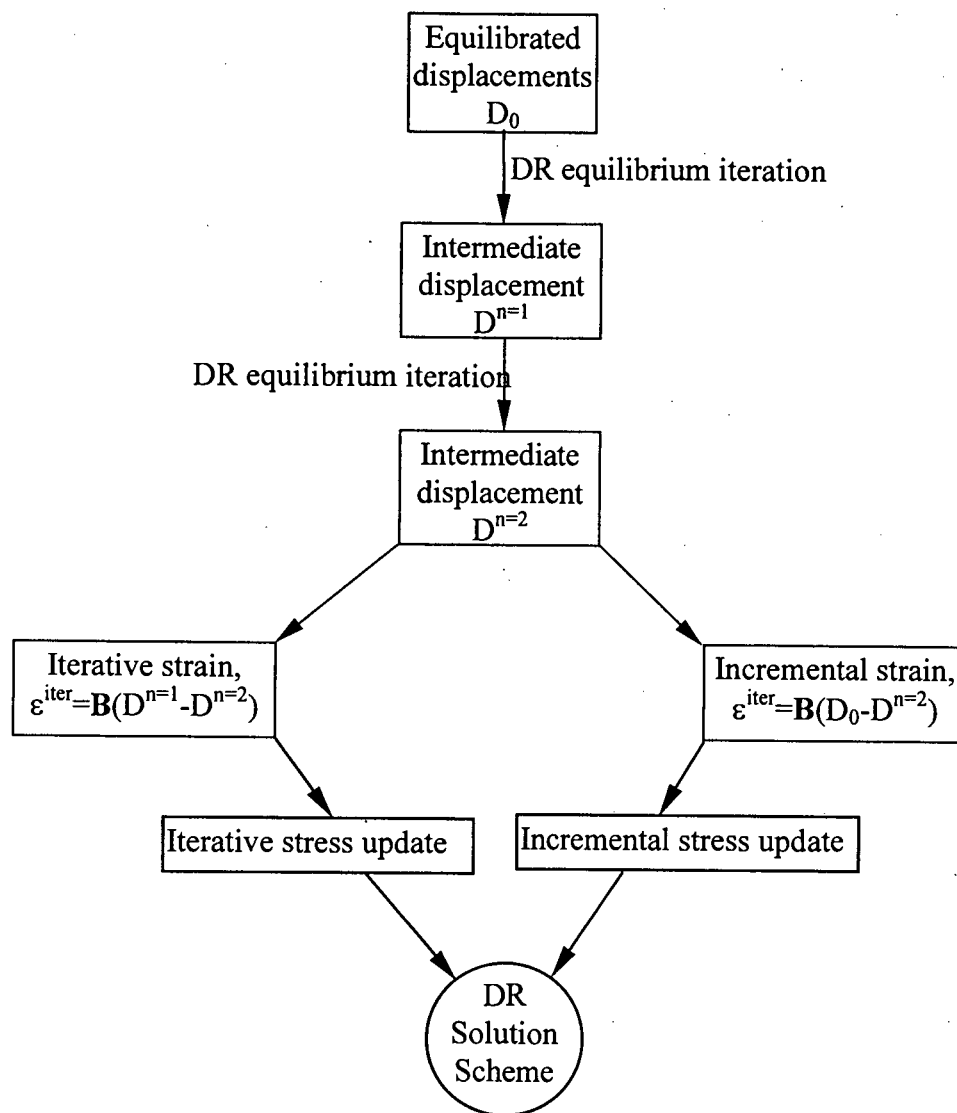
Figure 3-2:   Flow chart explaining the iterative and incremental stress updates.

3.7   SUMMARY OF CHAPTER 3

Solution techniques are discussed in this chapter. Especially, the methods Dynamic Relaxation (DR) technique are explained in details. As the results of any nonlinear FEM depends on the efficiency and accuracy of the solution method, so the stabilization, optimization and damping parameter determinations of DR solution technique are discussed here. Tracing the whole equilibrium curves in cases of snap-through and snap-backs are discussed
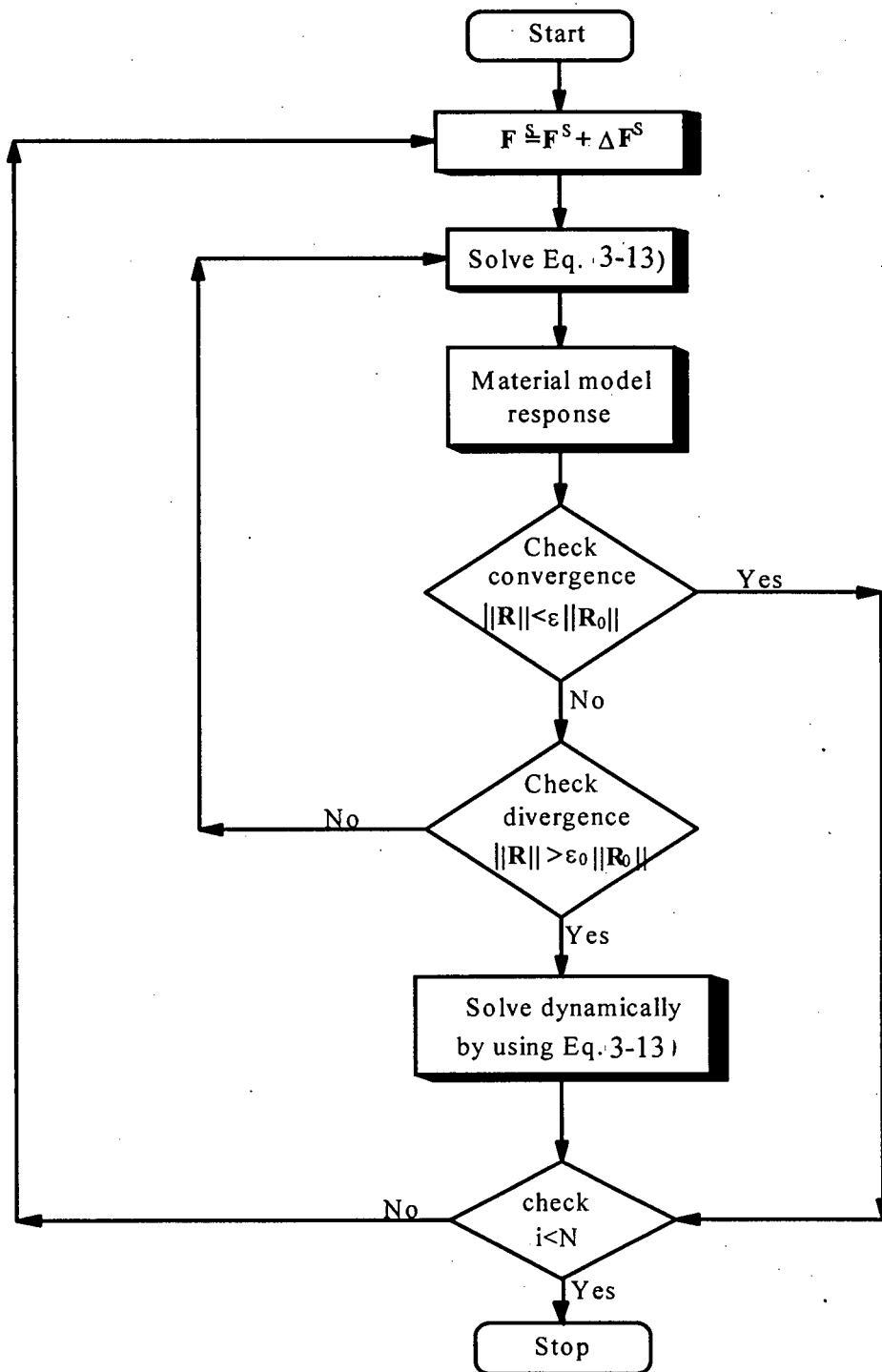
Figure 3-3: Flow chart for load control solution
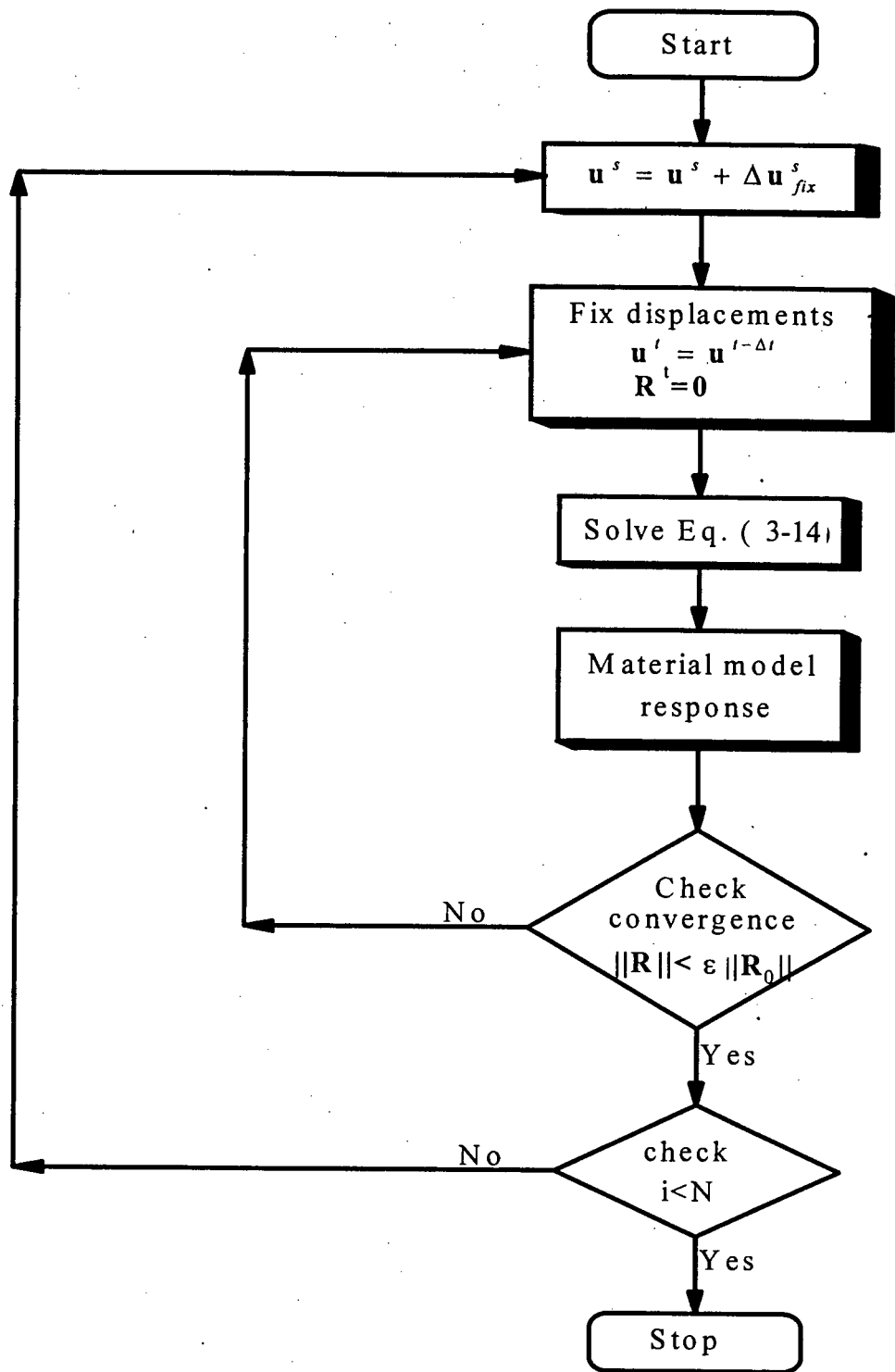
Figure 3-4:   Flow chart for displacement control solution.

CHAPTER 4

4   FORMULATION OF THE DIFFERENT INTERFACES AND PARAMETRIC STUDY

4.1   FORMULATION OF THE INTERFACES

4.2   GOODMAN TYPE ELEMENT

The zero thickness interface element was first proposed by Goodman et al. (1968) for use in simulating the behavior of jointed rock masses. This rectangular element includes four nodes and eight displacement degrees of freedom (Figure 4-1). When using the element in the analysis of geologic media, at each node point along the interface a pair of nodes is placed at the same initial geometric location; the thickness of the element is thus initially zero. The element equations are derived on the basis of nodal relative displacement components of the continuum elements on either side of the interface. The relative displacements are then related to absolute displacements.
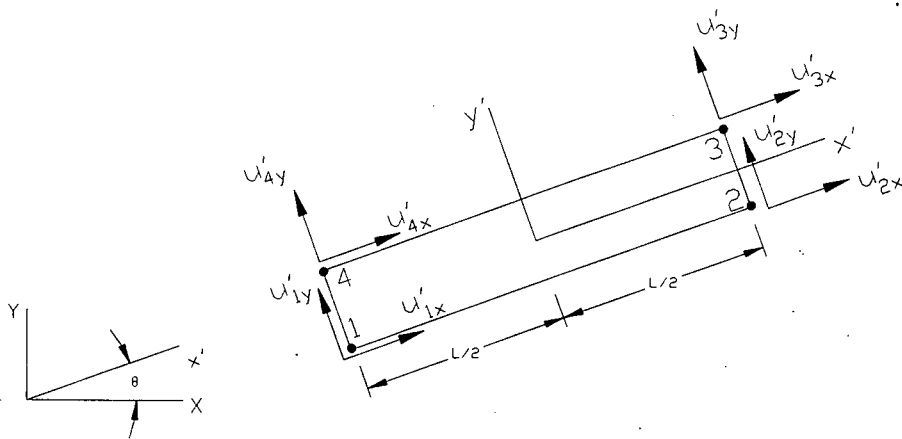
Figure 4-1:   Four–Node Zero Thickness Element of Goodman et al. (Kaliakin, V. N. and Li, J, 1995)

4.2.1 Original Formulation

The vector of absolute nodal displacement degrees of freedom with respect to the local coordinate system (x'-y') is given by:

$$\{u'\} = \{u'_{1x} \ u'_{1y} \ u'_{2x} \ u'_{2y} \ u'_{3x} \ u'_{3y} \ u'_{4x} \ u'_{4y}\}^T \tag{4-1}$$

Where, the superscript T denotes the of matrix transposition. Associated with the above displacement components is a corresponding vector of nodal forces:

$$\{f^{e'}\} = (f'_{1x} \ f'_{1y} \ f'_{2x} \ f'_{2y} \ f'_{3x} \ f'_{3y} \ f'_{4x} \ f'_{4y})^T \tag{4-2}$$

The vector of relative displacements is defined as

$$\{w\} = \begin{Bmatrix} w_t \\ w_n \end{Bmatrix} = [N^*]\{u'\} \tag{4-3}$$

Where, w_t and w_n represent tangential and normal relative displacement, respectively, along the interface. The matrix relating relative and absolute displacements is given by

$$[N^*] = \begin{bmatrix} -N_1 & 0 & -N_2 & 0 & N_2 & 0 & N_1 & 0 \\ 0 & -N_1 & 0 & -N_2 & 0 & N_2 & 0 & N_1 \end{bmatrix} \tag{4-4}$$

Where,

$$N_1 = 1/2 - x'/L \tag{4-5}$$

$$N_2 = 1/2 + x'/L \tag{4-6}$$

represent standard linear functions.

The tangential and normal forces per unit length of interface, σ_t and σ_n respectively, are related to the relative displacements through a suitable constitutive relation. Since the aim is to focus on the deficiencies associated with zero-thickness interface elements and not on the constitutive relations used, the following simple relation shall be employed herein

$$\left\{ \begin{matrix} \sigma_t \\ \sigma_n \end{matrix} \right\} = \begin{bmatrix} d_{11} & 0 \\ 0 & d22 \end{bmatrix} \left\{ \begin{matrix} w_t \\ w_n \end{matrix} \right\} = [D]\{w\} = [D][N^*]\{u'\} \tag{4-7}$$

More complex constitutive relations for such elements have been presented by various researchers.

The constitutive parameters d_{11} and d_{22} appearing in equation (4-7) represent the tangential and normal stiffness per unit length, respectively, along the interface. Alternately, d_{11} and d_{22} can be thought of as tangential and normal penalty numbers.

Considering $\{w\}$ as a generalized "strain", the element stiffness matrix is computed from

$$[K^e] = \int_x [N^*]^T [D][N^*] dx' = \int_\xi [N^*]^T [D][N^*] \det[J] d\xi \tag{4-8}$$

Since the element is rectangular, the Jacobian [J] is constant, allowing the above integrations to be performed analytically (similar results could of course be realized using standard two-point Gauss-Legendre quadrature). The resulting element stiffness matrix with respect to local element coordinates, is thus:

$$[K^e] = \frac{L}{6} \begin{bmatrix} 2d_{11} & 0 & d_{11} & 0 & -d_{11} & 0 & -2d_{11} & 0 \\ & 2d_{22} & 0 & d_{22} & 0 & -d_{22} & 0 & -d_{22} \\ & & 2d_{11} & 0 & -2d_{11} & 0 & -d_{11} & 0 \\ & & & 2d_{22} & 0 & -2d_{22} & 0 & -d_{22} \\ & & & & 2d_{11} & 0 & d_{11} & 0 \\ & \text{sym.} & & & & 2d_{22} & 0 & d_{22} \\ & & & & & & 2d_{11} & 0 \\ & & & & & & & 2d_{22} \end{bmatrix} \tag{4-9}$$

The element equations must next be transformed to system coordinates (x-y). Noting that the local and system coordinates are related through

$$\begin{Bmatrix} x' \\ y' \end{Bmatrix} = \begin{bmatrix} \cos\theta & \sin\theta \\ -\sin\theta & \cos\theta \end{bmatrix} \begin{Bmatrix} x \\ y \end{Bmatrix} = [R] \begin{Bmatrix} x \\ y \end{Bmatrix} \qquad (4\text{-}10)$$

it follows that the element stiffness matrix and force vector, with respect to system coordinates, are computed in the usual manner; that is,

$$(4\text{-}11)$$

$$[K^e] = [R^*]^T [K^{e'}][R^*]$$

$$\{f^e\} = [R^*]^T \{f^{e'}\} \qquad (4\text{-}12)$$

where,

$$[R^*] = \begin{bmatrix} [R] & 0 & 0 & 0 \\ 0 & [R] & 0 & 0 \\ 0 & 0 & [R] & 0 \\ 0 & 0 & 0 & [R] \end{bmatrix} \qquad (4\text{-}13)$$

4.2.2   Modified Formulation (Present Study)

It has been found from the literature survey that Goodman type element with zero thickness creates problems in convergence of the solution. This element has a tendency to penetrate adjacent element and in order to stop that vertical penetration of element, vertical stiffness w is increased to a large number. Due to the presence of this large pivotal element in the system stiffness matrix, the solution becomes difficult. The resulting system of linear/nonlinear equation becomes ill-conditioned.

In order to improve the performance of original Goodman type element, thickness of element is added to the original formulation. This is achieved through modifying the equation (4-5) and (4-6) as follows:

$$\left(N_1 = (1/2 - x'/L)/t\right)$$

$$\left(N_2 = (1/2 + x'/L)/t\right)$$

Where, t = thickness of the element

In the force calculation of the interface element thickness is used. In this way severe numerical problem can be alleviated.

4.3 KATONA TYPE INTERFACE

The formulation is limited to static and two dimensional geometry; however, the inclusion of inertia and three dimensional geometry is straightforward. Further it is assumed that deformations are small so that changes in the interface angle are negligible, and there is no thermal coupling. Two computational advantages were inherent in the proposed interface element. Frist, the constraint equations along with the associated normal and tangential interface forces were incorporated into an incremental virtual work statement. Secondly, the interface element produces an element **constraint matrix** and element **load vector** analogous to a typical element stiffness matrix and load vector. Thus, the interface element can be assembled into the global equations by standard techniques.

4.3.1 Original Formulation

(a)   Virtual work and constraint equations

A standard finite element displacement formulation (without constraints) based on incremental virtual work, i.e. internal virtual work is equal to external virtual work, or:

$$\delta u^T \{Ku - P\} = 0 \qquad (4-14)$$

Where,

$$
\begin{aligned}
\mathbf{u} &= \text{incremental displacement vector} \\
\mathbf{K} &= \text{tangent global stiffness matrix} \\
\mathbf{P} &= \text{incremental load vector}
\end{aligned}
$$

Here $\delta \mathbf{u}^T$ is an arbitrary virtual displacement, so that satisfaction of equation (4-14) requires that $\mathbf{Ku} = \mathbf{P}$ (usually solved iteratively).

If equation (4-14) represented a finite element assembly of two bodies initially in contact at node pairs as suggested in Figure 4-2, then, of course, the two bodies can deform independently resulting in overlapping and/or separation along the interface. At the other extreme, if the node pairs at the interface are constrained to move together, a completely bonded response is obtained. Between these two extremes, a slipping response can be obtained by constraining only the displacements normal to the interface at each node pair.

Formally, any set of linear nodal point constraint equations can be expressed as:
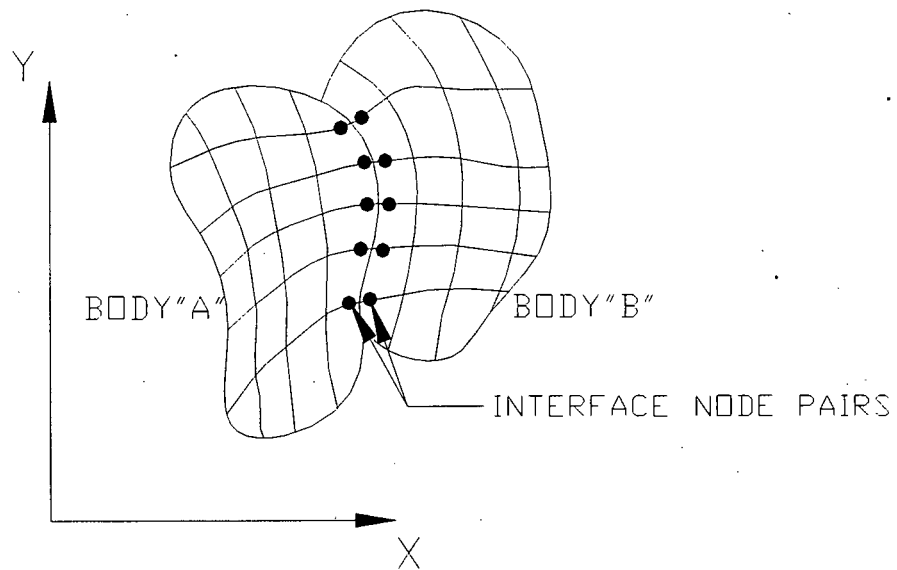
Figure 4-2:   Idealization of two bodies with initially mating pairs along the interface (Katona, 1983)

$$(4\text{-}15)$$

$$\mathbf{Cu} - \hat{\mathbf{a}} = 0$$

Where,

$\mathbf{C}$ = constraint coefficient matrix

$\hat{\mathbf{a}}$ = specified constraints (e.g. displacement gaps)

Associated with each constraint equation in equation (4-15) there exists an unknown internal constraint force λ enforcing constraint. For convenience, equation (4-15) can be expressed in a scalar (work) form as:

$$\delta\lambda^T \{\mathbf{Cu} - \mathbf{a}\} = 0 \qquad (4\text{-}16)$$

where $\delta\lambda$ is an arbitrary variation of the constraint forces so that satisfaction of equation (4-16) implies equation (4-15).

To this end, the virtual work of the constraint forces have not been accounted and the internal constraint forces produce internal virtual work when the constraint is given a virtual movement (variation), i.e., $\delta\{\mathbf{Cu\text{-}a}\}^T \lambda$. Since $\mathbf{C}$ and $\mathbf{a}$ are constants, this becomes:

Constraint virtual work = $\delta u^T \mathbf{C}^T \lambda \qquad (4\text{-}17)$

Physically this is analogous to imposing constraints with stiff springs between node pairs wherein the internal spring force corresponds to the constraint force. However, in this case the constraint forces are primary unknowns.

To complete the formulation, we add the internal virtual work given by equation (4-17) to the virtual work statement in equation (4-14) and append the constraint requirement in equation (4-16) to get the general virtual work statement including constraints:

$$\delta\begin{Bmatrix} \mathbf{u} \\ \lambda \end{Bmatrix}^T \left\{ \begin{bmatrix} \mathbf{K} & \mathbf{C}^T \\ \mathbf{C} & 0 \end{bmatrix} \begin{Bmatrix} \mathbf{u} \\ \lambda \end{Bmatrix} - \begin{Bmatrix} \mathbf{P} \\ \mathbf{a} \end{Bmatrix} \right\} = 0 \qquad (4\text{-}18)$$

Thus, the coupled matrix equations above from the global system to be solved for $\mathbf{u}$ and λ. Note that the separate partitioning of the global system into $\mathbf{u}$ and λ is a mere

formality and not required in the actual assembly. Indeed, the constraint equations may be treated at the element level by forming an element constraint matrix, $\mathbf{C}^*$ and vector $\mathbf{f}$ as:

$$\mathbf{C}^* = \begin{matrix} \mathbf{u} & \lambda \\ \left\{ \begin{matrix} \mathbf{O} & \mathbf{C}^T \\ \mathbf{C} & \mathbf{O} \end{matrix} \right\} \end{matrix} \qquad (4\text{-}19)$$

$$\mathbf{f} = \left\{ \begin{matrix} \mathbf{0} \\ \mathbf{a} \end{matrix} \right\} \qquad (4\text{-}20)$$

Here. The matrix and vector quantities associated with $\mathbf{u}$ pertain to only those degrees of freedom affected by the constraints. Since $\mathbf{C}^*$ is symmetric it can be assembled like any stiffness element as can the element load vector $\mathbf{f}$. Global storage locations for λ can be easily established by defining **dummy** nodes in the finite element mesh. However, to maintain narrow bandedness of the assembled matrix (equation (4-18)), the dummy nodes should be numbered as closely as possible to the nodes being constrained.

(b)   Interface element constraint matrix and load vector

To separate the foregoing to friction-contact interfaces, we assume that any interface can be modeled as a sequence of node pairs (Figure 4-2), so that attention can be focused on a single node pair (interface element) as shown in Figure 4-3. Here, the interface element is defined in x', y' coordinates which are rotated ϕ degrees from the global x, y coordinate system. At the end of any load step k, the interface responses are characterized by interface forces λ^k_n and λ^k_s and/or relative movements Δ^k_n and Δ^k_s where subscripts n and s refer to normal and tangent directions, and the superscript identifies the load step. No superscript implies and increment, e.g., $\lambda_n = \lambda^k_n - \lambda^{k-1}_n$.
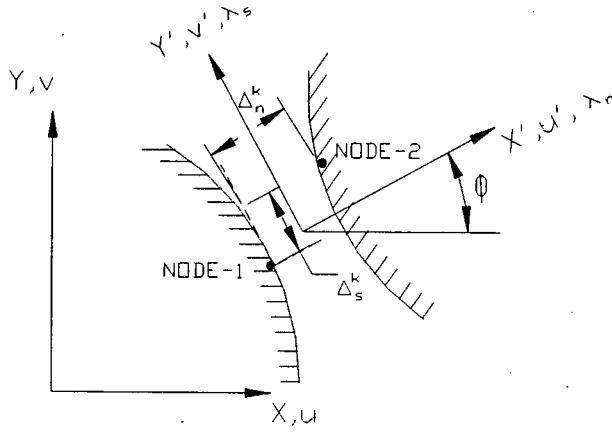
Figure 4-3 :   Interface element representation in separate state, initial state at x',y'
            origin(Katona, 1983)

Assuming both nodes of the element (nodes 1 and 2 in Figure 4-3) are initially in the same location prior to loading, the relative movements are given by the nodal displacements in the x', y' system as normal

$$\Delta^k_n = (u'_2 - u'_1)^k \tag{4-21}$$

$$\Delta^k_s = (v'_2 - v'_1)^k \tag{4-22}$$

We can now identify three **interface states** impose them during a load step: fixed, slip and free.

(1)   Fixed state: for this case the relative normal and tangential movement between the nodes is specified by two constraint equations:

$$\begin{bmatrix} -\cos\varphi & -\sin\varphi & \cos\varphi & \sin\varphi \\ \sin\varphi & -\cos\varphi & -\sin\varphi & \cos\varphi \end{bmatrix} \begin{Bmatrix} u_1 \\ v_1 \\ u_2 \\ v_2 \end{Bmatrix} = \begin{Bmatrix} a \\ b \end{Bmatrix} \tag{4-23}$$

Where,

a = specified normal separation (increment)

b = specified relative slip (increment)

In the above, the local u' and v' displacement increments have been replaced by global u, v displacement increments so that equation 4-23 can be used to define element constraint matrix $\mathbf{C}^*$ and load vector $\mathbf{f}$ in global displacement coordinates as implied in the equation 4-19 and 4-20. The top portion of Table I explicitly defines $\mathbf{C}^*$ and $\mathbf{f}$ and may be assembled like any stiffness element.

Table 4-1:   Element constraint matrix $\mathbf{C}^*$ and load vector $\mathbf{f}$ for three interface states (Katona, 1983)

State	u_1	v_1	u_2	v_1	λ_n	λ_s	load
Fix	0	0	0	0	-c	S	0
	0	0	0	0	-s	-c	0
	0	0	0	0	c	-s	0
	0	0	0	0	s	c	0
	-c	-s	c	s	0	0	a
	s	-c	-s	c	0	0	b
Slip	0	0	0	0	-c	0	-sT
	0	0	0	0	-s	0	cT
	0	0	0	0	c	0	sT
	0	0	0	0	s	0	-cT
	-c	-s	c	s	0	0	a
	0	0	0	0	0	1	T
Free	0	0	0	0	-c	0	cN-sT
	0	0	0	0	-s	0	sN+cT
	0	0	0	0	c	0	-cN-sT
	0	0	0	0	s	0	-sN-cT
	0	0	0	0	1	0	N
	0	0	0	0	0	1	T

$c = \cos\phi$, $s = \sin\phi$

If a and b are both specified zero, the normal gap and relative slip do not change during the load step, i.e., both nodes experience identical displacement increments. If on the other hand, we wish to return the nodes to their initial position (no gaps), we set:

$$a = -\Delta_n^{k-1}, \ b = -\Delta_s^{k-1}.$$

(2)   Slip State: The slipping state is characterized by constraining the normal displacement increments and specifying the tangential interface force increment, i.e.;

$$(-\cos\varphi \quad -\sin\varphi \quad \cos\varphi \quad \sin\varphi) \begin{Bmatrix} u_1 \\ v_1 \\ u_2 \\ v_2 \end{Bmatrix} = a \qquad (4\text{-}24)$$

$$\lambda_s = T \qquad (4\text{-}25)$$

Since λ_s is specified, the element constraint matrix and load vector can be put in the form shown in the centre portion of Table 4-1 wherein the matrix size remains 6x6 for computational convenience.

To simulate a friction-contact interface, the specified values (i.e. T and a in the above equations) are generally determined iteratively dependent on the previous state of the interface (fix, slip or free) and the frictional model. For this case, simple Coulomb friction is assumed, thus the maximum possible interface tangent force at end of load step k is:

$$F^k = \mu \left| \lambda_n^{\,k} \right| sgn\left(\lambda_s^{\,k} \right) \qquad (4\text{-}26)$$

Where: F^k = maximum frictional tangent force
                 μ = coefficient of friction

$$sgn\left(\lambda_s^{\,k} \right) = \begin{cases} +1, \text{ for } \lambda_s^{\,k} > 0 \\ -1, \text{ for } \lambda_s^{\,k} < 0 \end{cases}$$

Accordingly, the specified incremental tangent force is $T = F^k - \lambda_s^{k-1}$

(3)   Free State: The free state requires suppressing both constraint equations and specifying the normal and tangent interface force increments, i.e.,

$$\lambda_n = N \qquad (4\text{-}27)$$

$$\lambda_s = T \qquad (4\text{-}28)$$

The corresponding interface element matrix and load vector are shown in the bottom portion of the Table I where, again, the element matrix size is maintained as 6x6 for computational convenience in global assembly.

Iterative procedures for determining the correct interface state and load vector parameters (a, b, N and/or T) are discussed next. In passing, however, it is observed that a fourth interface state characterizes by tangential displacement constraints and specified normal forces could be easily established as, for example, in simulating a gear-tooth interface.

(c)   Interface iterative procedure

Given the interface solution at load step k-1, denoted by Δ_n^{k-1}, Δ_s^{k-1}, λ_n^{k-1} and λ_s^{k-1}, we seek to determine the solution increments Δ_n, Δ_s, λ_n and λ_s so that the solution at the end of load step k, denoted by $\alpha^k = \alpha + \alpha^{k-1}$ ($\alpha^k = \Delta_n^k$, Δ_s^k, λ_n^k or λ_s^k), is properly determined at the end of load step k

In general the solution must be determined iteratively wherein a particular state (fix, slip or free) is assumed and solved to obtain a trial solution. The trial solution is used to determine if the assumed state is correct, and if not, what state is more likely to be correct. At the same time, the trial solution is used to estimate new load vector parameters a, b or a, T or N , T depending on whether the new state is assumed fix, slip or free, respectively.

Table 4-2 offers an exhaustive set physical criteria to test the validity of an assumed state. The table may be viewed as a 3x3 decision matrix wherein the previously assumed state forms rows and the new candidate states form columns. For example, if the previously assumed state was fixed, row1 of the decision matrix is queried to determine if the net normal interface force λ_n^k is compressive and if the net tangent interface force λ_s^k is less than the maximum frictional value F^k.

Table 4-2:　Decision Matrix For Selecting New State During Iteration Within Load Step (Katona, 1983)

Iteration → I ↓	Fix	Slip	Free
i-1 Fix	$\lambda_n^k <0$ and $\lambda_s^k < F^k$	$\lambda_n^k <0$ and $\lambda_s^k > F^k$	$\lambda_n^k <0$
Slip	$\lambda_n^k <0$ and $\Delta_s F^k <0$	$\lambda_n^k <0$ and $\Delta_s F^k >0$	$\lambda_n^k >0$
Free	$\Delta_n^k <0$		$\Delta_n^k >0$

If not, the fixed assumption is incorrect (at least this iteration) and the new candidate state is slip or free depending on whether λ_n^k is tensile or compressive.

Other entries in Table 4-3 are generally self explanatory except, perhaps, for the free-to-fix case (matrix position 3, 1). Here the implication is that interface penetration ($\Delta_n^{\cdot k} <0$) was observed in Table 4-2 so that we wish to assume a fixed state for the next iteration.

Table 4-3:　Specified Values For Constraint Load Vector (Katona, 1983)

Iteration → I ↓	Fix	Slip	Free
k-1 Fix	a=0 b=0	a=0 $T = F^k - \lambda_s^{k-1}$	$N = -\lambda_n^{k-1}$ $T = -\lambda_n^{k-1}$
Slip	a=0 b=0	a=0 $T = F^k - \lambda_s^{k-1}$	$N = -\lambda_n^{k-1}$ $T = -\lambda_s^{k-1}$
Free	$a=-\Delta_n^{k-1}$ $b=\Delta s \mid \Delta s^k \mid$	$a=-\Delta_n^{k-1}$ $T = F^k$	$N = 0$ $T = 0$

Accordingly, the normal gap is closed by specifying $a = -\Delta_n^{k-1}$. With regard to specifying the slip gap increment, we first observe that the ratio a /Δ_n is that portion of the

normal gap increment which does not cause penetration. Thus, it is reasonable to assume that slip gap increment can be specified in this proportion, i.e., $b = \Delta_s | a / \Delta_n |$.

4.3.2 Modified Formulation (Present Study)

The basic formulation and implementation of Katona type interface element was carried out with a incremental only solution scheme. In the original FEM program of CANDE, there was no provision for iteration for the minimization of the error of the solution.

Recently, there is a huge development in the solution scheme of nonlinear equations arising from the weak variational formulation of the governing elliptic/hyperbolic differential equations. All these equations solvers are of vector iterative nature. This class of solvers are very efficient both in speed and memory storage and they are good for parallel/distributed computing as well. With this end-in-view the original Katona type interface element has been modified to fit into the solution scheme of DR.

In any vector iterative technique formation of the global stiffness matrix is avoided due to the involvement of large cost. But original Katona needs incorporating the element constraint matrix (Table 4-1). This problem is solved by imposing the required constraint at the transfer of global trial solution to the elementary level for strain (subsequently stress) calculation. The constrained load vector (Table-4-3) is implemented at the end of calculation of all trial internal forces. The decision matrix (Table 4-2) is implemented at the beginning of application of each constraint equation and load vector imposition.

4.4   DESAI TYPE INTERFACE

The distinguished features in the development and use of a thin solid element to simulate interface behavior lie in the special treatment of the constitutive laws for the thin-layer element, choice of its thickness, incorporation of various modes of deformation (Figure 4-4) and implementation for a number of problems with displacement, mixed and hybrid finite element procedures.
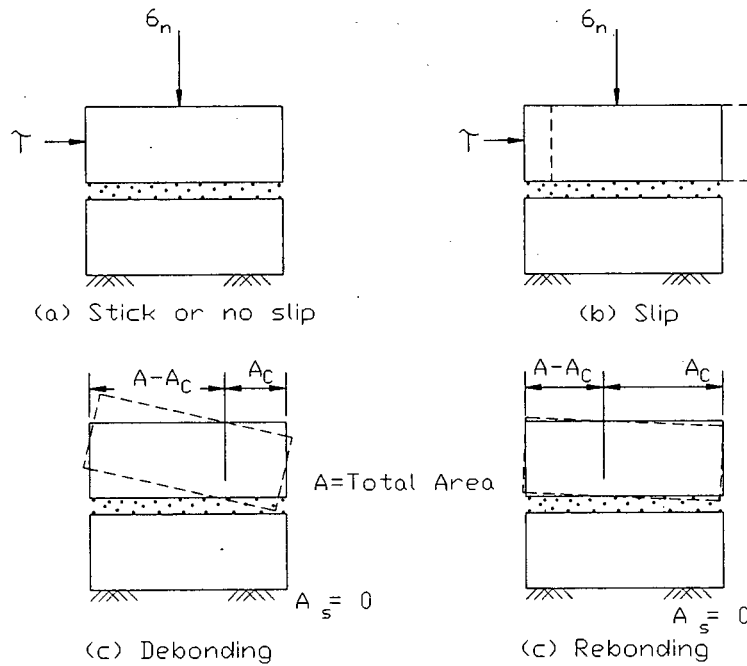
Figure 4-4:   Schematic of Modes of Deformation at Interface(Desai, C.S, Zaman, M.M., Lightner, J.G. and Siriwardane, H.J., 1984)

4.4.1   Original Formulation

a)   Incremental Stress-Strain Relation

Schematic diagrams of the thin-layer element for two and three dimensional idealizations are shown in Figure 4-5. The element is treated essentially like any other solid (soil, rock or structural) element. However, its constitutive matrix $[C]_i$ is expressed as :

$$\{d\sigma\} = [C]_i \{d\epsilon\}$$ (4-29)

Where, $\{d\sigma\}$ = vector of increments of stresses,

$\{d\epsilon\}$ = vector of increments of strain

and the constitutive matrix $[C]_i$ is given by

B=average contact dimension

(a) Two-dimensional

(b) Three-dimensional
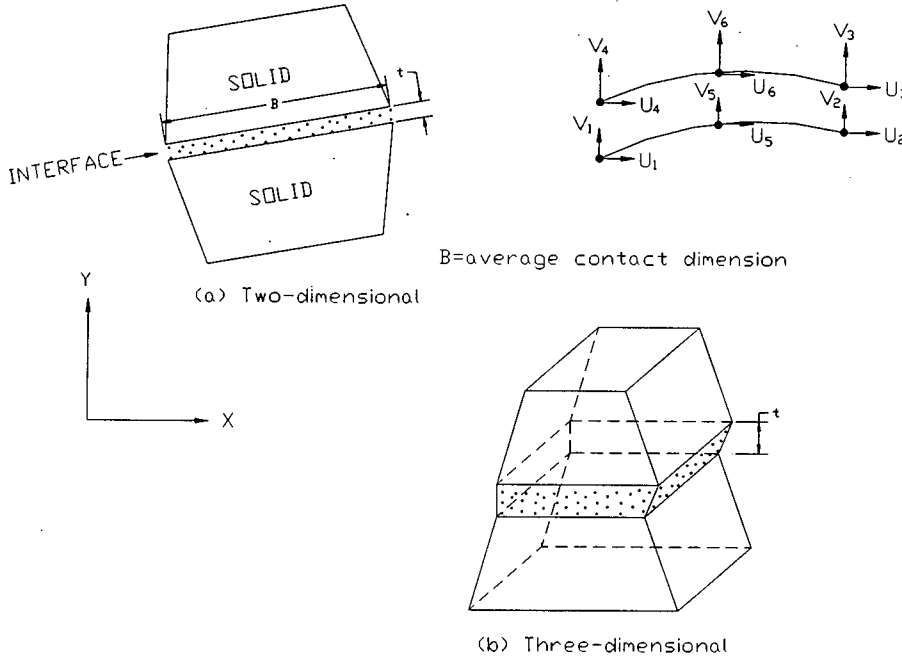
Figure 4-5:   Thin-layer interface element(Desai, C.S, Zaman, M.M., Lightner, J.G. and Siriwardane, H.J., 1984)

$$[C]_i = \begin{bmatrix} [C_{nn}]_i & [C_{ns}]_i \\ [C_{sn}]_i & [C_{ss}]_i \end{bmatrix}$$ (4-30)

where $[C_{nn}]$ = normal component, $[C_{ss}]$ = shear component and $[C_{ns}]$, $[C_{sn}]$ represent coupling effects. Since it is difficult to determine the coupling terms from laboratory tests, at this time, they are not included.

A basic assumption made is that the behaviour near the interface invloves a finite thin zone (Figure 4-5) rather than a zero thickness as assumed in previous formulations. As stated earlier, it may not be appropriate to assign an arbitrary high value for the normal stiffness. Since the interface is surrounded by the structural and geological materials, normal properties during the deformation process must be dependent upon the characteristics of the thin interface zone as well as the state of stress and properties of the surrounding elements. Based on these considerations, it was proposed to express the normal stiffness as:

$$[C_n]_i = \left| C_n \left(\alpha\,^i_m, \ \beta\,^g_m, \ \gamma\,^{st}_m \right) \right| \tag{4-31}$$

where α_m^i, β_m^g, γ_m^{st} ($m = 1,2, \ldots\ldots$) denotes the properties of the interface, geological and structural elements, respectively. From here onwards the second subscript in $[C_{nn}]$ etc. is dropped. Equation 4-31 can be written as

$$\left[\overline{C}_n\right]_i = \lambda_1 [C_n]_i + \lambda_2 \left[C_n^g\right] + \lambda_3 \left[C_n^{st}\right] \tag{4-32}$$

where, $[C_n]_i$ denotes normal behavior of the thin interface element, and λ_1, λ_2 and λ_3 are the participation factors varying from 0 to 1. Equation 4-32 is expressed as an addition of various components. However, it is possible to define it by using a different (polynomial) expression. One of the simplifications would be to assume $\lambda_2 = \lambda_3 = 0$ and $\lambda_1 = 1$, implying that the normal component is based on the normal behavior of the thin-layer element evaluated just as the adjacent soil element. It is possible to arrive at appropriate values for λ_1 based on a trial and error procedure in which numerical solutions are compared with laboratory or field observations. Often, it was found that satisfactory results can be obtained by assigning the interface normal component the same properties as the geological material.

For most application presented herein, $\lambda_1 = 1$ and $\lambda_2 = \lambda_3 = 0$ were adopted. As long as the significant deformation mode is stick, these values provide satisfactory results. The contribution of the participation factors becomes important when opening or debonding initiates. Preliminary work towards determination of the participation factors for normal

stiffness in cyclic loading has shown $\lambda_1 = 0.75$, $\lambda_2 = 0.25$ and $\lambda_3 = 0$. Now, work towards derivation of these factors by comparison with laboratory data is in progress.

The shear component $[C_s]_i$ is obtained from direct shear or other interface shear testing devices (Figure 4-6(a)). In this study $[C_s]_i$ is assumed to be composed of a shear modulus G_i for the interface. The expression used for tangent G_i is given by:

$$G_T(\sigma_n, \tau, u_r) = \frac{\delta[\tau(\sigma_n u_r)]}{\delta u_r} \times t \Big|_{\sigma_n} \qquad (4\text{-}33)$$

Where, t = thickness of the element (Figure 4-6(b) and u_r = relative displacement)

(b) Deformations at the interface

(a) Schematic of Direct Shear Test
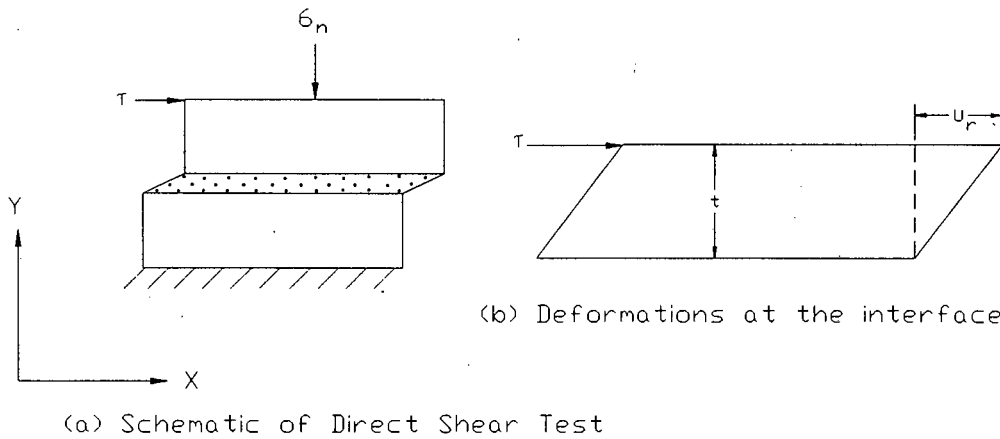
Figure 4-6   Behavior at Interface(Desai, C.S, Zaman, M.M., Lightner, J.G. and Siriwardane, H.J., 1984)

b) Constitutive modeling

The thin layer interface element can be formulated by assuming it to be a linear elastic, non-linear elastic or elastic-plastic. The development of its stiffness characteristic follows essentially the same procedure as solid elements, that is the stiffness matrix, $[k]_i$ is written as:

$$[k]_i = \int_v [B]^T [C^{ep}]_i [B] dV \qquad (4\text{-}34)$$

Where, $[B]$ = transformation matrix, V = volume and $[C^{ep}]_i$ is the constitutive matrix. Then the element equations are written as

$$[K]_i \{q\} = \{Q\} \qquad (4\text{-}35)$$

where, $\{q\}$ = vector of nodal displacements and $\{Q\}$ = vector of nodal forces.

For linear elastic behavior, $[C^e]_i$ can be expressed as

$$[C^e]_i = \begin{bmatrix} C_1 & C_2 & C_2 & 0 & 0 & 0 \\ C_2 & C_1 & C_2 & 0 & 0 & 0 \\ C_2 & C_2 & C_1 & 0 & 0 & 0 \\ 0 & 0 & 0 & G_{i2} & 0 & 0 \\ 0 & 0 & 0 & 0 & G_{i2} & 0 \\ 0 & 0 & 0 & 0 & 0 & G_{i2} \end{bmatrix} = \begin{bmatrix} [C_n]_i & 0 \\ 0 & [C_s]_i \end{bmatrix} \qquad (4\text{-}36)$$

Where,

$$C_1 = \frac{E(1-v)}{(1+v)(1-2v)}$$

$$C_2 = \frac{Ev}{(1+v)(1-2v)}$$

E is the elastic (Young's) modulus, v is Poisson's ratio and G_{ii} (I = 1,2,3) are the shear moduli defined in equation 4-33. If the shear behavior is assumed to be isotropic, $G_{i1} = G_{i2} = G_{i3}$. Here it is assumed that the shear response is uncoupled from the normal response

74

represented by $[C_n]$. For two dimensional idealization, the special form of $[C^e]_i$ and its inverse form, $[D^e]_i$ are given as:

$$[C^e]_i = \begin{bmatrix} C_1 & C_2 & 0 \\ C_2 & C_1 & 0 \\ 0 & 0 & G_i \end{bmatrix}$$

(4-37)

$$[D^e]_i = \begin{bmatrix} \dfrac{1-v^2}{E} & \dfrac{-v(1+v)}{E} & 0 \\ \dfrac{-v(1+v)}{E} & \dfrac{1-v^2}{E} & 0 \\ 0 & 0 & \dfrac{1}{G_i} \end{bmatrix}$$

(4-38)

the latter is used in a mixed finite element procedure.

For non-linear elastic behavior such as hyperbolic simulation, E, v and G can be defined as variable moduli based on triaxial and direct shear tests. For example G_i can be written as

$$G_i = K\gamma_w \left(\frac{\sigma_n}{p_a}\right)^n \left(1 - \frac{R_{ft}}{c_a + \sigma_n \tan \varphi}\right)^2$$

(4-39)

Where K, n and R_f are material parameters, γ_w = unit weight of water, p_a = atmospheric pressure, c_a = cohesion and ϕ = angle of friction. Alternatively, the shear modulus can be obtained by expressing the τ vs. u_r relation in a polynomial form described subsequently.

In addition to the foregoing linear and non-linear elastic models, the proposed formulation also allows for elastic-plastic behavior. Then the constitutive matrix for the interface is written as

75

$$[C]_i^{ep} = [C^e (k_s, k_n \{du_r^p\})]_i \qquad (4\text{-}40)$$

where, $\{du_r^p\}$ = vector of incremental relative displacements. The second part of equation 4-40 is found on the basis of yield and flow criteria of the theory of plasticity. Here conventional criteria such as Mohr-Coulomb can be used with yield function, f, and plastic potential function, Q; for associated plasticity f = Q. To allow for dilatancy in the case of rock joints different f and Q can be used in the context of non-associative plasticity.

4.4.2 Modified Formulation (Present Study)

Desai type element differs from the rest of the interface elements in the description of material behavior inside the interface. So, proper material description lays the foundation of modified Desai type interface element.

In the present study, material behavior is described as nonlinear anisotropically hardening-softening elasto-plastic dilating frictional material (Siddiquee, 1994). The peak angle of internal friction and the stress-strain (ε_1-ε_3) at peak angle of internal friction depend on the void ratio of sand. The relationship can be shown as:

$$R_{max} = f(e) \qquad (4\text{-}41)$$

Where,

$$R_{max} = \left(\frac{\sigma_1}{\sigma_3}\right)_{max}$$

$$\sin(\phi_{peak}) = \frac{1 - R_{max}}{1 + R_{max}} \qquad (4\text{-}41)$$

So, the material model used here in this study is a frictional model which has a nonlinear ϕ~γ relationship for the beginning and runs up to peak softening (critical state of void ratio).
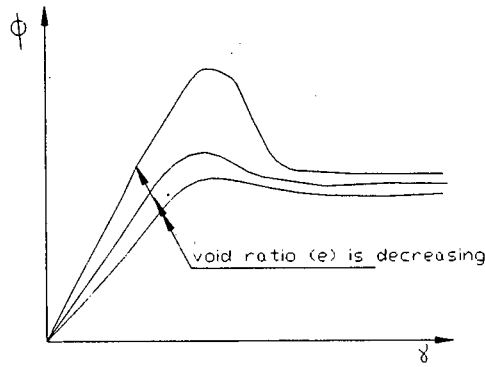
Figure 4-7:   Typical relationship of $\phi\sim\gamma$ depending on void ratio, e.

The modified Desai type interface element uses shear strain parameter (γ) instead of relative displacement (U_r).   This may be achieved very easily, just dividing U_r with the thickness t.

4.5   MATERIAL DESCRIPTION

Depending on the type of interface element, material property varies widely. In most of the interface element capture the behavior of the slippage. So, the properties, related to slip mode should be provided as accurately as possible. Separation or penetration creates numerical instabilities in the analysis. In order to avoid this problem, relatively high value of stiffness in vertical direction (perpendicular to the joint) is provided for the interface element.

4.5.1   Interface Element

The material properties of interface element depend on the method of its formulation. There are some properties, like stiffness of the interface element, which do not vary much among the different elements. The following are description of interface element properties:

a)   Goodman Type: This type of interface element requires the following parameters to be defined.

Table 4-4:   Parameters of Goodman Type Interface

Name of the parameter	Symbol used	Typical range of value
Normal stiffness	K_n	$10^4 - 10^8$ psi
Shear stiffness	K_s	$10^2 - 10^6$ psi
Residual shear	K_{sres}	1 – 10 psi
Cohesion	c	0.0 – any value
Angle of internal friction	ϕ	0.0 – 89.9 deg.
Thickness	t	Less than side of an element

The residual shear stiffness is activated where there is a mode of separation starts to persuade. Usually, a residual shear stiffness of low value is used instead of regular shear stiffness in order to simulate separation and avoid numerical instabilities.

b)   Katona Type: this type of interface element requires the following parameters to be defined.

Table 4-5:   Parameters of Katona Type Interface

Name of the parameter	Symbol used	Typical range of value
Cohesion	C	0.0 – any value
Angle of internal friction	ϕ	0.0 – 89.9 deg.

This element has the minimum number of parameters to be defined. It requires only the cohesion and angle of internal friction (peak value) of the interface material. This element is actually a zero thickness interface element.

c) Desai Type: this type of interface element requires the following parameters to be defined.

Table 4-6: Parameters of Desai Type Interface

Name of the parameter	Symbol used	Typical range of value
Young's modulus	E	$10^4 - 10^8$ psi
Shear modulus	G	$10^3 - 10^7$ psi
Poisson's ratio	ν	$0.10 - 0.30$
Stress-strain relationship	$\phi \sim \gamma$	Depends on density
Thickness	t	Less than side of an element

It is very interesting to note that this type of interface element does not require any parameters like, e or ϕ. Because description to the constitutive law is good enough to take care of the different modes of interface element, like slip, rebonding etc.

4.5.2 Surrounding Material

The property of the surrounding material connecting two sides of the interface elements depends mainly on the type of the material. It can vary on the computational requirement as well. Granular material can be modeled as elastic or elasto-perfectly plastic or elasto-plastic hardening material. Depending on the choice of the material model, cost of computation and accuracy of the analysis increases. In this study all the analysis carried out assuming linear elastic parameters, Young's modulus and poisson's ratio. There are provision for the inclusion of conventional material models like Cam-clay or J_2-plasticity models of Cap models. Due to the limitation of computation time, present study is limited to linear elastic model only.

79

4.6   PARAMETRIC STUDY

In order to evaluate the general performance of the interface elements, a detailed parametric study has been designed. As the parameters of different interface elements are different, it is rather difficult to prepare a scheme to vary different parameters systematically. The most sensitive parameters are varied to study the effect of the parameters on the stress-deformation evolution of the problem.

4.6.1   Test Problem

Interface elements are usually used in geotechnical engineering to model smear-zone between two dissimilar material formed during driving of pile/sheet pile or retaining wall construction or soil reinforcement. In all the case of application, the interface element is expected to model slip mode as its primary mode of deformation. So, in this study a direct shear test is investigated. The geometry, boundary condition and the loading are as follows:
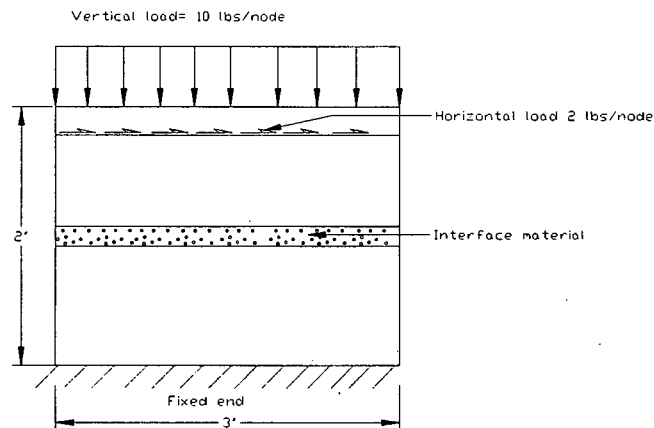
Figure 4-8:   Typical FEM model of direct shear box for parametric study
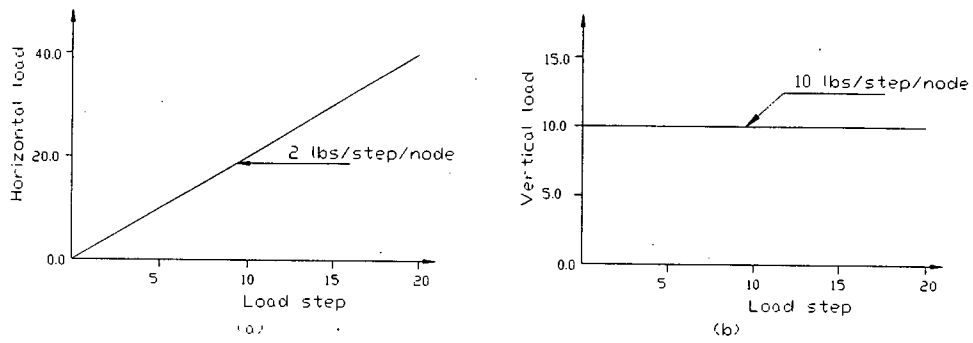
Figure 4-9: Loading schemes
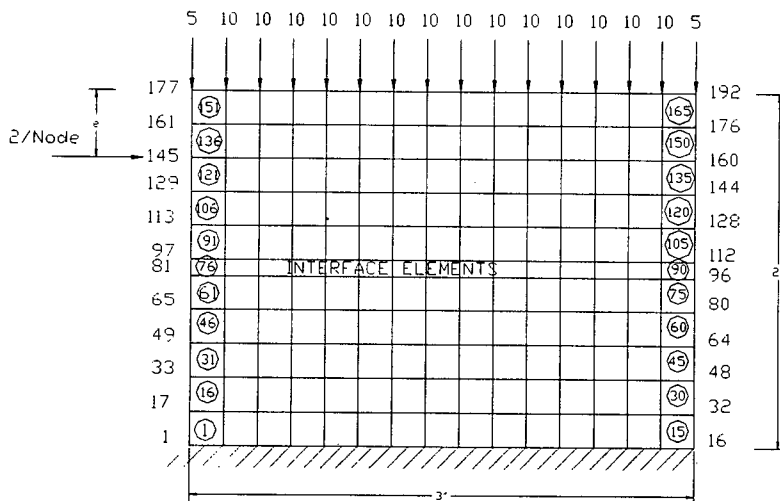
Figure 4-10: Finite Element Mesh of Direct Shear Box

Identification of Parameters

Three types of interface elements are studied in this research with some modification in its original formulation. There are a number of parameters involved in each interface. It is very difficult to perform a detailed parametric study of all the parameters involved. So, the most sensitive parameters are picked from the literature survey and studied in this research. The following Table shows the most sensitive parameters chosen for the parametric study.

Table 4-7:   Parameters selected for parametric study

Name of the interface	Parameters studied
Goodman Type	K_n, K_s, c, ϕ, t
Katona Type	ϕ, loading
Desai Type	e, t, loading

4.6.3   Design of Analysis Scheme

The scheme of the parametric study is designed in such a way that shows the difference among all the interface elements clear to all. The following Table 4-8 shows the cases of parametric study performed for different types of interface and the different values of the parameters.

Table 4-8: Values of Parameters Used to Evaluate Different Interface Elements

Case	Interface Type	Intrface Stiffness K_N in psi K_S in psi	Intrface c in psi ϕ in deg.	Soil Model E_S in psi (Elastic)	Interface Thickness inch	Load eccentricity (from top) in inch
1	Normal element	-	-	E_S=30000	0.25	0.20
1	Goodman	K_N=10^5 K_S=100	c=50 ϕ=20	E_S=30000 v=0.30	0.10	1.0
2	Goodman	K_N=10^5 K_S=10^5	c=50 ϕ=20	E_S=30000 v=0.30	0.10	1.0
3	Goodman	K_N=10^5 K_S=10^5	c=0.0 ϕ=20	E_S=30000 v=0.30	0.10	1.0
4	Goodman	K_N=10^4 K_S=10^4	c=0.0 ϕ=20	E_S=30000 v=0.30	0.10	1.0
5	Goodman	K_N=10^4 K_S=10^4	c=0.0 ϕ=20	E_S=30000 v=0.30	0.05	1.0
6	Goodman	K_N=10^4 K_S=10^4	c=0.0 ϕ=20	E_S=30000 v=0.30	0.02	1.0
7	Goodman	K_N=10^4 K_S=10^4	c=0.0 ϕ=20	E_S=30000 v=0.30	0.10	0.80
8	Goodman	K_N=10^4 K_S=10^4	c=0.0 ϕ=20	E_S=30000 v=0.30	0.10	0.40
1	Katona	-	c=0.0 ϕ=5	E_S=30000 v=0.30	0.05	0.40
2	Katona	-	c=0.0 ϕ=10	E_S=30000 v=0.30	0.05	0.40
3	Katona	-	c=0.0 ϕ=20	E_S=30000 v=0.30	0.05	0.40
4	Katona	-	c=0.0 ϕ=30	E_S=30000 v=0.30	0.05	0.40
5	Katona	-	c=0.0 ϕ=30	E_S=30000 v=0.30	0.05	0.80
1	Desai	-	ϕ-γ=f(e) e=0.66	E_S=30000 v=0.30	0.10	0.80
2	Desai	-	e=0.75	-do-	0.10	0.80
3	Desai	-	e=0.61	-do-	0.10	0.80
4	Desai	-	e=0.66	-do-	0.10	1.00
5	Desai	-	e=0.66	-do-	0.10	0.20

4.6.4　FEM Details of The Analysis

In the FEM discritization, four noded iso-parametric elements are used for surrounding material. This element, when integrated with 1-point gives optimal solution. But due to use of this 1-point integration, there may be some zero energy or hour-glass mode, which can destroy the solution. This is prevented in the present analysis with the detection of these modes and subsequent elimination (Siddiquee, 1994).

The interface elements of Goodman type are formulated as one-dimensional arrays and are integrated using 1-point integration. Katona type interface elements are just links between the two nodes of the elements. It has got no properties other than cohesion and friction. Desai type elements are normal four-node elements with proper material properties.

CHAPTER 5

5.1   GENERAL

There are a total number of 19 cases of parametric study including the first one as a direct shear test without any interface element. In order to evaluate the numerical performance of each of the cases, a number of outputs have been processed in a presentable form. Four types of output are presented for each case and these are as follows:

a)   deformed mesh for load steps 1, 5, 10, 15 and 20;

b)   force-displacement and average stress-strain plot for the interface elements over the whole range of loading;

c)   shear strain contours for load steps 5, 10 and 15; and

d)   displacement field for load steps 1, 5, 10 and 15.

All results are presented according to the order of cases shown Table 4-8. The plot (a) of deformed meshes and the others (b), (c) and (d) are shown according to the order of cases shown in Table 4-8. For better presentation and understanding, the Figures are numbered serially starting from the deformed meshes. The sorted patterns of numbering the Figures based on their caption are as follows:

i)   **Deformed mesh:**

- Normal element: Figure 5-1(a) to Figure 5-1(e);

- Goodman type interface, case-1: Figure 5-2(a) to Figure 5-2(e); to

- Goodman type interface, case-8: Figure 5-9(a) to Figure 5-9(e);

- Katona type interface, case-1: Figure 5-10(a) to Figure 5-10(e); to

- Katona type interface, case-5: Figure 5-14(a) to Figure 5-14(e);

- Desai type interface, case-1: Figure 5-15(a) to Figure 5-15(e); to

- Desai type interface, case-5: Figure 5-19(a) to Figure 5-19(e).

ii)   a) **Force vs. Displacement Plot:**

- Normal element: Figure 5-20(a);

- Goodman type interface, case-1: Figure 5-23(a), case-2: Figure 5-26(a), case-3: Figure 5-29(a), case-4: Figure 5-32(a), case-5: Figure 5-35(a), case-6: Figure 5-38(a), case-7: Figure 5-41(a), case-8: Figure 5-44(a);

- Katona type interface, case-1: Figure 5-47(a), case-2: Figure 5-50(a), case-3: Figure 5-53(a), case-4: Figure 5-56(a), case-5: Figure 5-59(a);

- Desai type interface, case-1: Figure 5-62(a), case-2: Figure 5-65(a), case-3: Figure 5-68(a), case-4: Figure 5-71(a), case-5: Figure 5-74(a).

ii)   b) **Stress vs. Strain variation Plot:**

- Normal element: Figure 5-20(b);

- Goodman type interface, case-1: Figure 5-24 (5), case-2: Figure 5-24(b), case-3: Figure 5-29(b), case-4: Figure 5-32(b), case-5: Figure 5-35(b), case-6: Figure 5-38(b), case-7: Figure 5-41(b), case-8: Figure 5-44(b);

- Katona type interface, case-1: Figure 5-47(b), case-2: Figure 5-50(b), case-3: Figure 5-53(b), case-4: Figure 5-56(b), case-5: Figure 5-59(b);

- Desai type interface, case-1: Figure 5-62(b), case-2: Figure 5-65(b), case-3: Figure 5-68(b), case-4: Figure 5-71(b), case-5: Figure 5-74(b).

iii)   **Shear strain contour:**

- Normal element: Figure 5-21(a) to Figure 5-21(c);

- Goodman type interface, case-1: Figure 5-24(a) to Figure 5-24(c), case-2: Figure 5-27(a) to Figure 5-27(d), case-3: Figure 5-29(a) to 5-30(c), case-4: Figure 5-33(a) to 5-33(c), case-5: Figure 5-36(a) to 5-36(c), case-6: Figure 5-39(a) to 5-39(c), case-7: Figure 5-42(a) to 5-42(c), case-8: Figure 5-45(a) to 5-45(c);

- Katona type interface, case-1: Figure 5-48(a) to Figure 5-48(c); case-2: Figure 5-51(a) to Figure 5-51(c); case-3: Figure 5-54(a) to Figure 5-54(c); case-4: Figure 5-57(a) to Figure 5-57(c); case-5: Figure 5-60(a) to Figure 5-60(c);

- Desai type interface, case-1: Figure 5-63(a) to Figure 5-63(c); case-2: Figure 5-66(a) to Figure 5-66(c); case-3: Figure 5-69(a) to Figure 5-69(c); case-4: Figure 5-72(a) to Figure 5-72(c); case-5: Figure 5-75(a) to Figure 5-75(c).

iv) Displacement field:

- Normal element: Figure 5-22(a) to Figure 5-22(d);

- Goodman type interface, case-1: Figure 5-25(a) to Figure 5-25(d), case-2: Figure 5-28(a) to Figure 5-28(d), case-3: Figure 5-31(a) to 5-31(d), case-4: Figure 5-34(a) to 5-34(d), case-5: Figure 5-37(a) to 5-37(d), case-6: Figure 5-40(a) to 5-40(d), case-7: Figure 5-43(a) to 5-42(d), case-8: Figure 5-45(a) to 5-45(d);

- Katona type interface, case-1: Figure 5-49(a) to Figure 5-49(d); case-2: Figure 5-52(a) to Figure 5-52(d); case-3: Figure 5-55(a) to Figure 5-55(d); case-4: Figure 5-58(a) to Figure 5-58(d); case-5: Figure 5-61(a) to Figure 5-64(d);

- Desai type interface, case-1: Figure 5-64(a) to Figure 5-64(d); case-2: Figure 5-67(a) to Figure 5-67(d); case-3: Figure 5-70(a) to Figure 5-70(d); case-4: Figure 5-73(a) to Figure 5-73(d); case-5: Figure 5-76(a) to Figure 5-76(d).

5.2   INDIVIDUAL PERFORMANCE

5.2.1   Without Any Special Interface Element

Figure 5-1(a) through Figure 5-1(e) show the deformed meshes of the analysis at load steps 1, 5, 10, 15 and 20. The displacements of the deformed meshes are amplified 10 times. As expected the whole shear box is acting as one and rotating against the constrained edge.

Figure 5-20(a) shows the average load vs. displacement along the loaded nodes. Figure 5-20(b) shows the stress-strain relationship at the gross points of the interface elements (supposed to be). From the observation of Figure 5-20(a) it is clear that horizontal load is increasing monotonically. While the vertical load remains constant. But Figure 5-20(b) shows that at mid depth of the shear box, horizontal stress increase is not much compared to the vertical stress increase.

Figure 5-21(a) through 5-21(c) shows the contour of shear strain at load steps 5, 10 and 15. It has been observed that upper edge of depth 0.75 inch is severely strained and the lower right corner is highly strained as well.

Figure 5-22(a) through 5-22(d) show the displacement fields at load steps 1, 5, 10 and 15. It has been observed that the first displacement field showed a downward movement of the nodes and the tendency becomes horizontal in the subsequent loading steps.

The performance of the normal elements using as interface element is for from the actual interface behavior.

5.2.2 Goodman Type Interface Element

Figure 5-2(a) through Figure 5-9(e) show the deformed meshes of the analysis of 8 (eight) cases (Table 4-8) at the load steps 1, 5, 10, 15 and 20. The displacements of the deformed mesh are amplified 5 times. From Figure 5-2(a) through Figure 5-2(e), it can be seen that major deformation has taken place inside the interface elements and it is progressively increasing from load step 5 through 20. One thing is clear from the last Figure of this series (Figure 5-2(e)) that as the horizontal load is applied to the upper nodes of the interface element, then there is a tendency of separation on the right edge and a tendency of penetration on the left edge.

Figure 5-3(a) through Figure 5-3(e) show the results of the study (case-3 of Table 4-8) about changing the normal and shear stiffness to one value. From the observation of the Figures 5-3(a) through Figure 5-3(e), it is clear that it has large effect on the deformation of the interface element. Also the tendency of separation or penetration is decreased. As this case is studied with a large cohesion value (50.0 psi) at the interface element, it has probably the minimum interface deformation, as there has been no slip or debonding at the interface.

Figure 5-4(a) through Figure 5-4(e) show the deformation of the meshes for the analysis with no cohesion (c = 0.0) to enforce the frictional slip. From the Figures of deformed meshes it is seen that large deformation occurred for this analysis than the

88

previous one. Hence, frictional slip has taken place. The tendency of separation and/or penetration remained at minimum.

Figure 5-5(a) through Figure 5-5(e) show the deformed meshes for the analysis with weak interface stiffness compared to the surrounding material stiffness. It is readily seen from the deformed meshes that there has been large deformation at the nodes of the interface element. But this analysis shows clear indication of mesh penetration on the left edge and mesh separation on the right edge.

All the above cases of analysis are performed with element thickness t = 0.10 inch. Figure 5-6(a) through Figure 5-6(e) and Figure 5-7(a) through Figure 5-7(e) show the deformed meshes of the analysis with element thickness t = 0.05 inch and t = 0.02 inch respectively. It is interesting to note that Figure 5-7(a) through Figure 5-7(e) show almost no tendency of mesh penetration or separation. So, with the decrease in the thickness of interface element, performance of the interface element increases. Figure 5-8(a) through Figure 5-8(e) and Figure 5-9(a) and Figure 5-9 (e) show the deformed meshes of the analysis with shear loading at 0.80 inch and 0.20 inch from the top respectively. It has been found that the tendency of the separation or penetration changes with the change in the location of shear loading. When shear loading is at 0.20 inch from the top (Figure 5-9(a) through Figure 5-9(e)) the pattern of penetration/separation is reversed compared to the shear loading at 0.80 inch from the top.

Figure 5-23(a) and Figure 5-23(b) show force-displacement and stress-strain relationship of the case-1 analysis. The force-displacement relationship at the loaded node for horizontal and vertical loads shows unique relationship. From the relationship of the horizontal load vs. displacement, it is seen that initially there has been less displacement/slip at the interface and it increases at larger load steps.

Figure 5-24(a) through Figure 5-24(c) show the shear strain contours of the results at load steps 5, 10 and 15. From the shear strain contours, it is clear that internal shearing has taken place inside the interface element and intensity of shearing is given near the left edge.

Figure 5-25(a) through Figure 5-5(d) show amplified displacement field. Initial motion of the displacement vectors is somewhat eccentric which is clear from Figure 5-25(a). Subsequently, with the increase in horizontal (shearing) load, the displacement vectors become more inclined to the direction of the resultant load.

Figure 5-26(a) and Figure 5-26(b) show the force-displacement and stress-strain relationship of case-2 analysis. From the relationship of the horizontal load vs. displacement it is seen that initially there has been less displacement or slip at the interface and it increases at large load steps. Figure 5-26(b) shows the stress-strain relationship inside the interface elements. It can be seen that horizontal or shear stress is increasing monotonically without a limit. The Mohr-Columb friction law is applied at the interface but as cohesion c is set to be 50 psi for this case of analysis and the applied stresses have not exceeded this value, so shear stress inside the interface increased monotonically.

Figure 5-27(a) through Figure 5-27(c) and Figure 5-28(a) through Figure 5-28(b) show the shear strain contours and displacement fields respectively. Figure 5-29(a) and Figure 5-29(b) show the force-displacement and stress-strain relationship of the case-3 analysis. From the shear (horizontal) load vs. displacement relationship, it can be observed that maximum shear displacement /slip is large in this case compared to the previous case. From the stress-strain curve for horizontal (shear) stress, it becomes transparent that horizontal stress is limited by the Mohr-Coulomb governing law (in the case of c =0). This is the main reason for larger shear deformation.

Figure 5-30(a) through Figure 5-30(c) and Figure 5-31(a) through Figure 5-31(d) show the shear strain contours and displacement field respectively for case-3. The displacement fields show no sign of any separation or penetration.

Figure 5-32(a) and Figure 5-32(b) show the force-displacement and stress-strain relationship of case-4 analysis. In this case interface stiffness is decreased by an order of 10. The result can be immediately seen from the relationship of force-displacement. The shear displacement increased for the previous analysis.

Figure 5-33(a) through Figure 5-33(c) and Figure 5-34(a) through Figure 5-34(d) show the shear strain contours and displacement fields respectively for case-4 analysis. Though the contours show more uniform distribution of shear strains, displacement vectors show a clear sign of penetration on the left edge and separation on the right edge in all stages of loading.

Figure 5-35(a) and Figure 5-35(b) show the force-displacement and stress-strain relationship of case-5 analysis. In this case interface thickness t is decreased to 0.05 inch. The results show the reduced shear displacement.

Figure 5-36(a) through Figure 5-36(c) and Figure 5-37(a) through Figure 5-37(d) show the shear strain contours and displacement fields respectively for case-5 analysis. It can be seen from the shear strain contours that the uniformity of the contours is increased. From the observation of the displacement fields it is seen that tendency for penetration/separation is reduced but existing.

Figure 5-38 (a) and Figure 5-38(b) show the force-displacement and stress-strain relationship of case-6 analysis. In this analysis thickness of the interface is reduced to 0.02 inch. The effect of this reduction is reflected in the reduction of shear displacement and more uniform shear movement shown in the shear strain contours in Figure 5-39(a) through Figure 5-39(c). The tendency of penetration/separation is also completely removed as seen from the displacement fields shown in Figure 5-40(a) through Figure 5-40(d).

Figure 5-41(a) and Figure 5-41(b) show the force-displacement and stress-strain relationship for the analysis of load case-7. Location of the shear loading is changed to 0.80 inch from the top in this analysis. This actually decreased the height of the shear loading from 1 inch from the top to 0.80 inch from the top. This actually decreased the penetration and separation as seen from displacement field Figures (Figure 5-43(a) through 5-43(d)).

Figure 5-44(a) and Figure 5-44(b) show the force-displacement and stress-strain relationship for the last case-8. In this case, location of loading is decreased further to 0.40 inch from the top. This shows a relatively slow rise in the horizontal stress in side the interface as seen in Figure 5-44(b).

Figures 5-45(a) through Figure 5-45(c) show very uniform shear strain contours. From the observation of Figure 5-46(a) through Figure 5-46(d), it is found that separation and penetration reversed their initial position. So, it becomes clear that penetration or separation were due to the eccentricity of the shear loading.

5.2.3   Katona Type Interface Element

Figure 5-10 (a) through Figure 5-14(e) show the deformed meshes for the analysis of 5 (five) cases (Table 4-8) at load steps 1, 5, 10, 15 and 20. The displacements of the deformed mesh are amplified 10 times in order to make the deformation perceptible. Deformed meshes of the first four cases (Figure 5-10(a) through Figure 5-13(e)) show decreasing total shear deformation inside the interface elements due to increasing friction angle from 5^0 through 10^0, 20^0 and finally to 30^0. Although there is a visible thickness of the element in all the Figures of deformed mesh still it has no significance in the element formulation. Katona type of interface is actually a zero thickness interface element. The gap or thickness is shown for better comprehension of the mechanism. The fifth case of the analysis is carried-out by applying shear load at different level (0.8 inch from the top). It shows less shear deformation inside the interface.

Figure 5-47(a) and Figure 5-47(b) show the force-displacement and stress-strain relationship of the case-1 of Katona type interface analysis. In this case friction is relatively low (5^0 only). Figure 47(a) shows that after the horizontal load is increased up to a level of the vertical load than the shear deformation due to slip (debonding) begins. Figure 5-47(b) supports the above notation.

Figure 5-48(a) through Figure 5-48(e) show the shear strain contours for case-1 analysis of Katona type interface. From the Figure of the contours it can be seen that formation of the interface shearing is progressive in nature unlike Goodman type elements deformation took place on both sides of the interface elements even at a very low friction angle at the interface.

Figure 5-49(a) through Figure 5-49(d) show the displacement fields for case-1. Initial displacement field at load step 1 shows a tendency of separation on the left edge of the shear box, but soon it is stabilized to shear horizontally. Upper part of the shear box shows perfectly horizontal movement as it is dragged in slip mode.

Figure 5-50(a) through Figure 5-58(d) show force-displacement, stress-strain relationship, shear strain contours and displacement fields for the cases-2, 3 and 4 for the Katona type interface analysis. In these cases only the interface friction angle have been changed from 10^0 through 20^0 and to 30^0. The results are similar in pattern. For force-displacement relationship, less shear deformation with the increase in friction angle is observed. Stress-strain relationship shows a larger sharp up rise point in horizontal stress increase before it becomes flat with the increase in friction.

Figure 5-59(a) and Figure 5-59(b) show the force-displacement and stress-strain relationship for the analysis of load case-5 of Katona type interface. In this analysis shear load is applied at 0.80 inch from the top, which is very near to the interface elements. This analysis shows very uniform shear deformation substantiated by shear strain contours shown in Figure 5-60(a) to 5-60(c) and displacement fields shown in Figure 5-61(a) to Figure 5-61(d).

5.2.4 Desai Type Interface Element

Figure 5-15(a) through Figure 5-19(e) show the deformed meshes for the analysis of case-1 to case-5 of Desai type interface at load steps 1, 5, 10, 15 and 20. The displacements of the deformed meshes are amplified 10 times. The first three cases (Figure 5-15(a) to Figure 5-17(e)) show the effect of the density of the material used as the interface material. The frictional property of the interface material is controlled through void ratio, e. it has been observed that when void ratio of the interface material is increased, peak angle of internal friction is reduced and subsequently more shear deformation occurred.

Figure 5-18(a) through Figure 5-18(e) show the deformed mesh for loading at 1.0 inch from the top and Figure 5-19(a) through Figure 5-19(e) show the deformed mesh for loading at 0.2 inch from the top. From the observation of these two series of deformed meshes, it is clear that due to eccentric loading, a tendency of separation and penetration takes place. But it is not as severe as it happened in case of Goodman Type interface elements. In this case thickness of the element reduced in an uneven formation.

Figure 5-62(a) and Figure 5-62(b) show the force-displacement and stress-strain relationship for analysis of case-1 of Desai type interface. The analysis is carried out to show the effect of material density on the shear movement of the interface element. There are other two analyses where material density is varied. Those are shown in Figure 5-65(a), Figure 5-65(b), Figure 5-68(a) and Figure 5-68(b). It has been shown that as with the increase in material density angle of internal friction increases deformation in the interface element decreases and stresses increase. Similarly, it may be seen that when density decreases, angle of internal friction decreases so deformation in the interface element increases and stresses decreases.

Figures 5-71(a) through Figure 5-71(d) show the results of analysis for case-4 and case-5 of Desai type interface elements. These analyses are carried out to see the effect of load eccentricity. The case-4 analysis is carried out using shear load at 1.0 inch from the top

and the case-5 analysis is carried out using shear load at 0.2 inch from top. It has been found that for higher eccentric shear loading (shown Figure 5-74, 5-75 and 5-76), there is a sign of penetration or separation. But it seems that Desai type of elements is less likely to penetrate.

5.3 COMPARISON OF THE INTERFACES

Detail performance of each of the three types of interface has been discussed in the previous section. The general behavior of each of these three interfaces has its own merits and demerits. Until now Goodman type of interface has been used in wide variety of application due to its simple formulation and implementation. Recently, Desai type of element is also getting popularity due to its realistic, practical formulation and implementation. Although formulation of Katona type of interface element is elegant, its implementation in nonlinear incremental iterative FEM code is not a straight forward. Table 5-1 shows details of the comparison of performance among those interfaces.

Table 5-1: Comparison of Performance of Interfaces Analysed

PARAMETERS	INTERFACES			
	Normal Element	Goodman Type	Katona Type	Desai Type
Normal Stiffness, K_N	Not applicable	Large effect both on convergence & solution	No effect	No effect
Shear Stiffness, K_S	Not applicable	Affects shear deformation	No effect	No effect
Stiffness of Surrounding Material, E_S	Affects overall deformation	Affects both normal & shear deformation	Affects shear deformation	Affect both shear & normal deformation
Cohesion, c	No applicable	Affects shear deformation	Affect shear deformation	No effect
Friction, ϕ	Not applicable	Affects shear deformation	Affects shear deformation	Large effect on the interface behavior
Thickness, t	Not applicable	Low thickness improves behavior	No effect at all	It has large effect on stress-strain relation
Load eccentricity	Has large effect	Creates penetration/ separation	Stress concentration on edges	Tendency of penetration/ separation
Simulation of slip mode	Bad	Allows slip with friction law	Allows friction with friction law & transfer stress below	Allow slip but with material constitutive law
Convergence property	Quick	Moderate	Slow	Quick

96
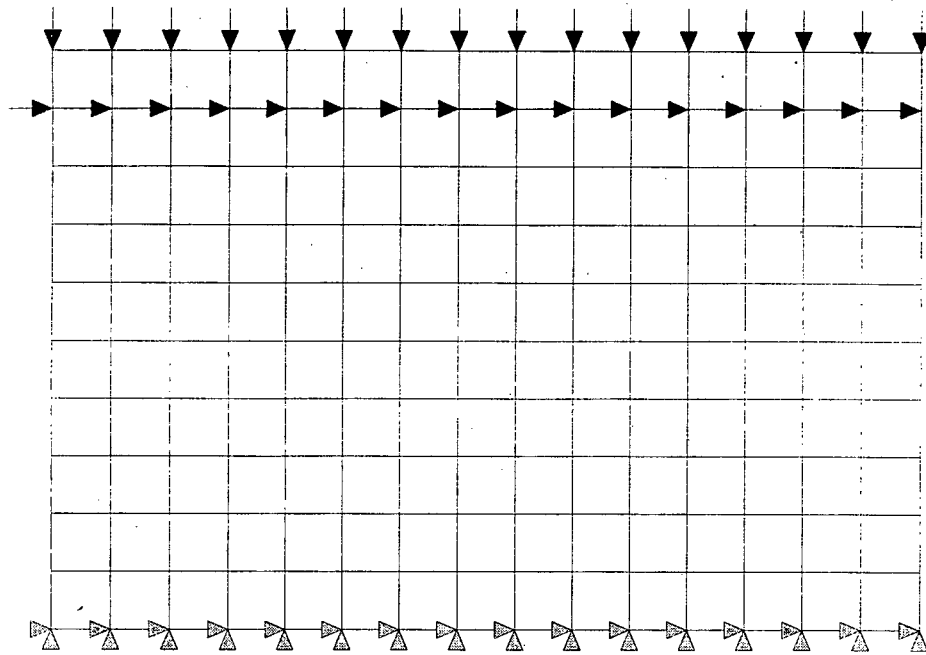
Figure 5-1(a): Deformed mesh for Case-1 of Normal Element at load
step 1.
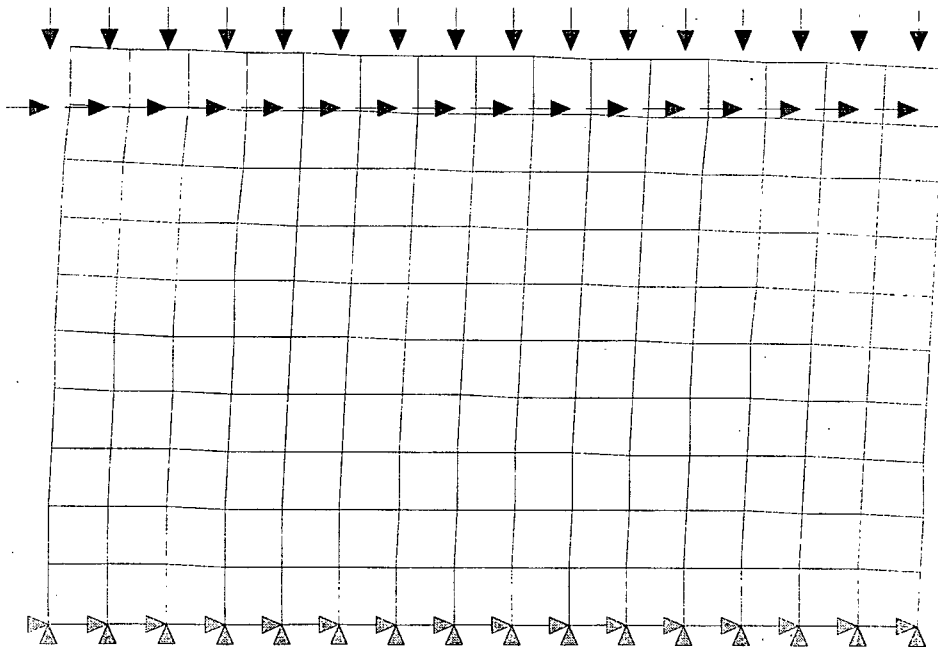
Figure 5-1(b): Deformed mesh for Case-1 of Normal Element at load
step 5.
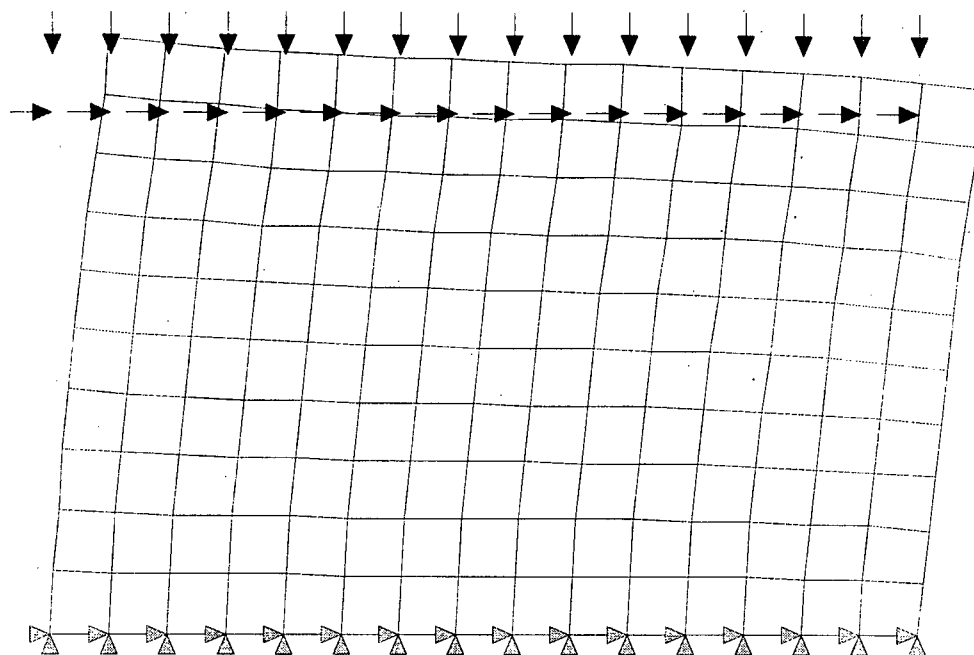
Figure 5-1(c): Deformed mesh for Case-1 of Normal Element at load step 10.
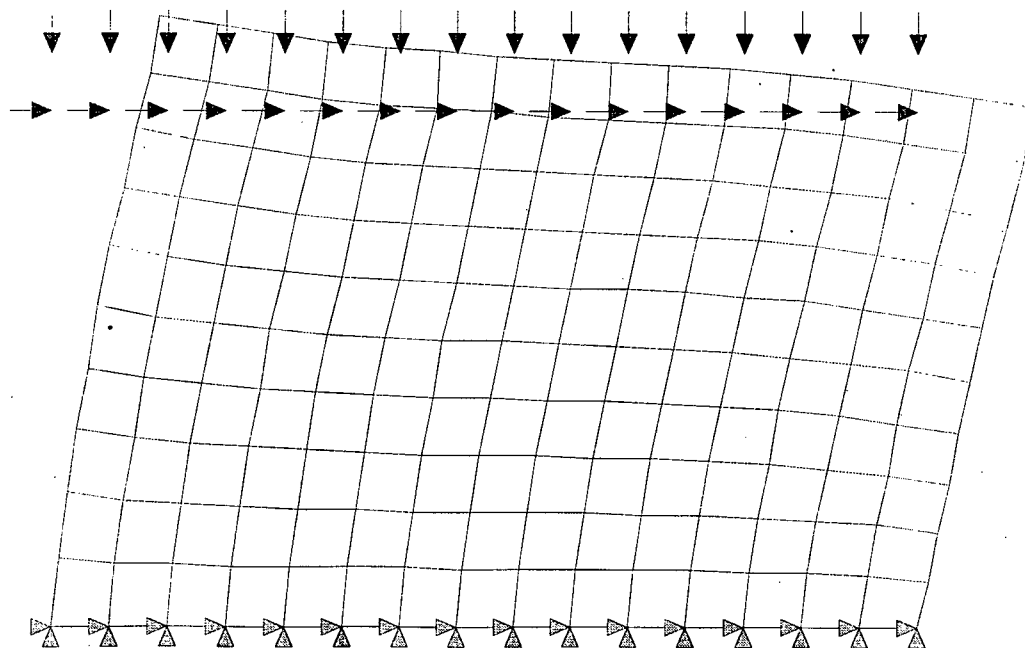
Figure 5-1(d): Deformed mesh for Case-1 of Normal Element at load step 15.
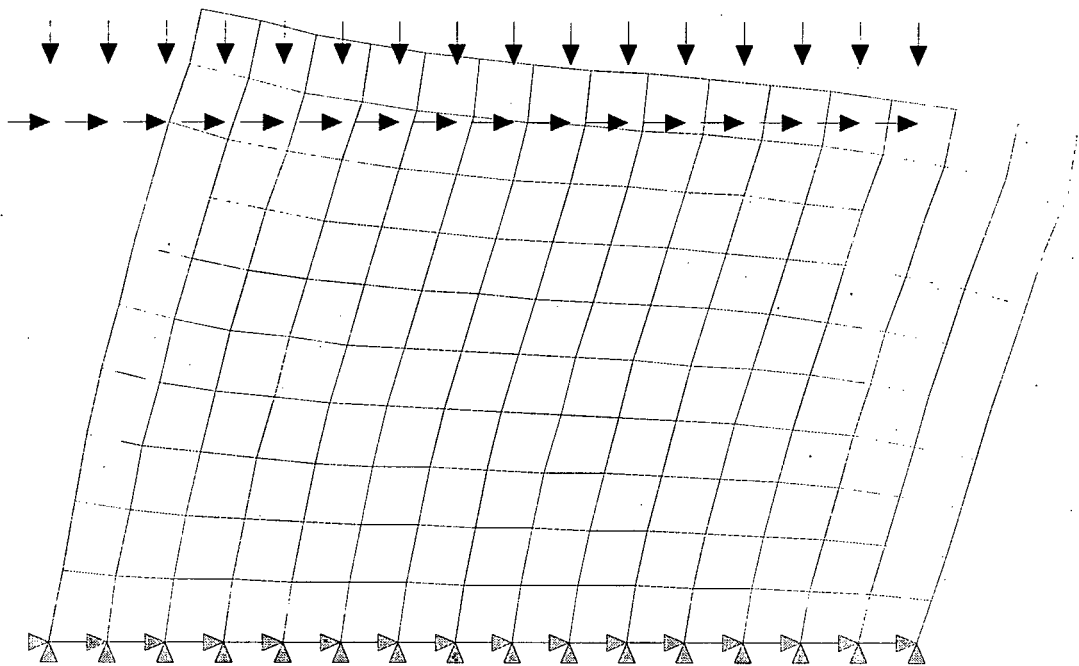
Figure 5-1(e): Deformed mesh for Case-1 of Normal Element at load
step 20.

99
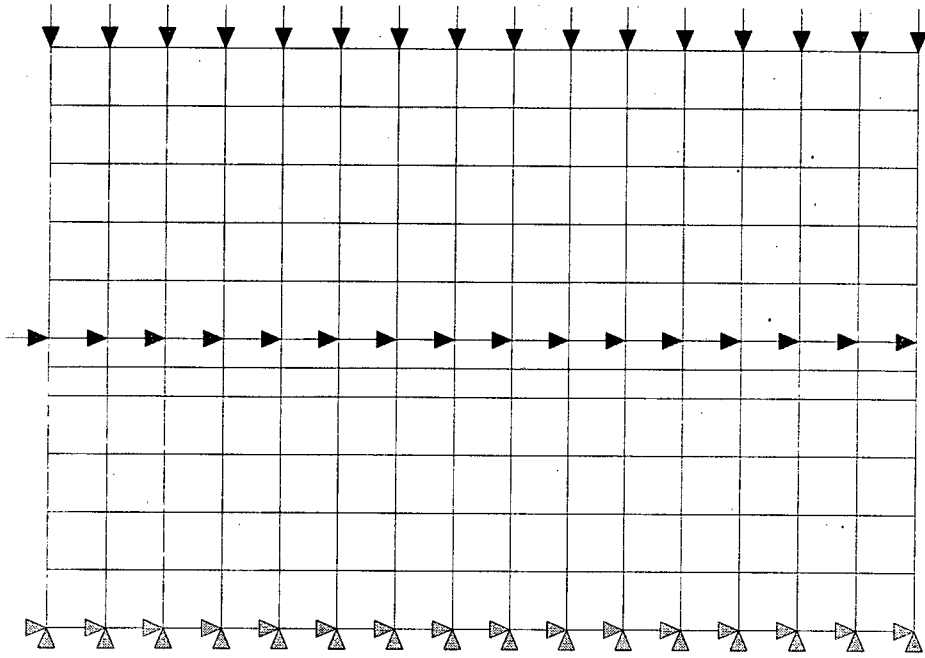
Figure 5-2(a): Deformed mesh for Case-1 of Goodman Type Interface at load step 1.
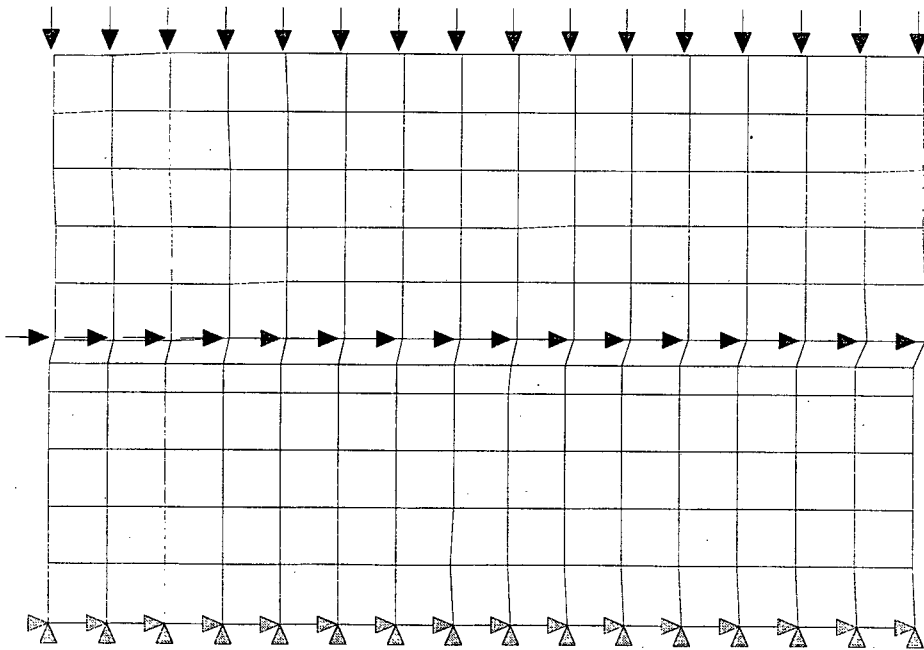
Figure 5-2(b): Deformed mesh for Case-1 of Goodman Type Interface at load step 5.

100
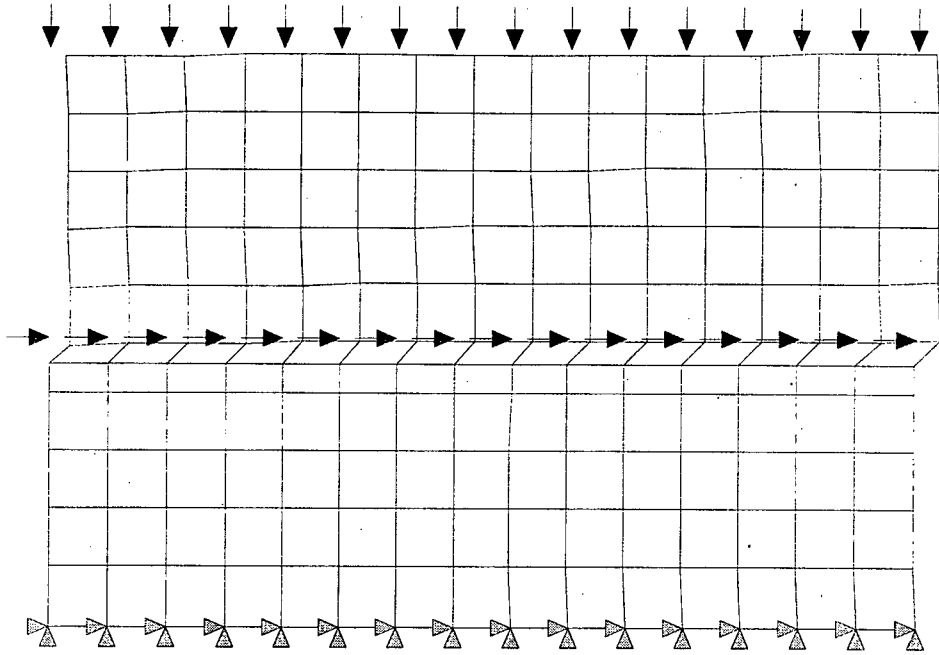
Figure 5-2(c): Deformed mesh for Case-1 of Goodman Type Interface at
load step 10.
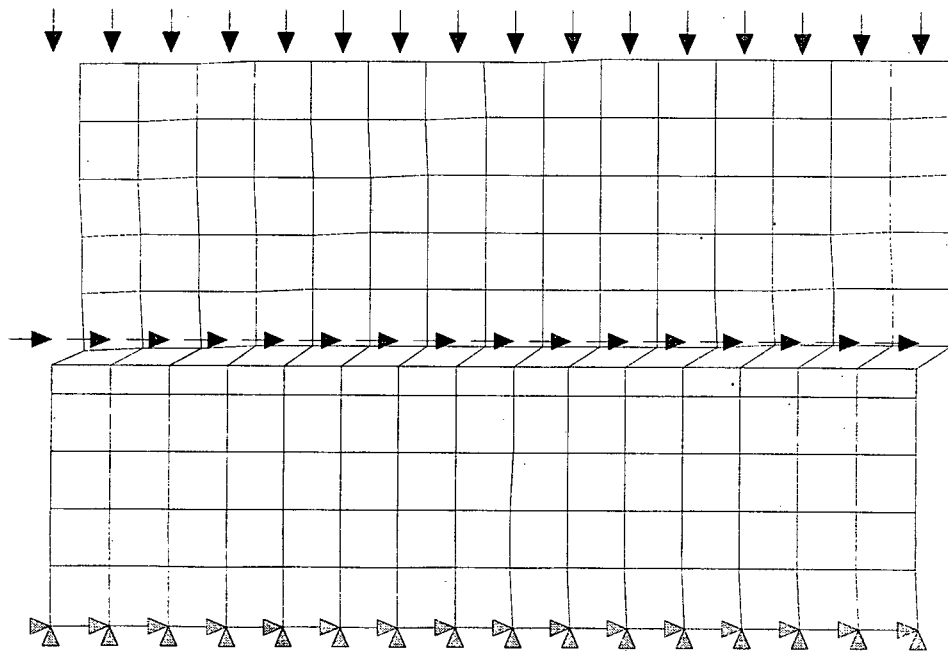
Figure 5-2(d): Deformed mesh for Case-1 of Goodman Type Interface at
load step 15.

101
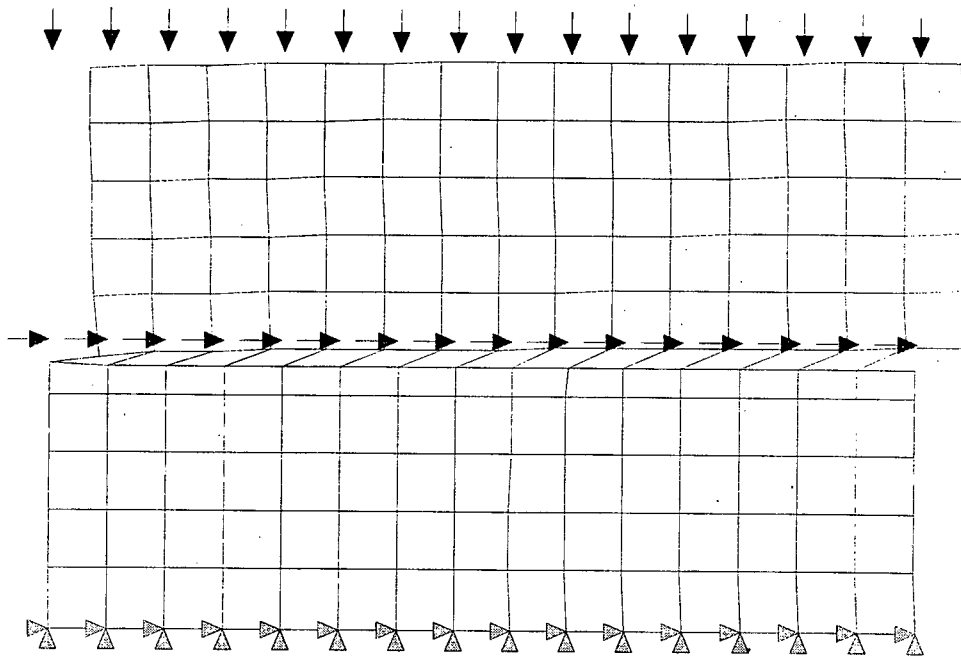
Figure 5-2(e): Deformed mesh for Case-1 of Goodman Type Interface at load step 20.
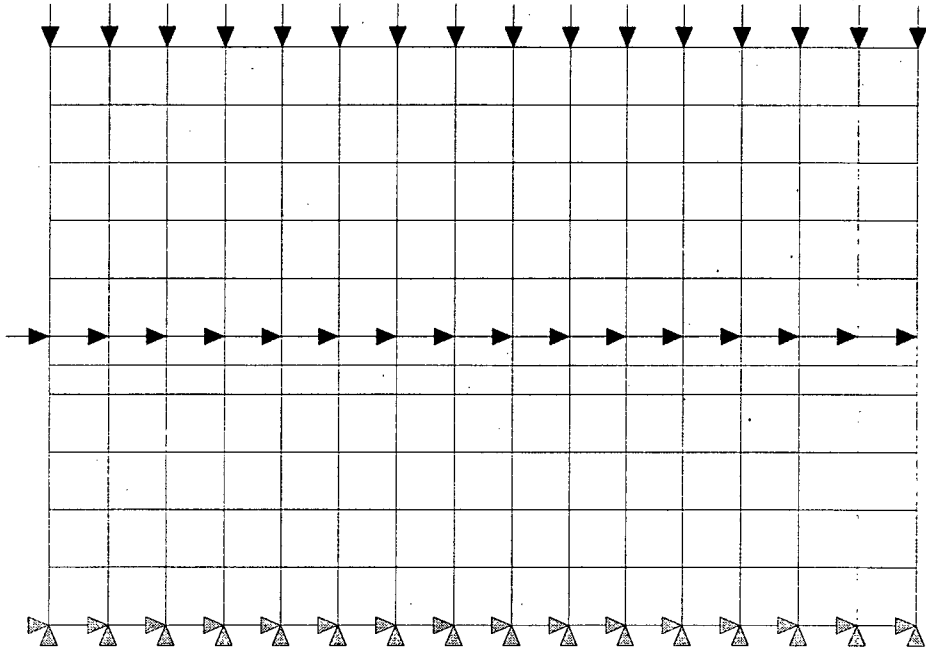
Figure 5-3(a): Deformed mesh for Case-2 of Goodman Type Interface at load step 1.
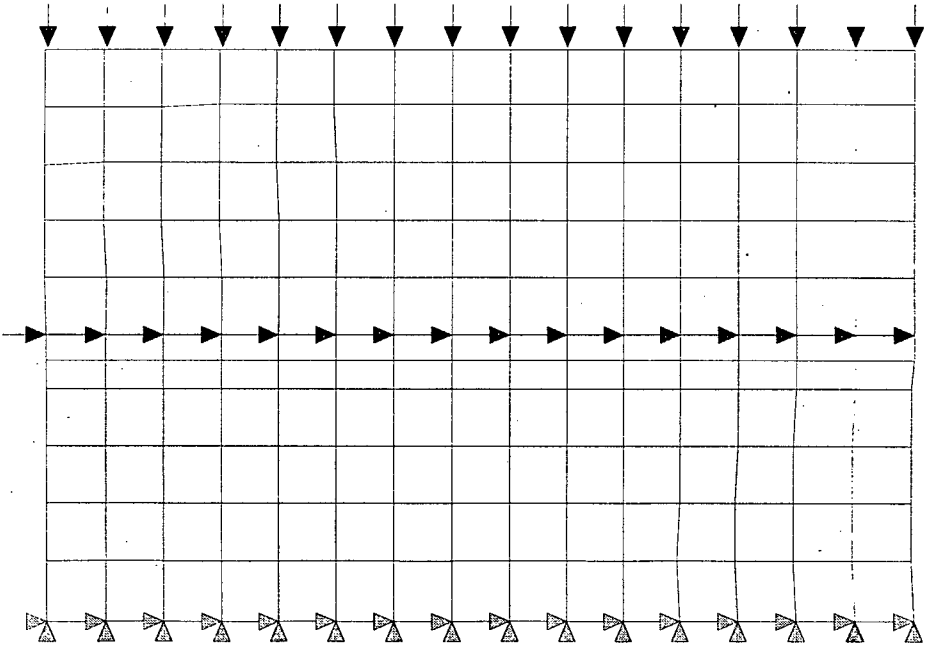
Figure 5-3(b): Deformed mesh for Case-2 of Goodman Type Interface at load step 5.

103
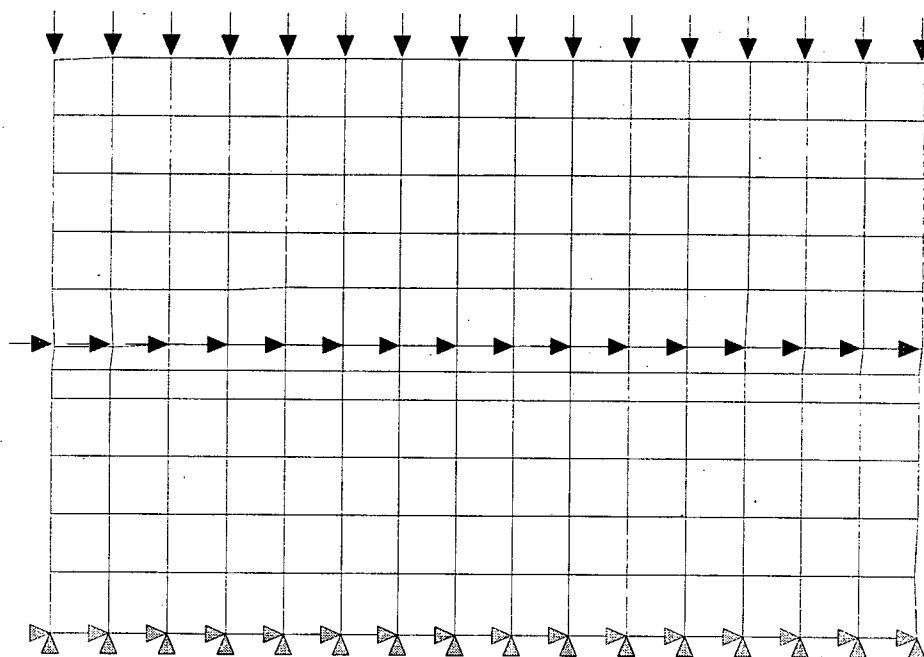
Figure 5-3(c): Deformed mesh for Case-2 of Goodman Type Interface at load step 10.
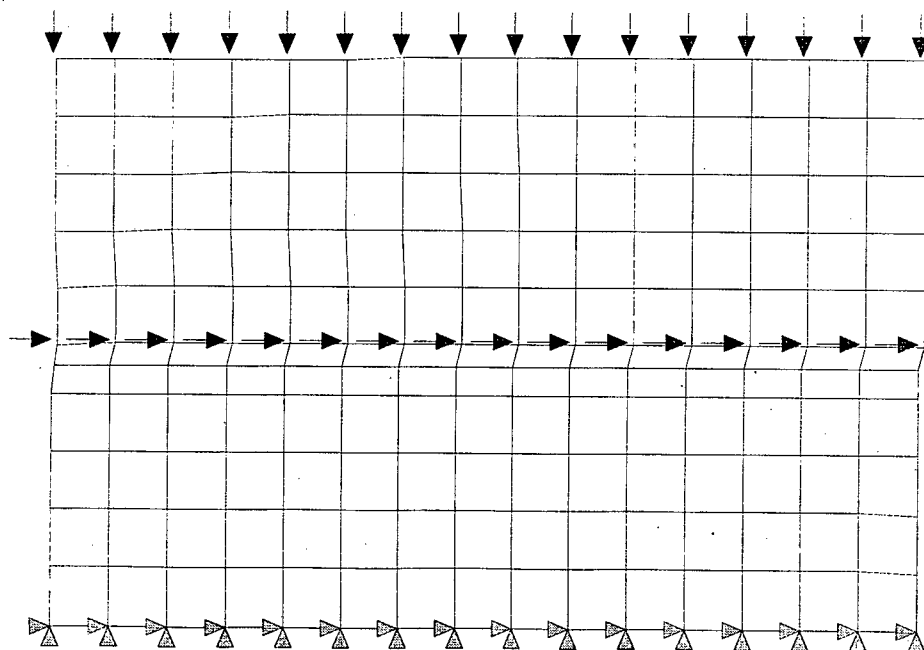
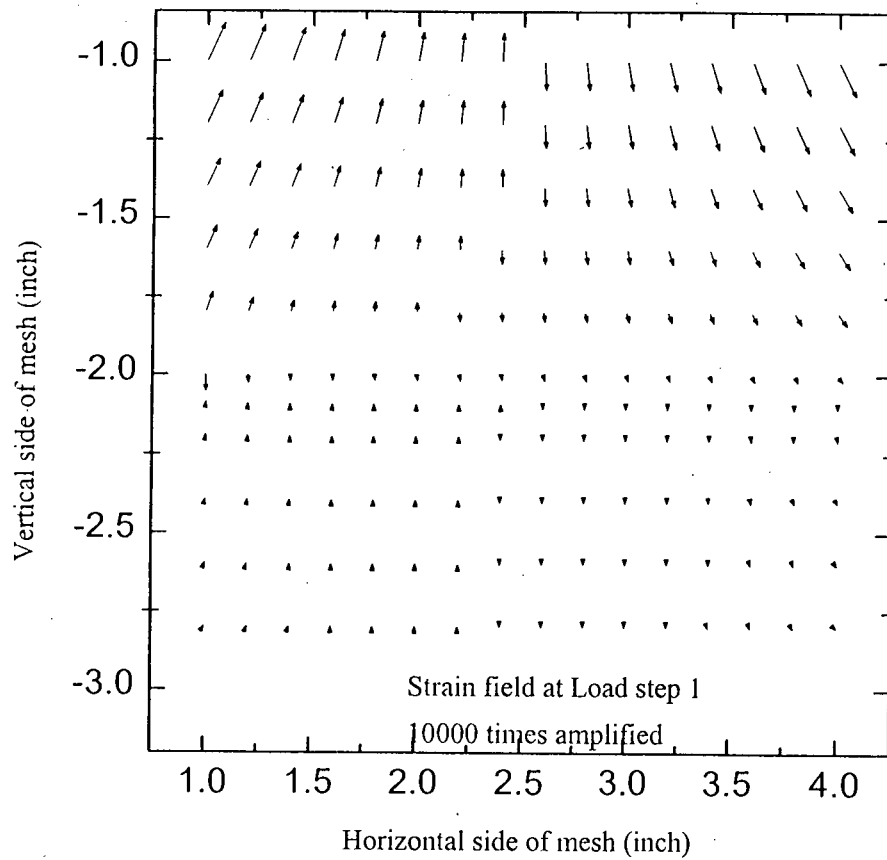Figure 5-3(d): Deformed mesh for Case-2 of Goodman Type Interface at load step 15.
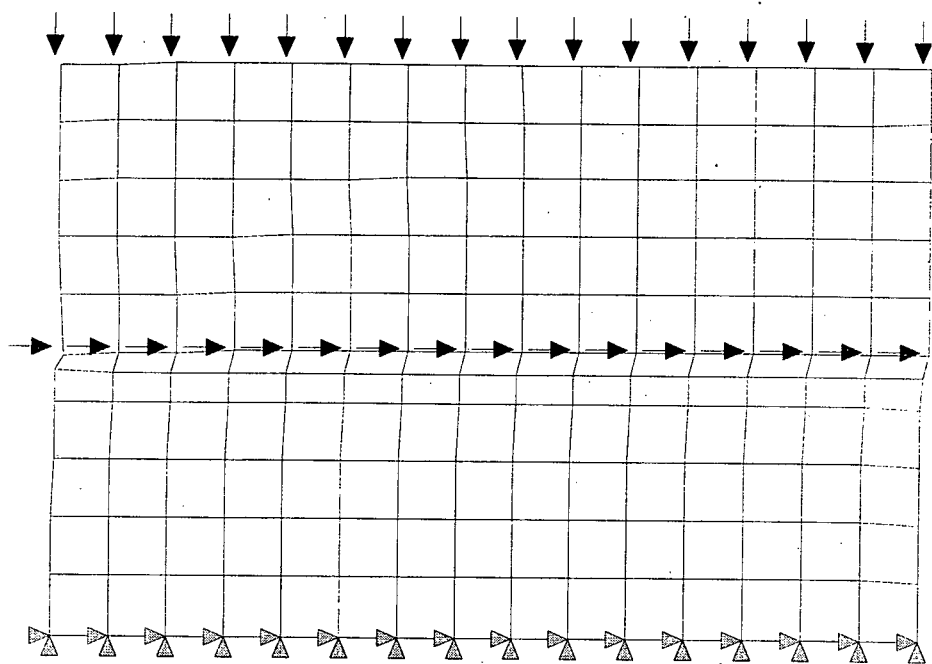
Figure 5-3(e): Deformed mesh for Case-2 of Goodman Type Interface at load step 20.
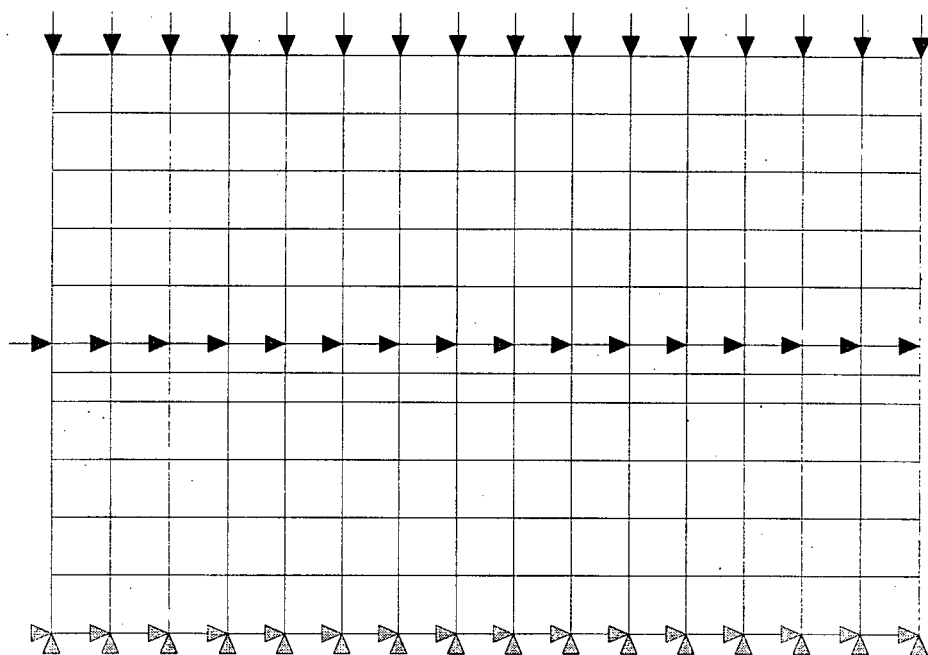
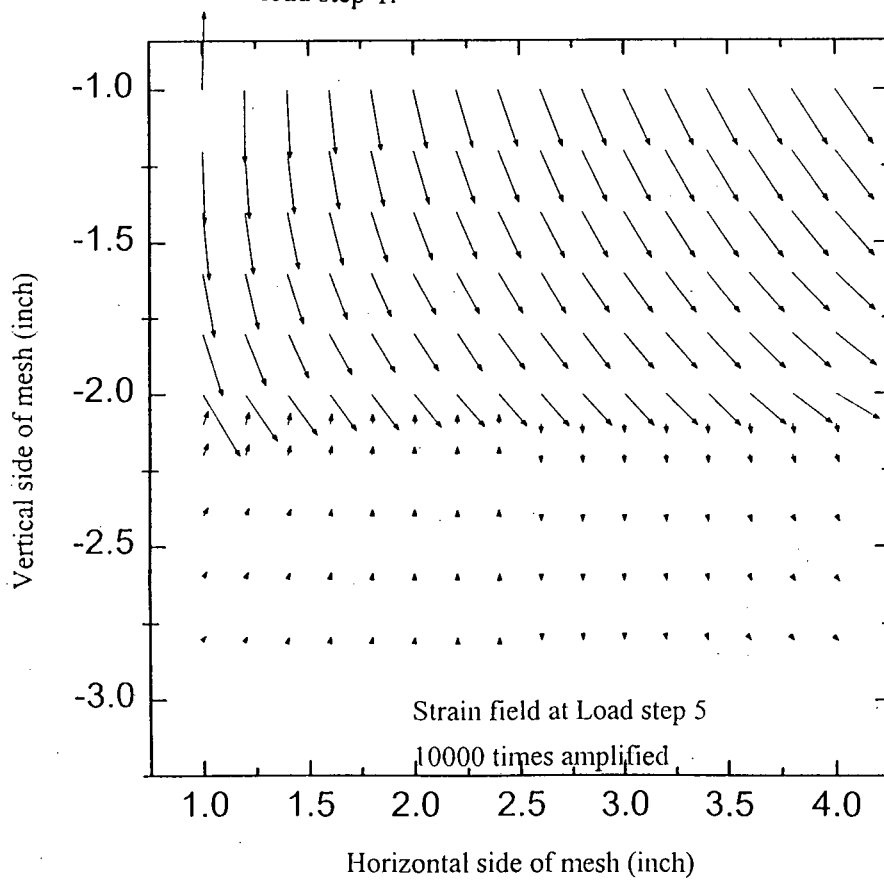Figure 5-4(a):: Deformed mesh for Case-3 of Goodman Type Interface at load step 1.
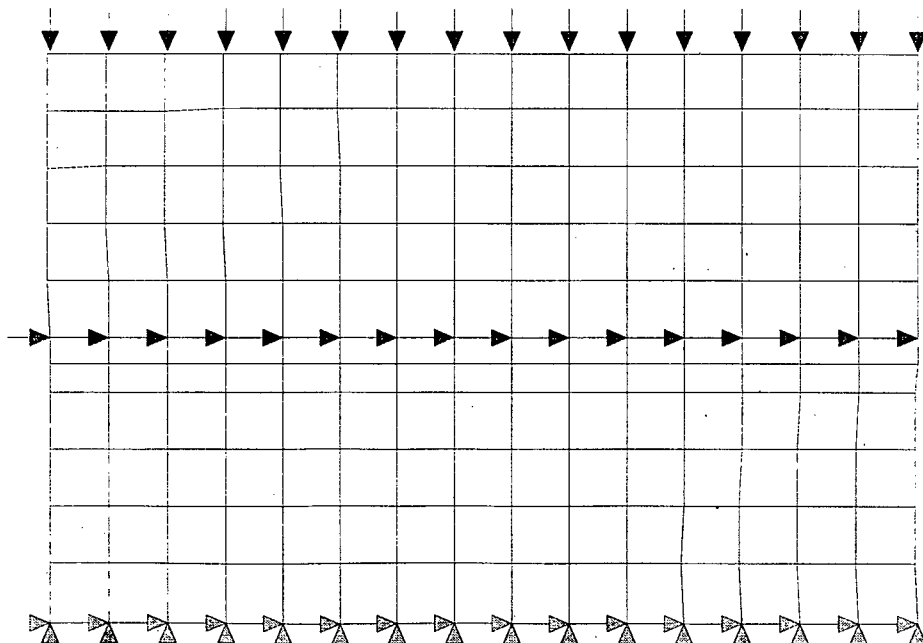
Figure 5-4(b): Deformed mesh for Case-3 of Goodman Type Interface at load step 5.
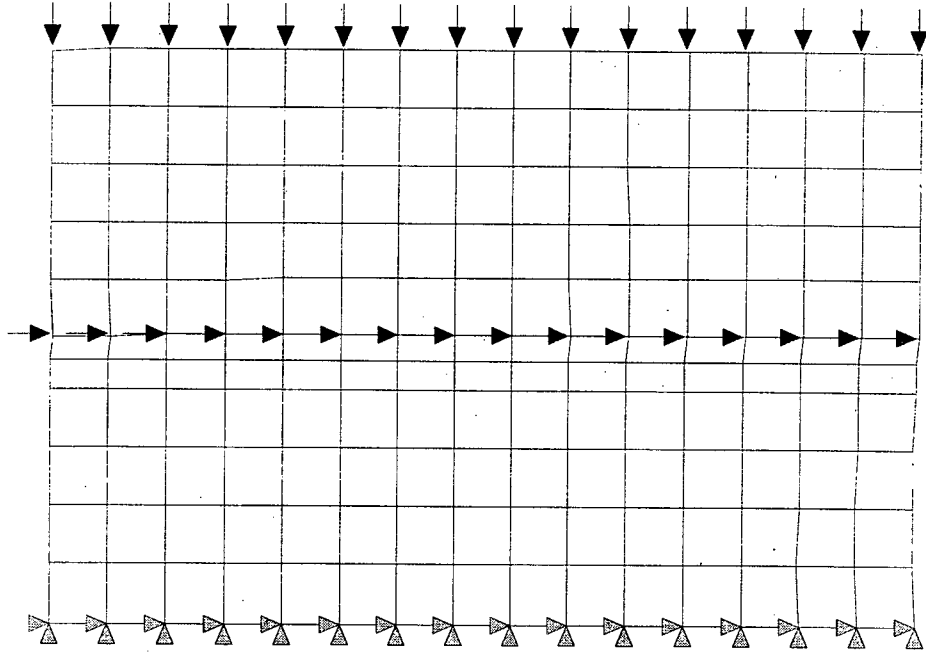
Figure 5-4(c): Deformed mesh for Case-3 of Goodman Type Interface at
load step 10.
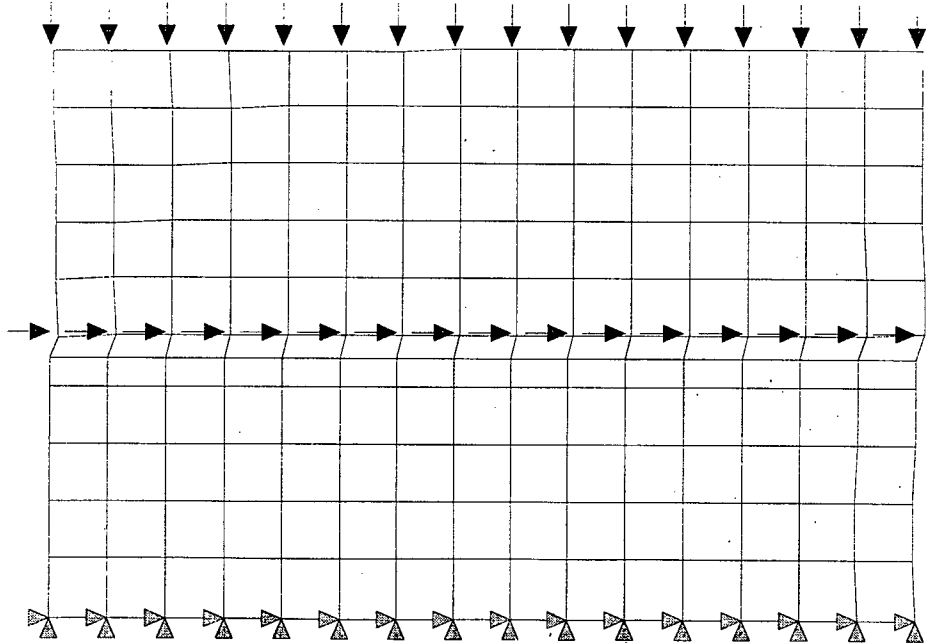
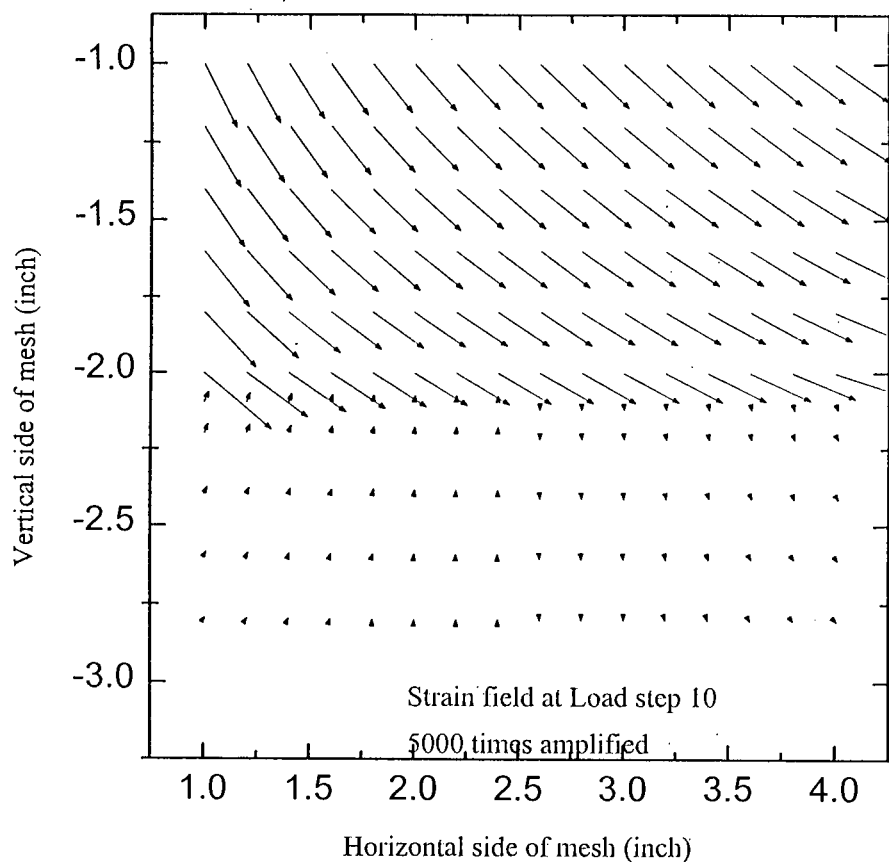Figure 5-4(d): Deformed mesh for Case-3 of Goodman Type Interface at
load step 15.
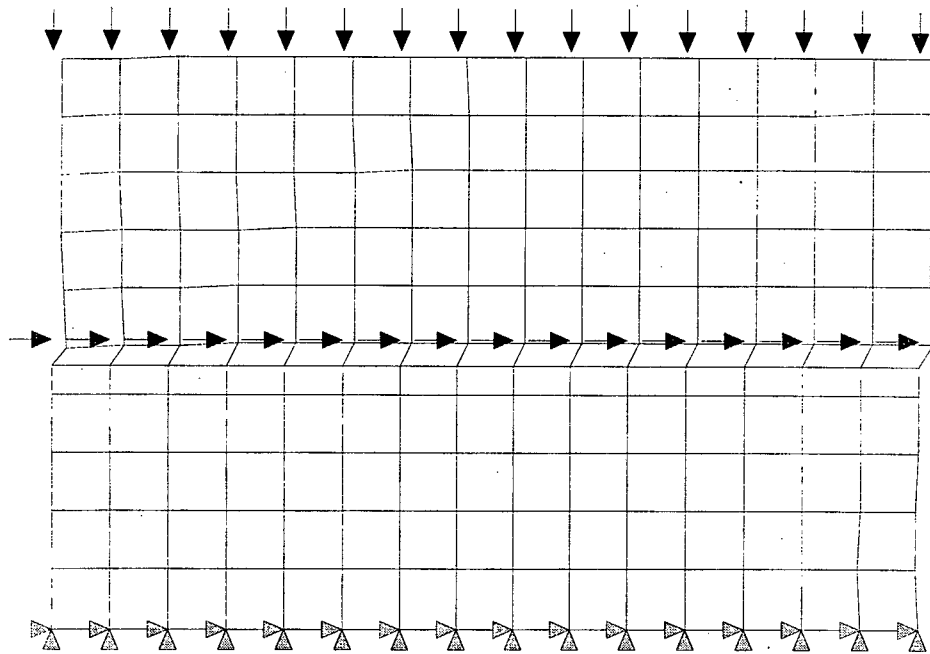
Figure 5-4(e): Deformed mesh for Case-3 of Goodman Type Interface at load step 20.
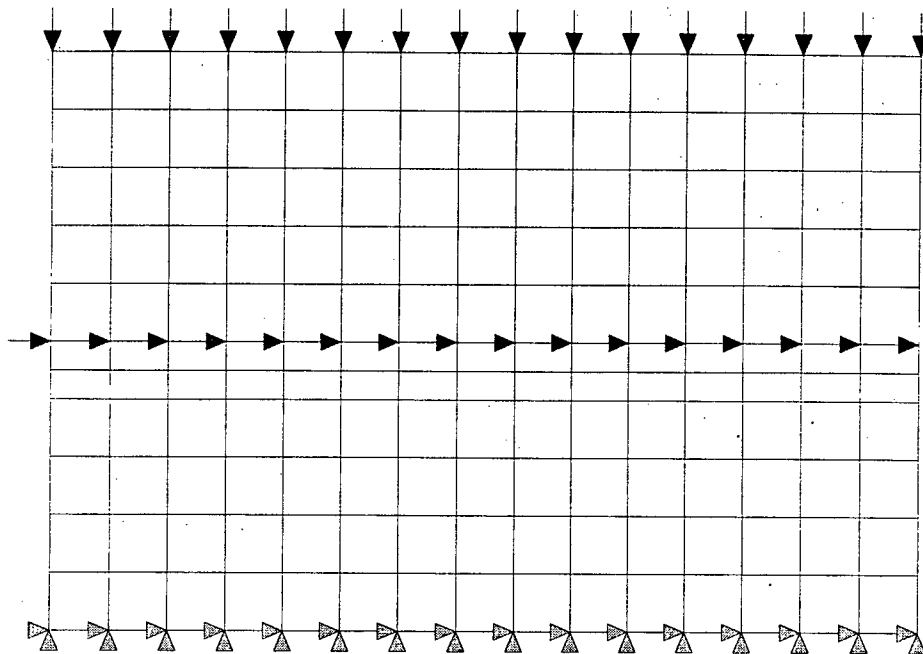
Figure 5-5(a): Deformed mesh for Case-4 of Goodman Type Interface at load step 1.
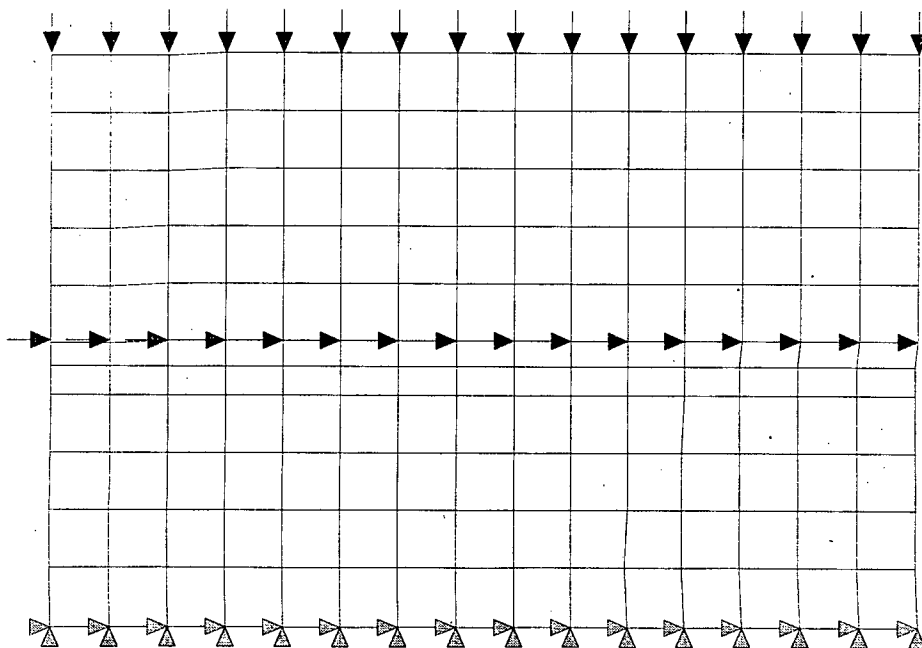
Figure 5-5(b): Deformed mesh for Case-4 of Goodman Type Interface at load step 5.

109
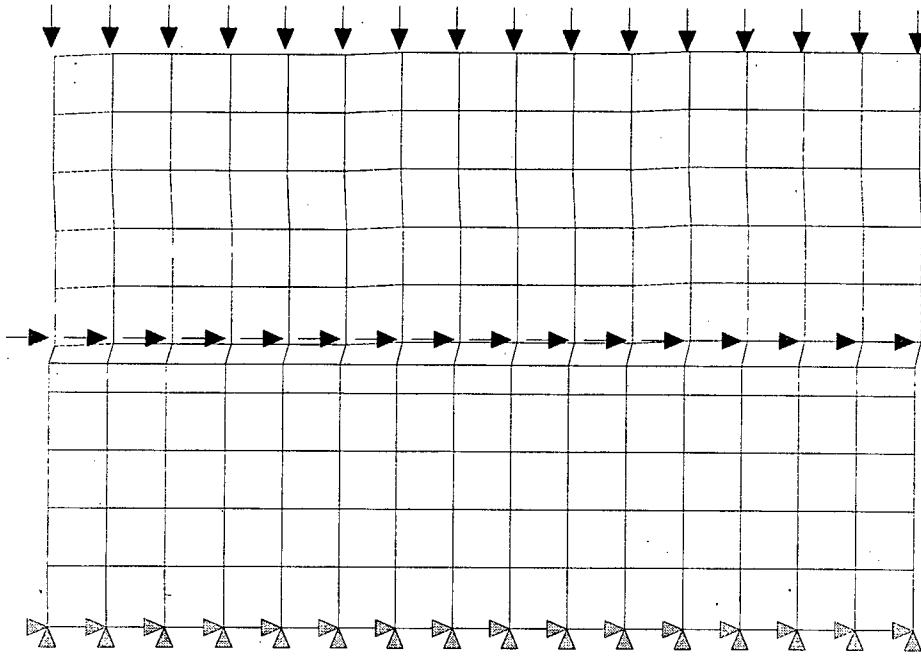
Figure 5-5(c): Deformed mesh for Case-4 of Goodman Type Interface at
load step 10.
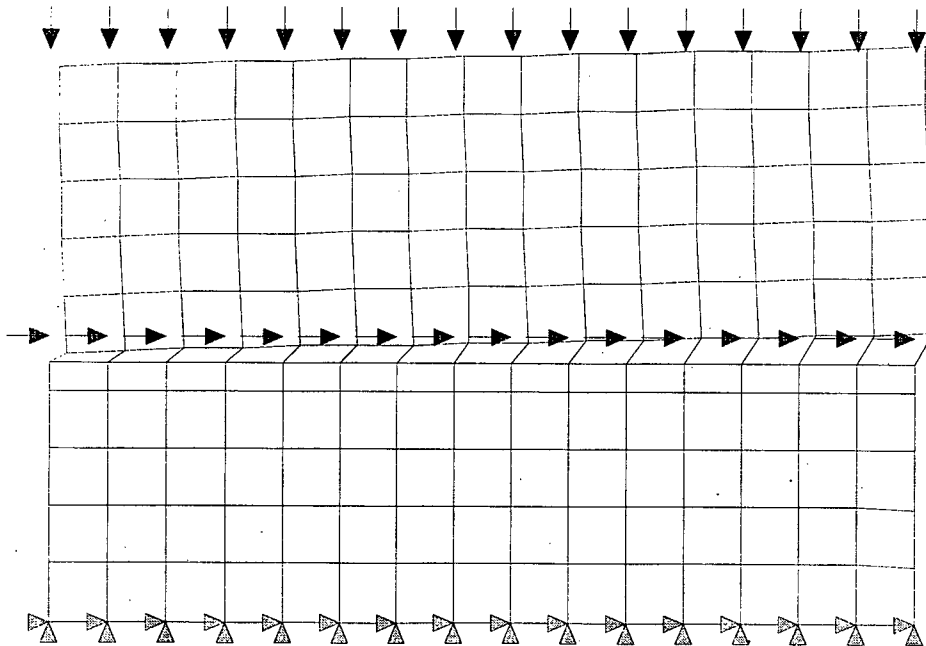
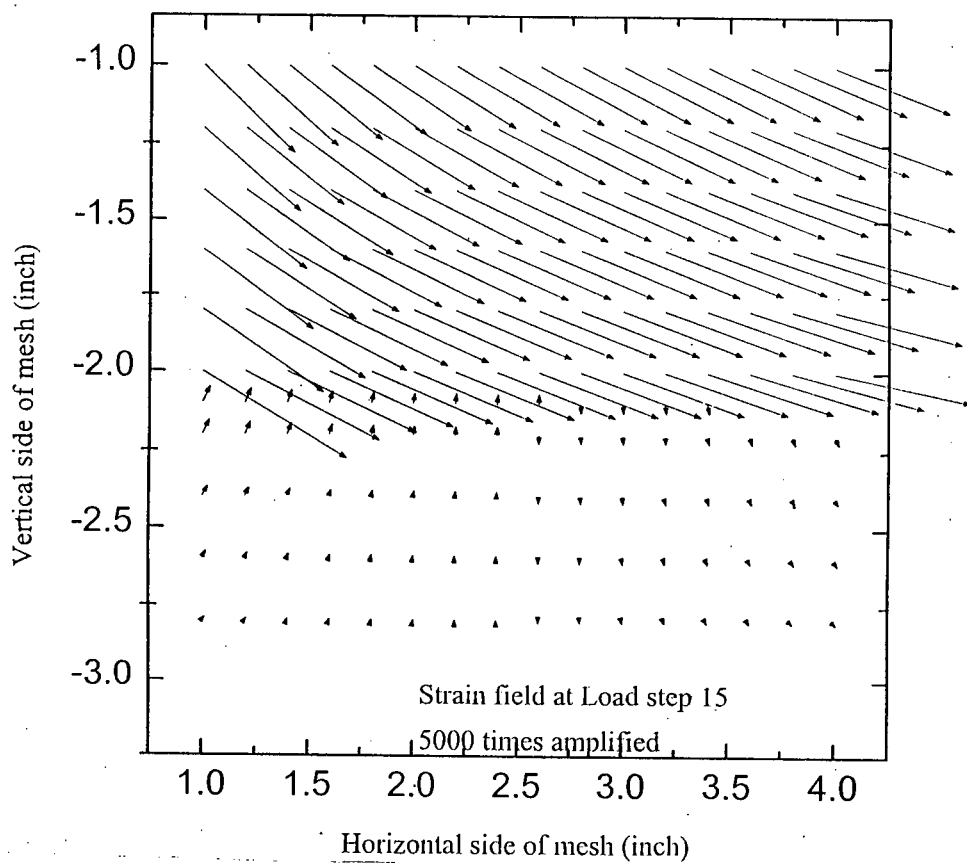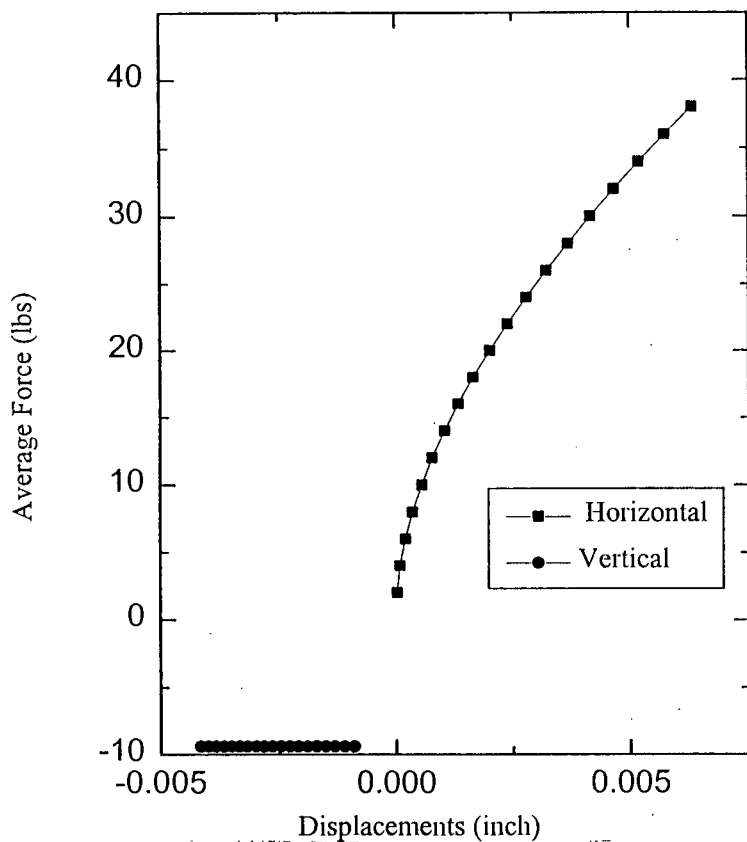Figure 5-5(d): Deformed mesh for Case-4 of Goodman Type Interface at
load step 15.

110
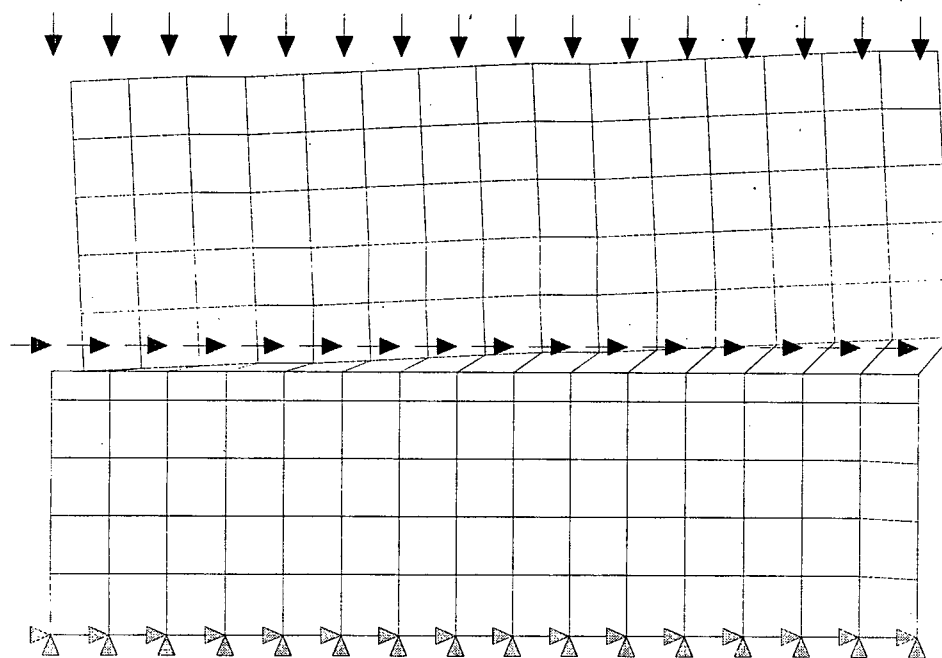
Figure 5-5(e): Deformed mesh for Case-4 of Goodman Type Interface at load step 20.
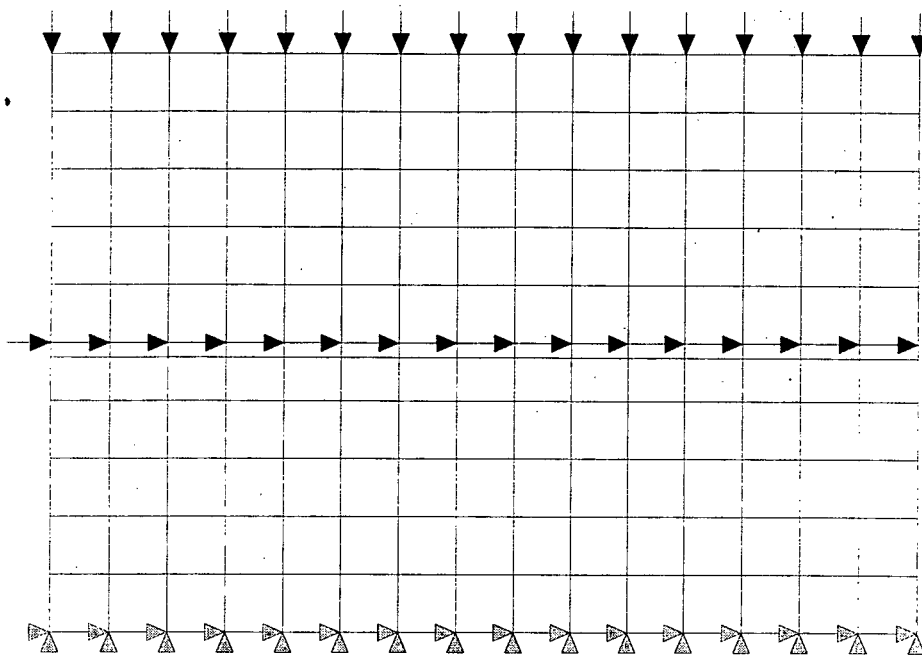
Figure 5-6(a): Deformed mesh for Case-5 of Goodman Type Interface at load step 1.
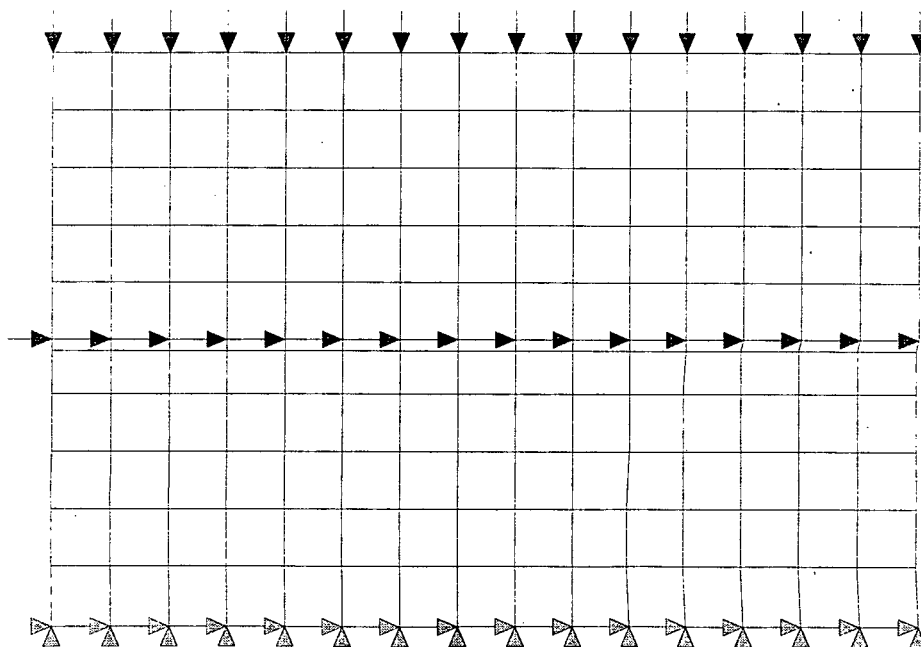
Figure 5-6(b): Deformed mesh for Case-5 of Goodman Type Interface at load step 5.
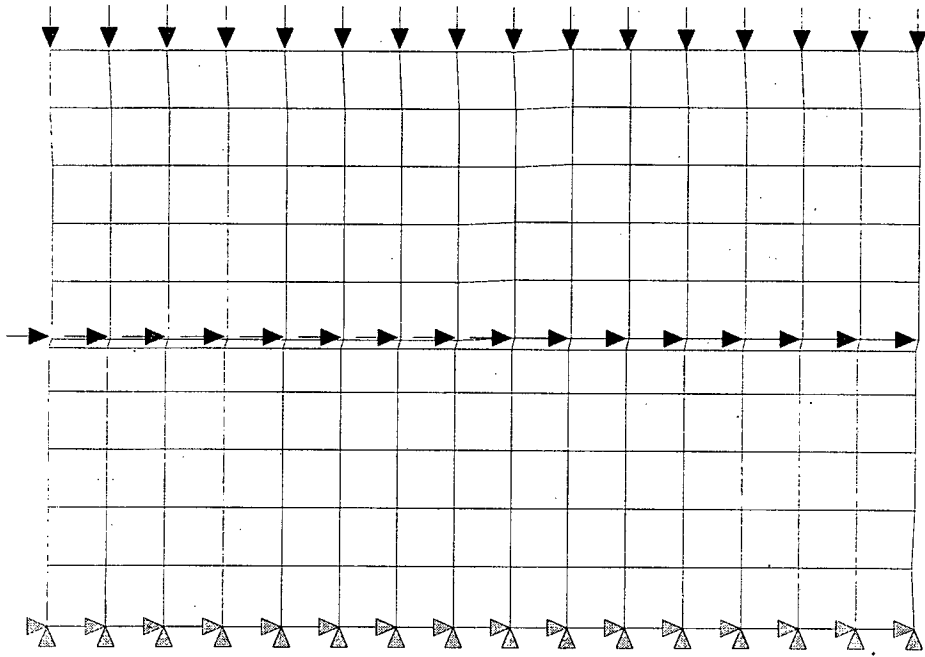
Figure 5-6(c): Deformed mesh for Case-5 of Goodman Type Interface at load step 10.
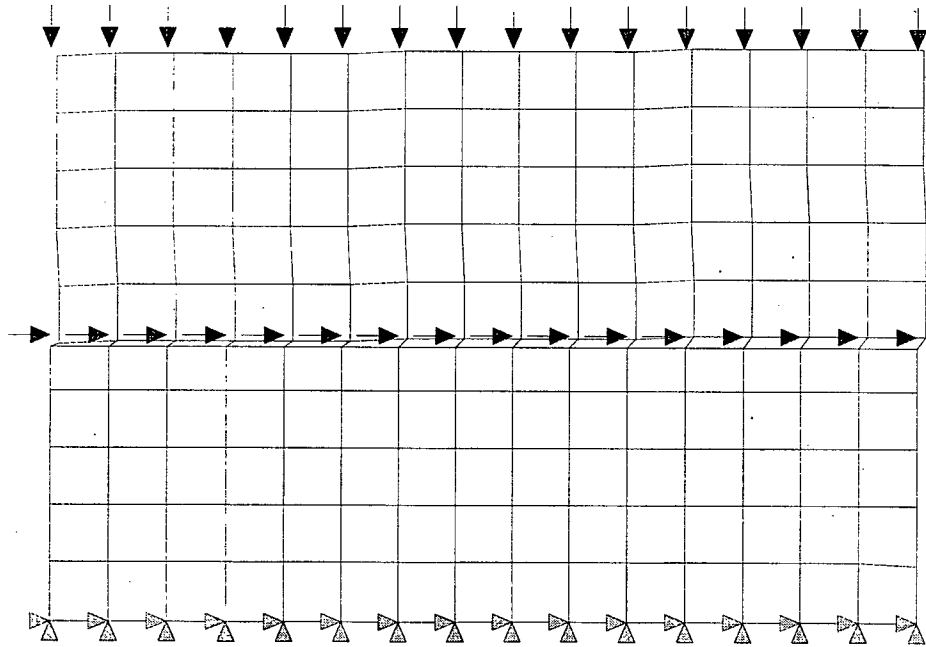
Figure 5-6(d): Deformed mesh for Case-5 of Goodman Type Interface at load step 15.
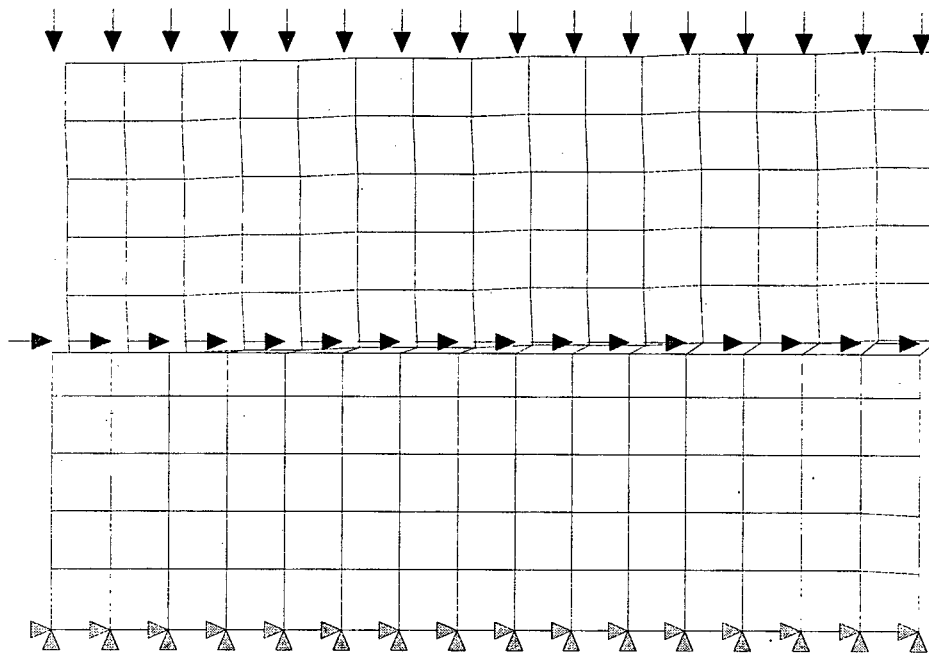
Figure 5-6(e): Deformed mesh for Case-5 of Goodman Type Interface at load step 20.
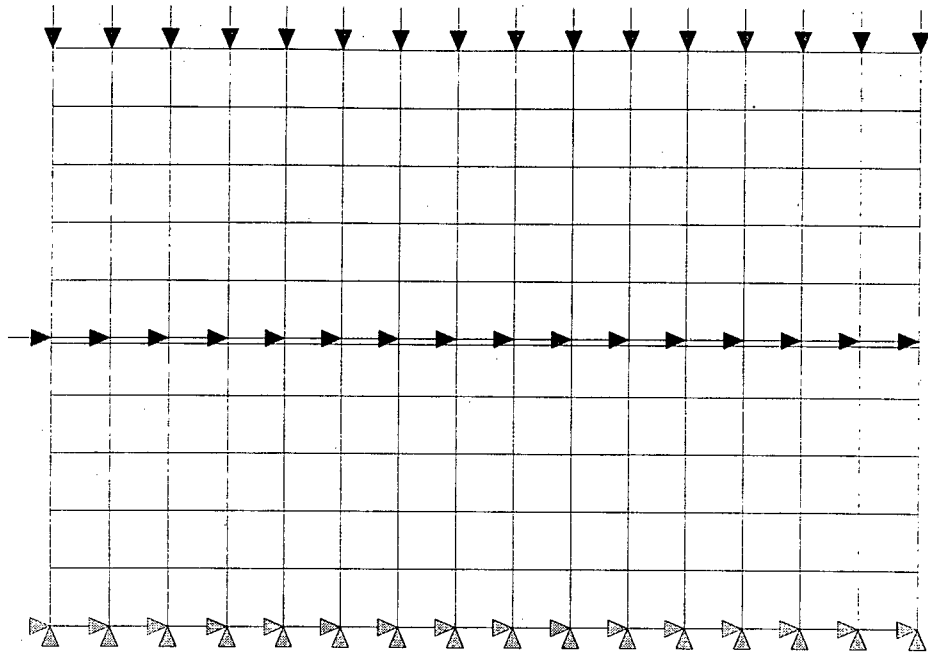
Figure 5-7(a): Deformed mesh for Case-6 of Goodman Type Interface at load step 1.
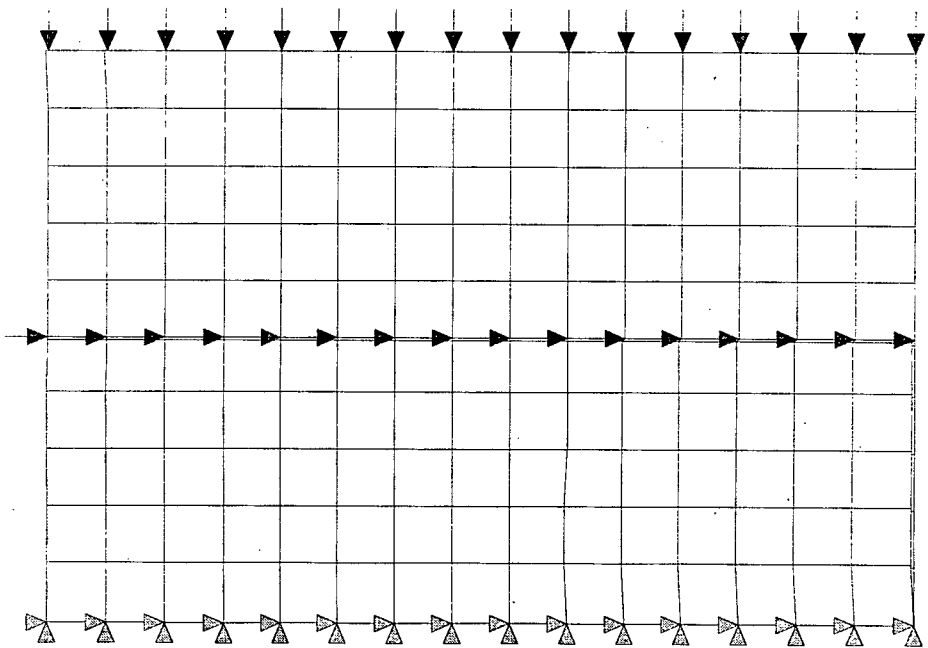
Figure 5-7(b): Deformed mesh for Case-6 of Goodman Type Interface at load step 5.
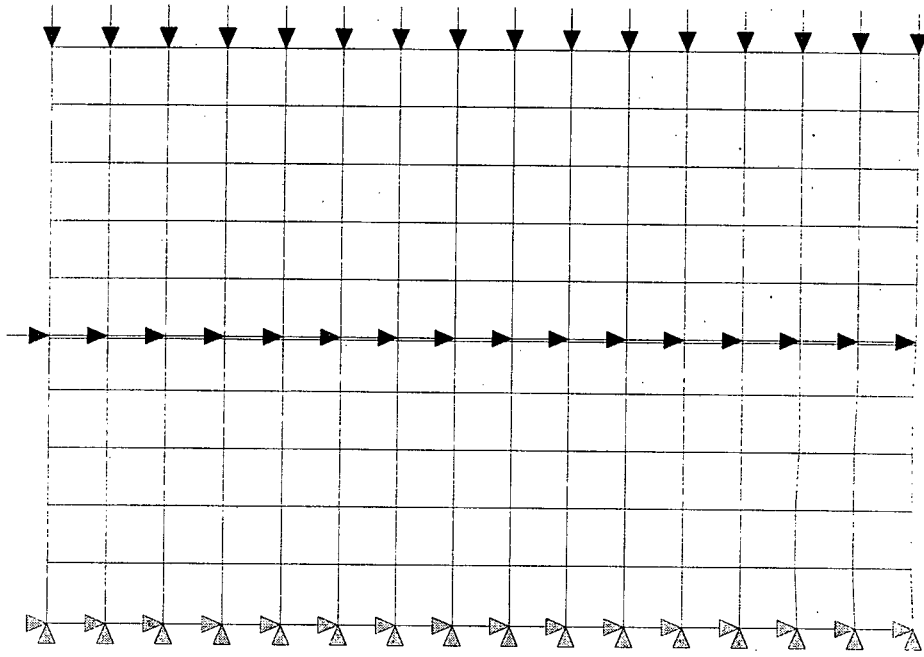
Figure 5-7(c): Deformed mesh for Case-6 of Goodman Type Interface at load step 10.
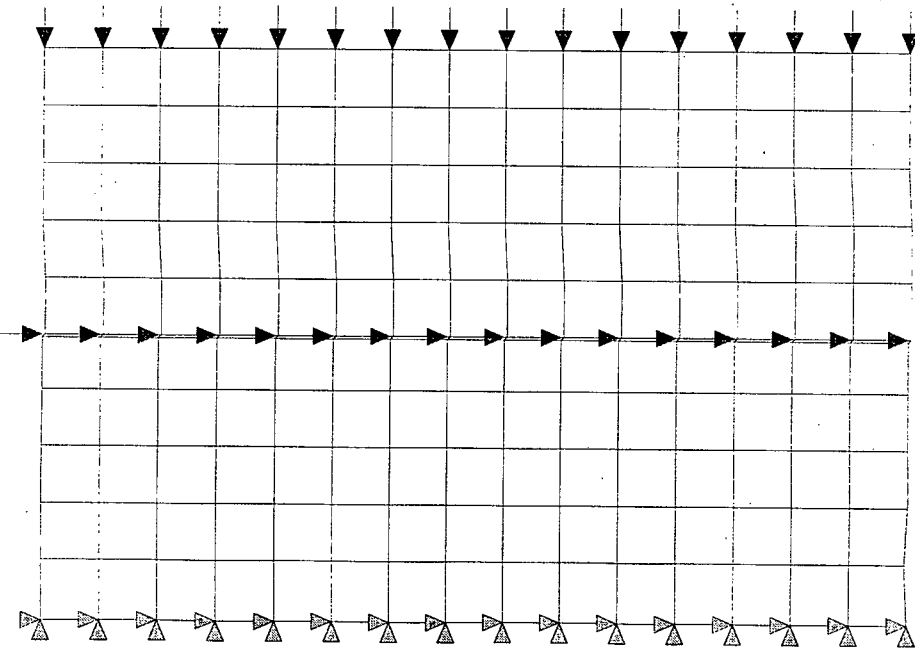
Figure 5-7(d): Deformed mesh for Case-6 of Goodman Type Interface at load step 15.
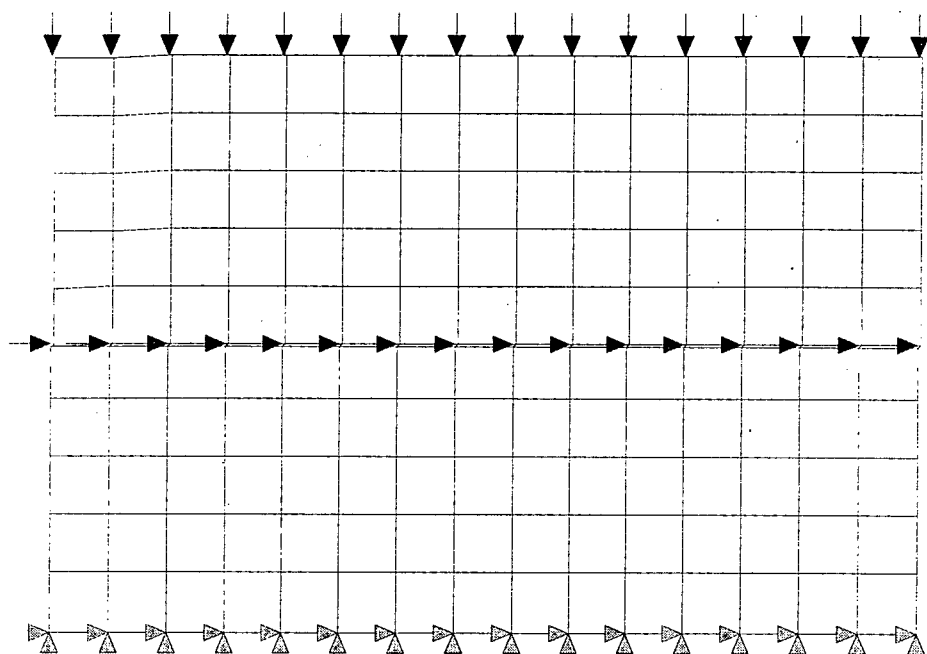
Figure 5-7(e): Deformed mesh for Case-6 of Goodman Type Interface at load step 20.
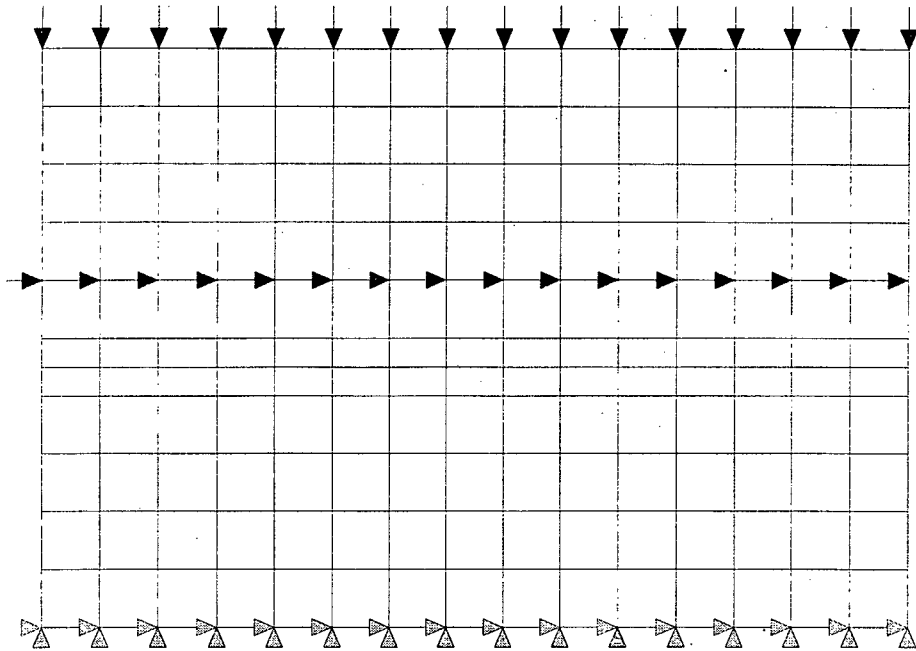
Figure 5-8(a): Deformed mesh for Case-7 of Goodman Type Interface at
load step 1.
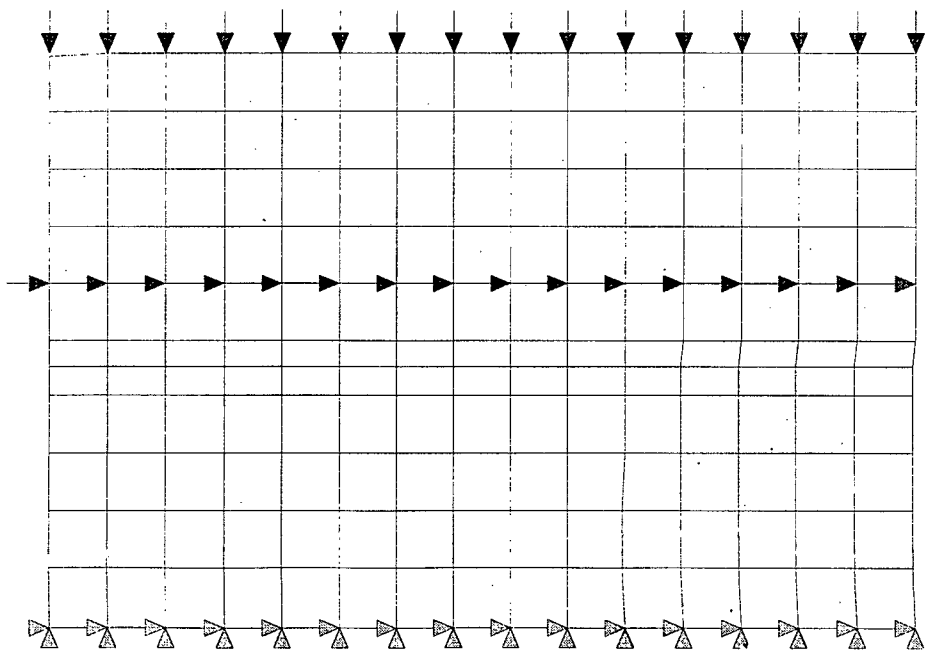
Figure 5-8(b): Deformed mesh for Case-7 of Goodman Type Interface at
load step 5.

118
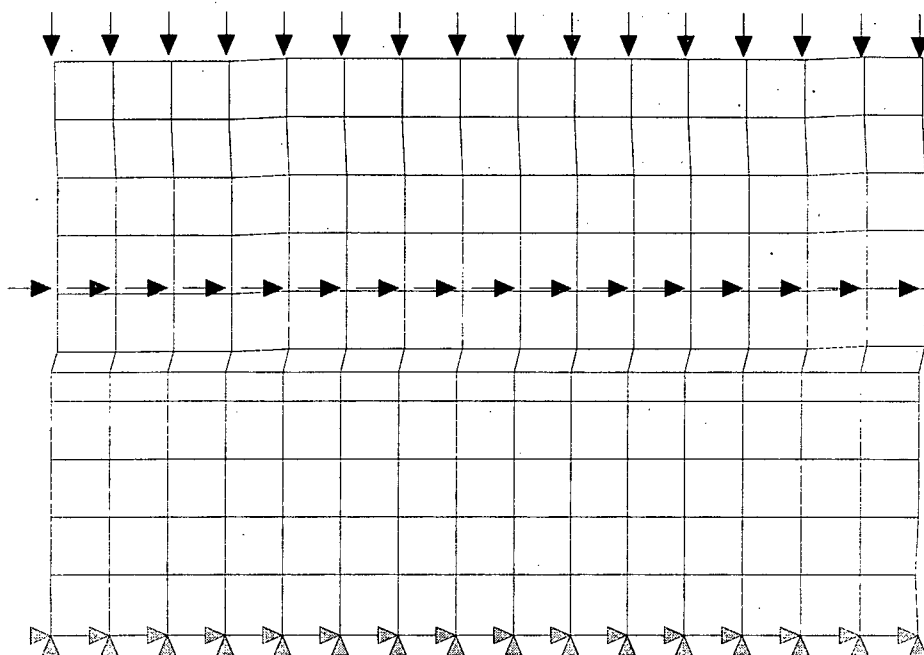
Figure 5-8(c): Deformed mesh for Case-7 of Goodman Type Interface at load step 10.
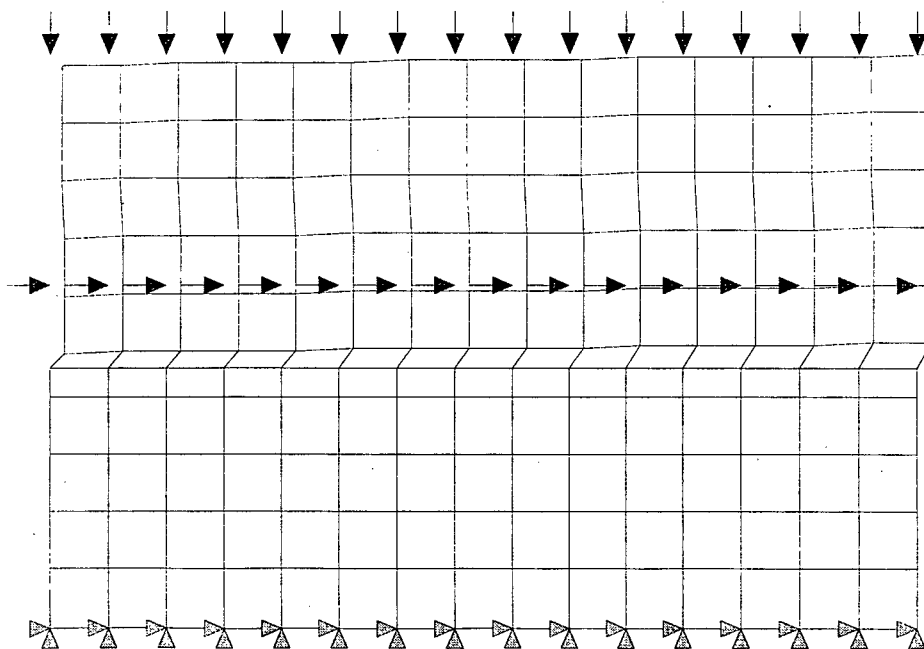
Figure 5-8(d): Deformed mesh for Case-7 of Goodman Type Interface at load step 15.

119
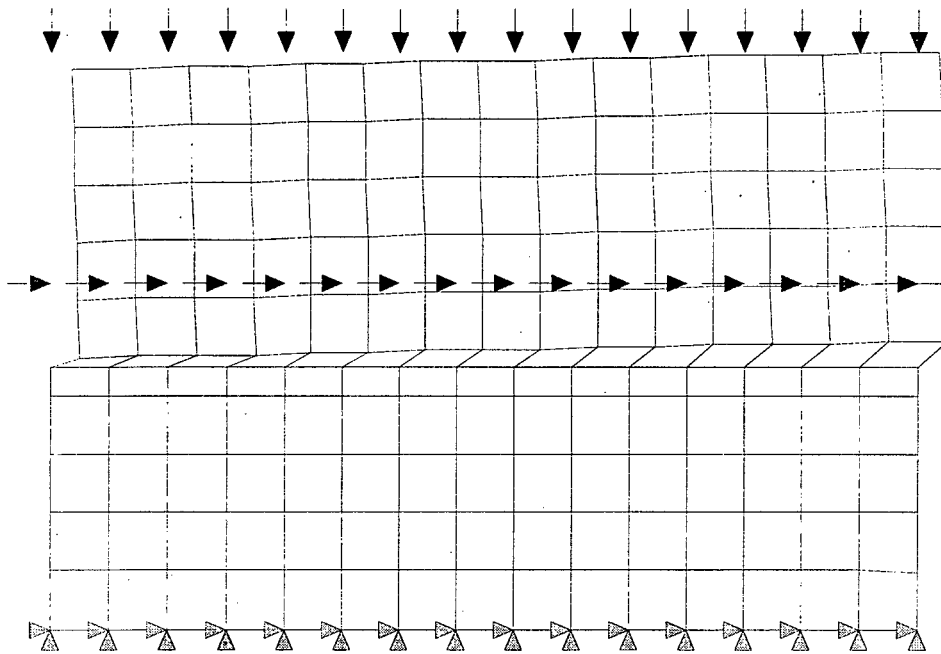
Figure 5-8(e): Deformed mesh for Case-7 of Goodman Type Interface at load step 20.
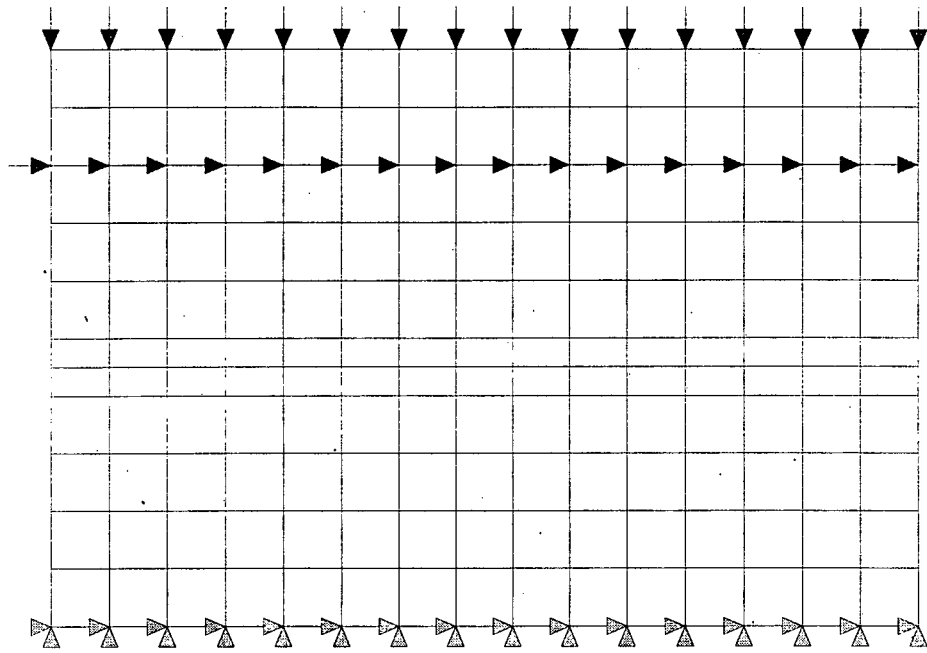
Figure 5-9(a): Deformed mesh for Case-8 of Goodman Type Interface at load step 1.
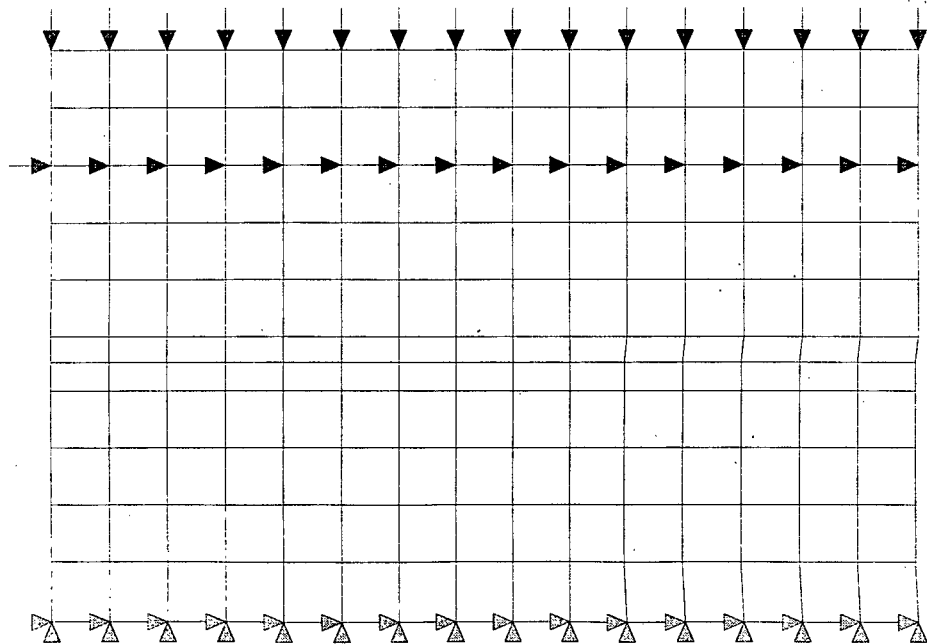
Figure 5-9(b): Deformed mesh for Case-8 of Goodman Type Interface at load step 5.
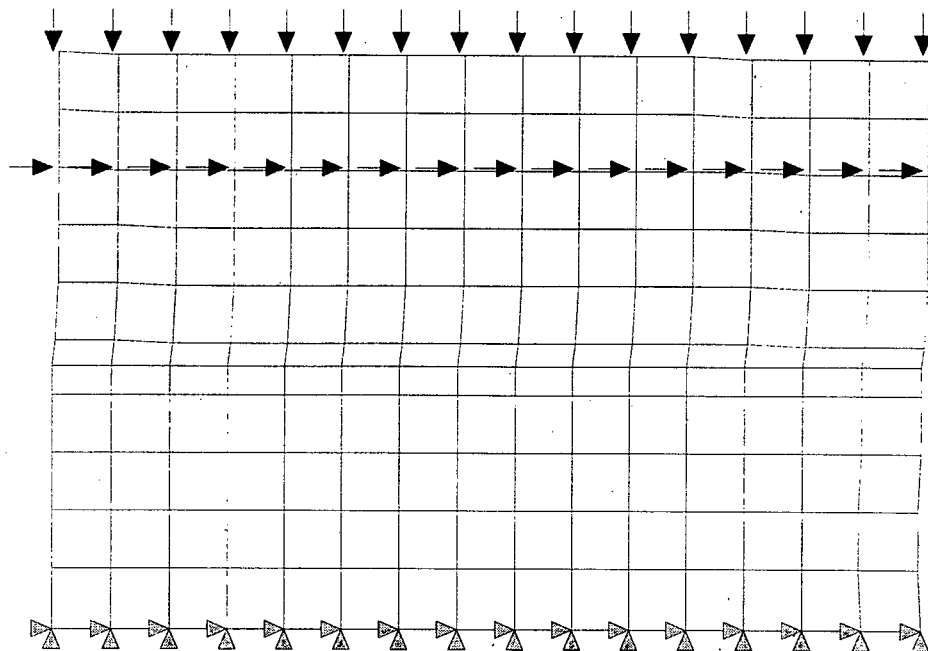
Figure 5-9(c): Deformed mesh for Case-8 of Goodman Type Interface at load step 10.
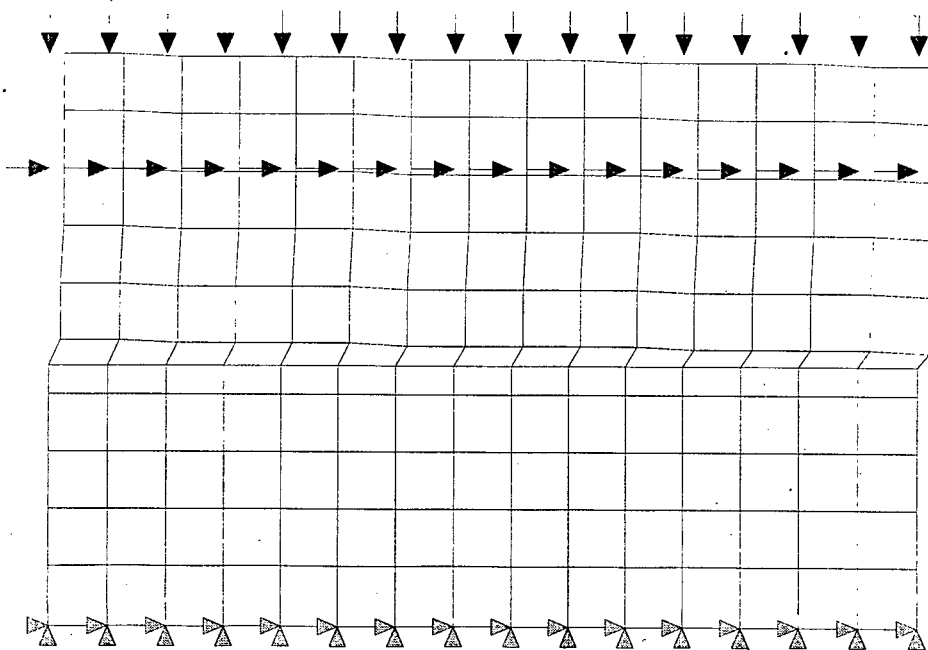
Figure 5-9(d): Deformed mesh for Case-8 of Goodman Type Interface at load step 15.
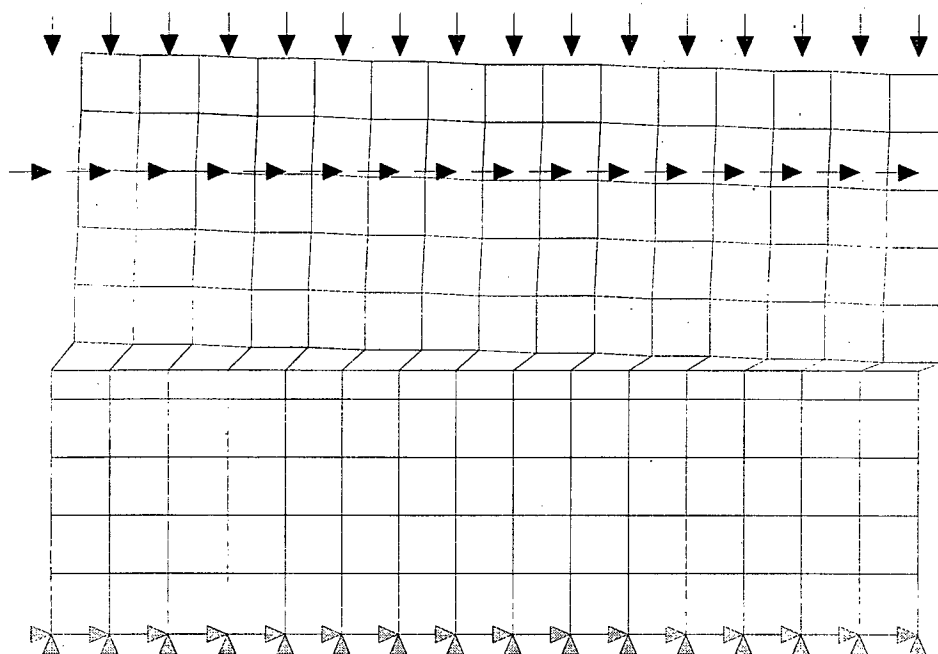
Figure 5-9(e): Deformed mesh for Case-8 of Goodman Type Interface at
load step 20.

123
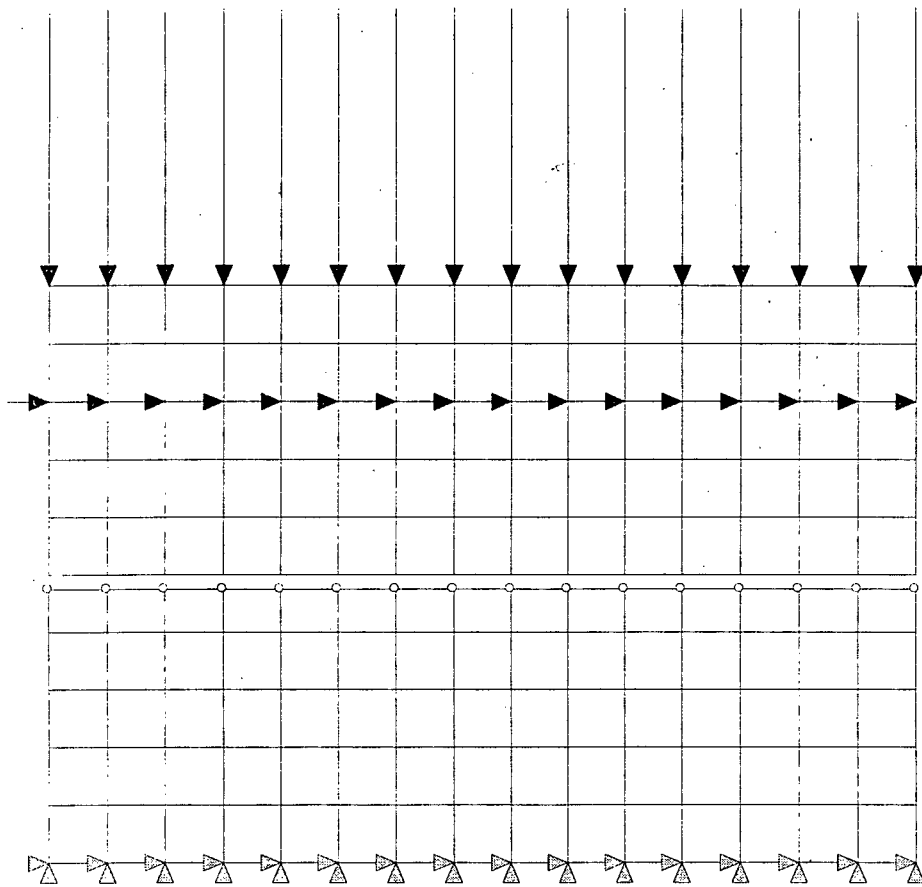
Figure 5-10(a): Deformed mesh for Case-1 of Katona Type Interface at load step 1.
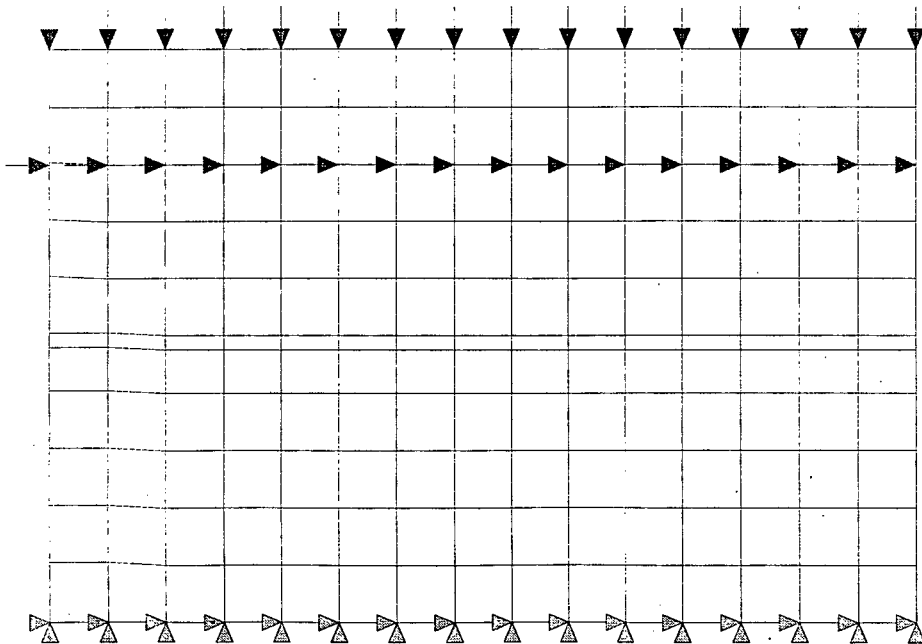
Figure 5-10(b): Deformed mesh for Case-1 of Katona Type Interface at load step 5.

124
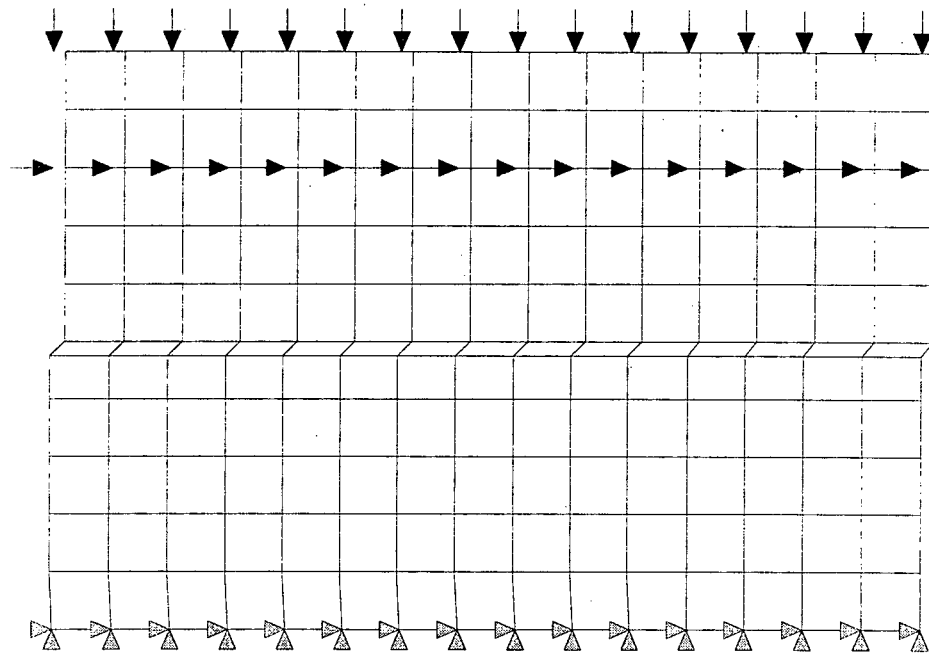
Figure 5-10(c): Deformed mesh for Case-1 of Katona Type Interface at load step 10.
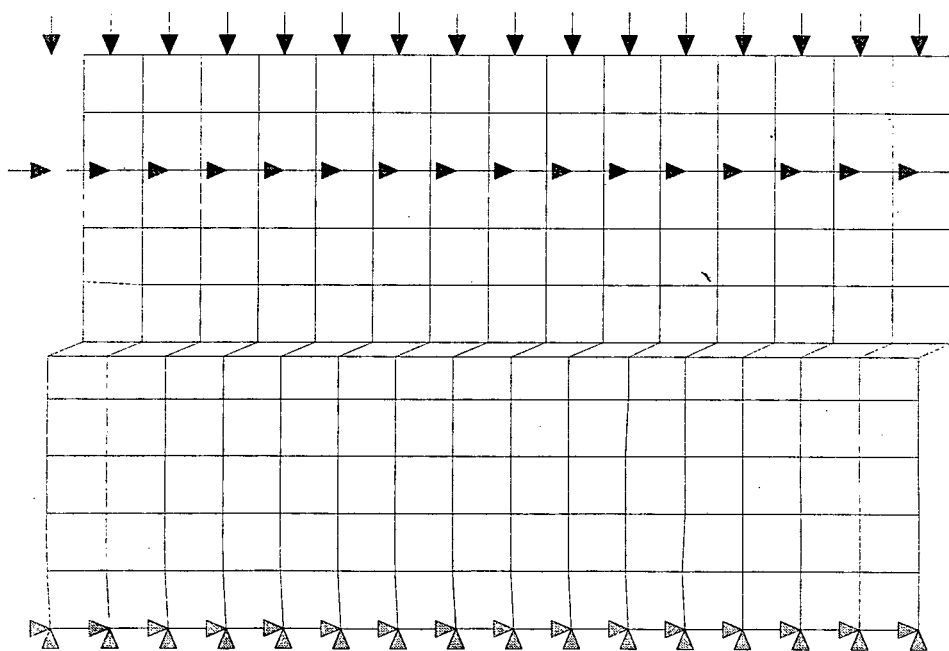
Figure 5-10(d): Deformed mesh for Case-1 of Katona Type Interface at load step 15.
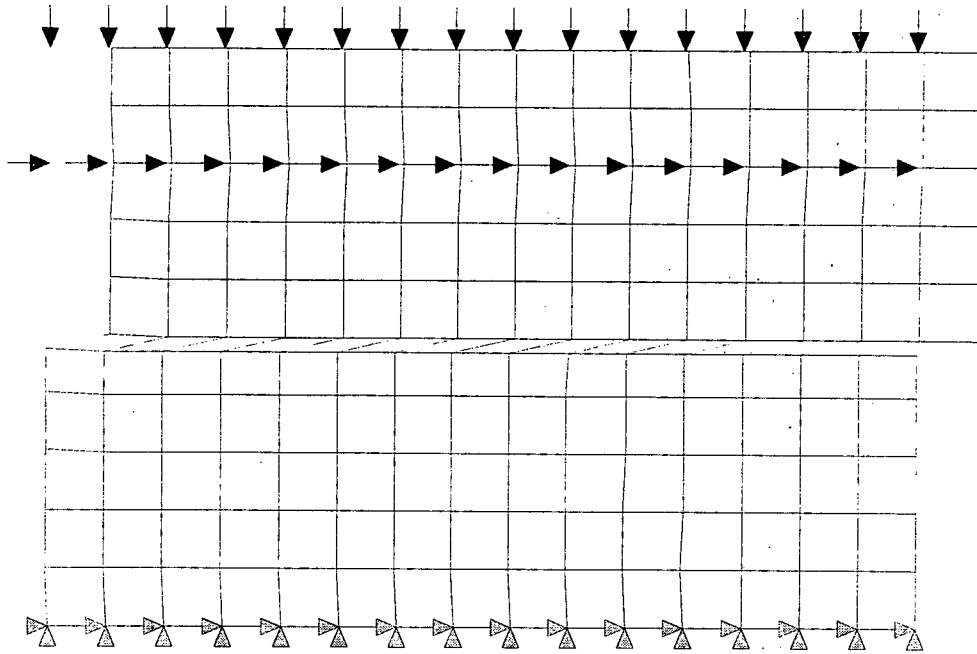
Figure 5-10(e): Deformed mesh for Case-1 of Katona Type Interface at load step 20.

126
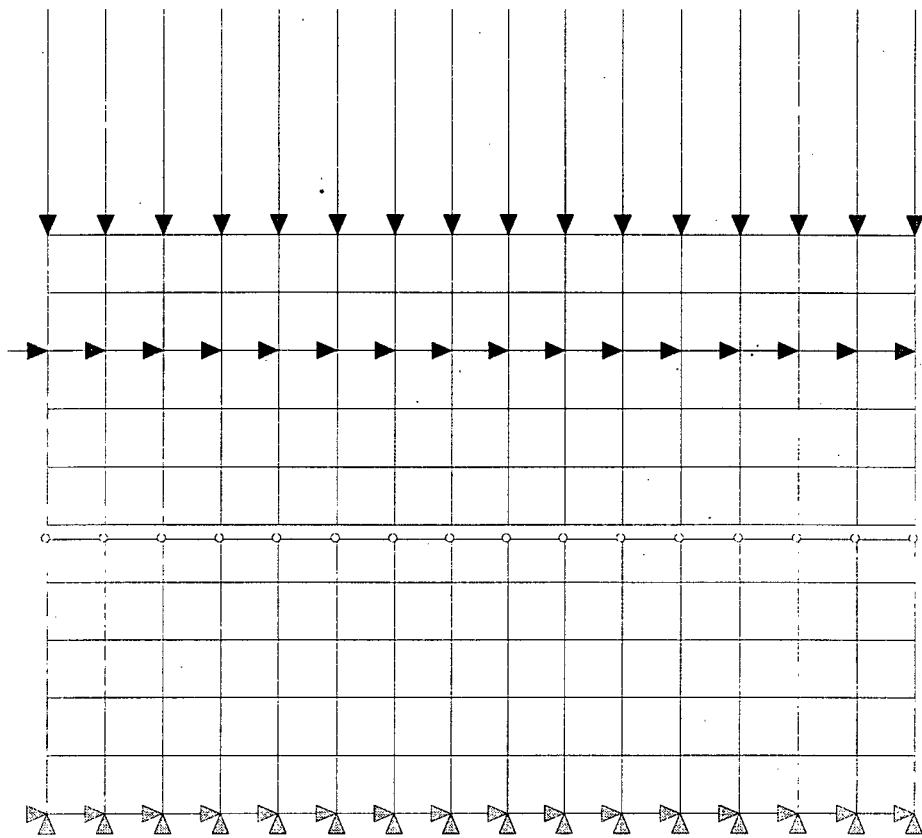
Figure 5-11(a): Deformed mesh for Case-2 of Katona Type Interface at load step 1.
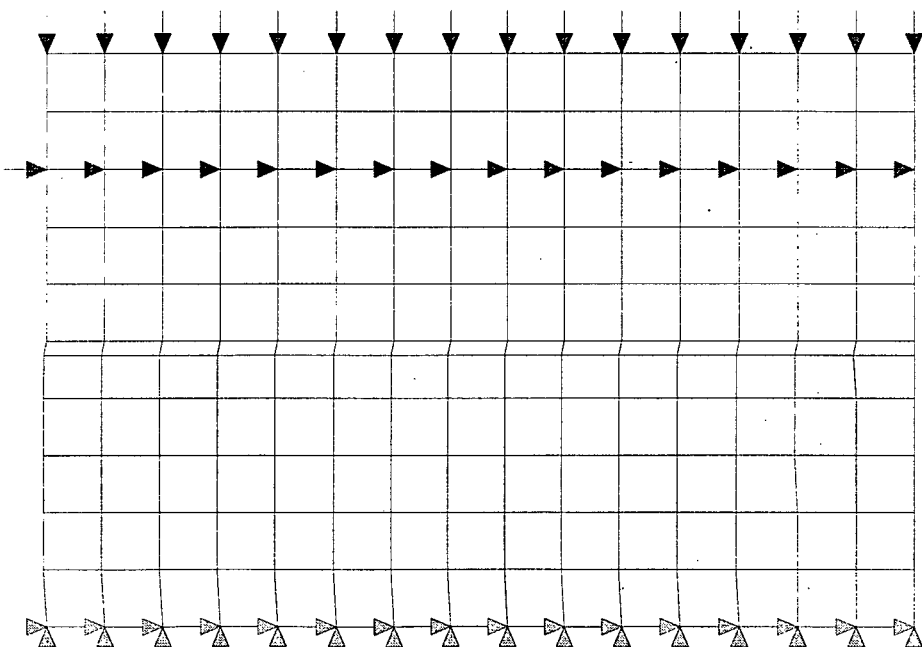
Figure 5-11(b): Deformed mesh for Case-2 of Katona Type Interface at load step 5.

127
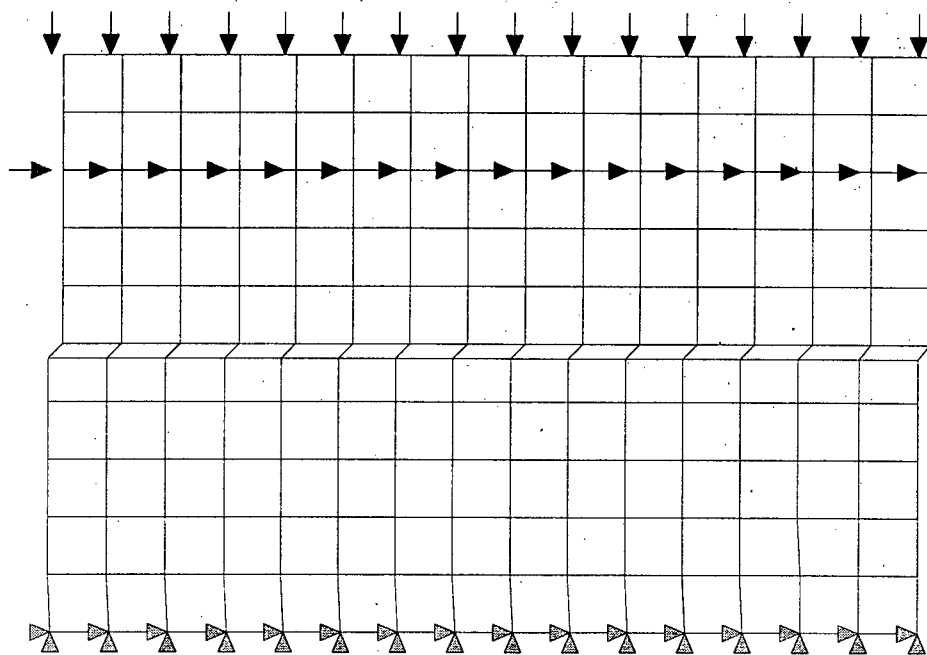
Figure 5-11(c): Deformed mesh for Case-2 of Katona Type Interface at load step 10.
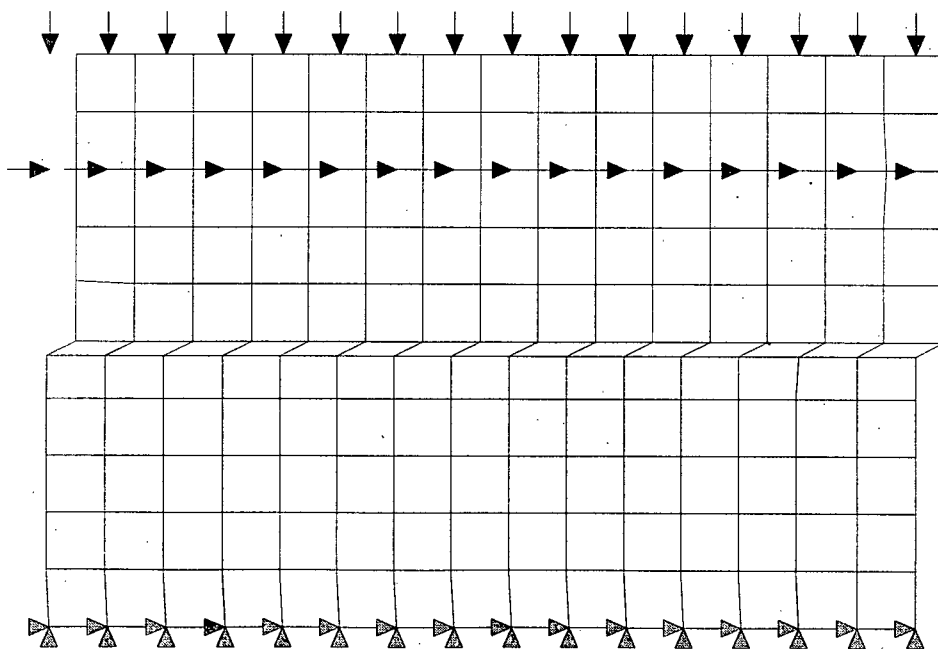
Figure 5-11(d): Deformed mesh for Case-2 of Katona Type Interface at load step 15.
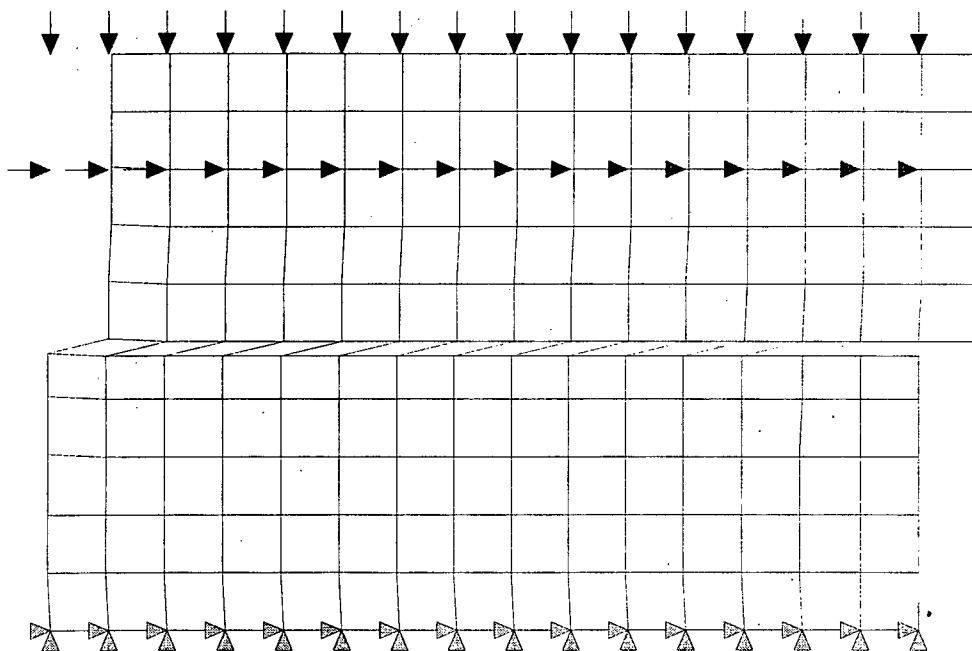
Figure 5-11(e): Deformed mesh for Case-2 of Katona Type Interface at load step 20.
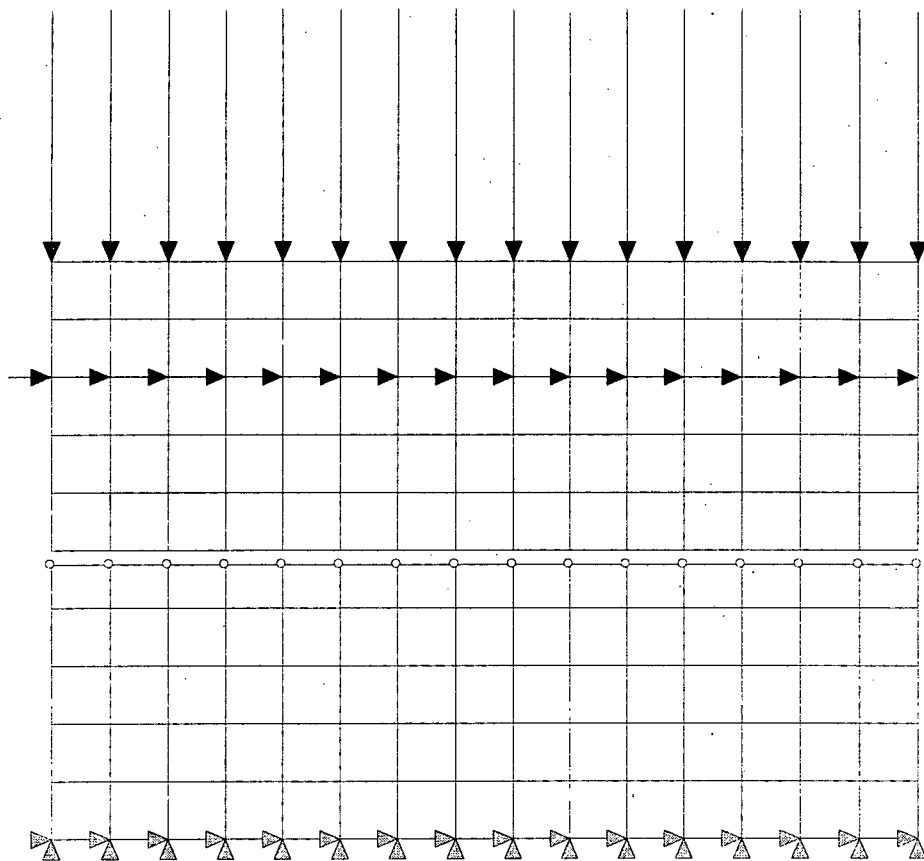
Figure 5-12(a): Deformed mesh for Case-3 of Katona Type Interface at load step 1.
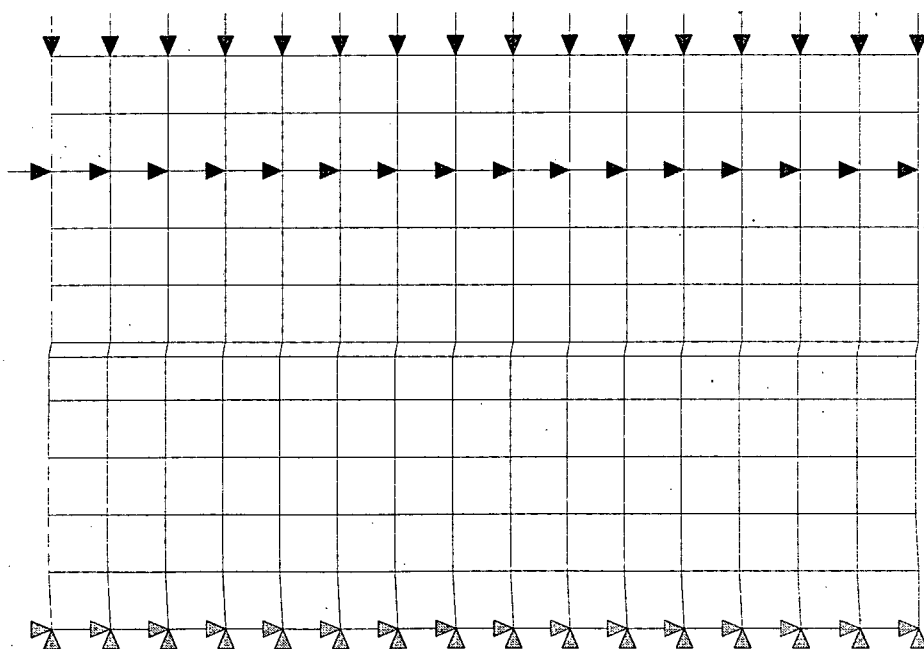
Figure 5-12(b): Deformed mesh for Case-3 of Katona Type Interface at load step 5.
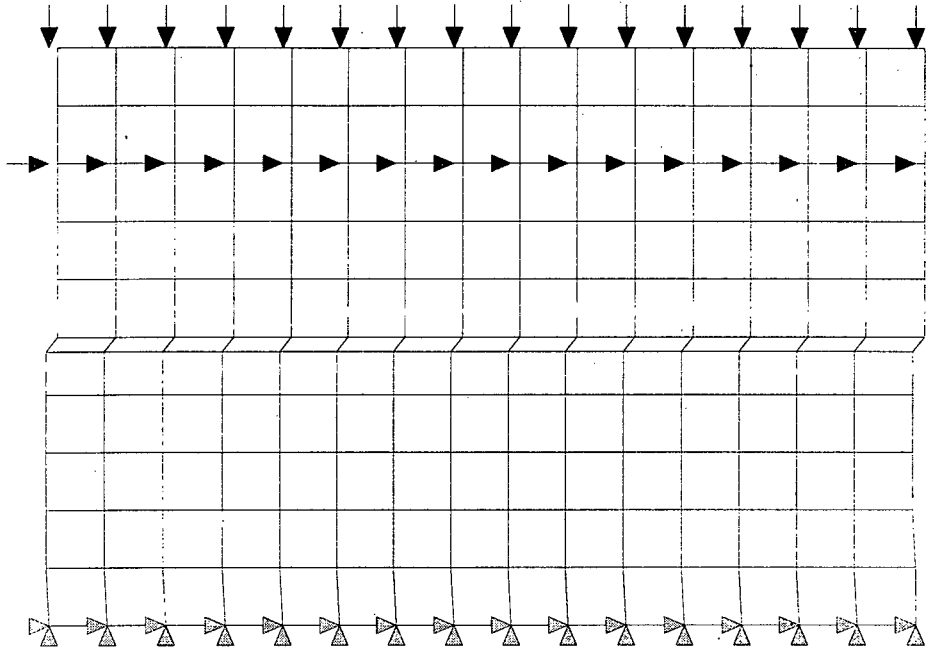
Figure 5-12(c): Deformed mesh for Case-3 of Katona Type Interface at load step 10.
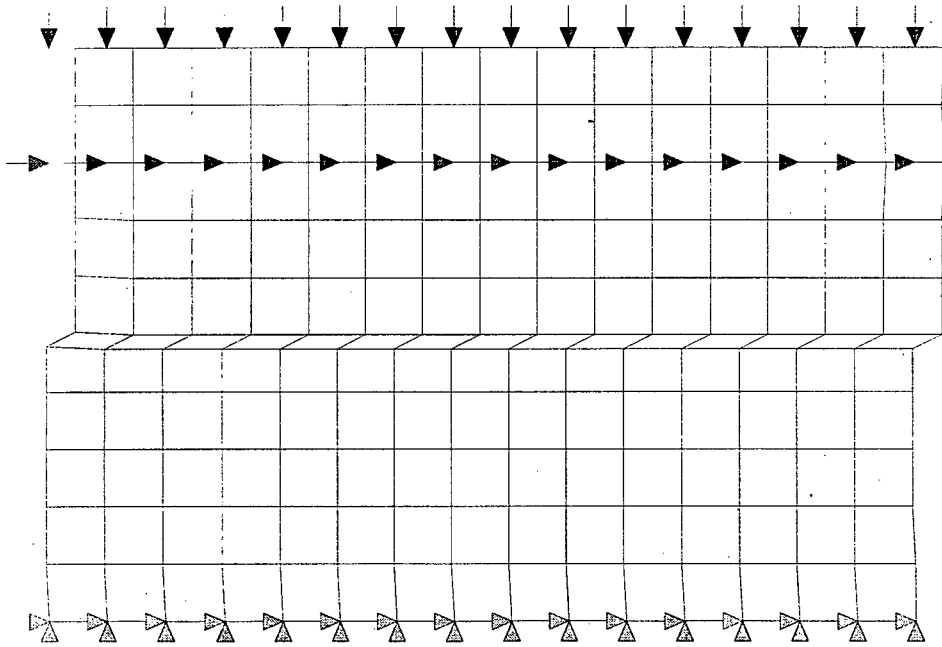
Figure 5-12(d): Deformed mesh for Case-3 of Katona Type Interface at load step 15.

131
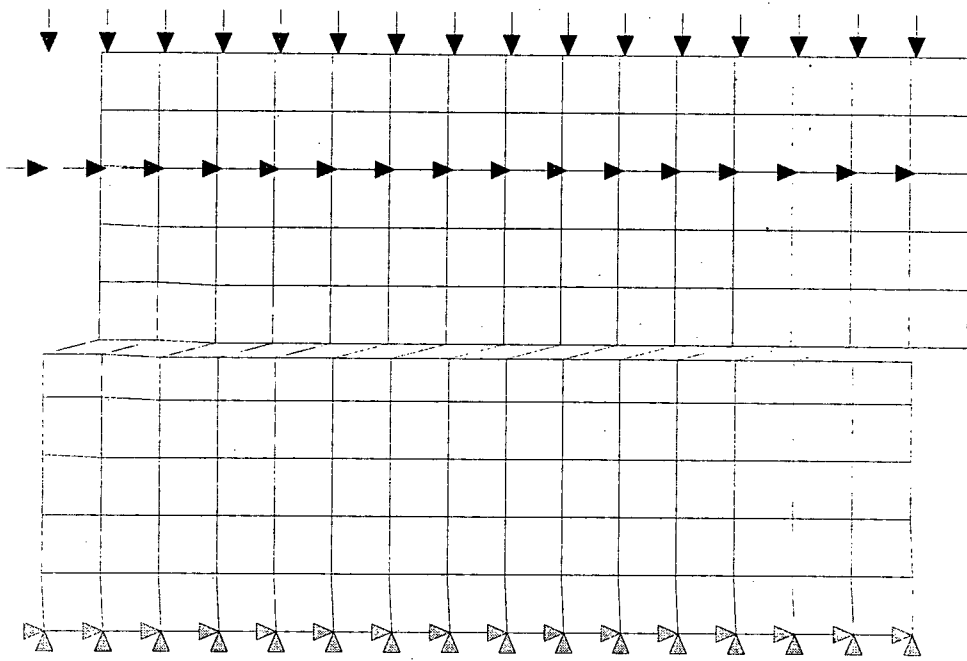
Figure 5-12(e): Deformed mesh for Case-3 of Katona Type Interface at load step 20.
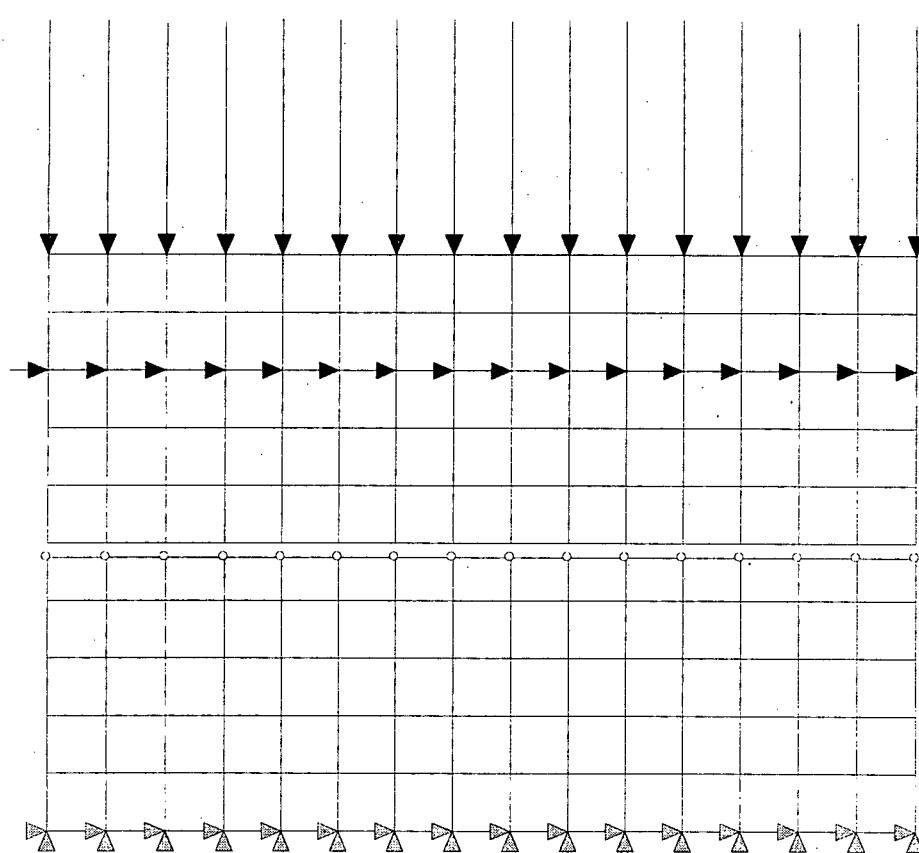
Figure 5-13(a): Deformed mesh for Case-4 of Katona Type Interface at load step 1.
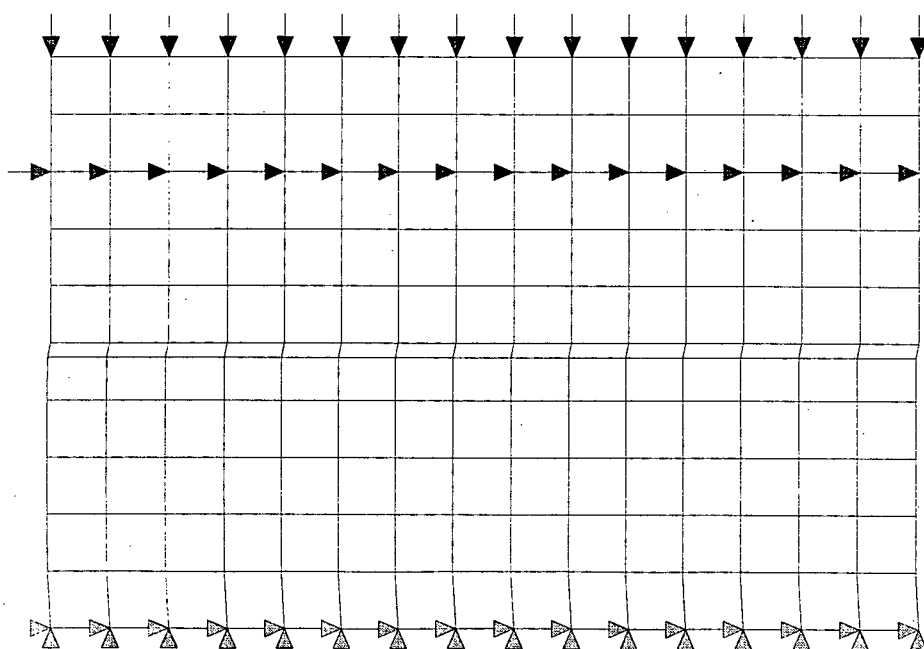
Figure 5-13(b): Deformed mesh for Case-4 of Katona Type Interface at load step 5.
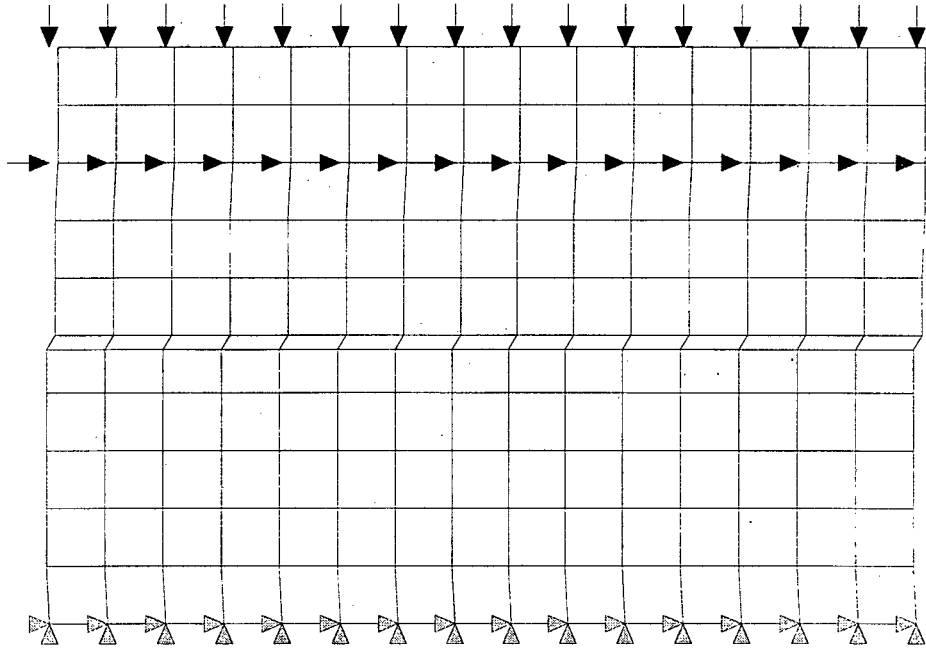
Figure 5-13(c): Deformed mesh for Case-4 of Katona Type Interface at load step 10.
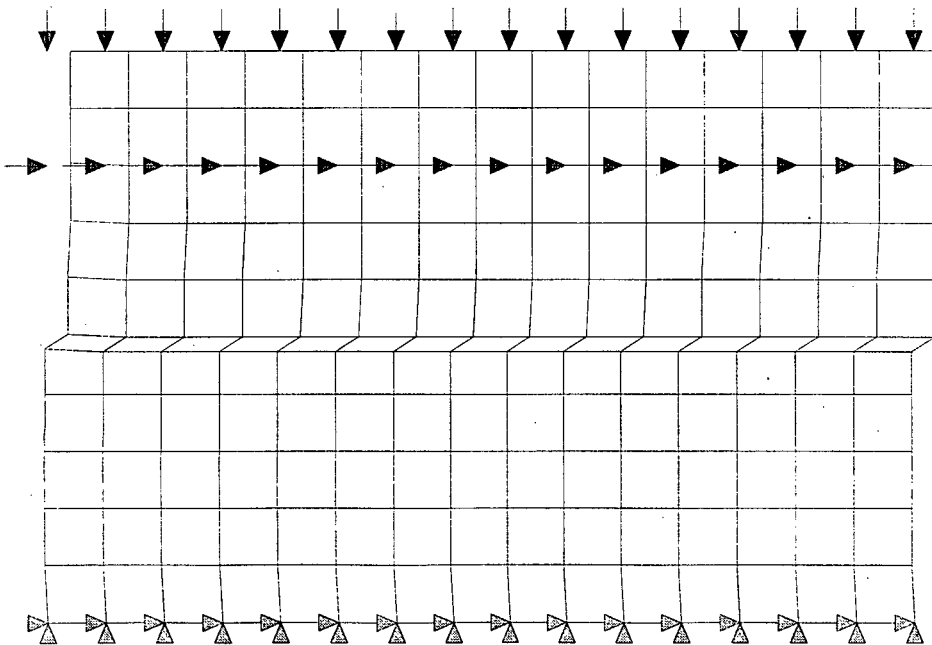
Figure 5-13(d): Deformed mesh for Case-4 of Katona Type Interface at load step 15.
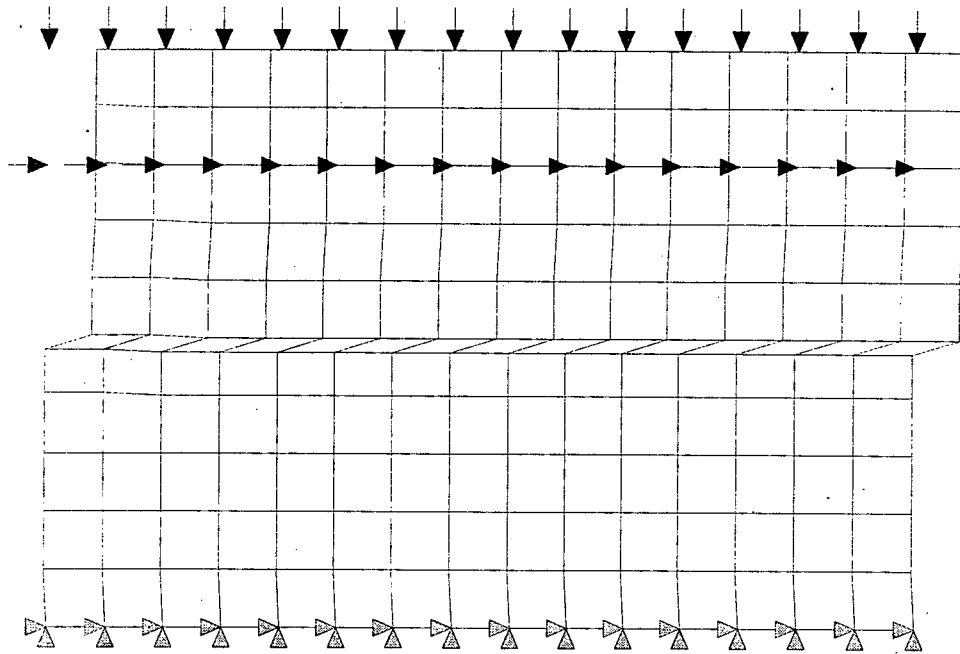
Figure 5-13(e): Deformed mesh for Case-4 of Katona Type Interface at load step 20.
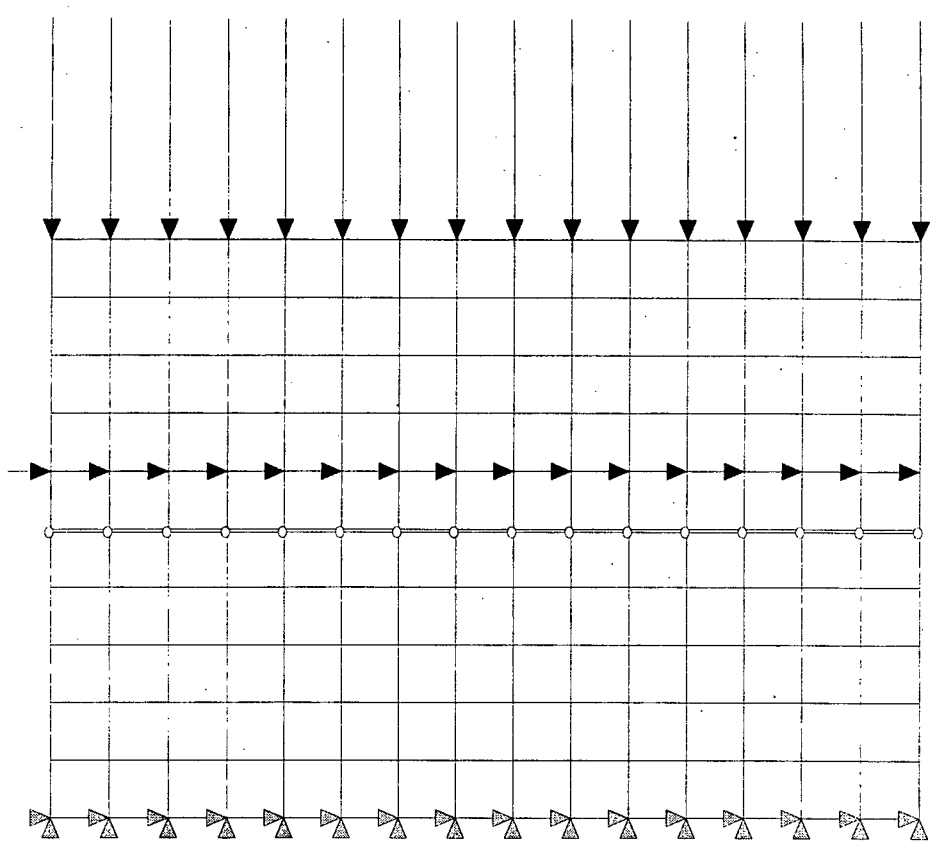
Figure 5-14(a): Deformed mesh for Case-5 of Katona Type Interface at load step 1.
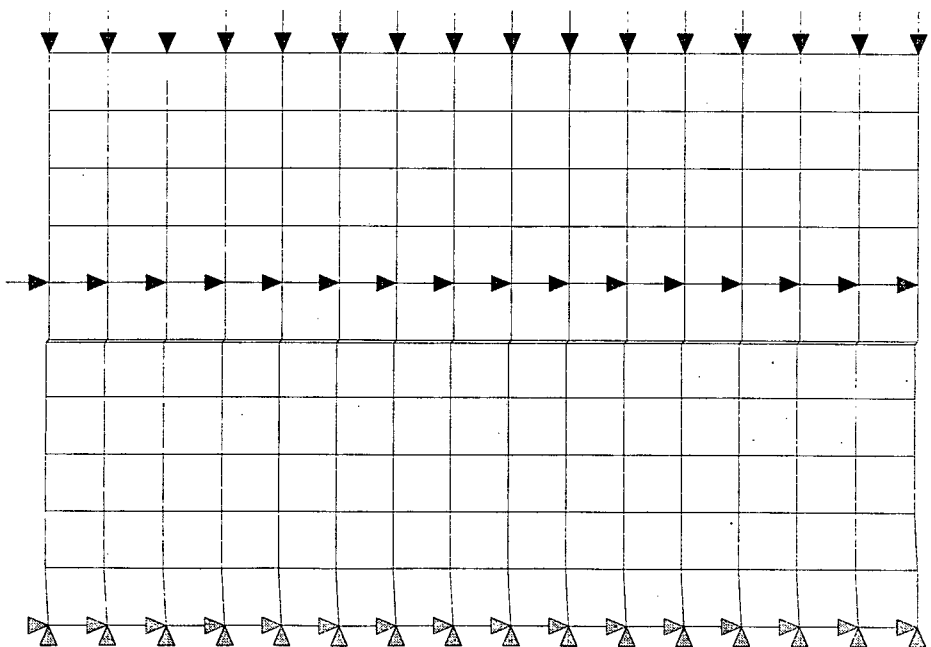
Figure 5-14(b): Deformed mesh for Case-5 of Katona Type Interface at load step 5.

136
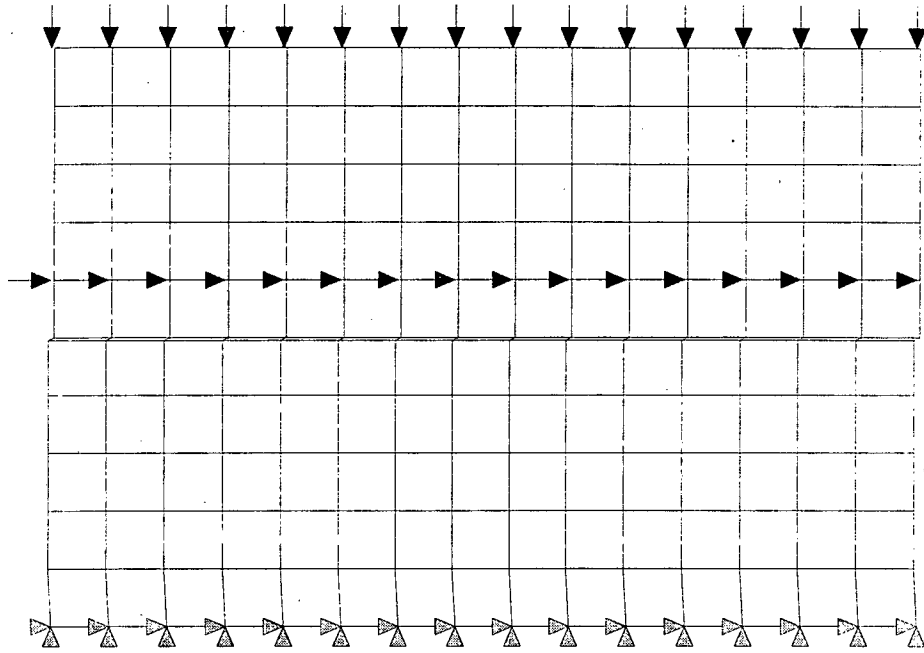
Figure 5-14(c): Deformed mesh for Case-5 of Katona Type Interface at load step 10.
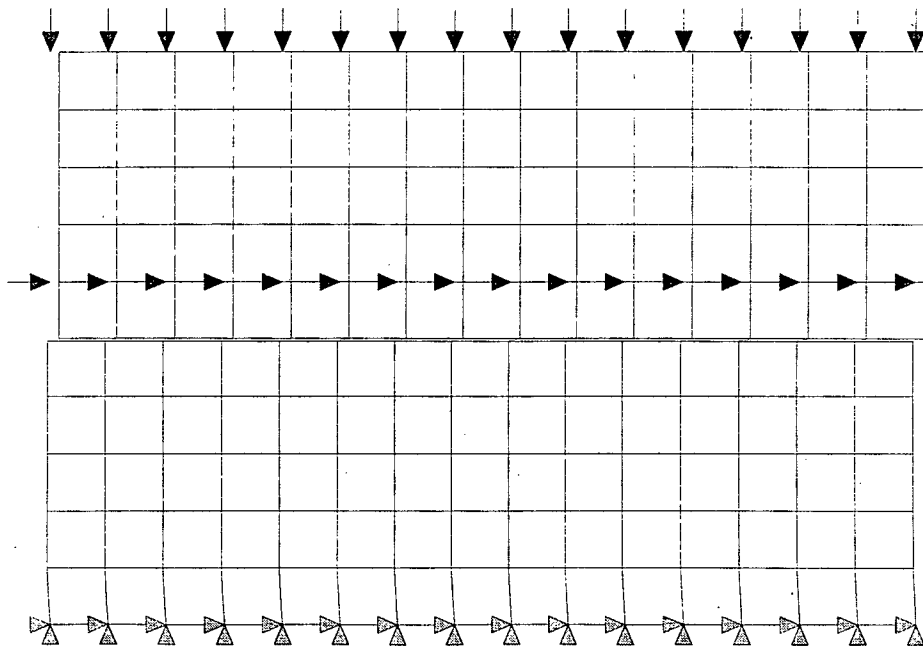
Figure 5-14(d): Deformed mesh for Case-5 of Katona Type Interface at load step 15.
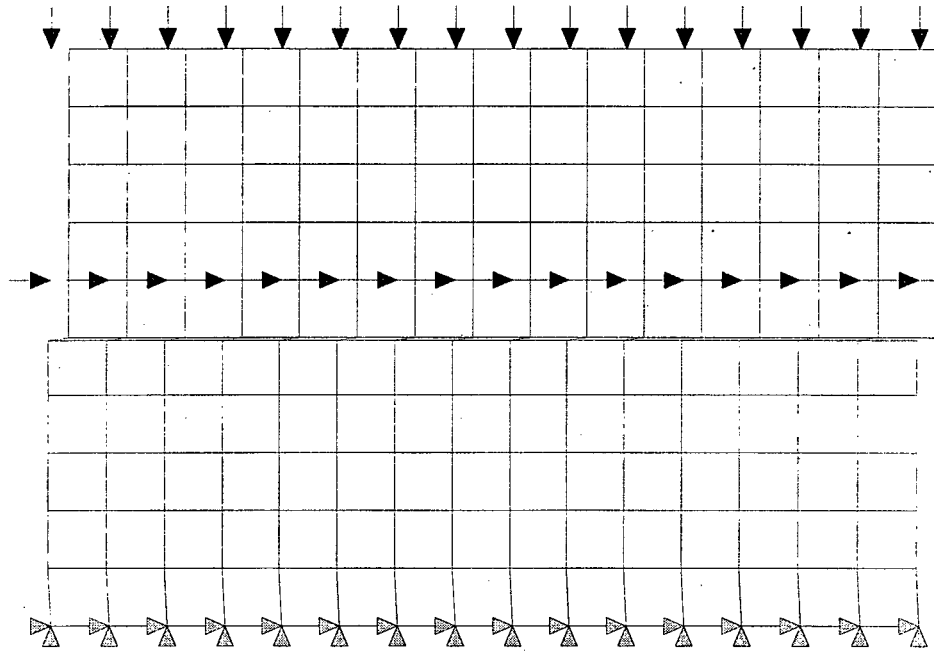
Figure 5-14(e): Deformed mesh for Case-5 of Katona Type Interface at
load step 20.
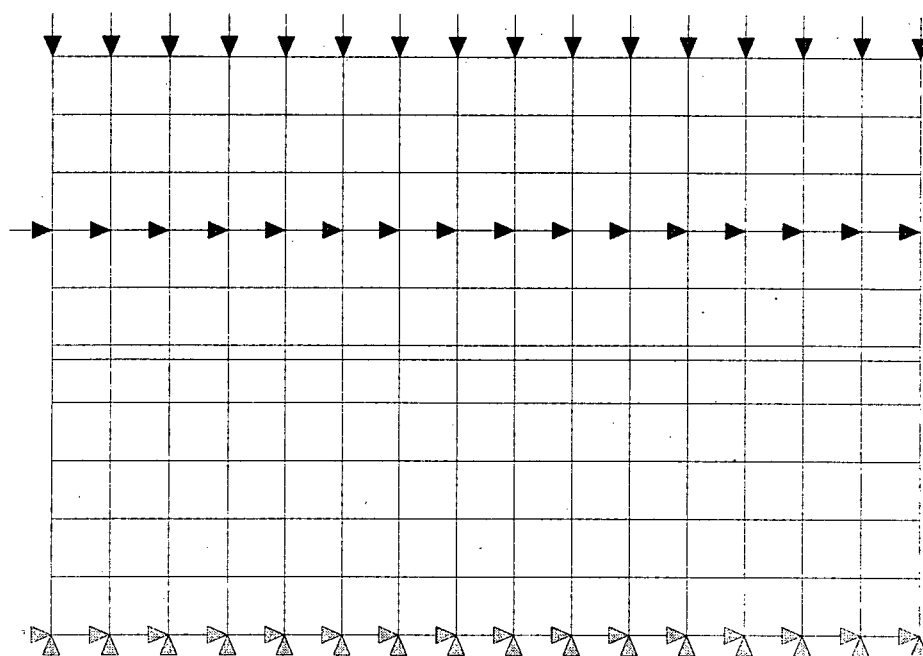
Figure 5-15(a): Deformed mesh for Case-1 of Desai Type Interface at load step 1.
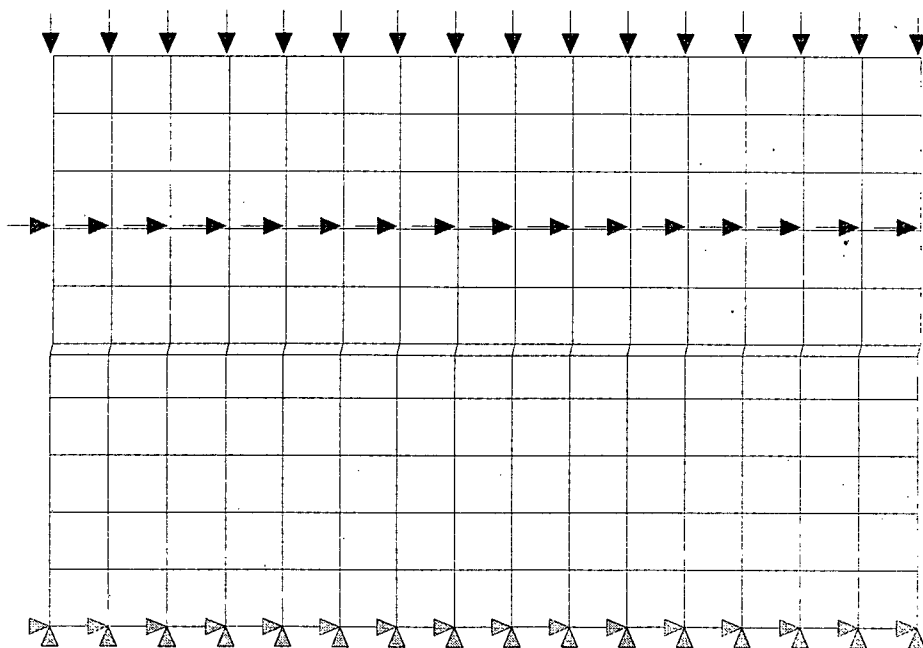
Figure 5-15(b): Deformed mesh for Case-1 of Desai Type Interface at load step 5.
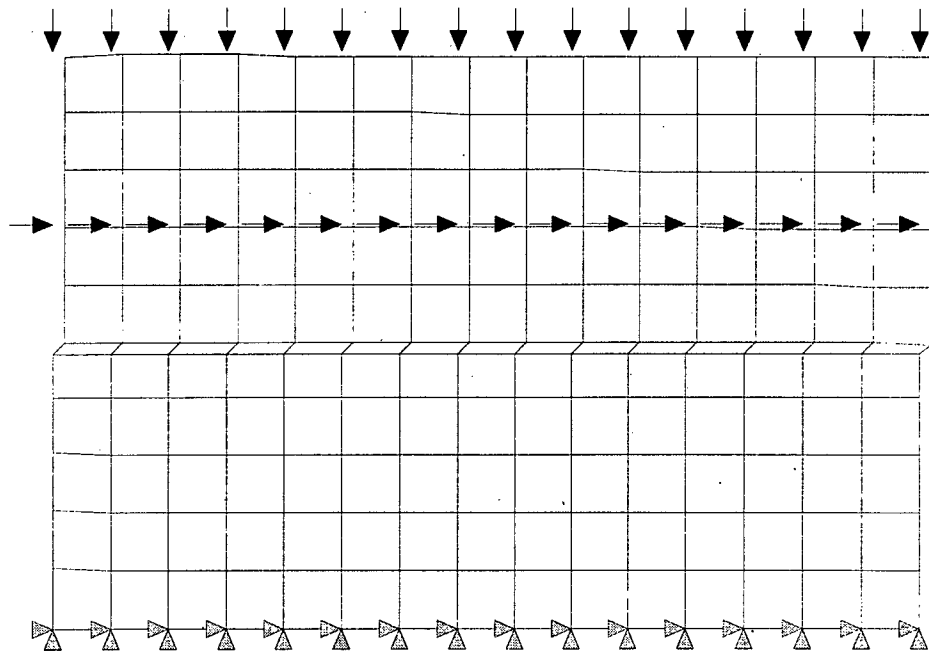
Figure 5-15(c): Deformed mesh for Case-1 of Desai Type Interface at load step 10.
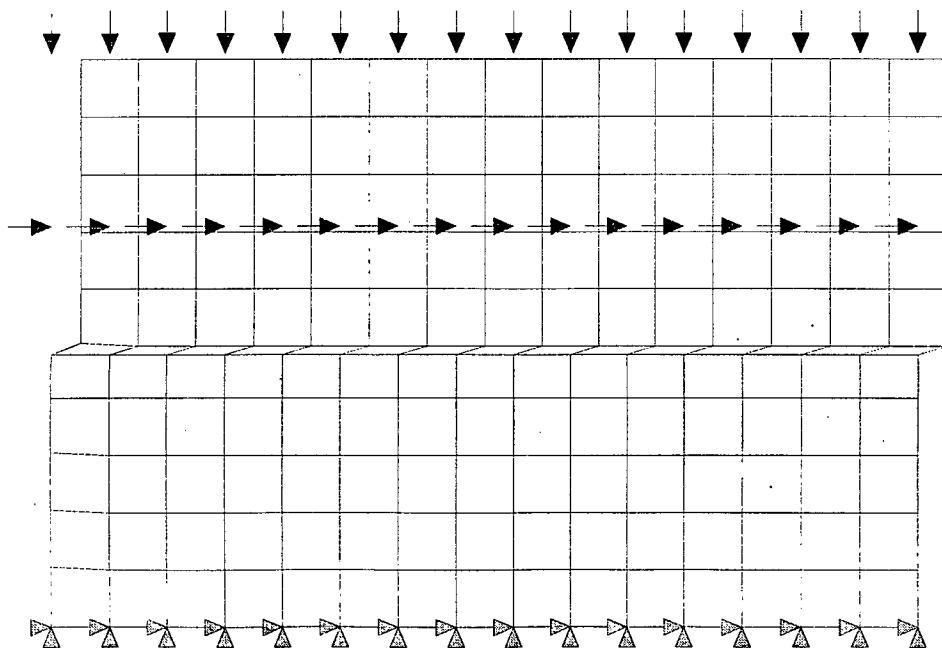
Figure 5-15(d): Deformed mesh for Case-1 of Desai Type Interface at load step 15.
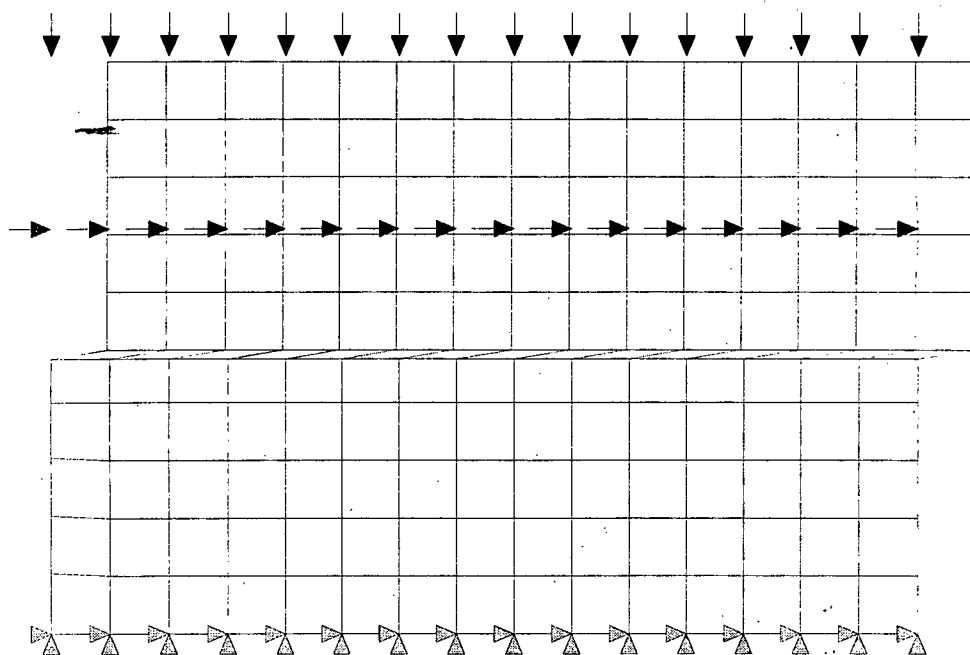
Figure 5-15(e): Deformed mesh for Case-1 of Desai Type Interface at load step 20.
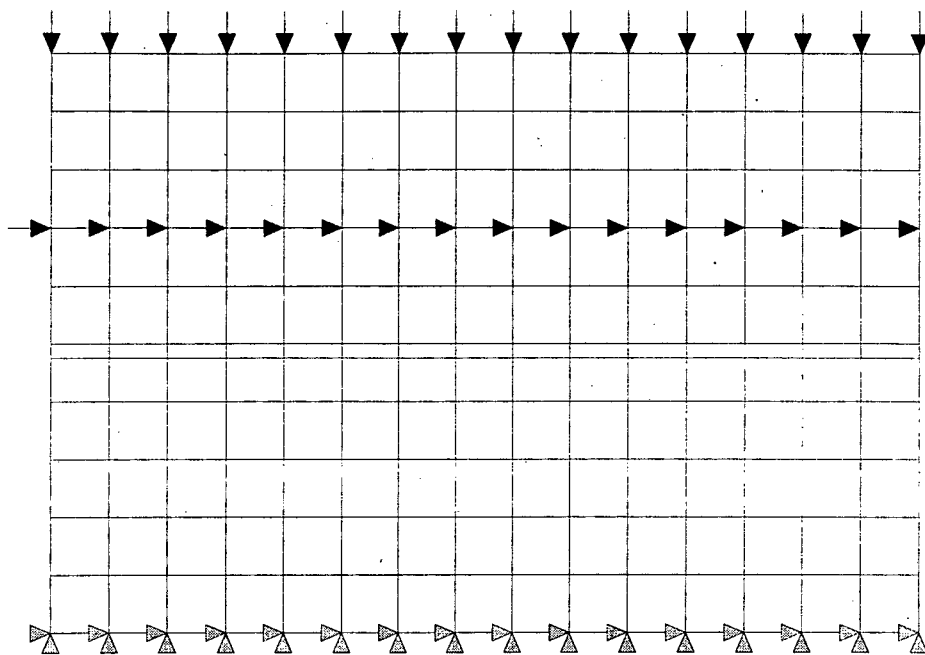
Figure 5-16(a): Deformed mesh for Case-2 of Desai Type Interface at load step 1.
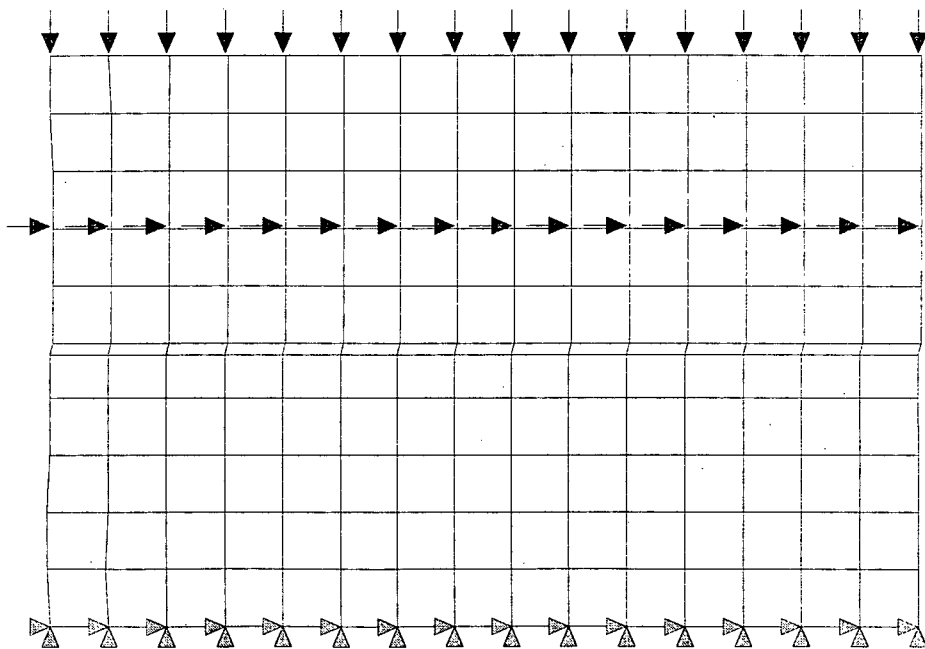
Figure 5-16(b): Deformed mesh for Case-2 of Desai Type Interface at load step 5.

142
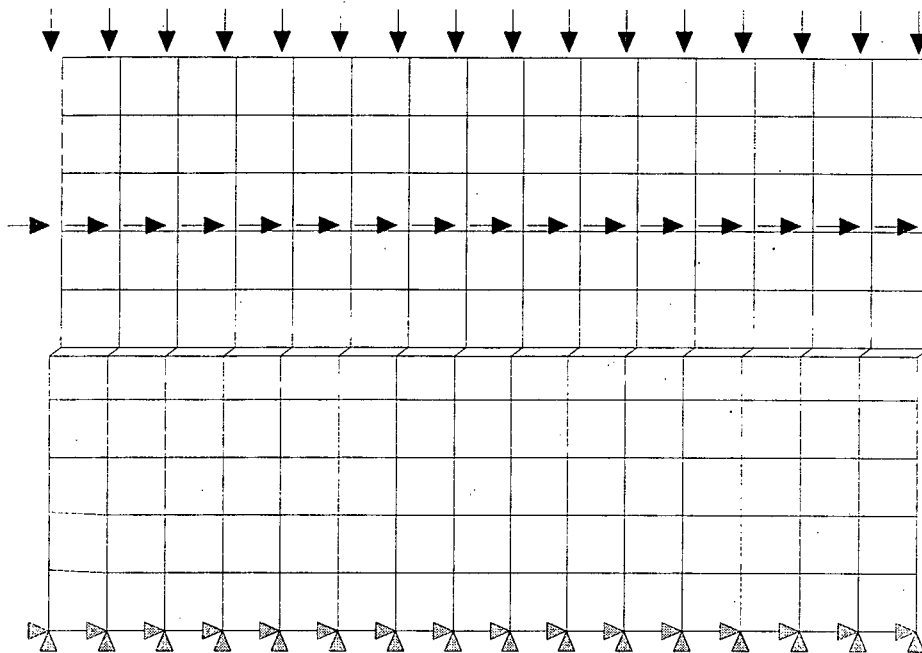
Figure 5-16(c): Deformed mesh for Case-2 of Desai Type Interface at load step 10.
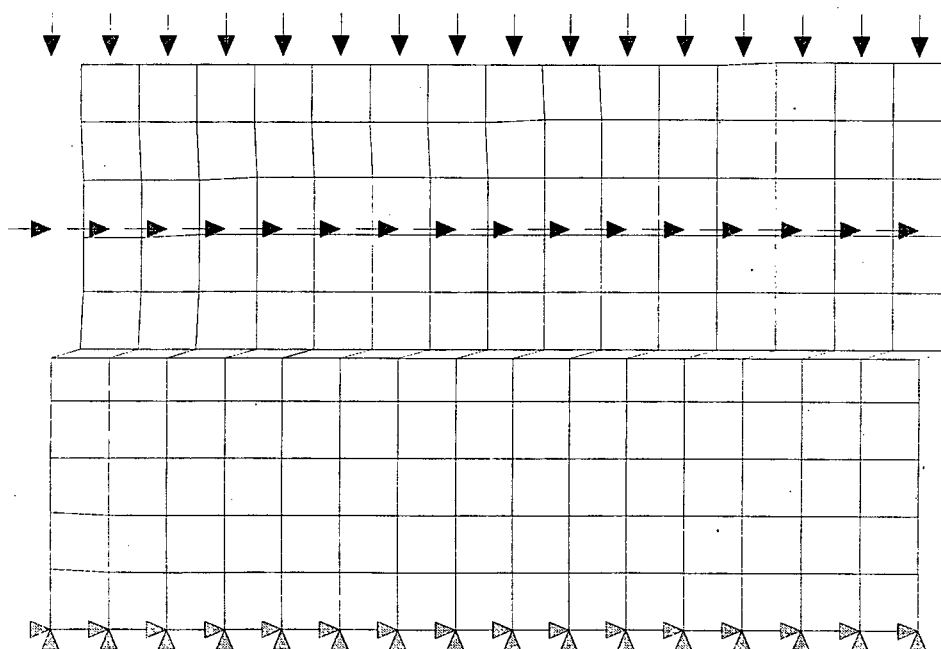
Figure 5-16(d): Deformed mesh for Case-2 of Desai Type Interface at load step 15.
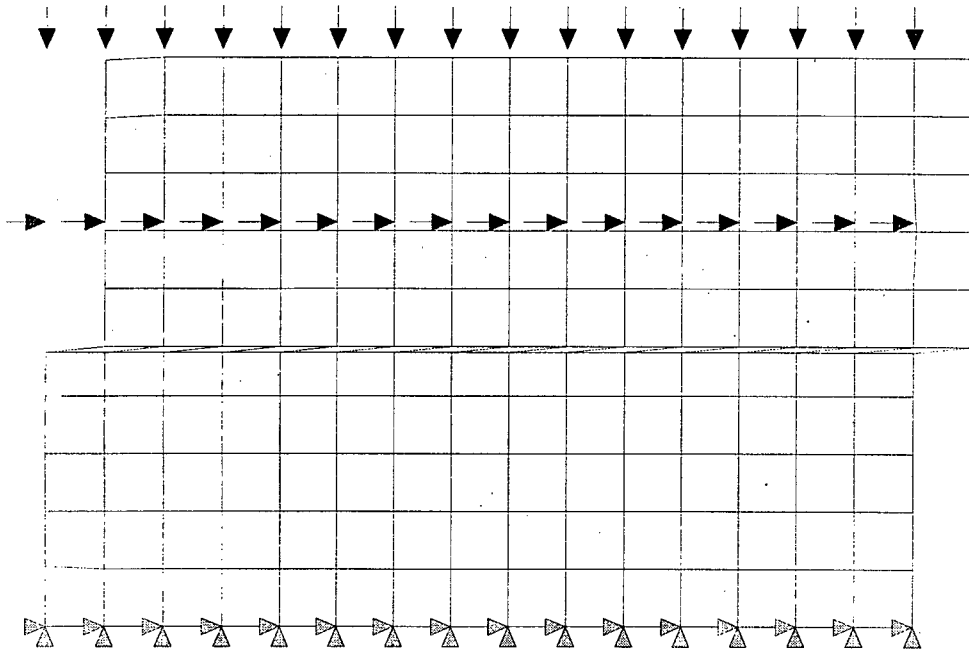
Figure 5-16(e): Deformed mesh for Case-2 of Desai Type Interface at load step 20.

144
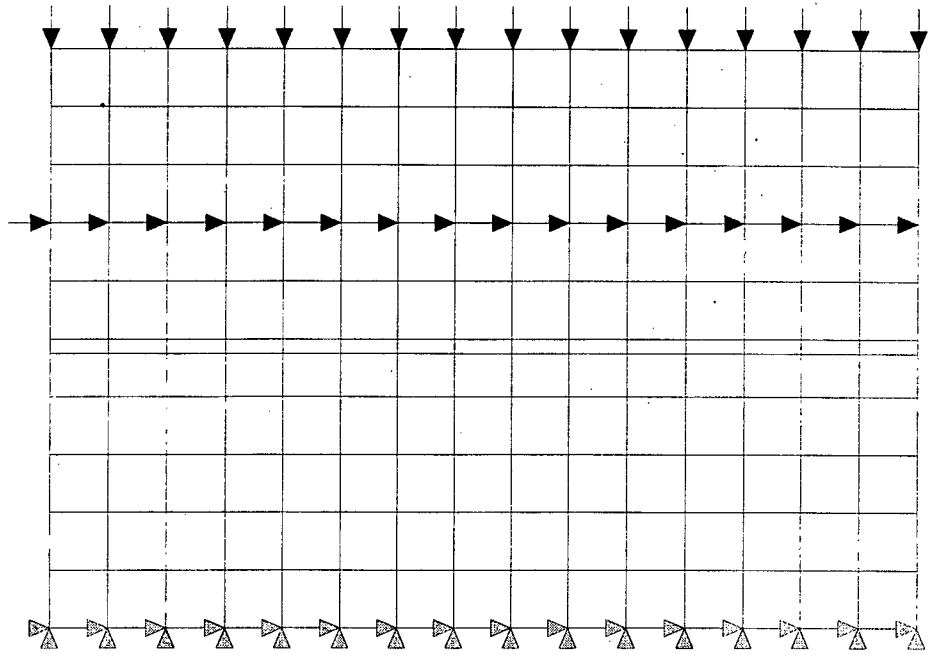
Figure 5-17(a): Deformed mesh for Case-3 of Desai Type Interface at load step 1.
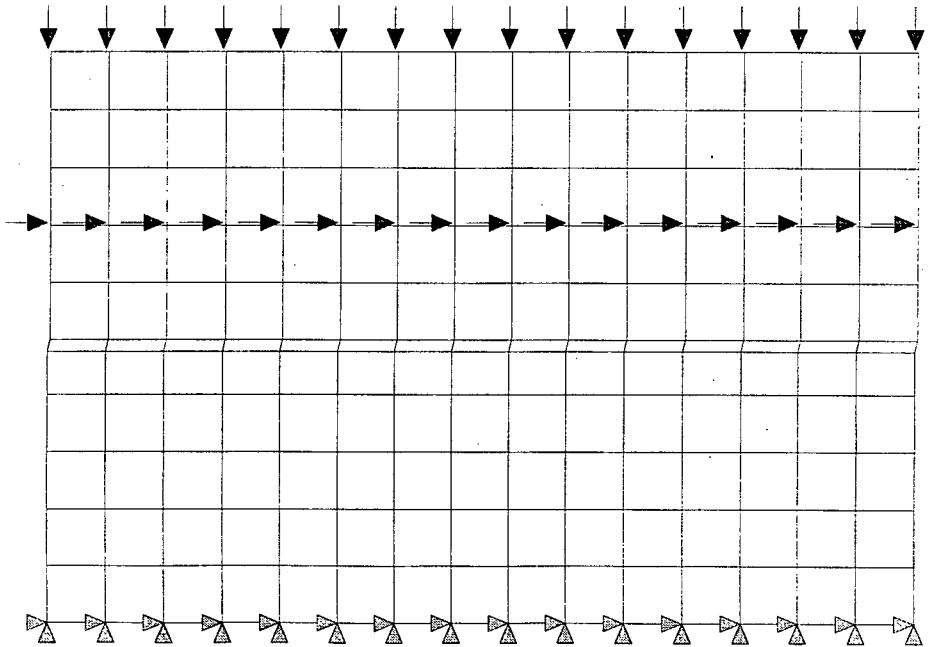
Figure 5-17(b): Deformed mesh for Case-3 of Desai Type Interface at load step 5.

145
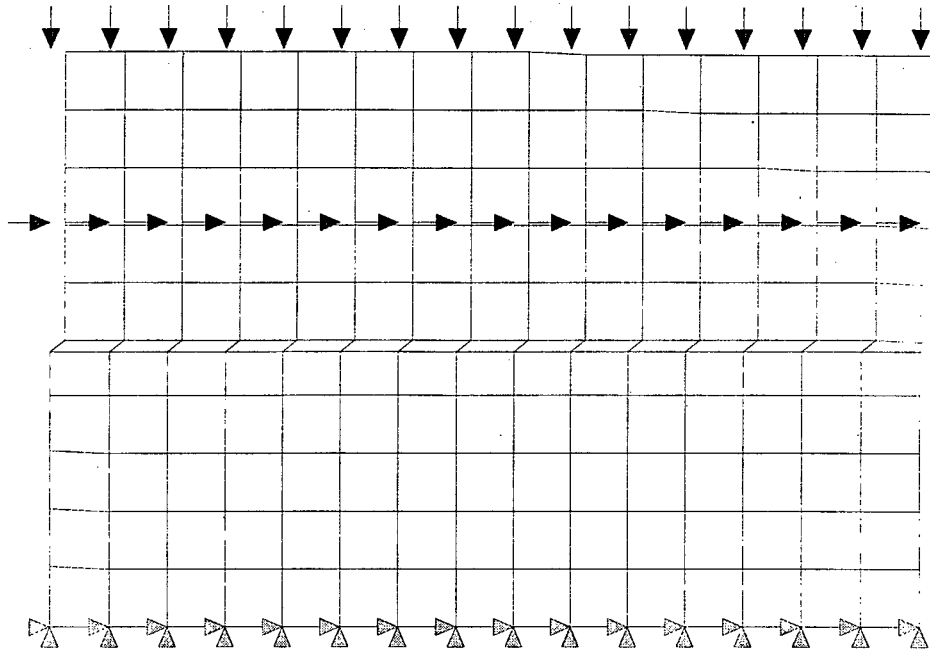
Figure 5-17(c): Deformed mesh for Case-3 of Desai Type Interface at load step 10.
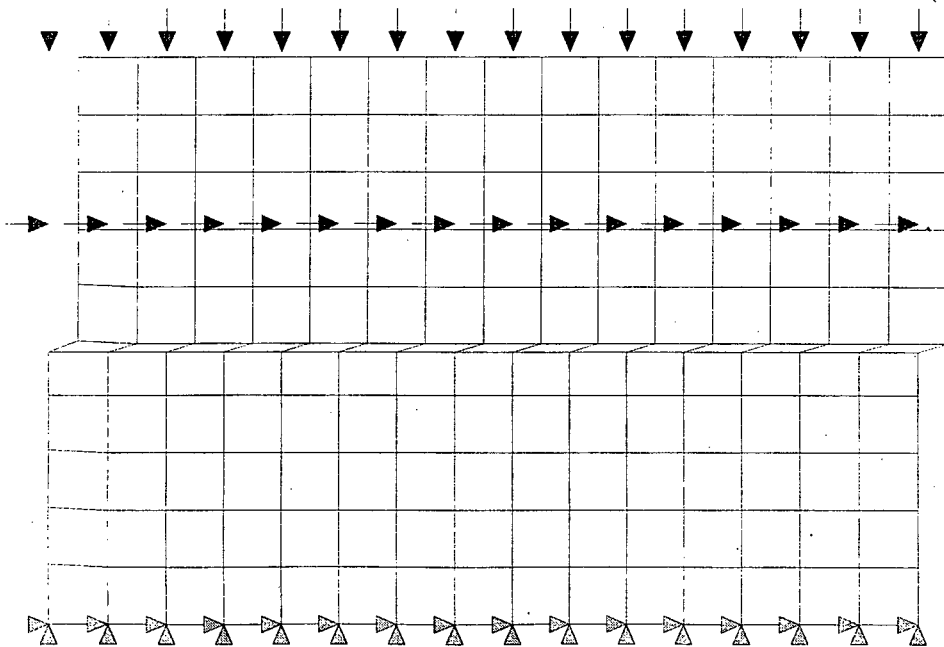
Figure 5-17(d): Deformed mesh for Case-3 of Desai Type Interface at load step 15.

146
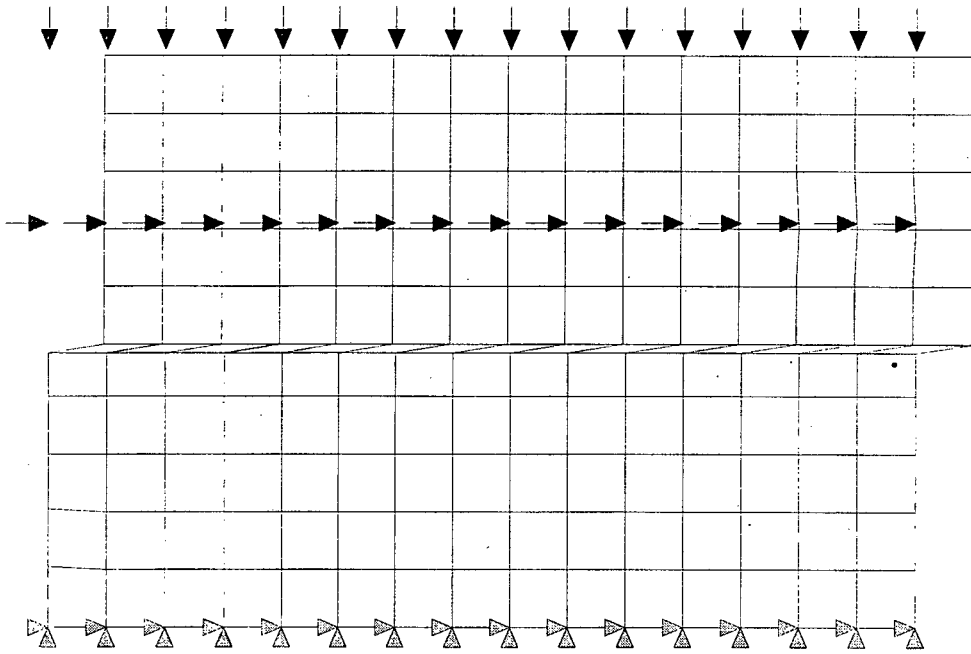
Figure 5-17(e): Deformed mesh for Case-3 of Desai Type Interface at load
step 20.
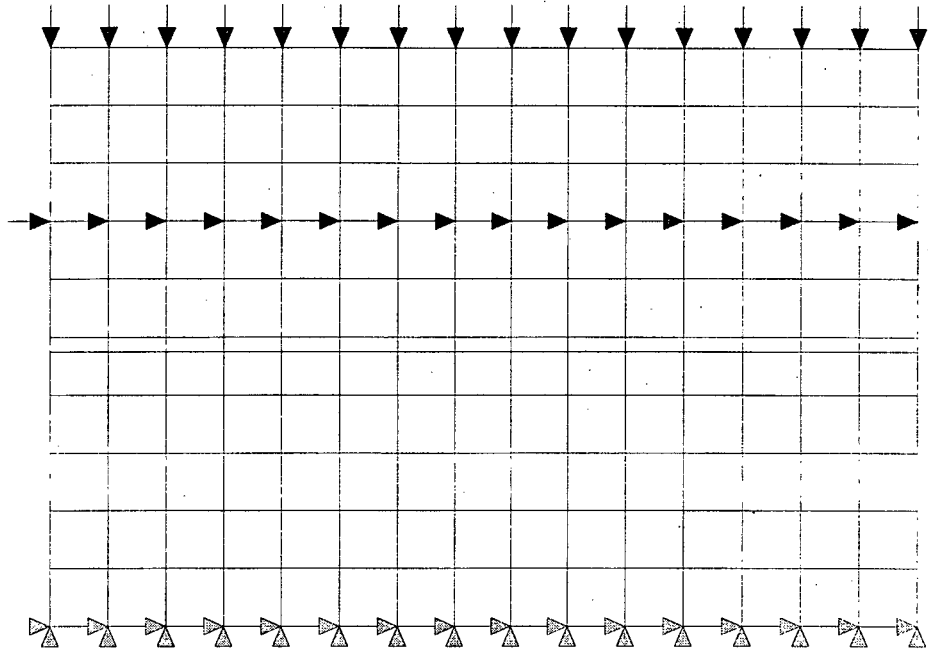
Figure 5-18(a): Deformed mesh for Case-4 of Desai Type Interface at load step 1.
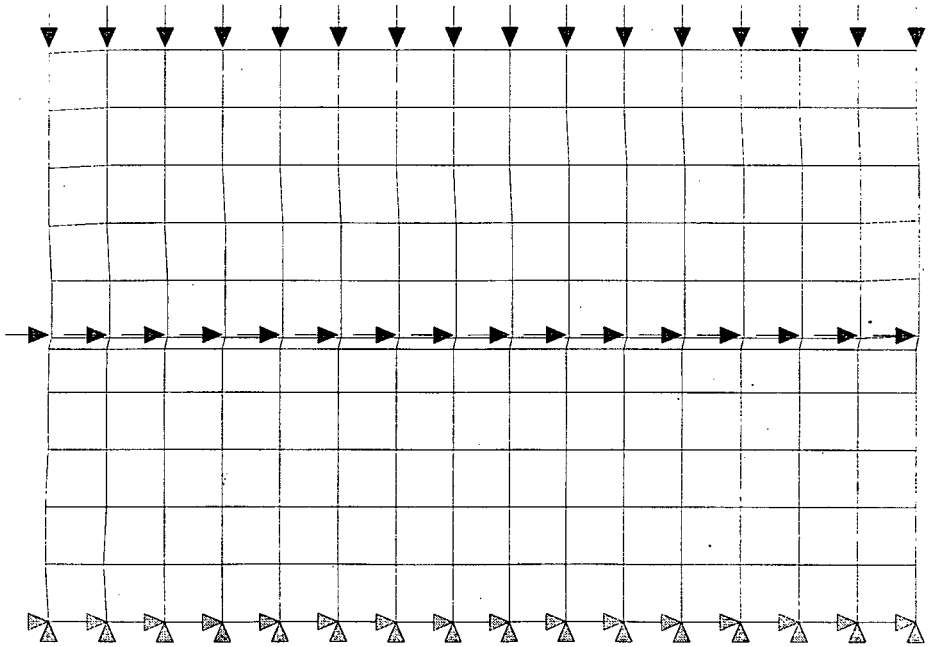
Figure 5-18(b): Deformed mesh for Case-4 of Desai Type Interface at load step 5.
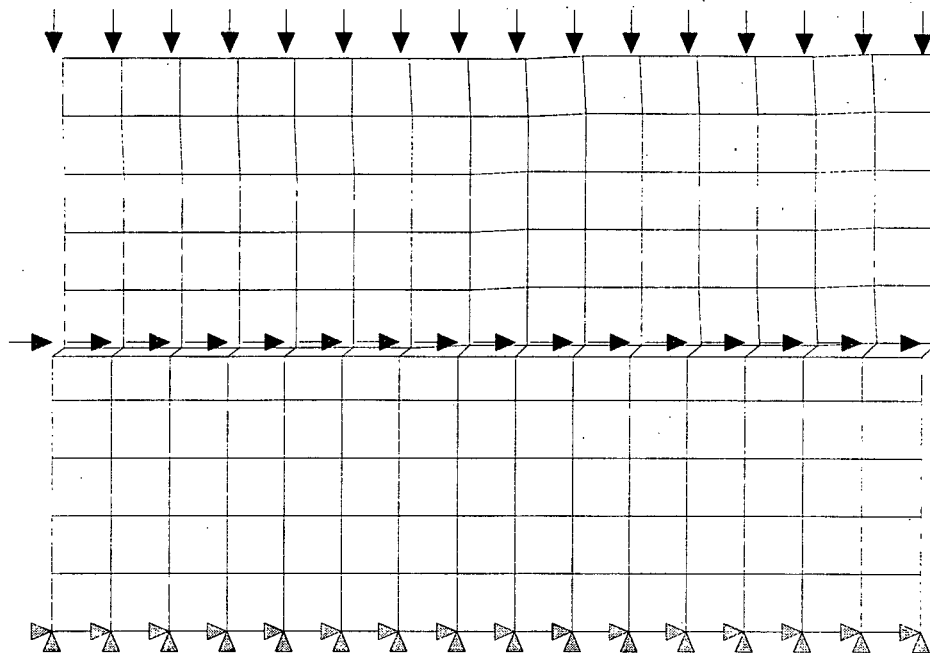
Figure 5-18(c): Deformed mesh for Case-4 of Desai Type Interface at load
step 10.
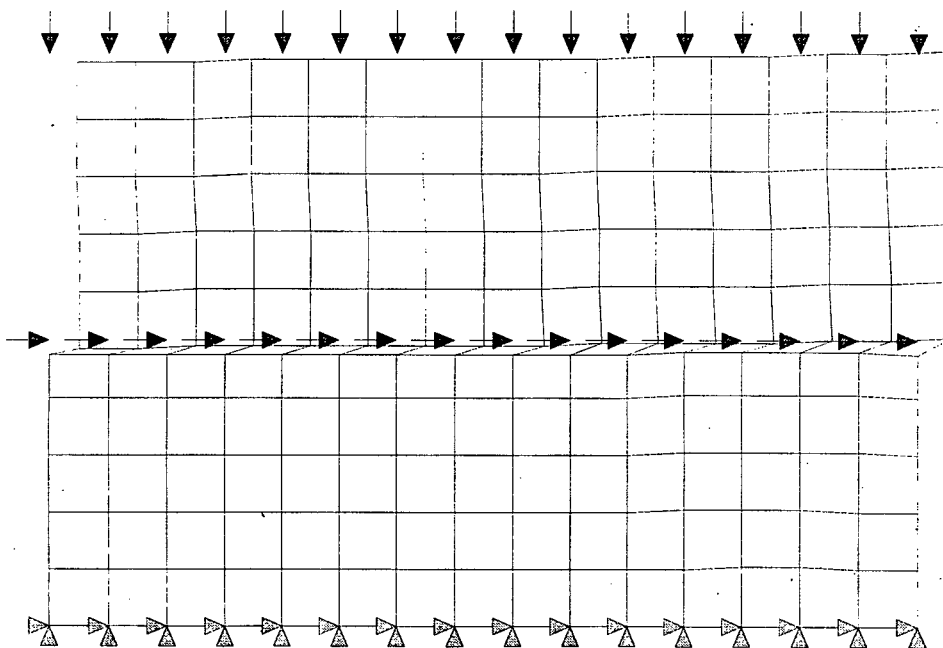
Figure 5-18(d): Deformed mesh for Case-4 of Desai Type Interface at load
step 15.
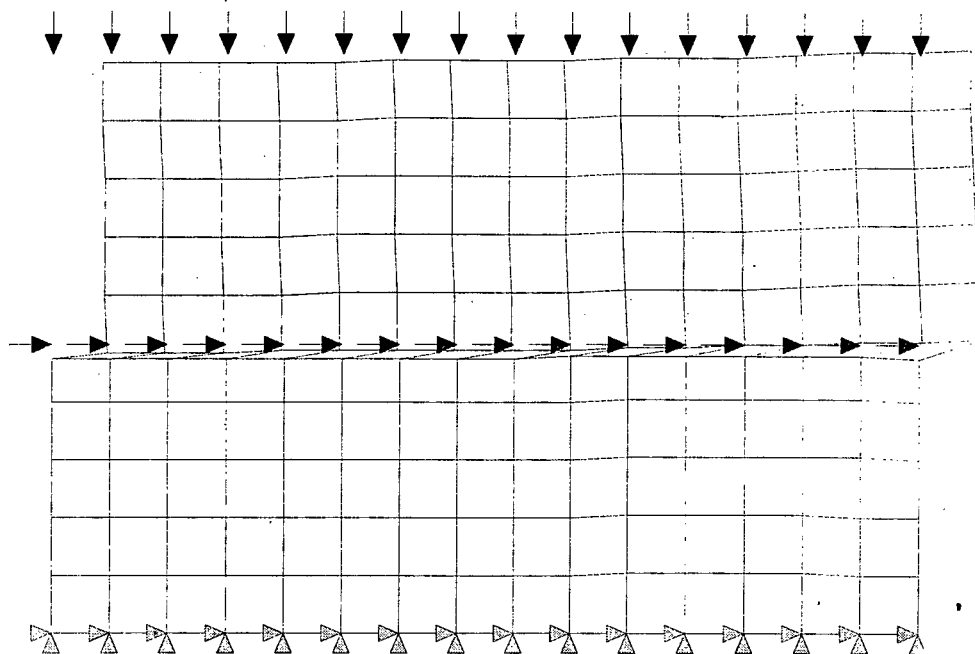
Figure 5-18(e): Deformed mesh for Case-4 of Desai Type Interface at load step 20.
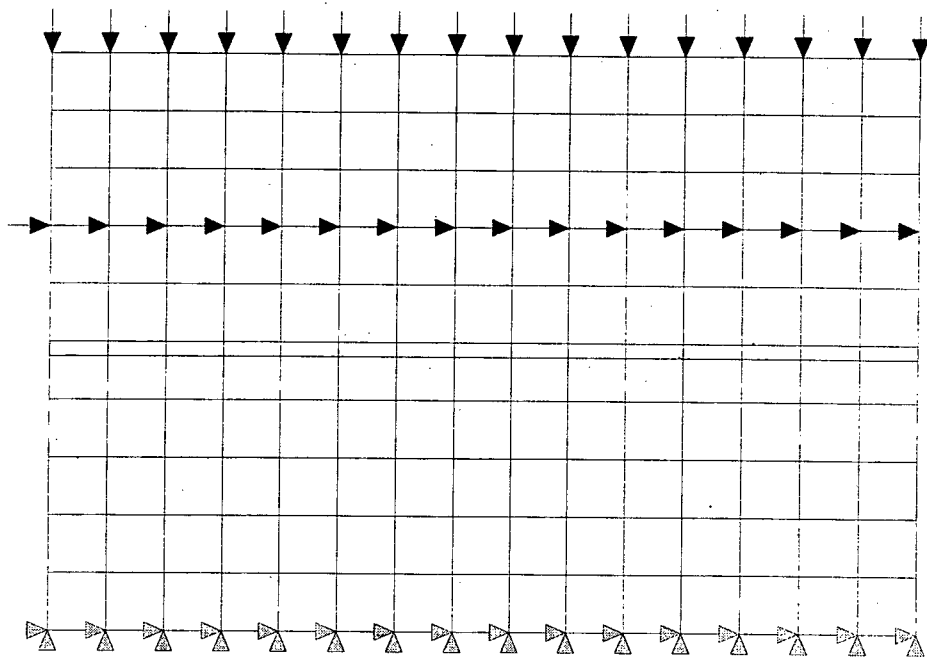
Figure 5-19(a): Deformed mesh for Case-5 of Desai Type Interface at load step 1.
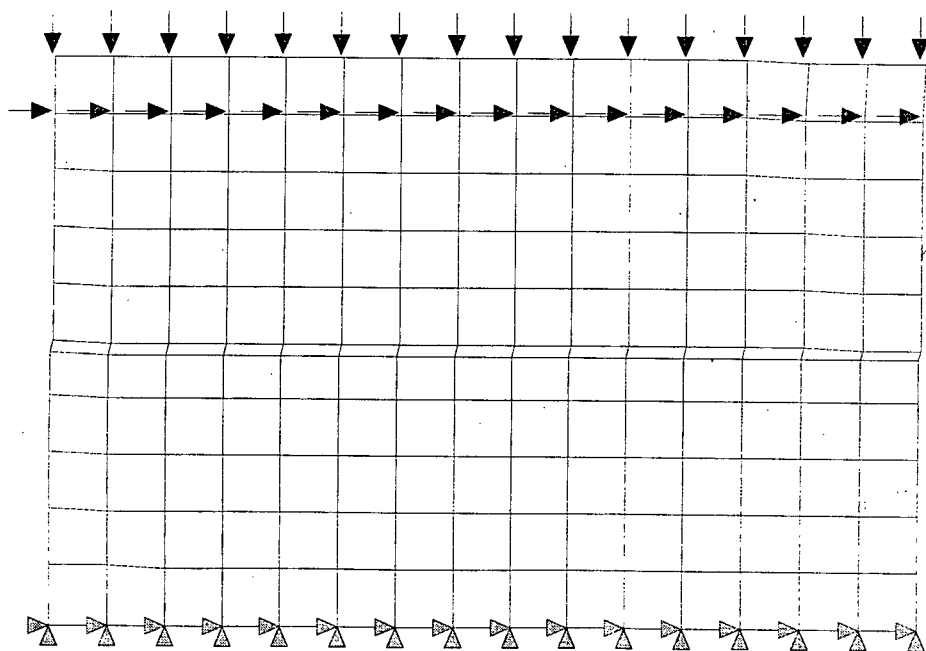
Figure 5-19(b): Deformed mesh for Case-5 of Desai Type Interface at load step 5.
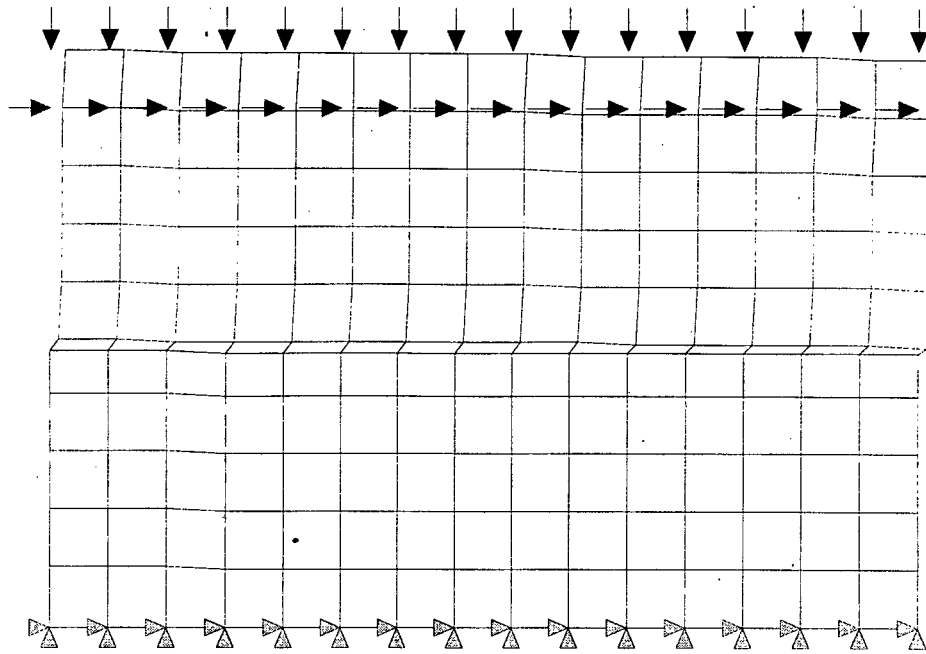
Figure 5-19(c): Deformed mesh for Case-5 of Desai Type Interface at load step 10.
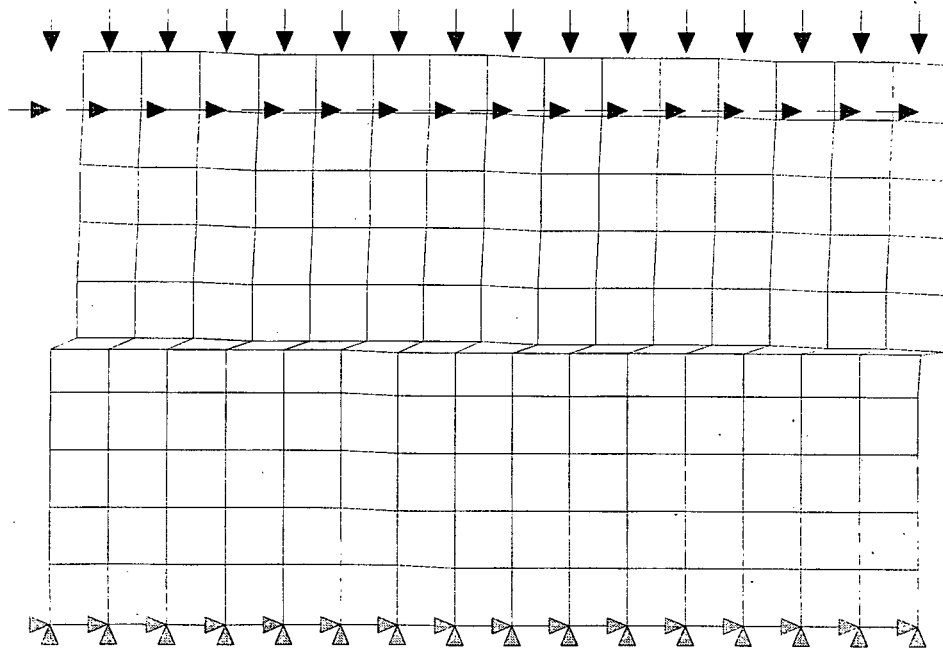
Figure 5-19(d): Deformed mesh for Case-5 of Desai Type Interface at load step 15.
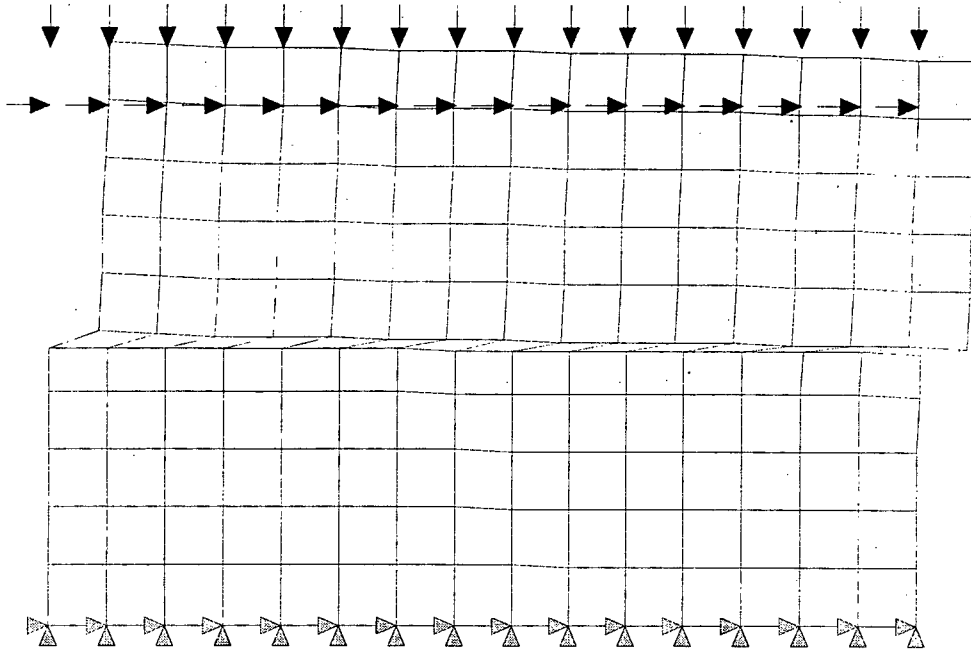
Figure 5-19(e): Deformed mesh for Case-5 of Desai Type Interface at load step 20.
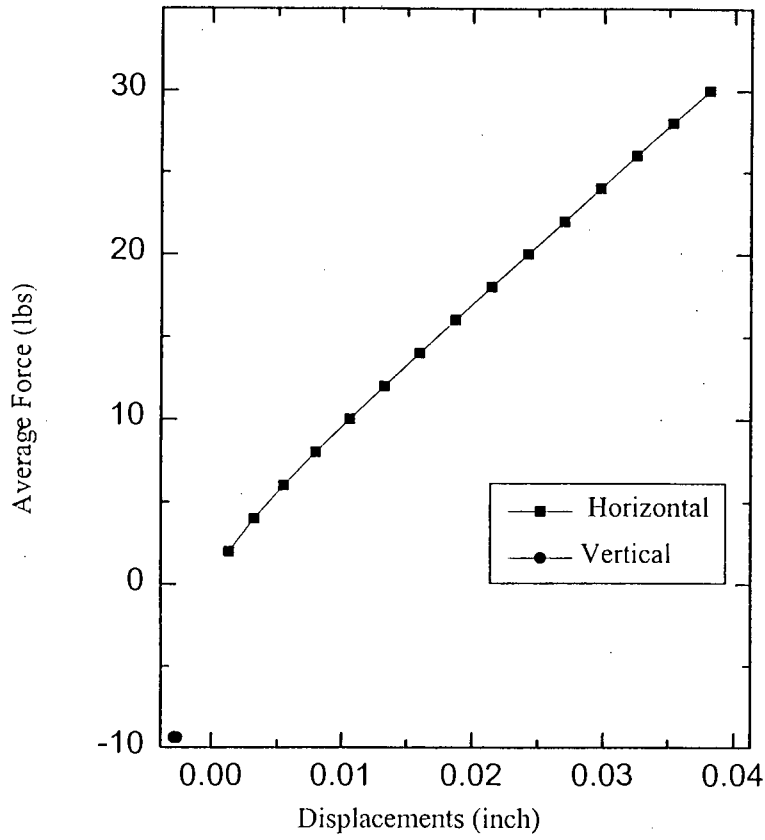
Figure 5-20(a): Average Force vs Displacement variation of Normal Element for Case-1.
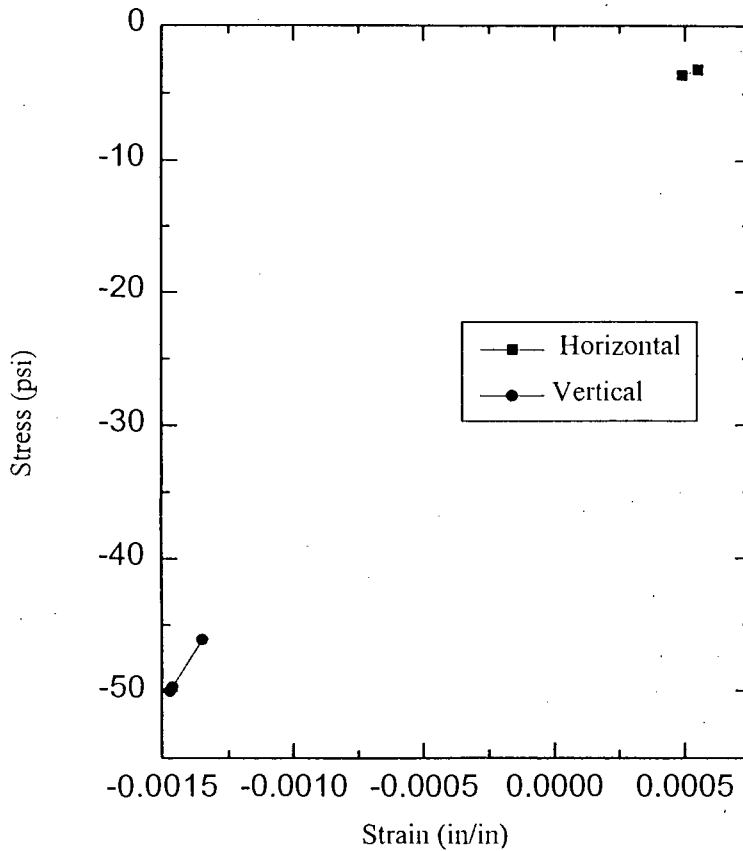
Figure 5-20(b): Stress vs Strain variation of Normal Element for Case-1.

Shear strain (ε_1-ε_3) contour (in percent)
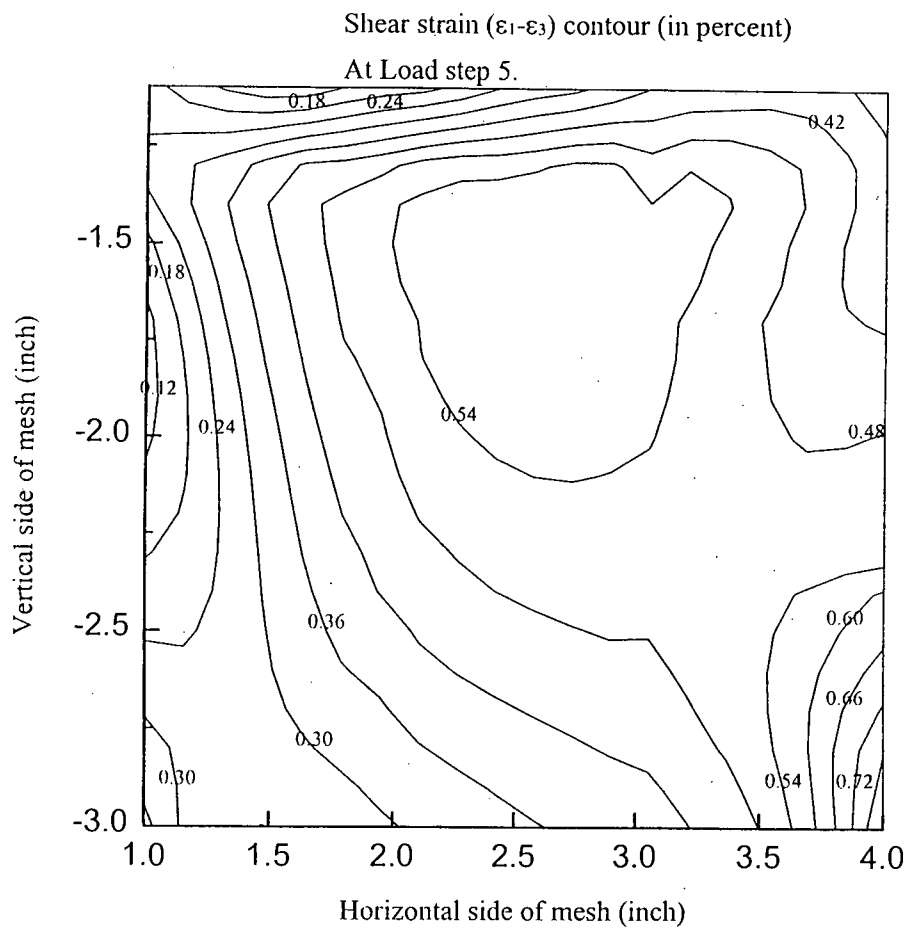
At Load step 5.

Figure 5-21(a): Shear strain contour for Case-1 of Normal Element at load step 5.

Shear strain (ε_1-ε_3) contour (in percent)
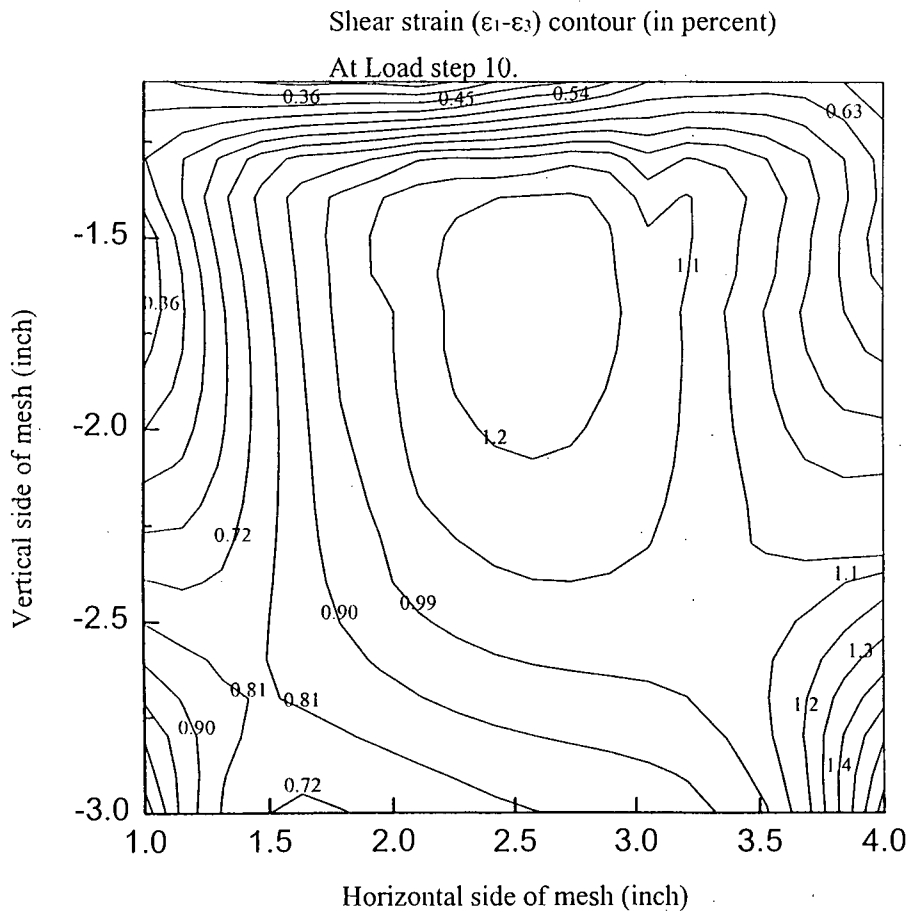
At Load step 10.

Figure 5-21(b): Shear strain contour for Case-1 of Normal Element at load step 10.
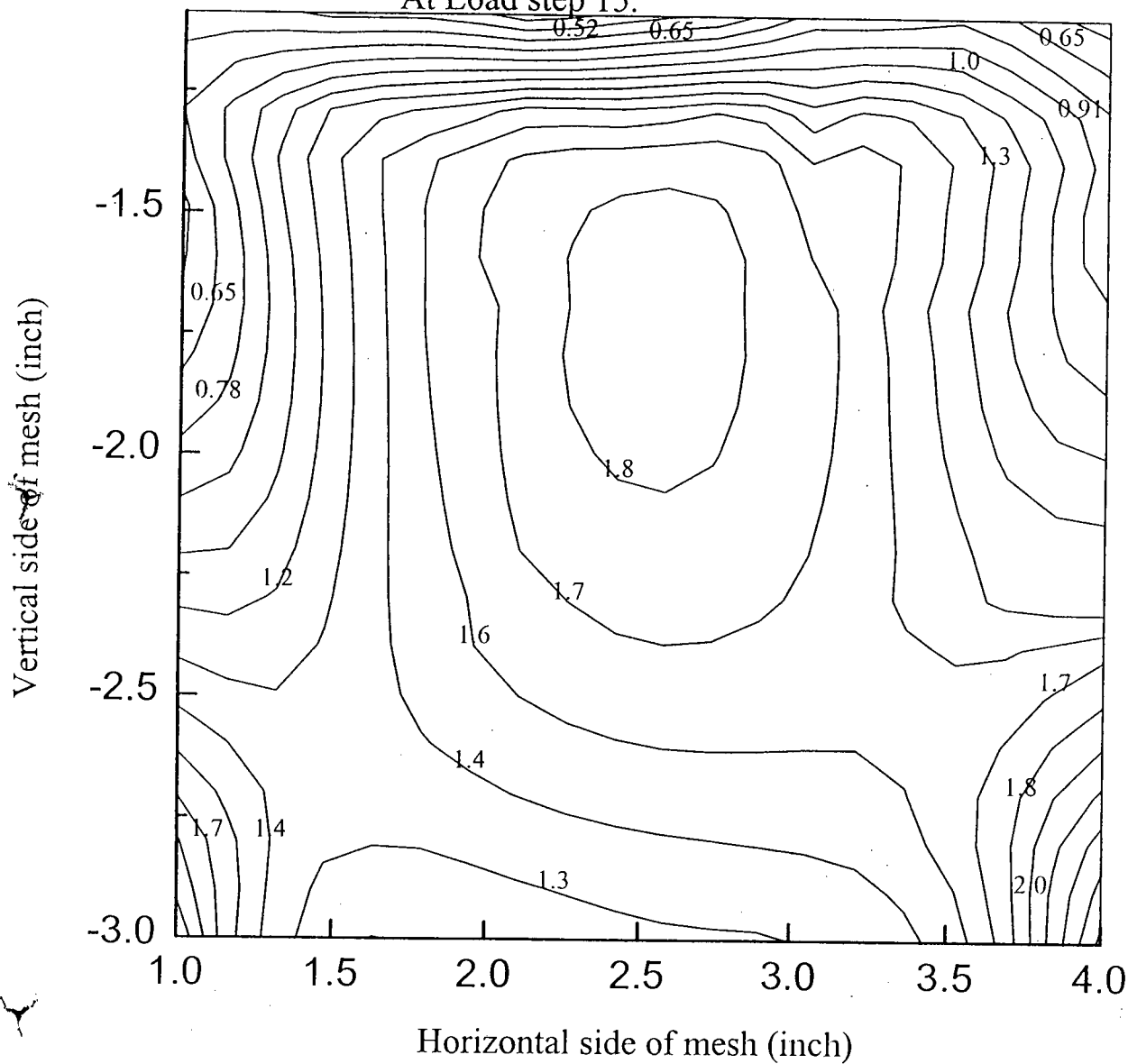
Figure 5-21(c): Shear strain contour for Case-1 of Normal Element at load
step 15.

156
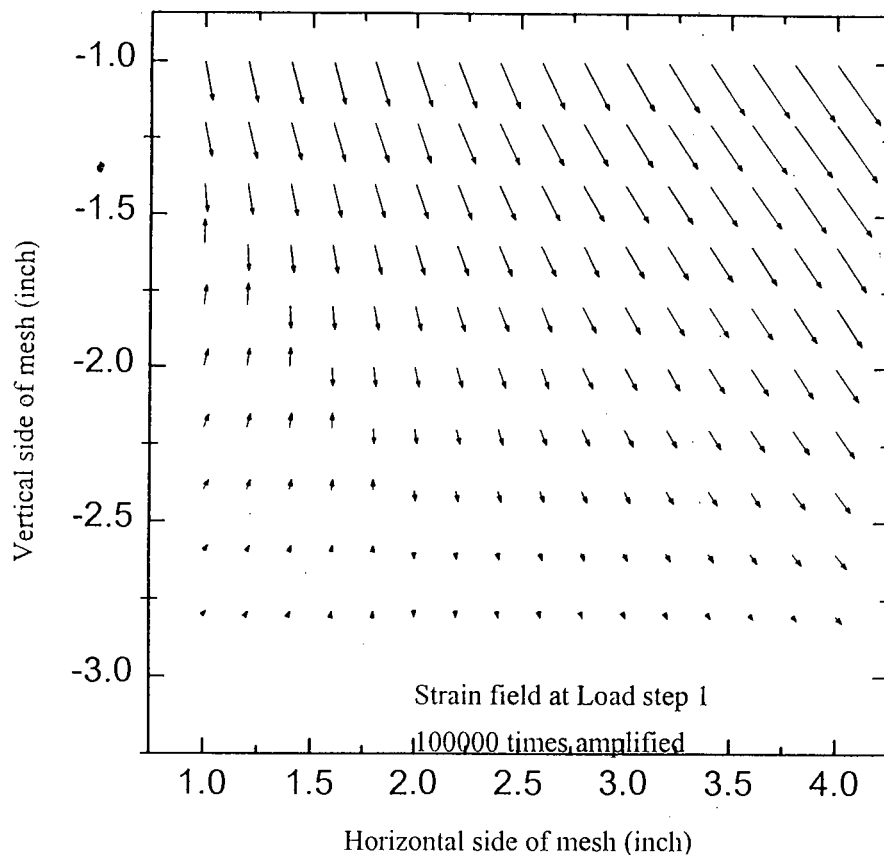
Figure 5-22(a):   Displacement field for Case-1 of Normal Element at load step 1.
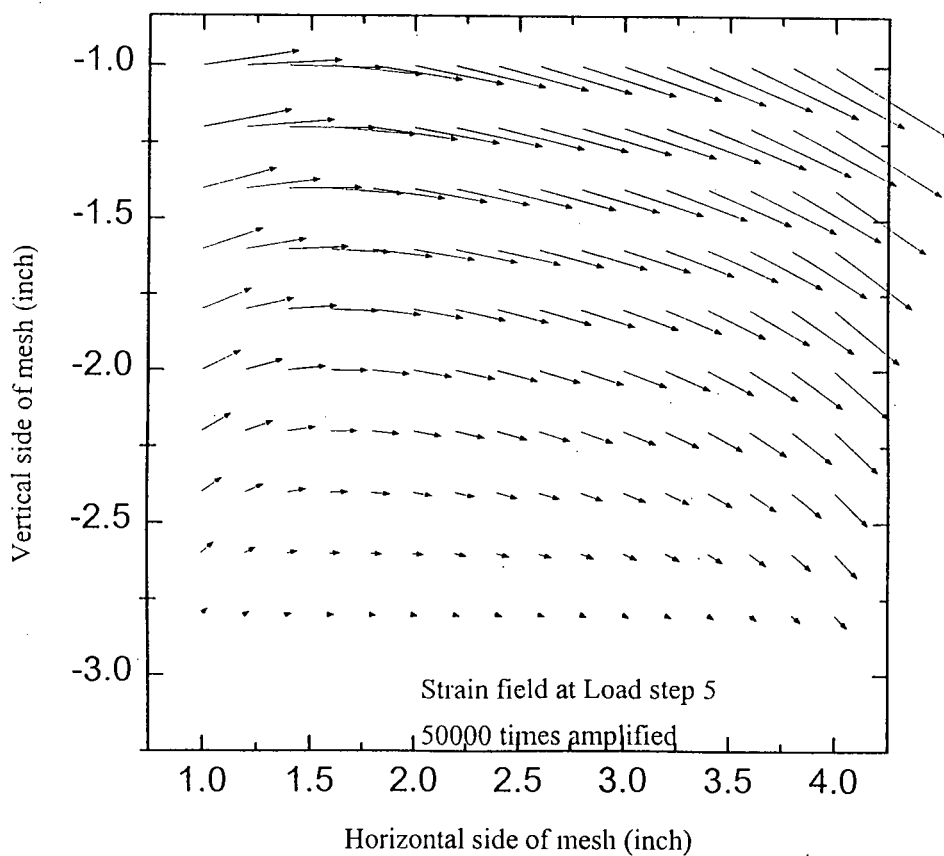
Figure 5-22(b):   Displacement field for Case-1 of Normal Element at load step 5.

157
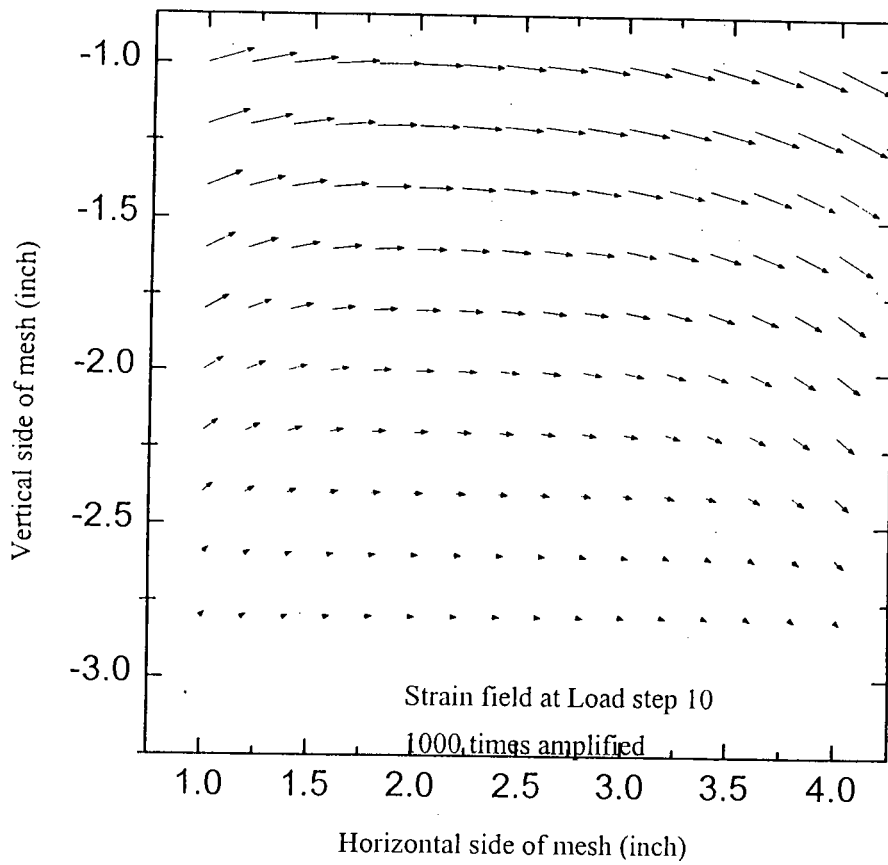
Figure 5-22(c): Displacement field for Case-1 of Normal Element at load
step 10.
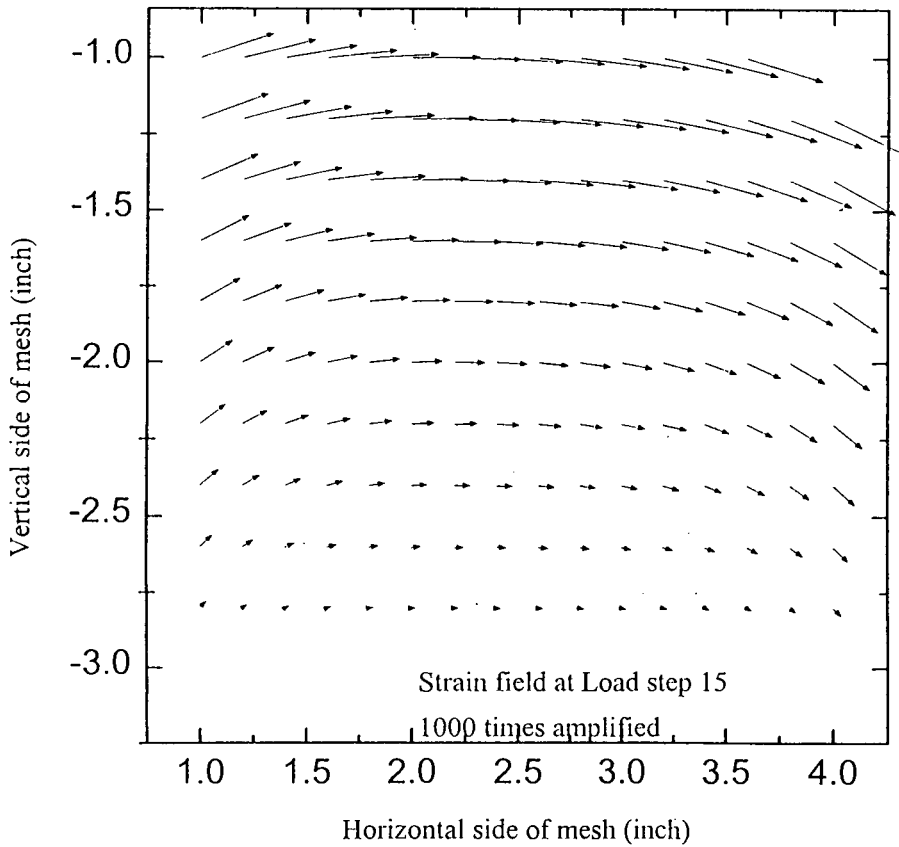
Figure 5-22(d):   Displacement field for Case-1 of Normal Elementat load
step 15.

158
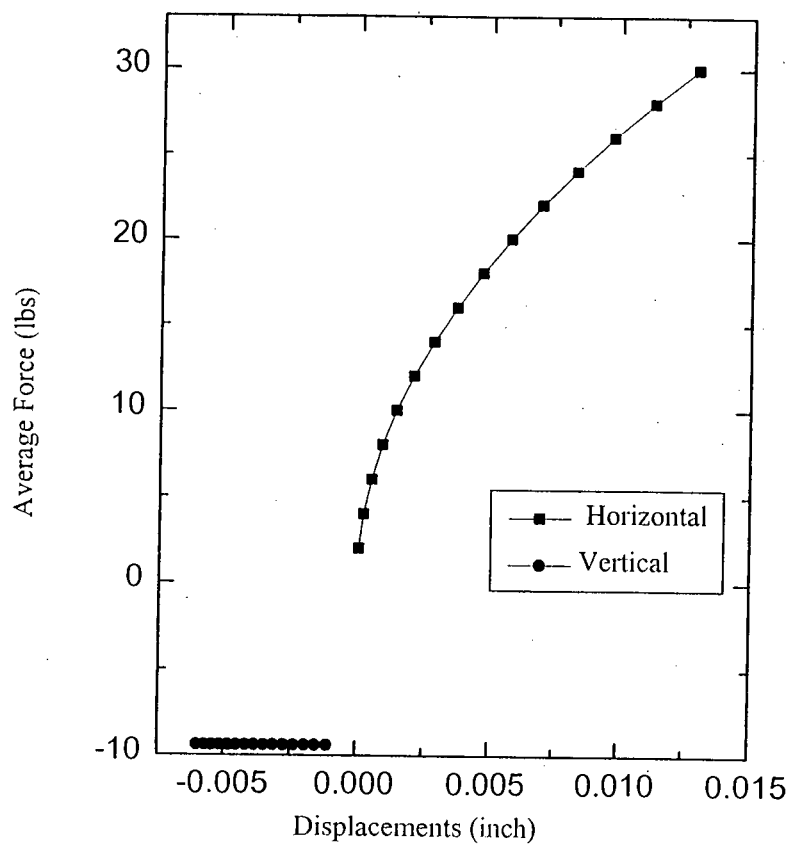
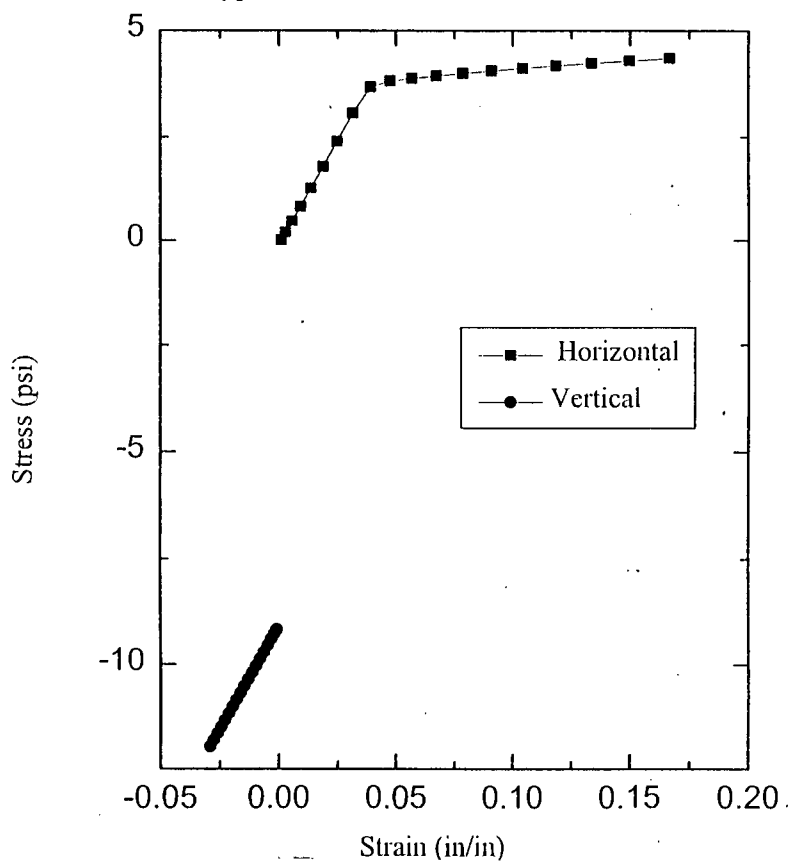Figure 5-23(a): Average Force vs Displacement variation inside of Goodman Type Interface for Case-1.
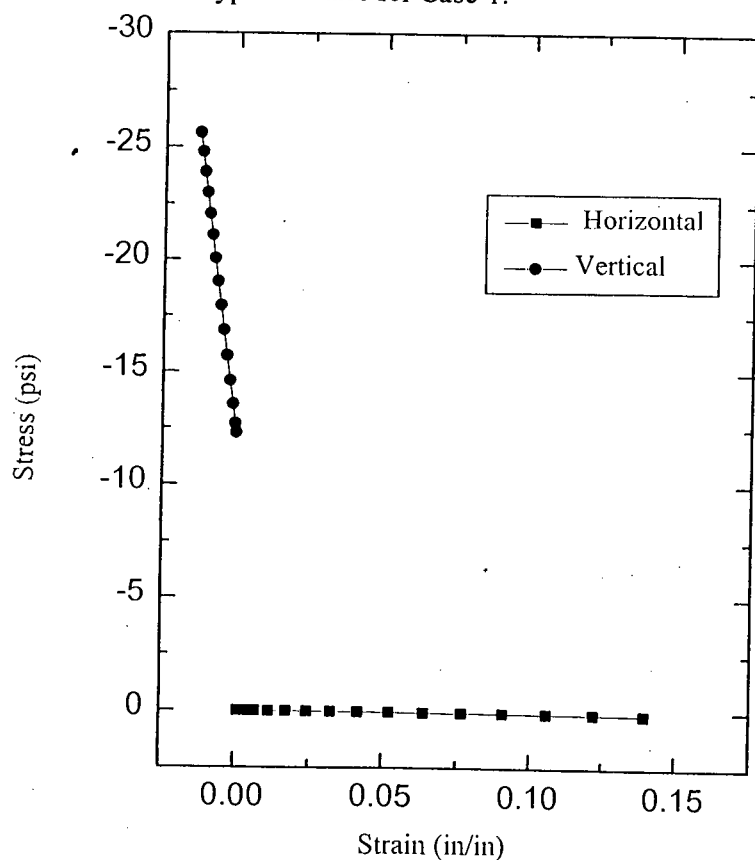
Figure 5-23(b): Stress vs Strain variation inside of Goodman Type Interface for Case-1.

Shear strain (ε_1-ε_3) contour (in percent)
At Load step 5.

Vertical side of mesh (inch)

Horizontal side of mesh (inch)
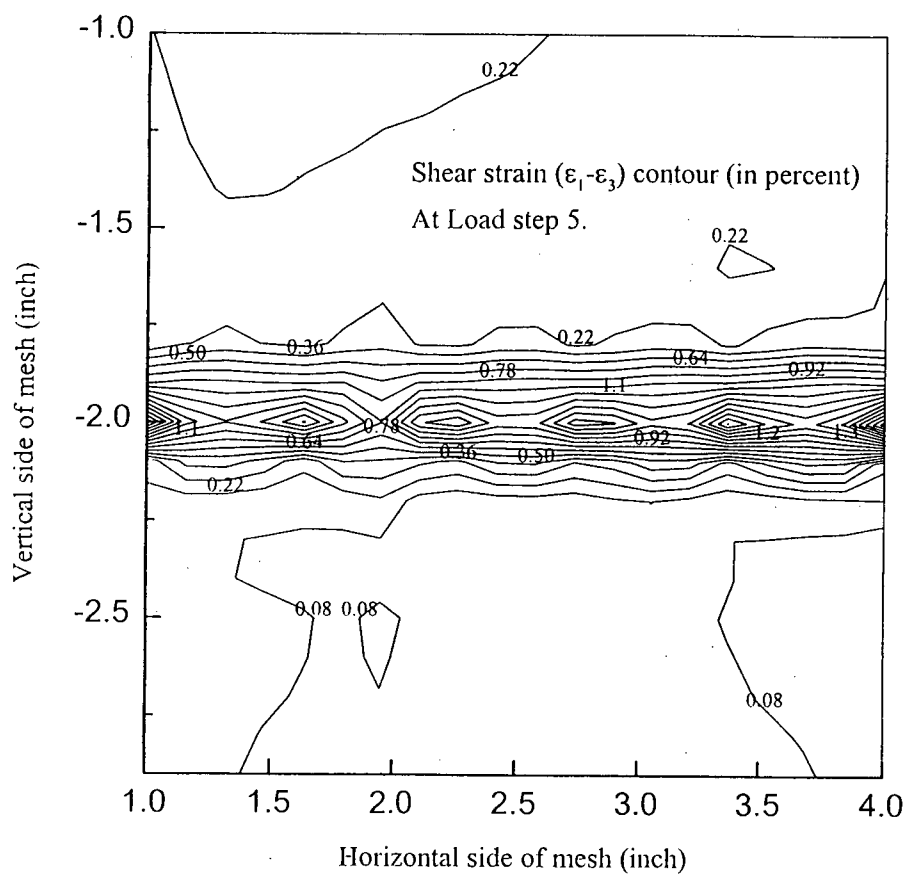
Figure 5-24(a):   Shear strain contour for Case-1 of Goodman Type Interface at load step-5.

Shear strain (ε_1-ε_3) contour (in percent)
At Load step 10.

Vertical side of mesh (inch)

Horizontal side of mesh (inch)
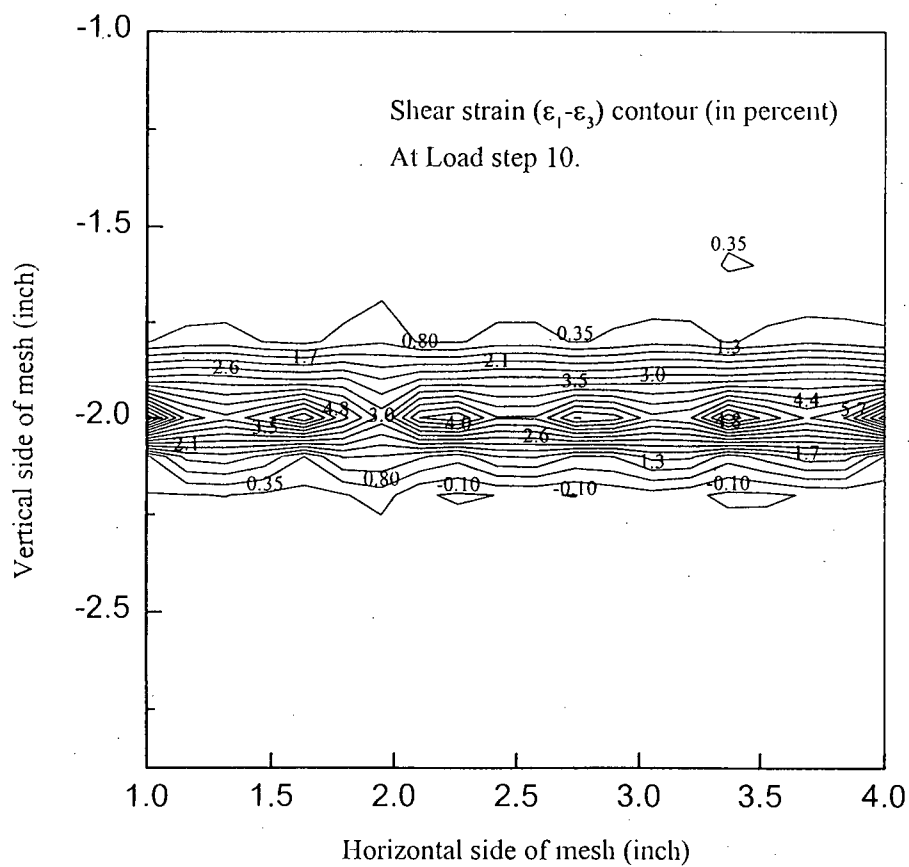
Figure 5-24(b):   Shear strain contour for Case-1 of Goodman Type Interface at load step-10.

160
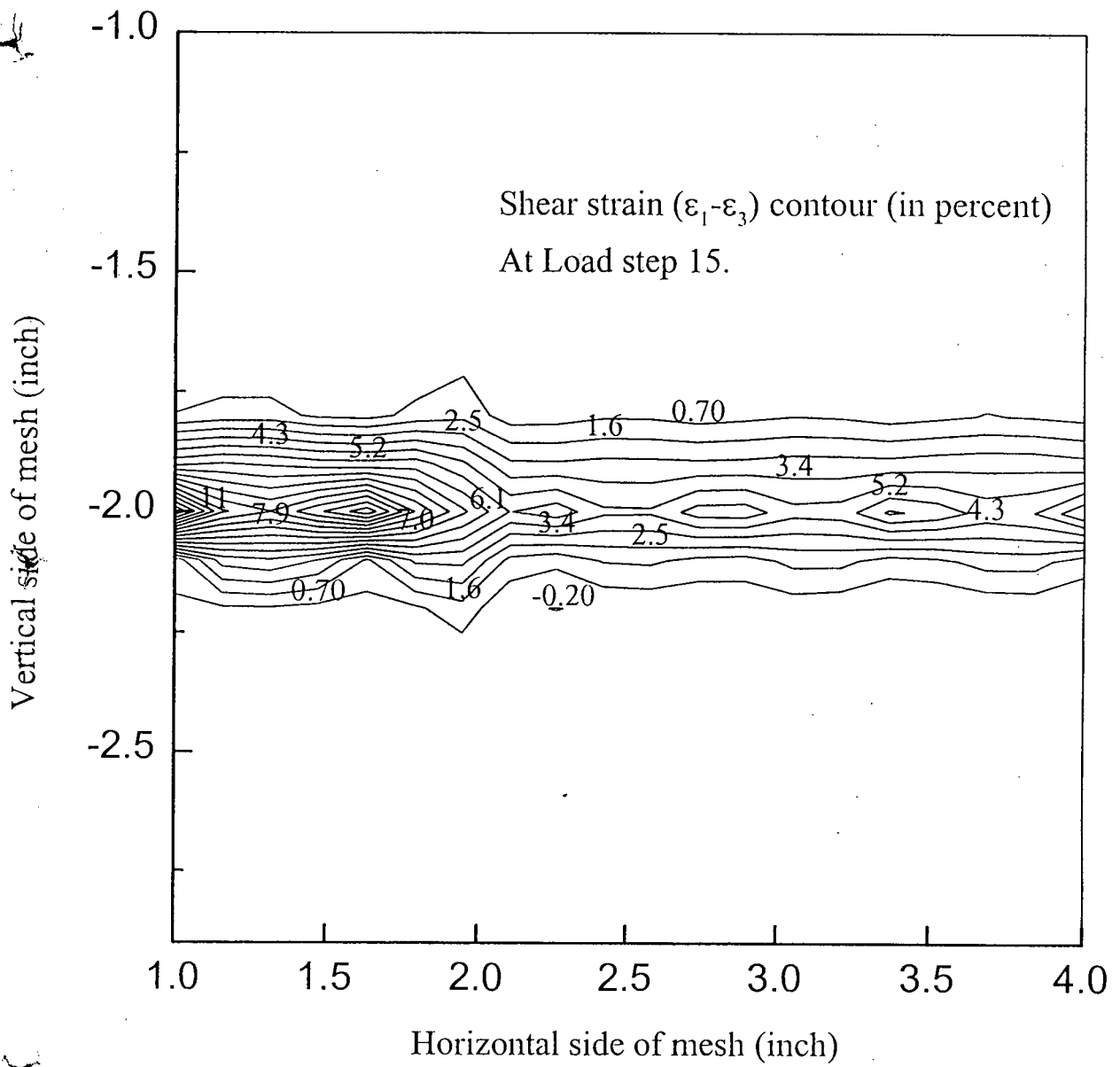
Figure 5-24(c):   Shear strain contour for Case-1 of Goodman Type Interface at load step-15.

Strain field at Load step 1

10000 times amplified

Horizontal side of mesh (inch)

Figure 5-25(a): Displacement field for Case-1 of Goodman Type Interface at load step-1.

Strain field at Load step 5

10000 times amplified

Horizontal side of mesh (inch)

Figure 5-25(b): Displacement field for Case-1 of Goodman Type Interface at load step-5.

162

Strain field at Load step 10

5000 times amplified

Vertical side of mesh (inch)

Horizontal side of mesh (inch)

Figure 5-25(c): Displacement field for Case-1 of Goodman Type Interface at load step-10.

Strain field at Load step 15

5000 times amplified

Vertical side of mesh (inch)

Horizontal side of mesh (inch)

Figure 5-25(d): Displacement field for Case-1 of Goodman Type Interface at load step-15.

163

Figure 5-26(a): Average Force vs Displacement variation inside of Goodman
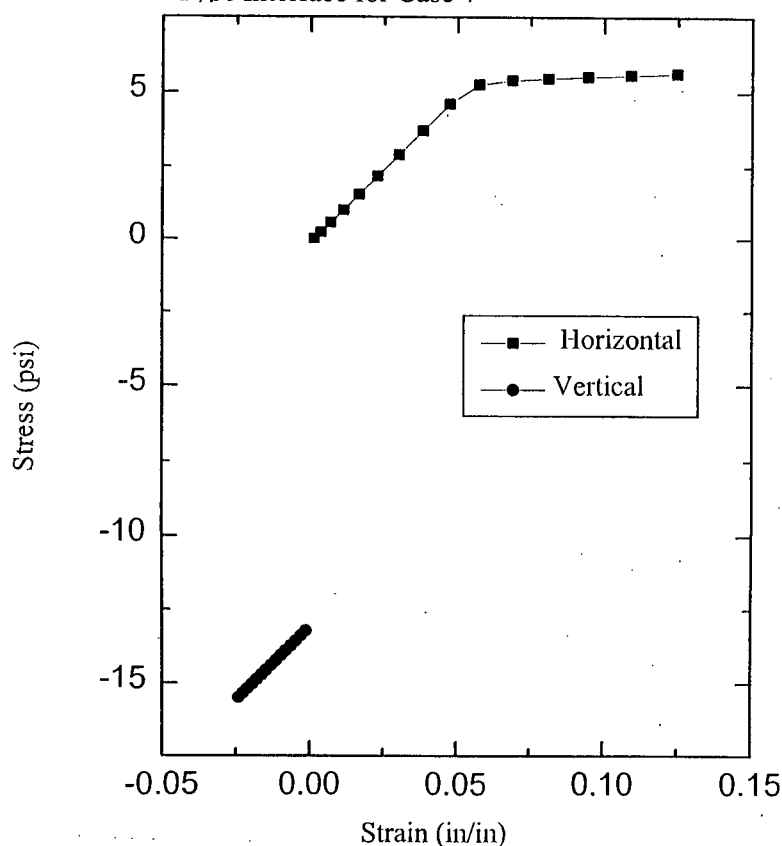Type Interface for Case-2.
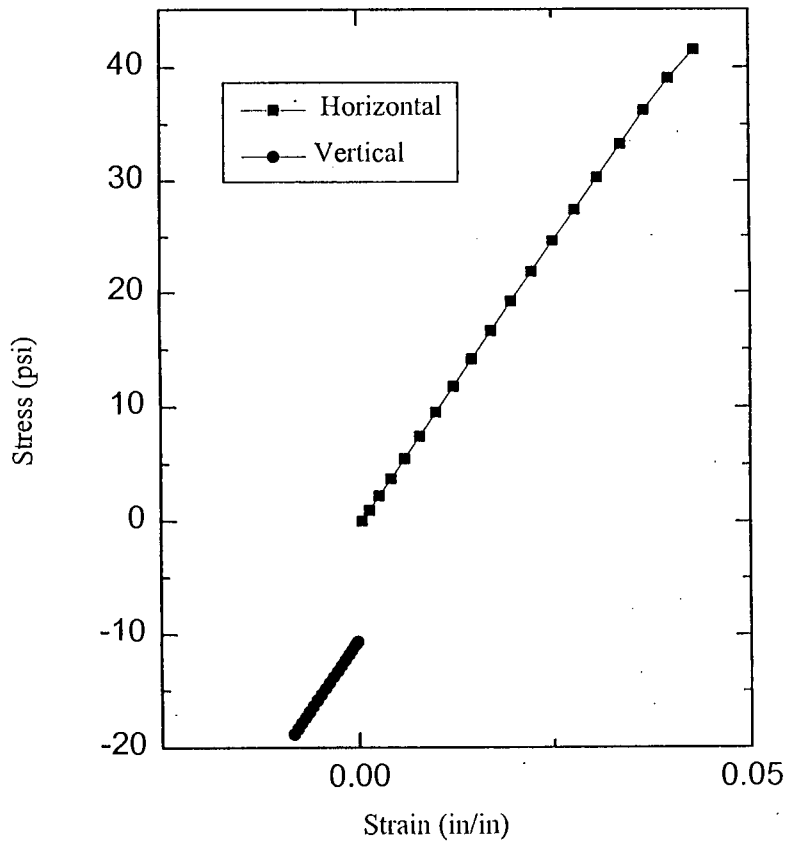
Figure 5-26(b): Stress vs Strain variation inside of Goodman Type Interface for
Case-2.
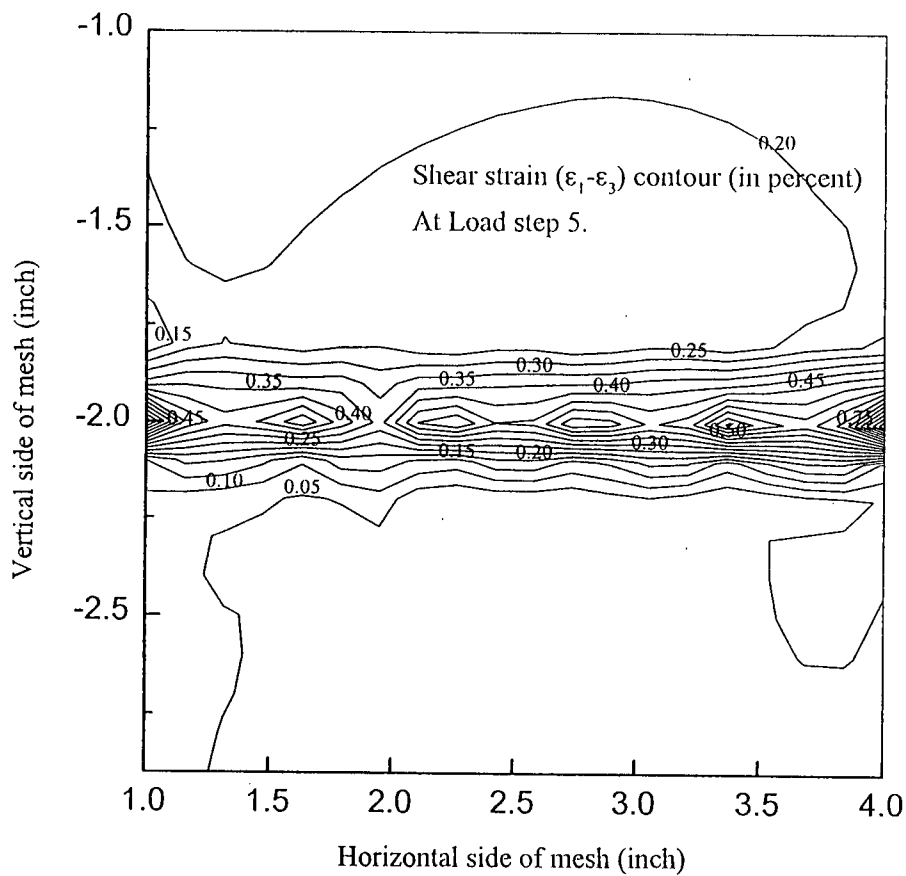
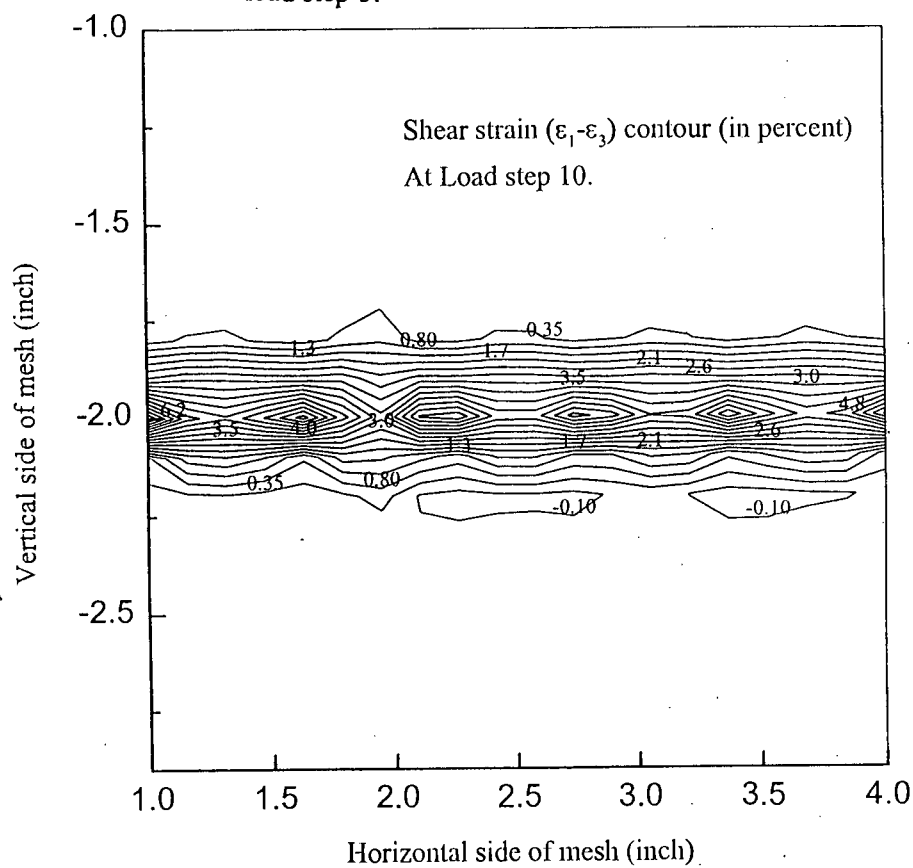Figure 5-27(a): Shear strain contour for Case-2 of Goodman Type Interface at load step-5.
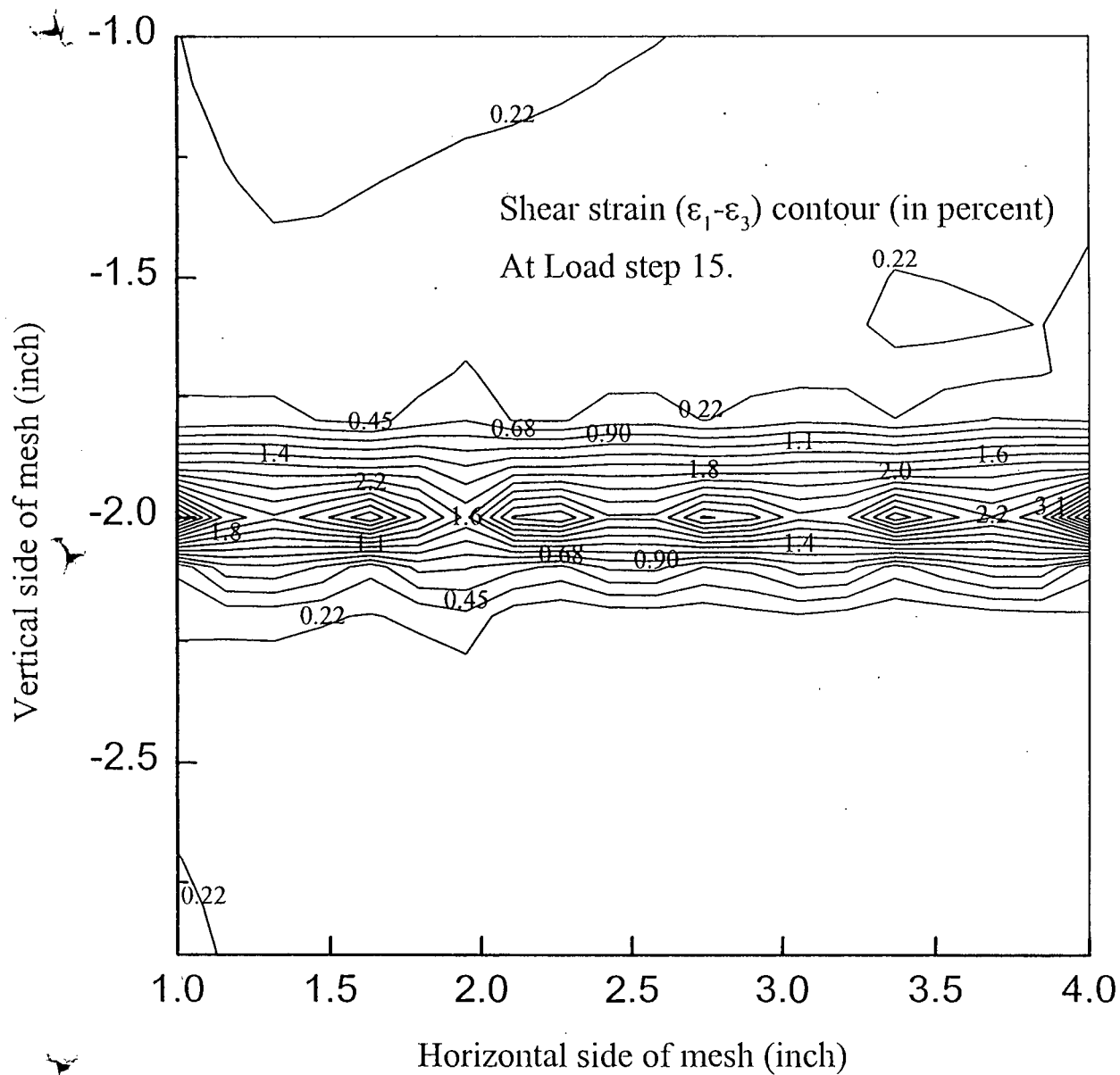
Figure 5-27(c): Shear strain contour for Case-2 of Goodman Type Interface at load step-15.
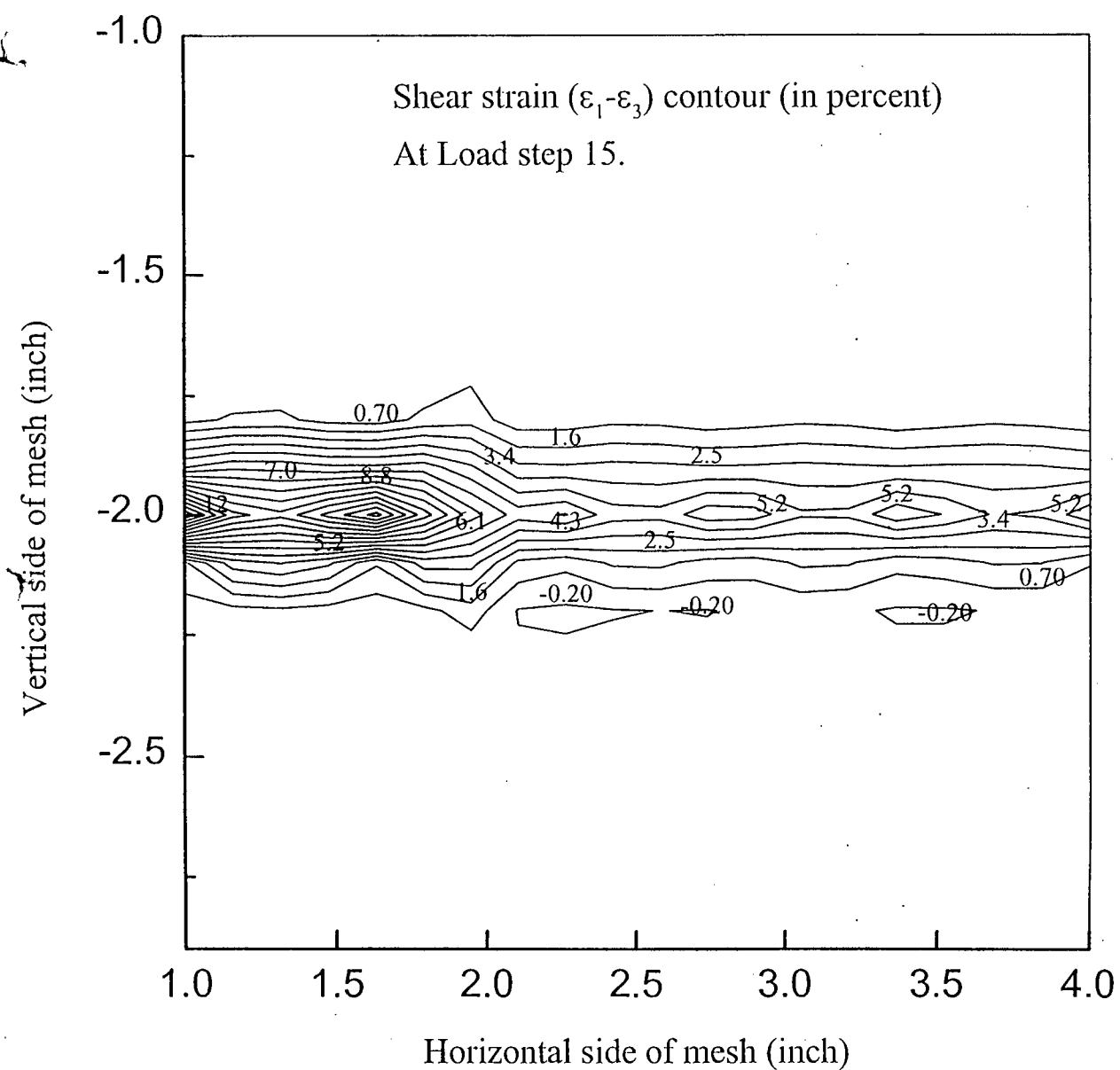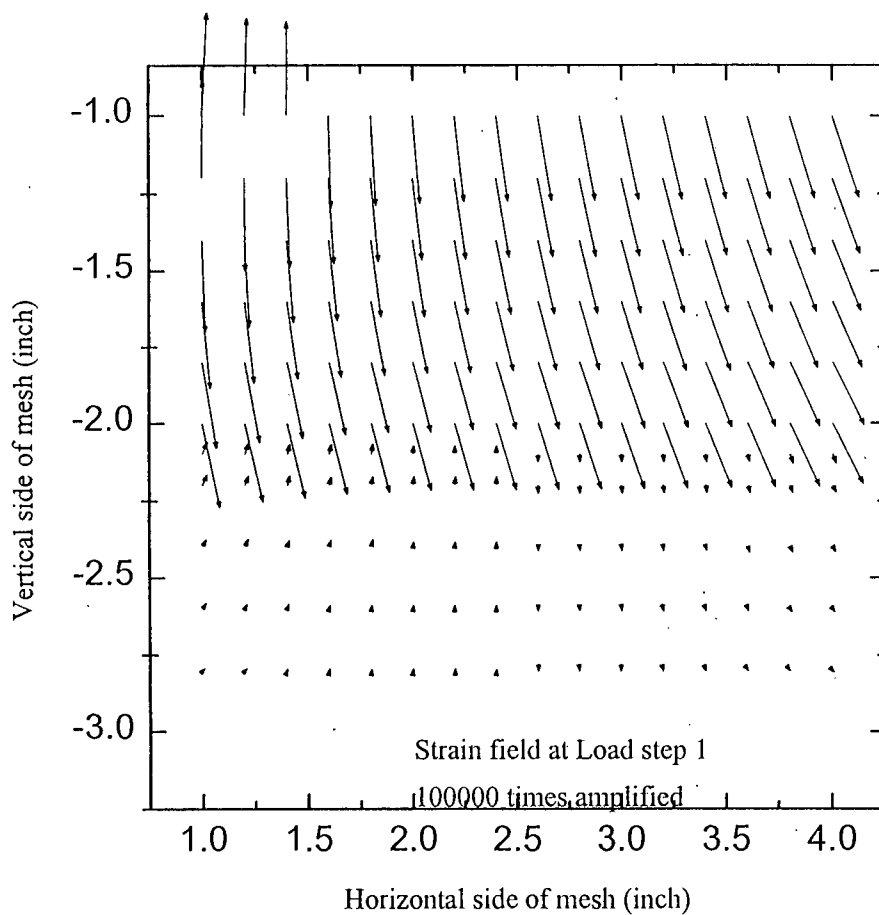
166
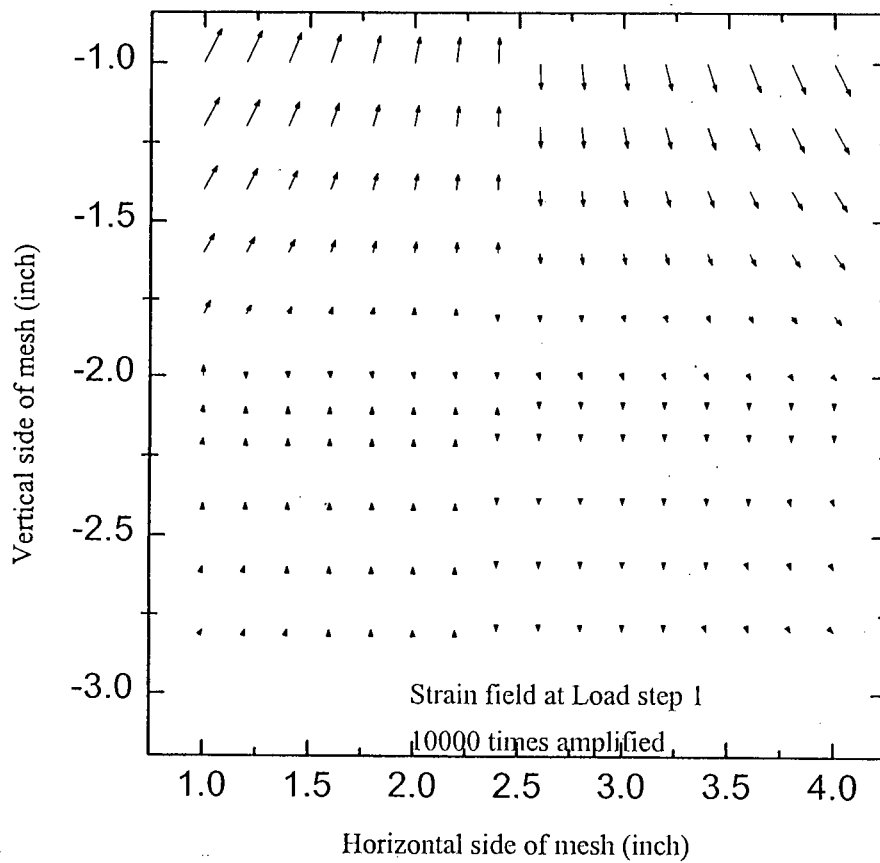
Figure 5-28(a): Displacement field for Case-2 of Goodman Type Interface at load step-1.
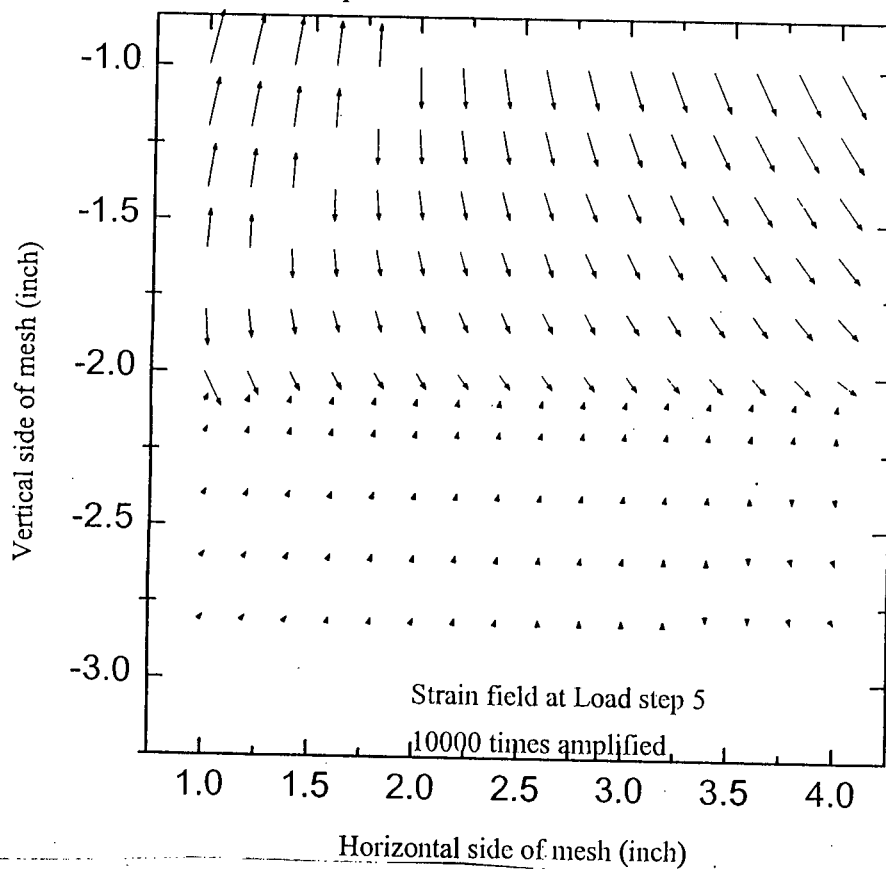
Figure 5-28(b): Displacement field for Case-2 of Goodman Type Interface at load step-5.
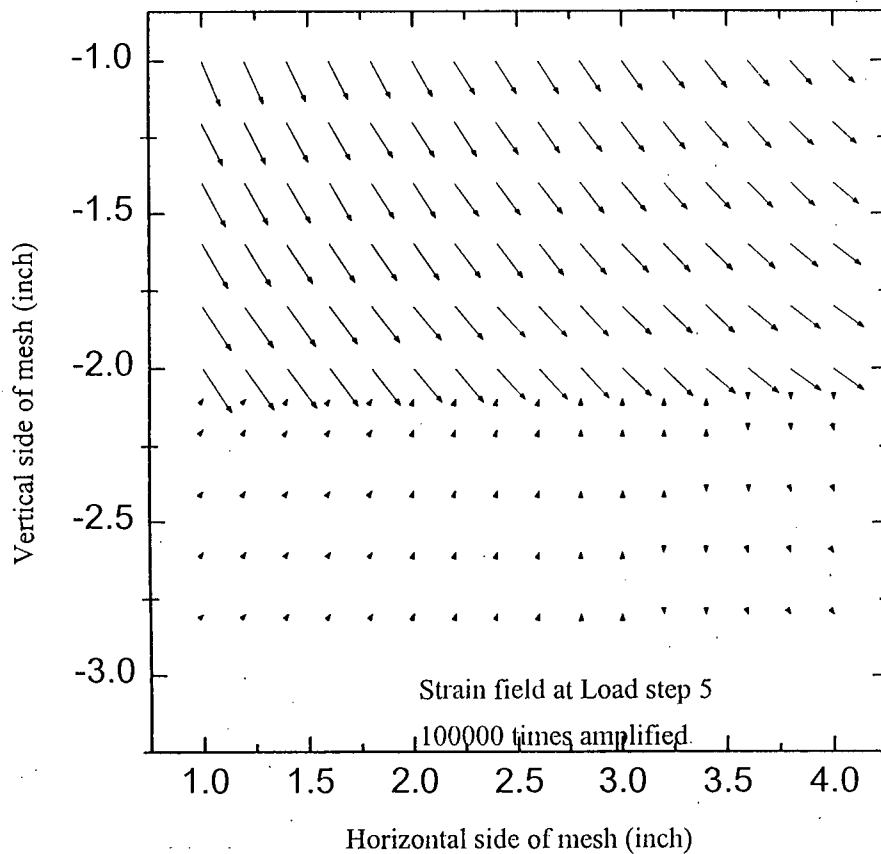
167
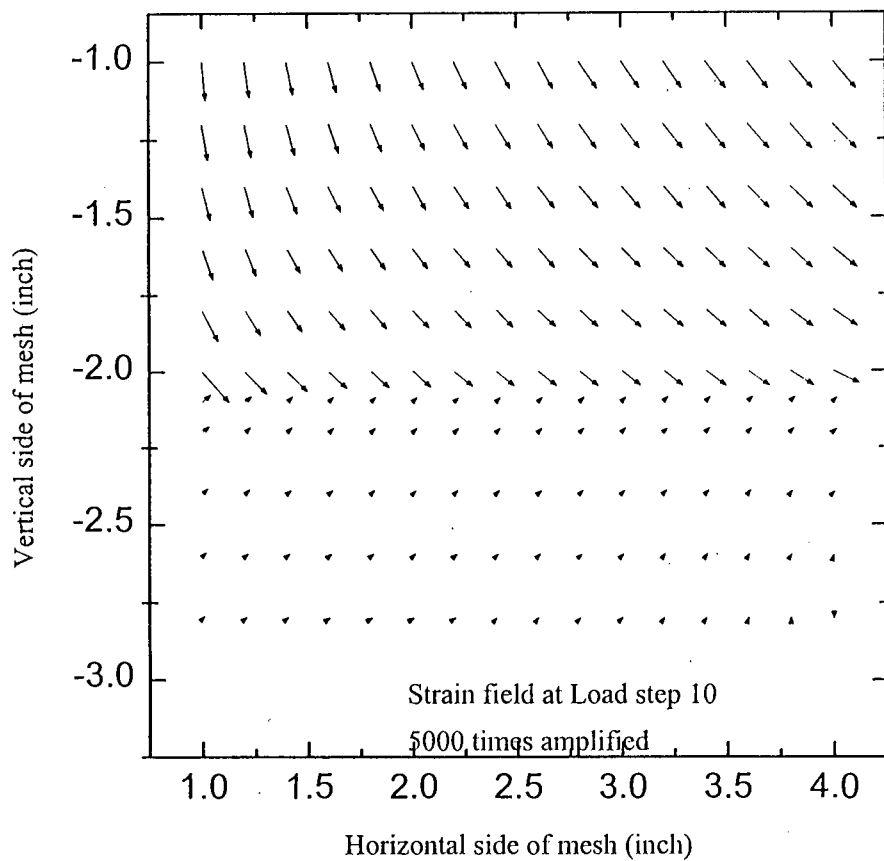
Figure 5-28(c): Displacement field for Case-2 of Goodman Type Interface at load step-10.
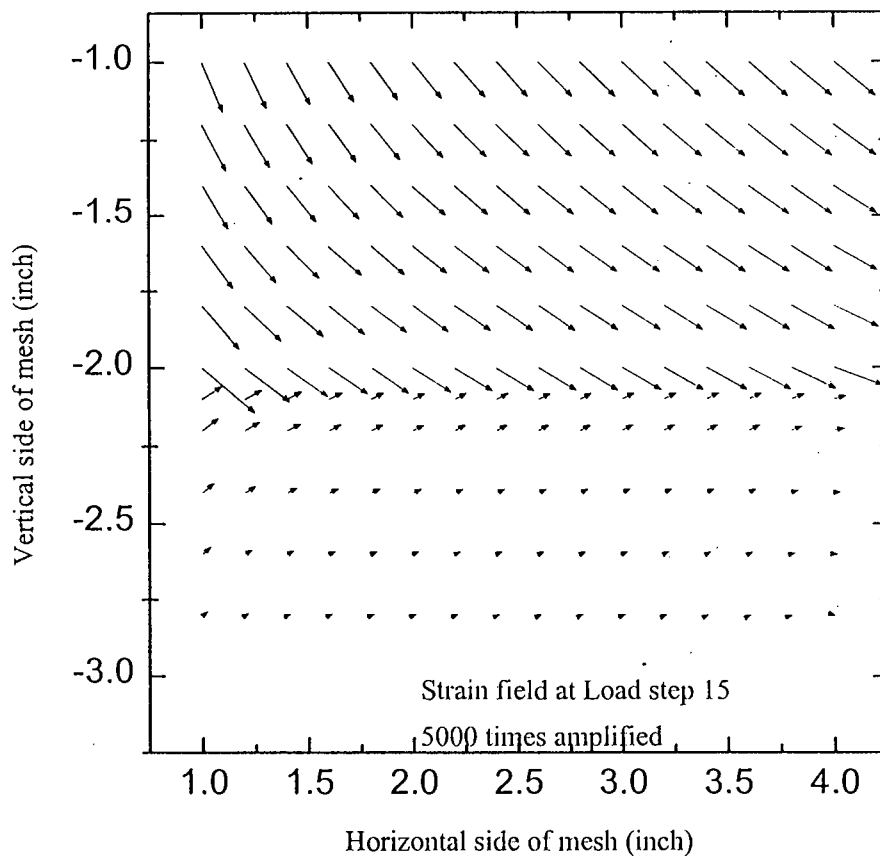
Figure 5-28(d): Displacement field for Case-2 of Goodman Type Interface at load step-15.
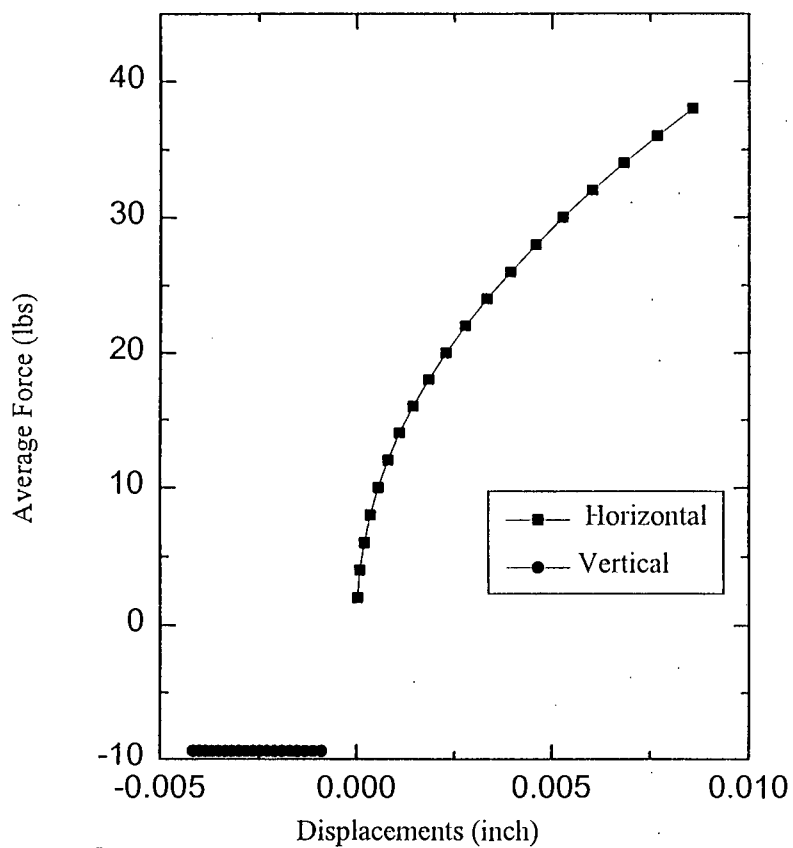
Figure 5-29(a): Average Force vs Displacement variation inside of Goodman
Type Interface for Case-3
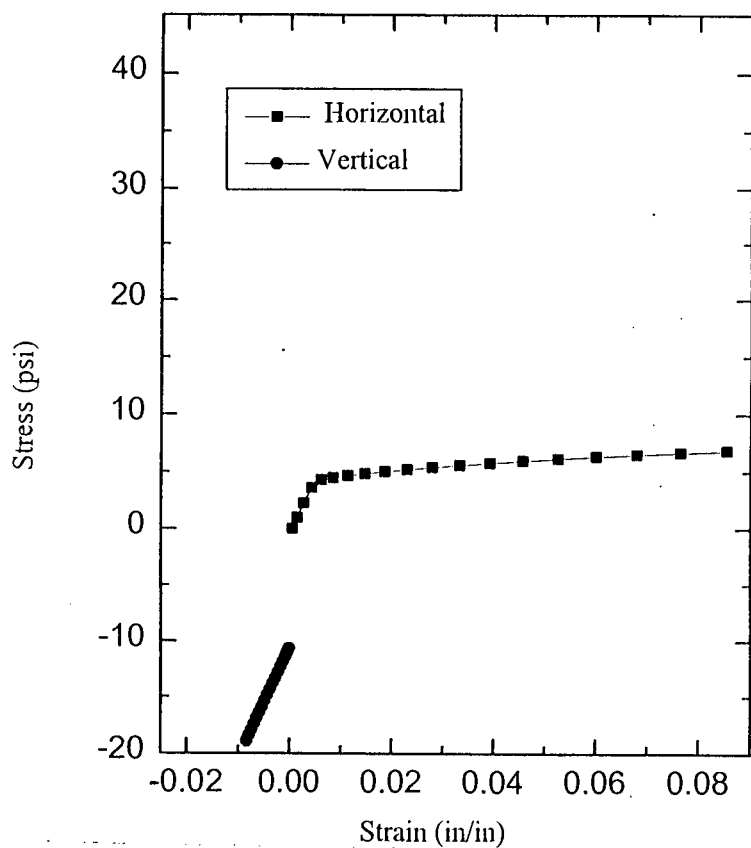
Figure 5-29(b): Stress vs Strain variation inside of Goodman Type Interface for
Case-3.
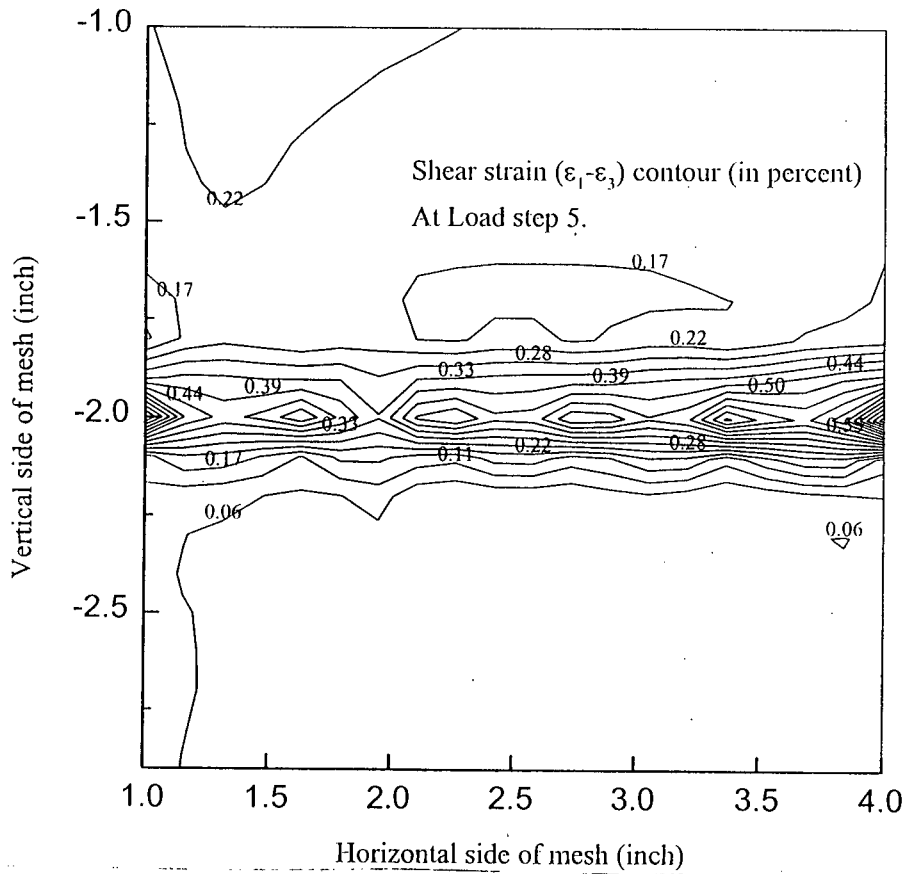
Figure 5-30(a): Shear strain contour for Case-3 of Goodman Type Interface at load step-5.
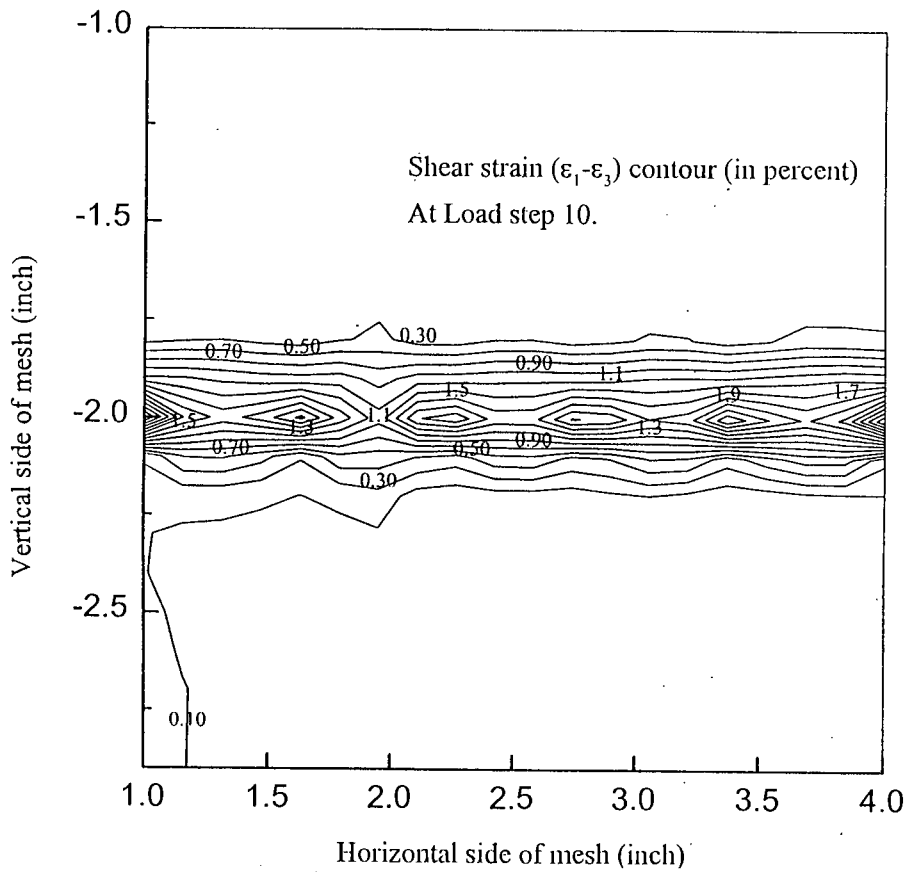
Figure 5-30(b): Shear strain contour for Case-3 of Goodman Type Interface at load step-10.
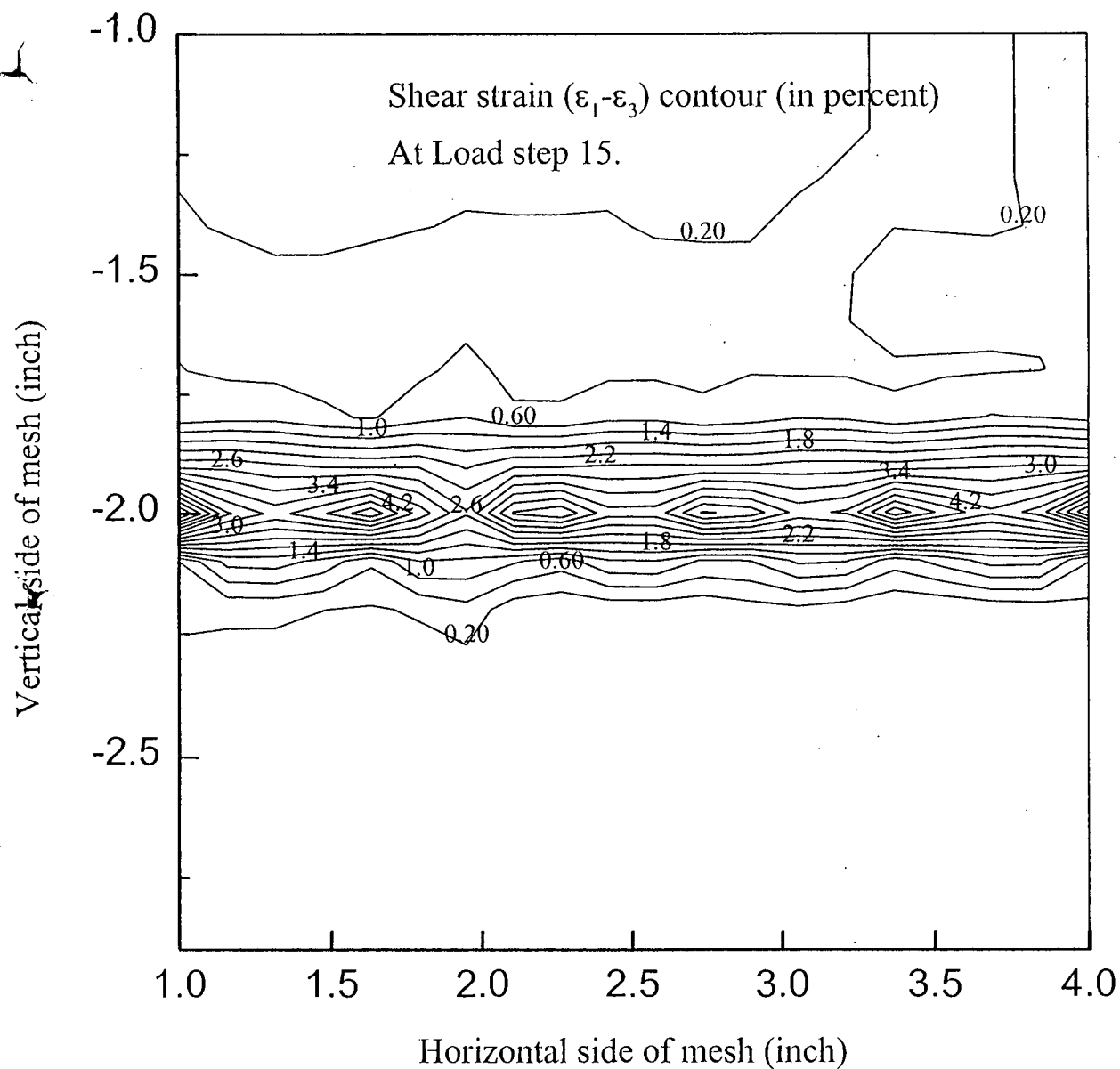
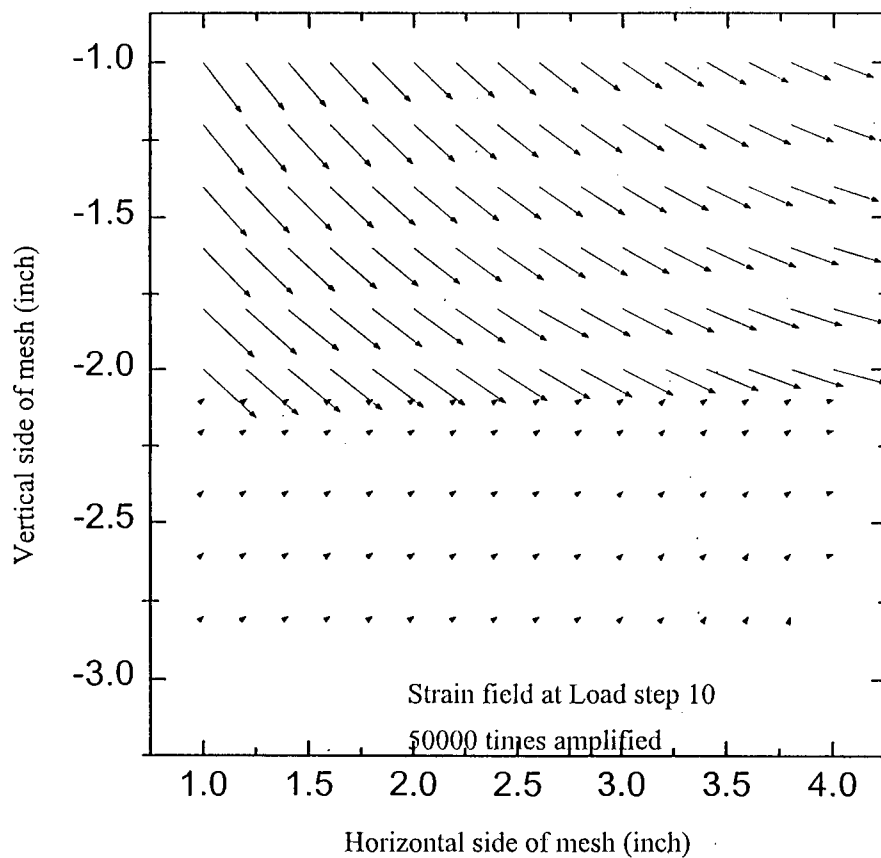Figure 5-30(c):   Shear strain contour for Case-3 of Goodman Type Interface at load step-15.

171
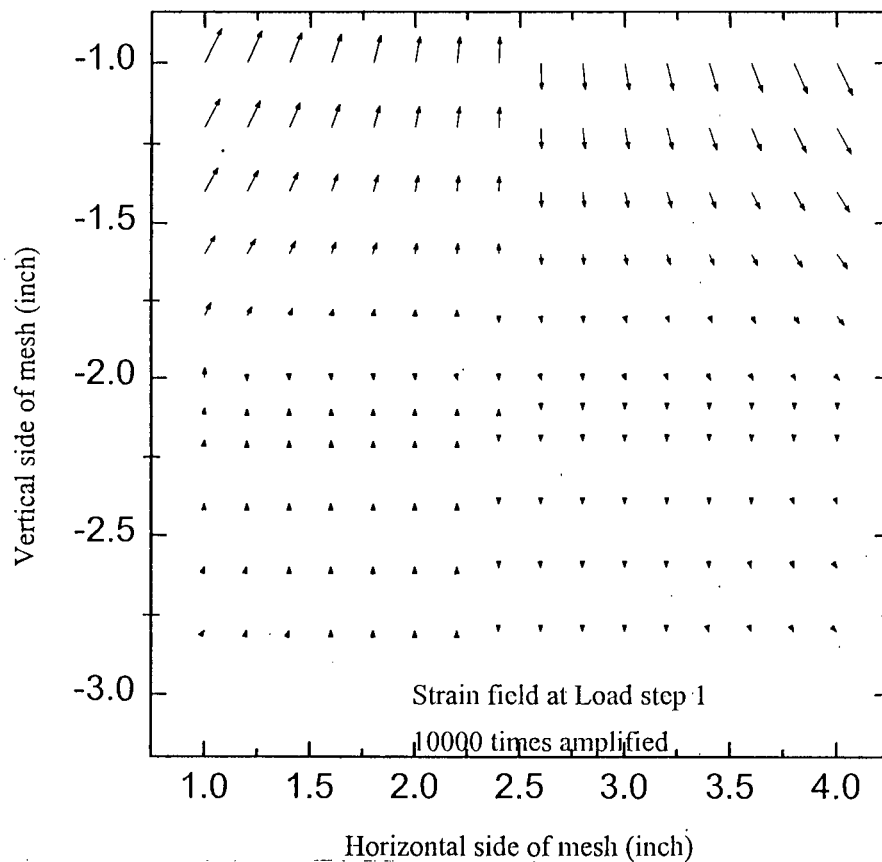
Figure 5-31(a): Displacement field for Case-3 of Goodman Type Interface at load step-1.
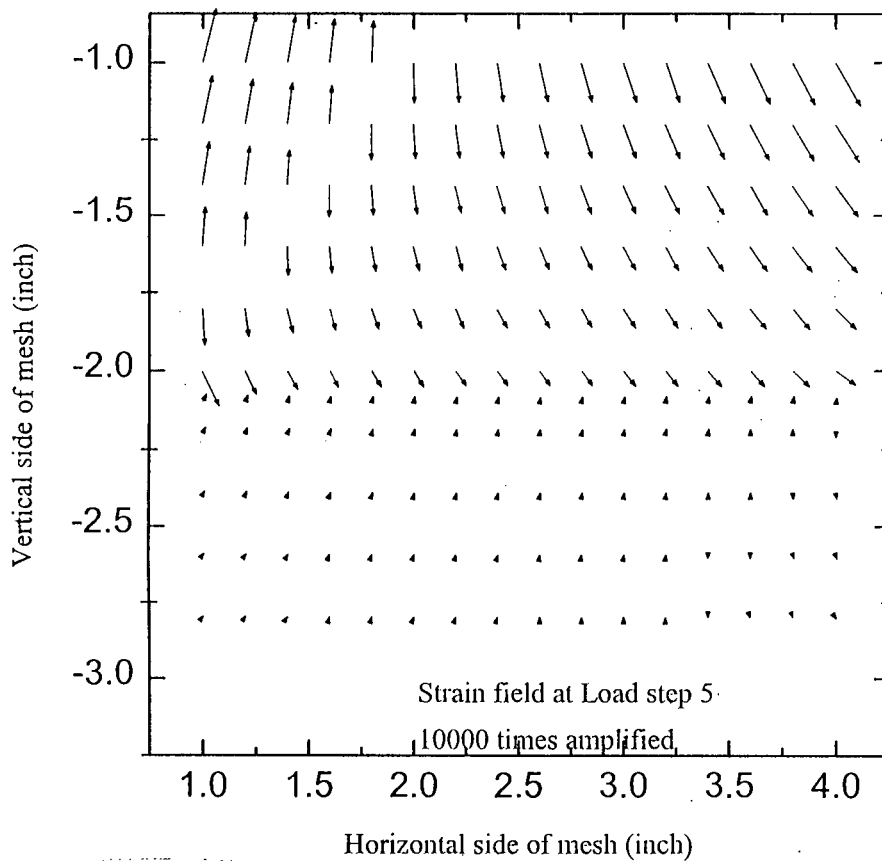
Figure 5-31(b): Displacement field for Case-3 of Goodman Type Interface at load step-5.
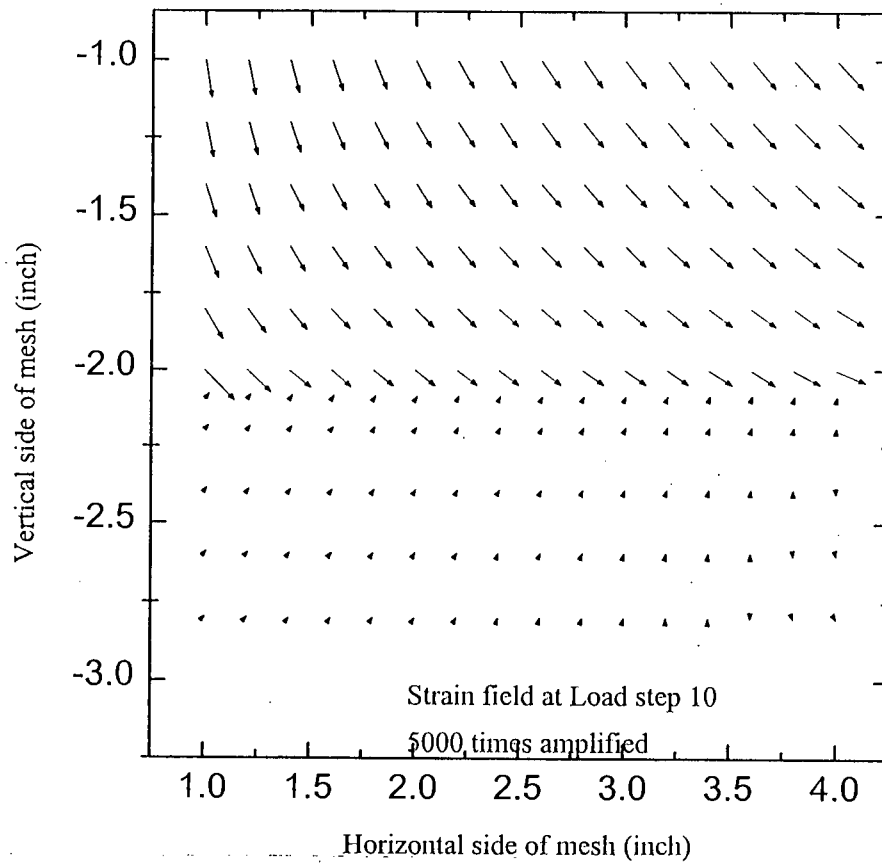
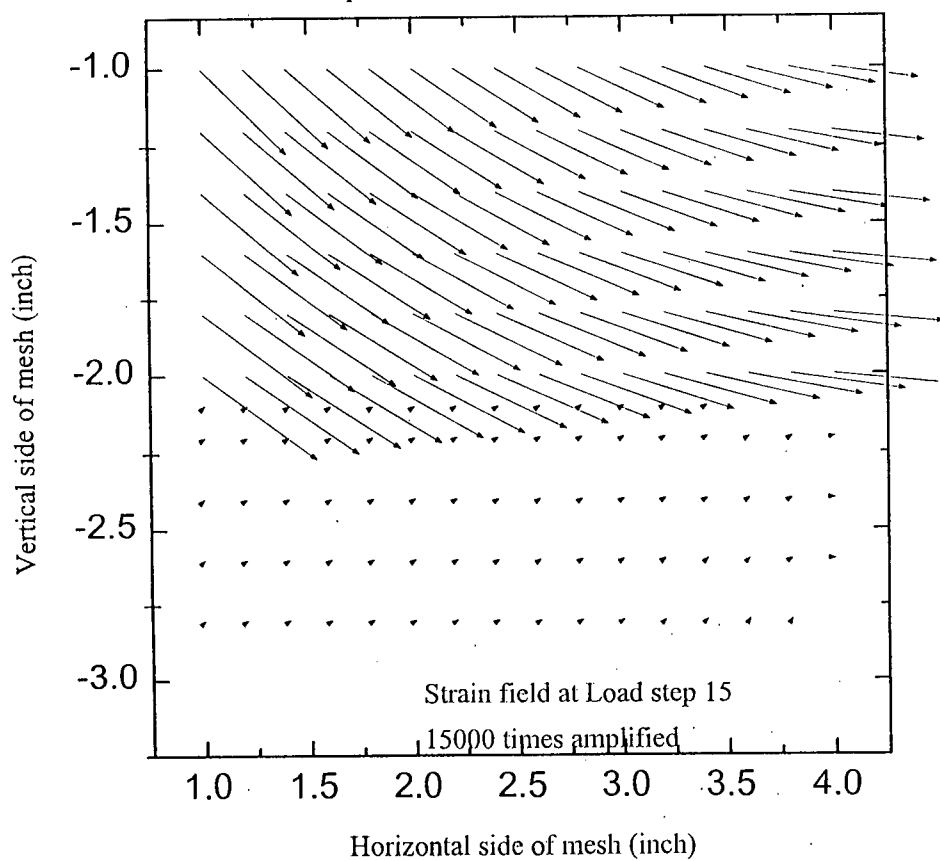Figure 5-31(c): Displacement field for Case-3 of Goodman Type Interface at load step-10.
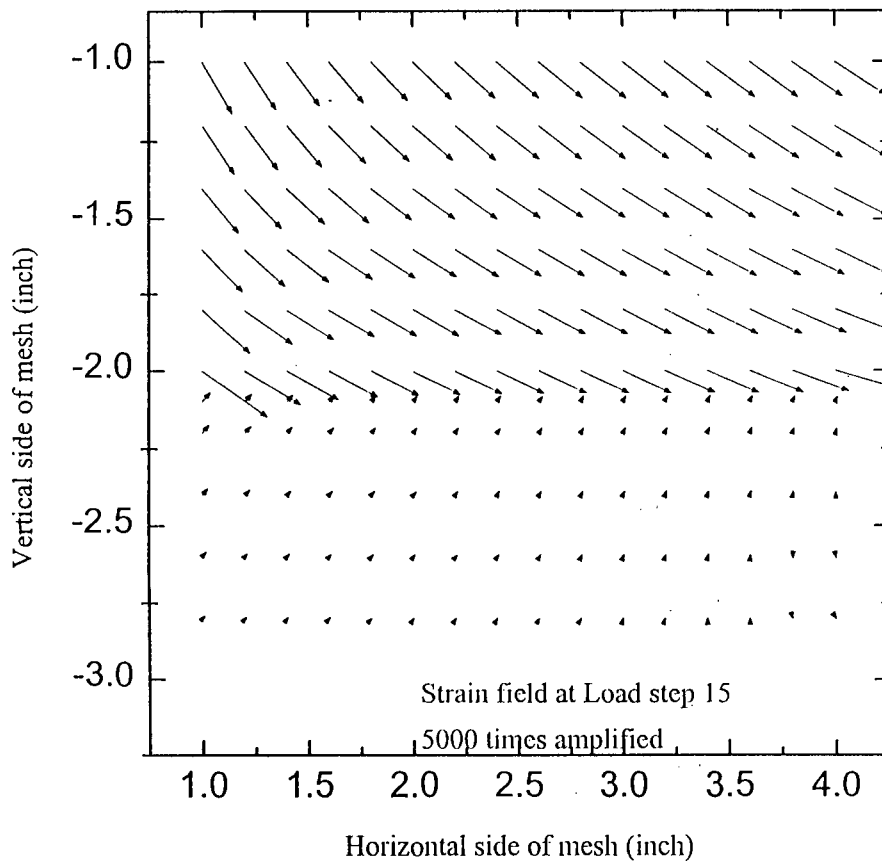
Figure 5-31(d): Displacement field for Case-3 of Goodman Type Interface at load step-15.
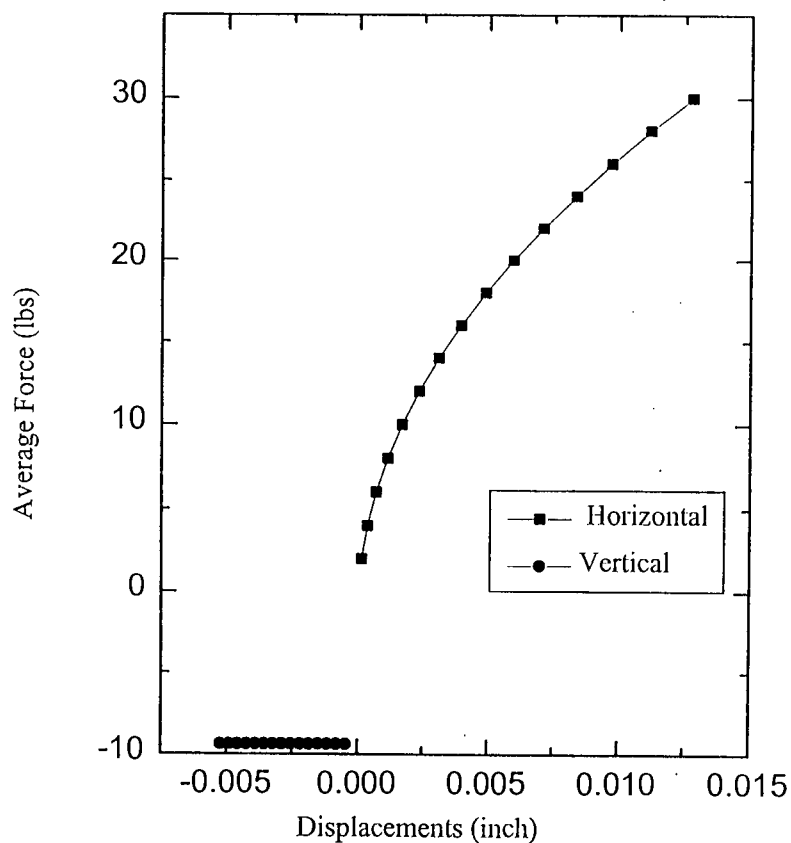
173
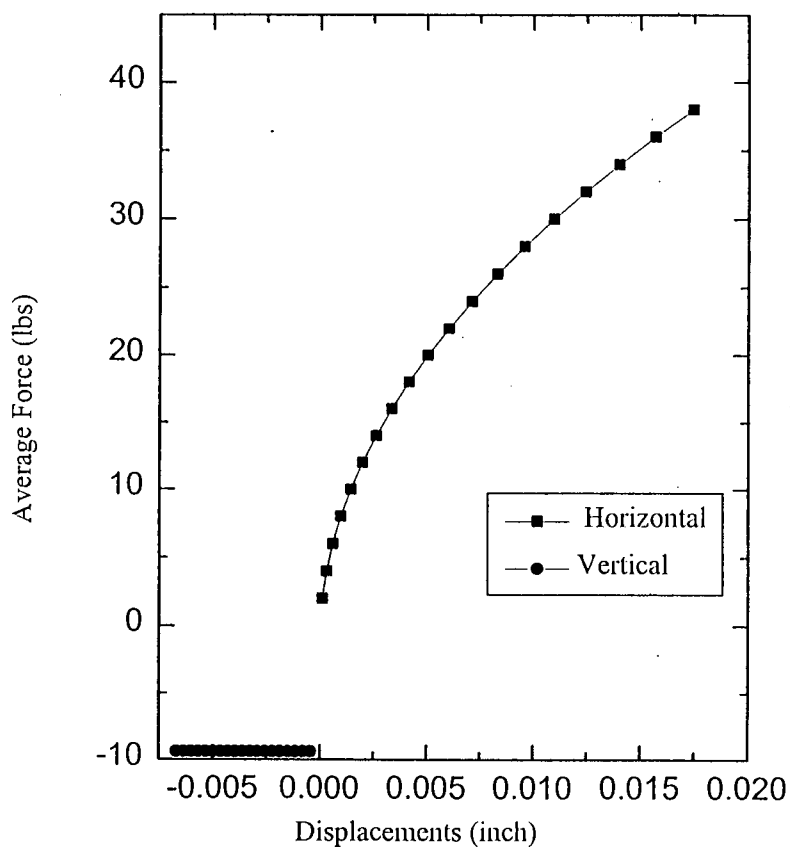
Figure 5-32(a): Average Force vs Displacement variation inside of Goodman
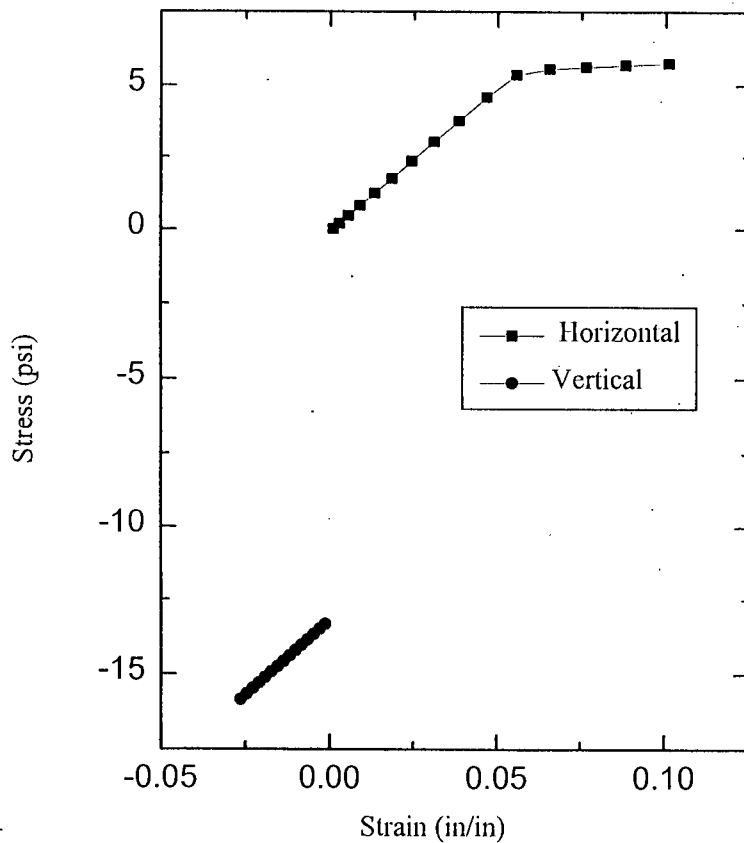Type Interface for Case-4
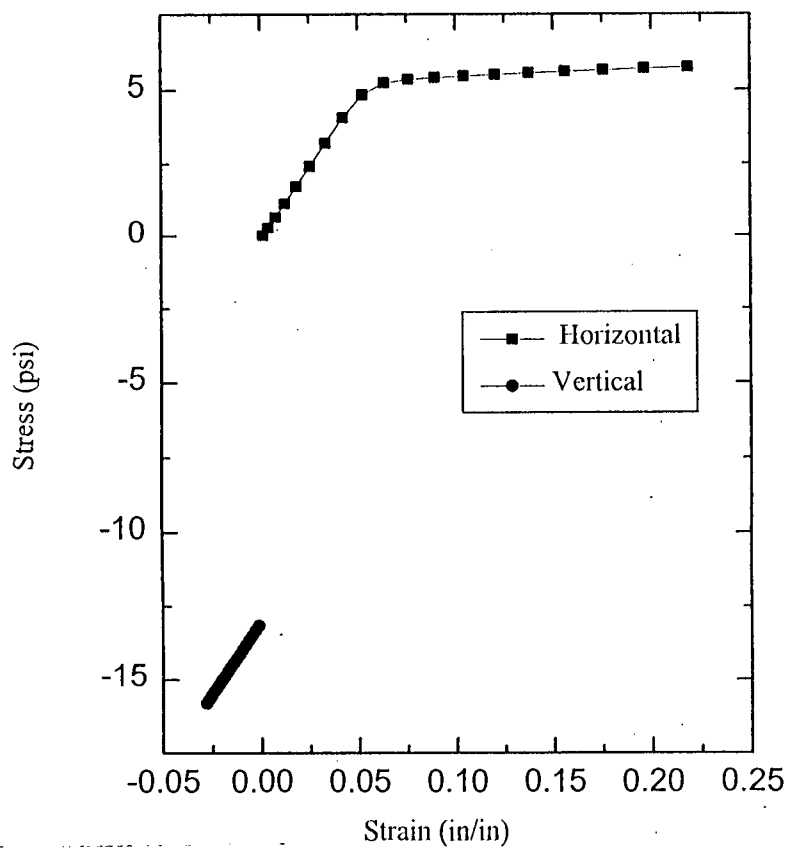
Figure 5-32(b): Stress vs Strain variation inside of Goodman Type Interface for
Case-4.
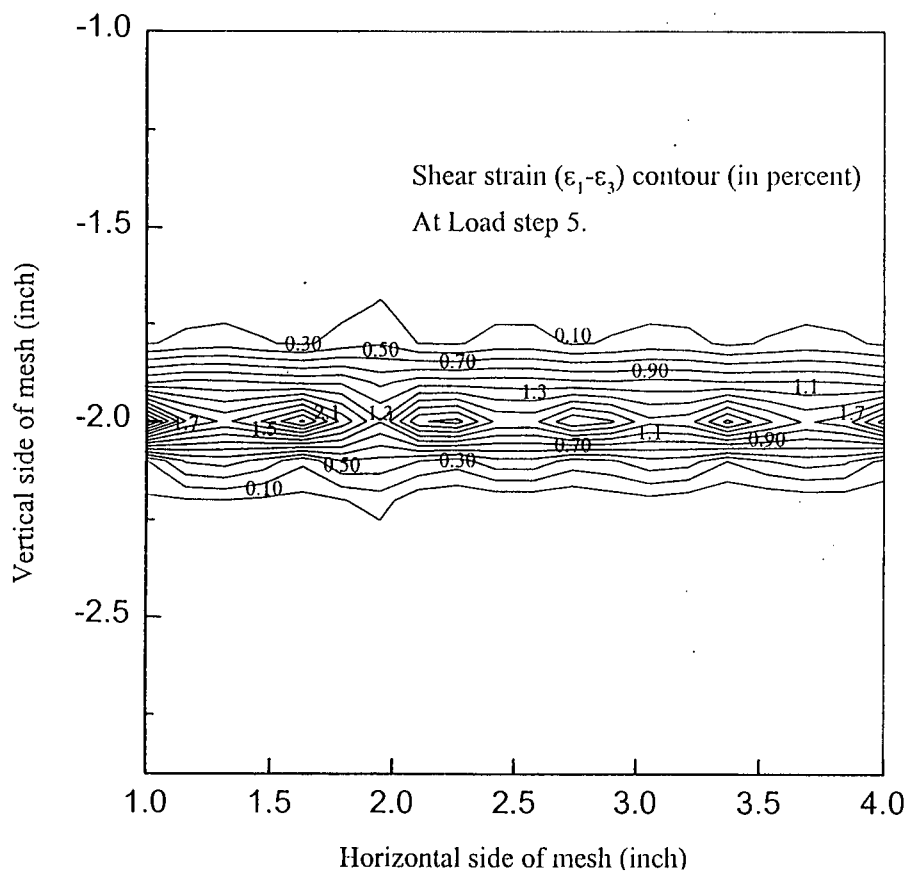
Figure 5-33(a): Shear strain contour for Case-4 of Goodman Type Interface at load step-5.
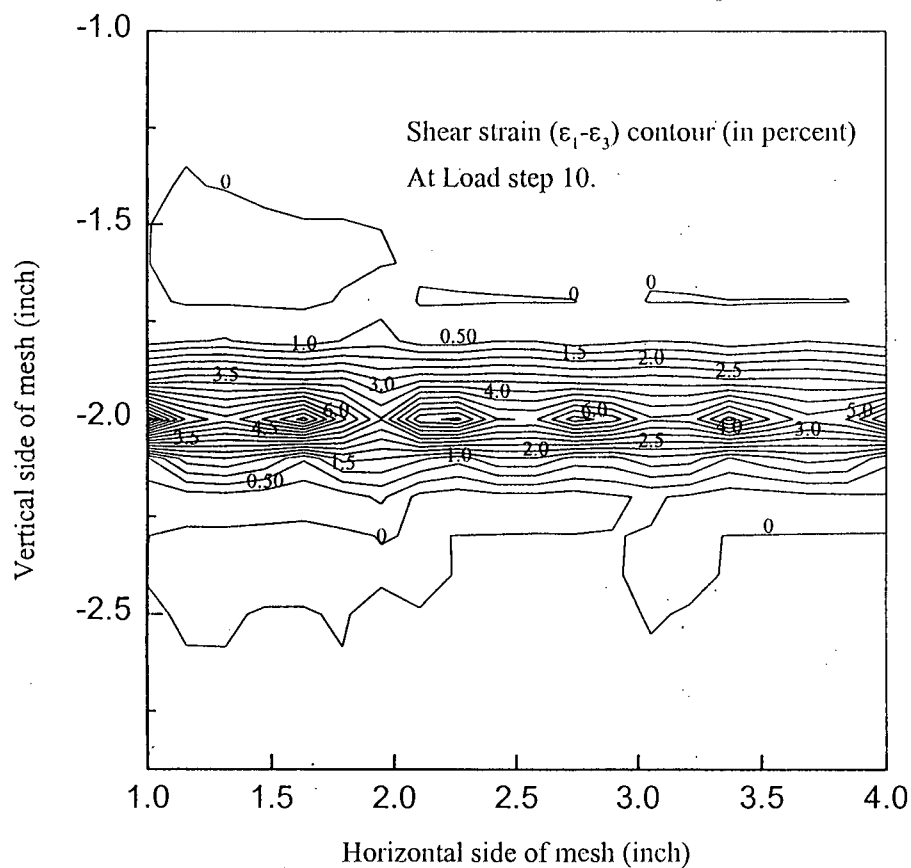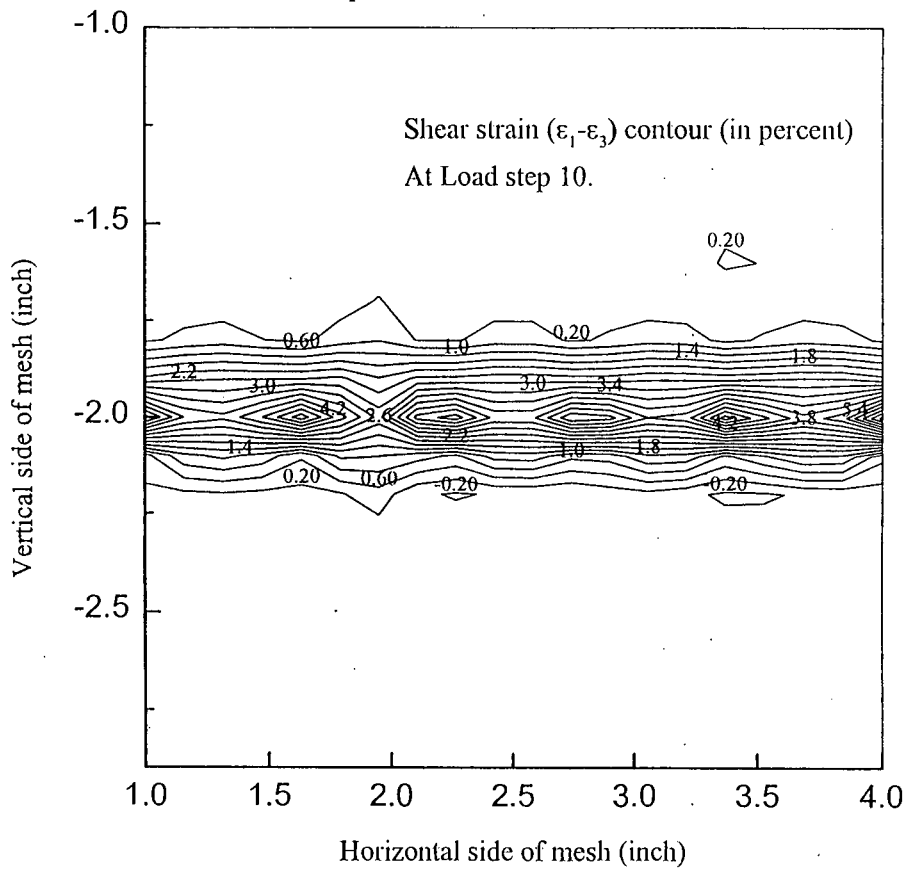

Figure 5-33(b): Shear strain contour for Case-4 of Goodman Type Interface at load step-10.
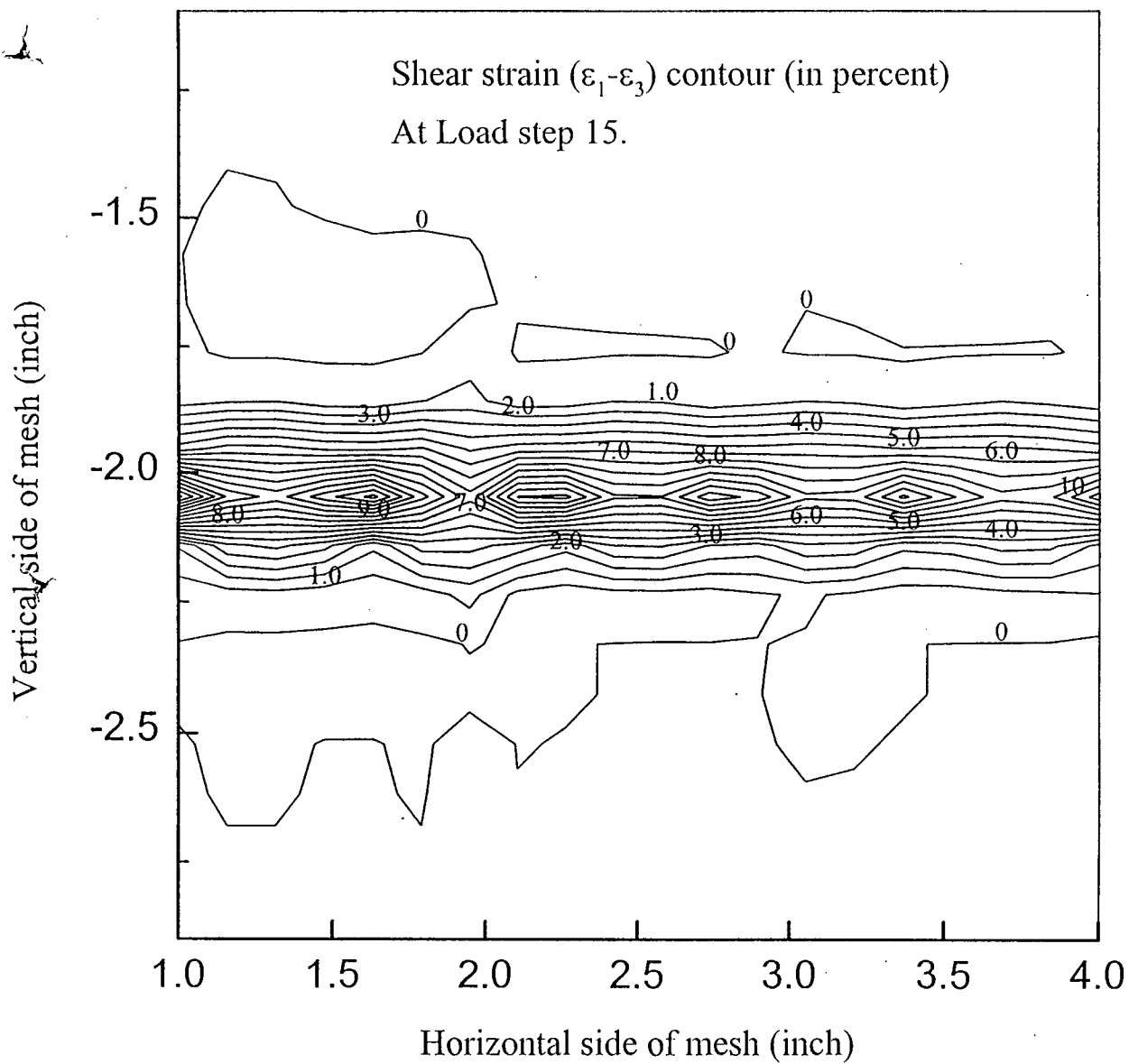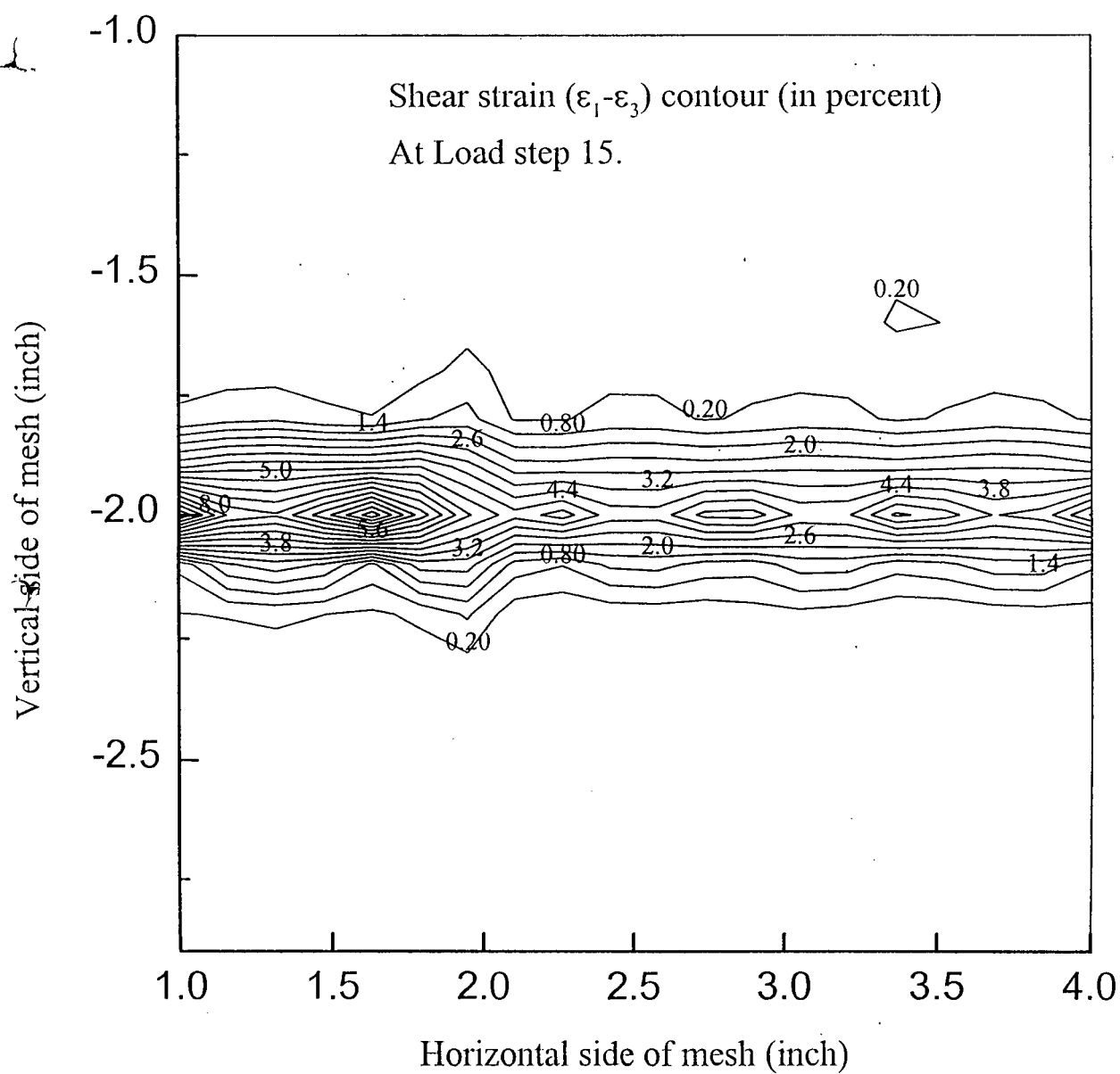
Figure 5-33(c): Shear strain contour for Case-4 of Goodman Type Interface at load step-15.
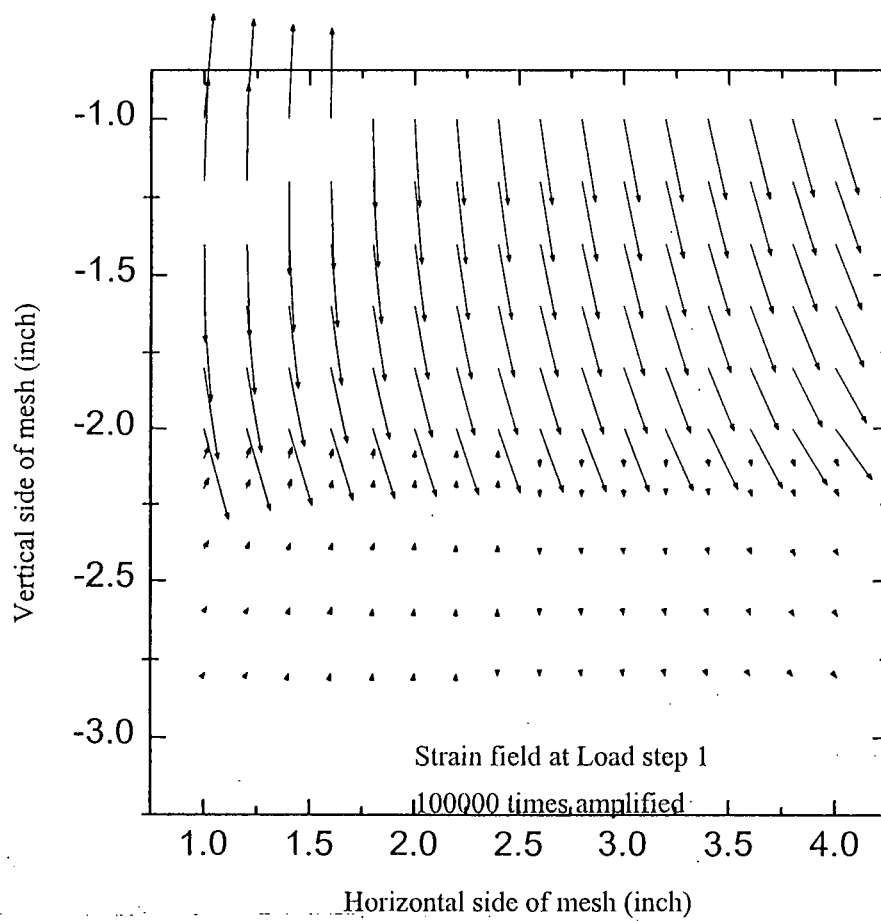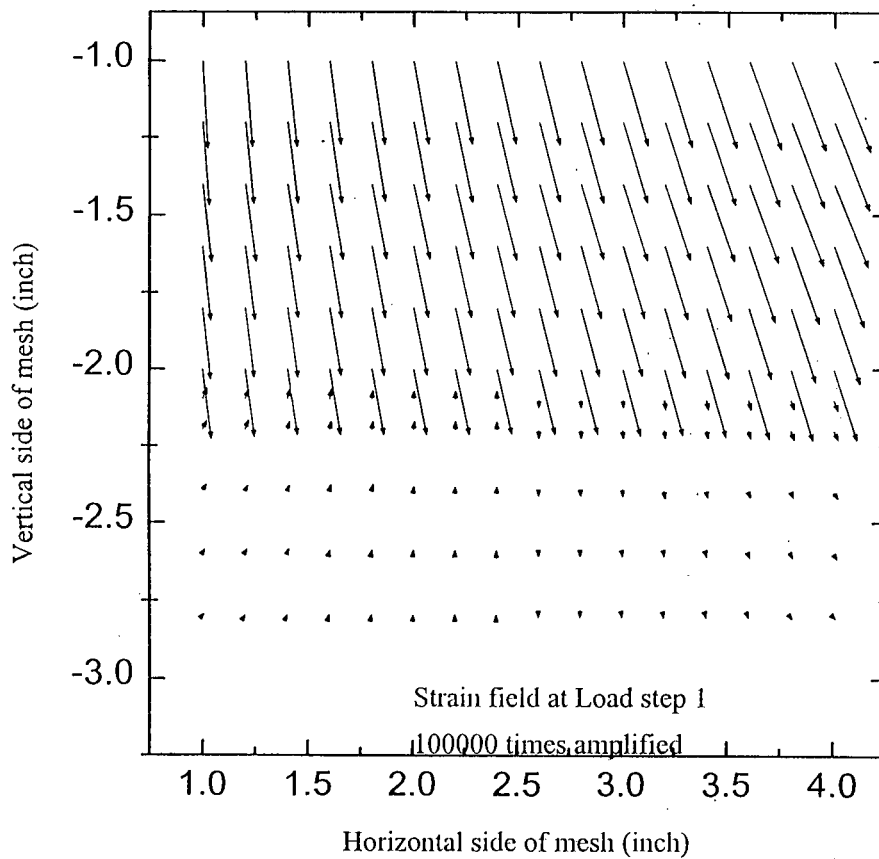
Figure 5-34(a): Displacement field for Case-4 of Goodman Type Interface at load step-1.
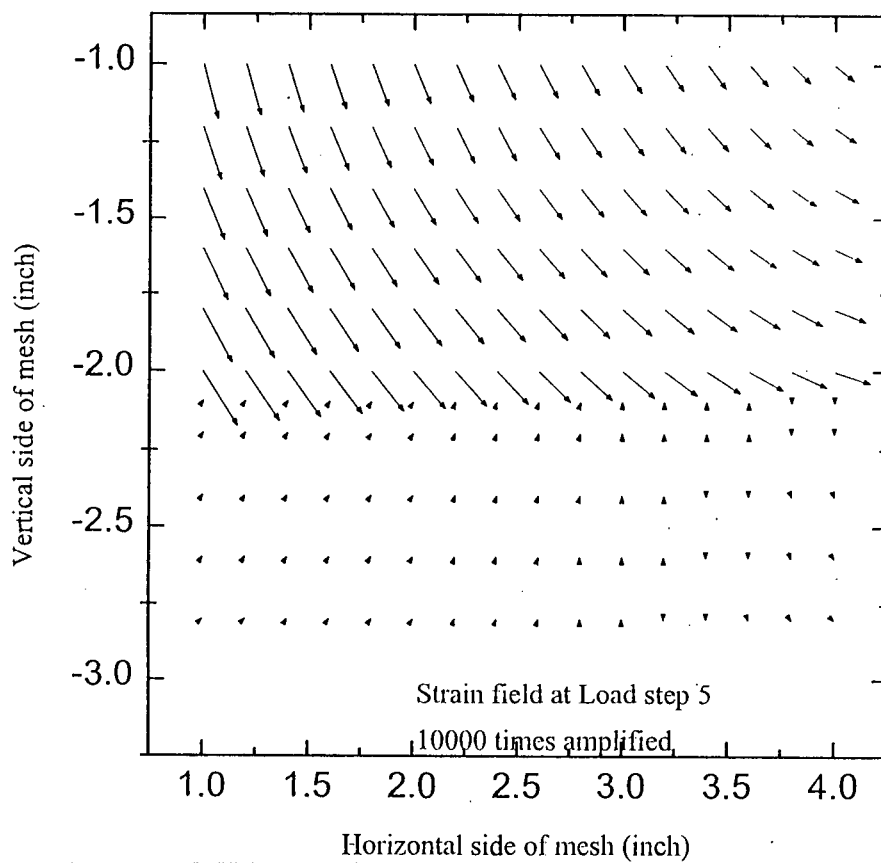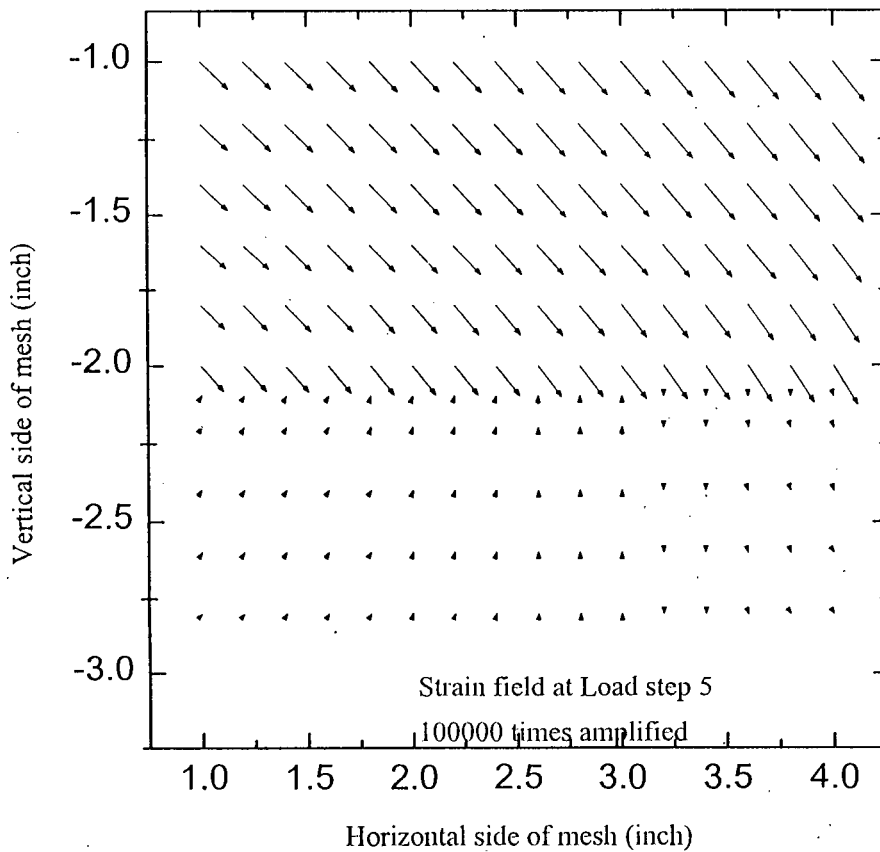

Figure 5-34(b): Displacement field for Case-4 of Goodman Type Interface at load step-5.

177
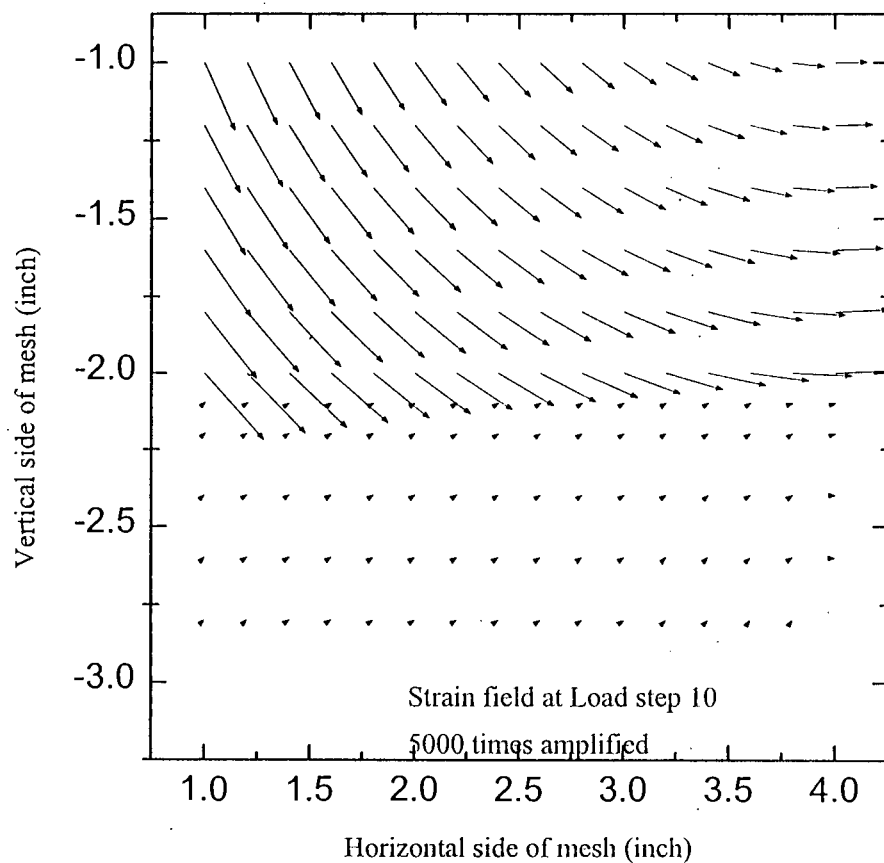
Figure 5-34(c):   Displacement field for Case-4 of Goodman Type Interface at
load step-10.
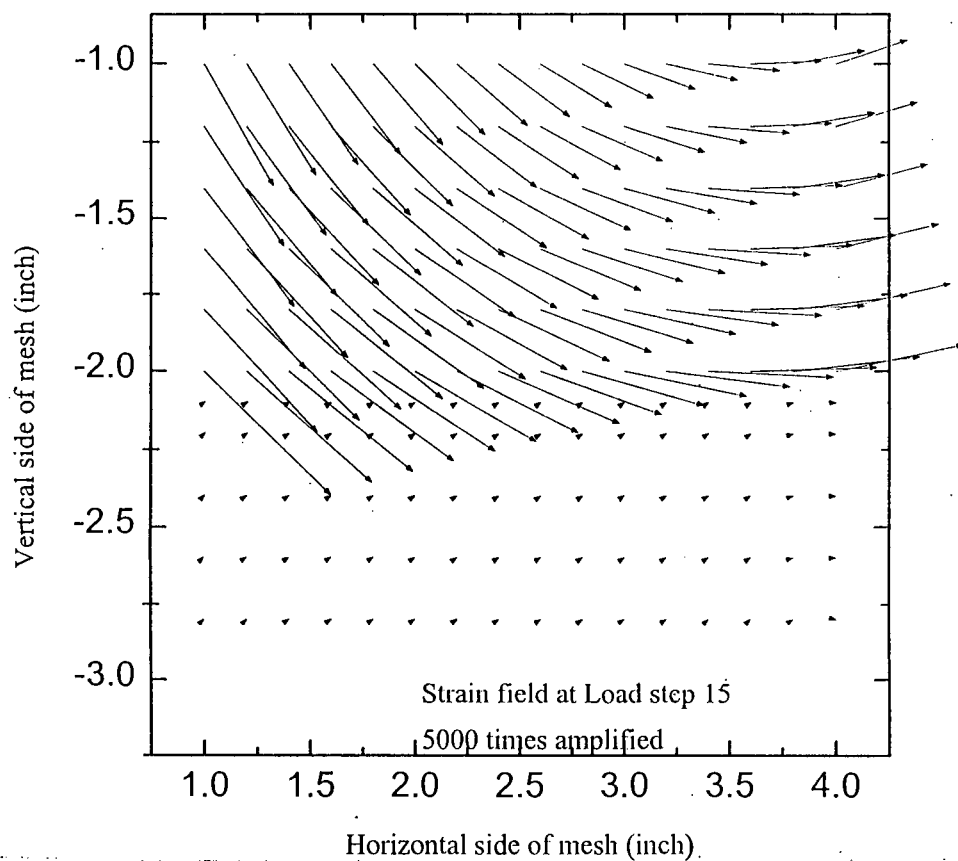
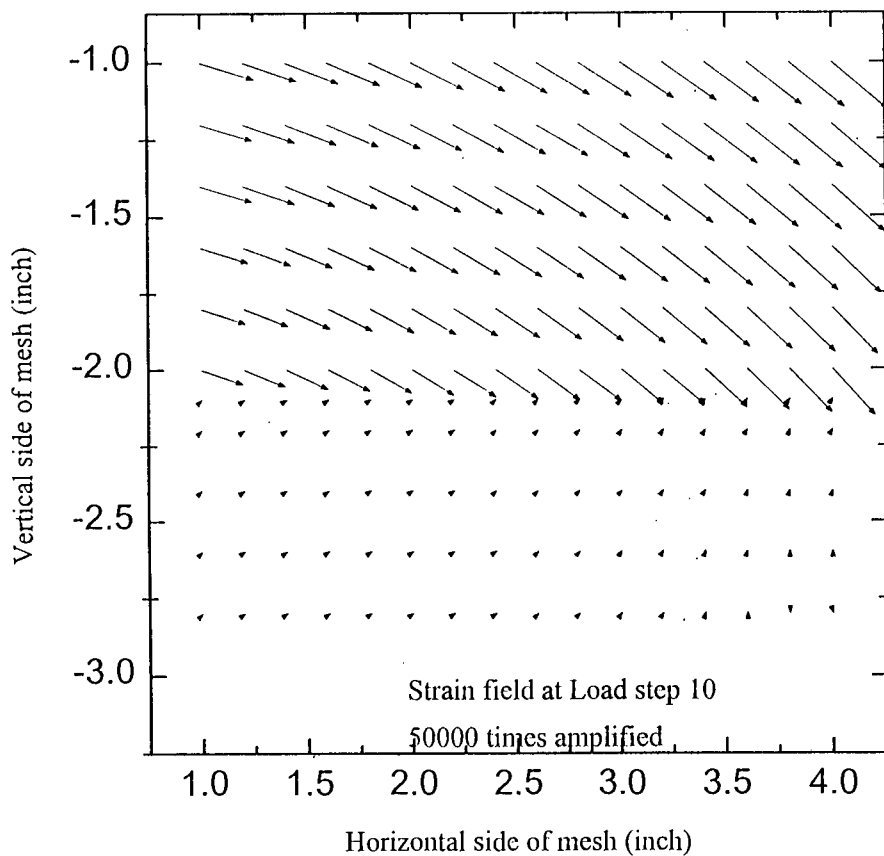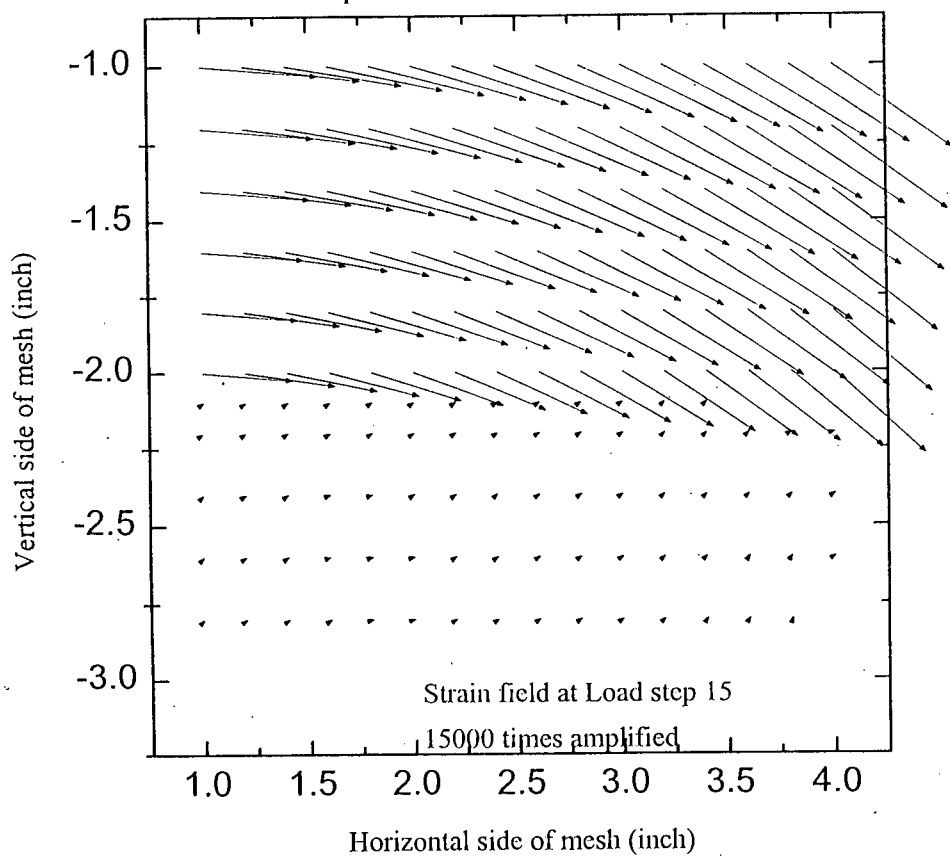Figure 5-34(d):   Displacement field for Case-4 of Goodman Type Interface at
load step-15.
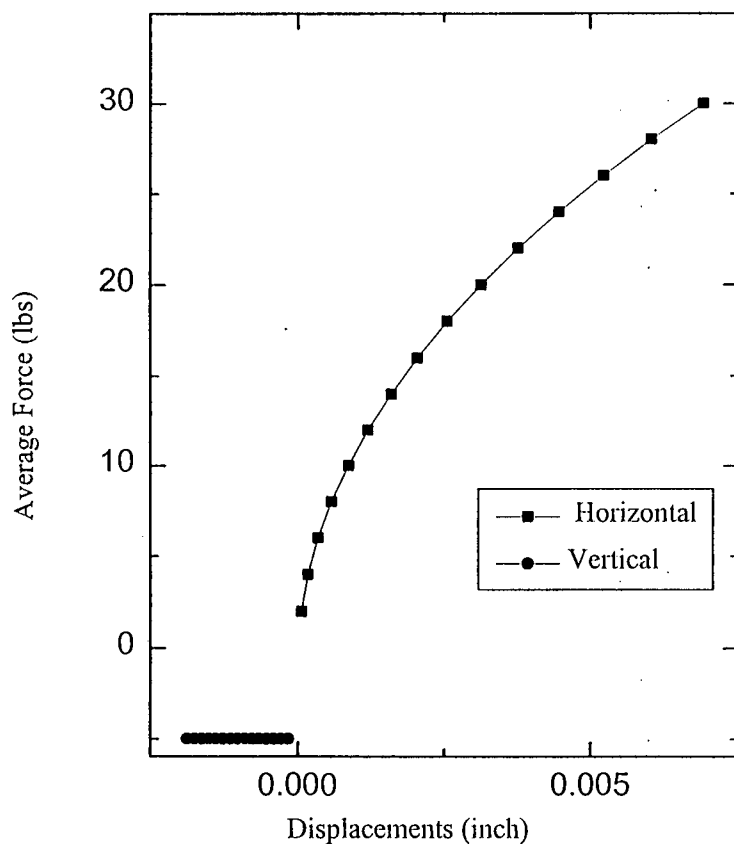
Figure 5-35(a): Average Force vs Displacement variation inside of Goodman Type Interface for Case-5
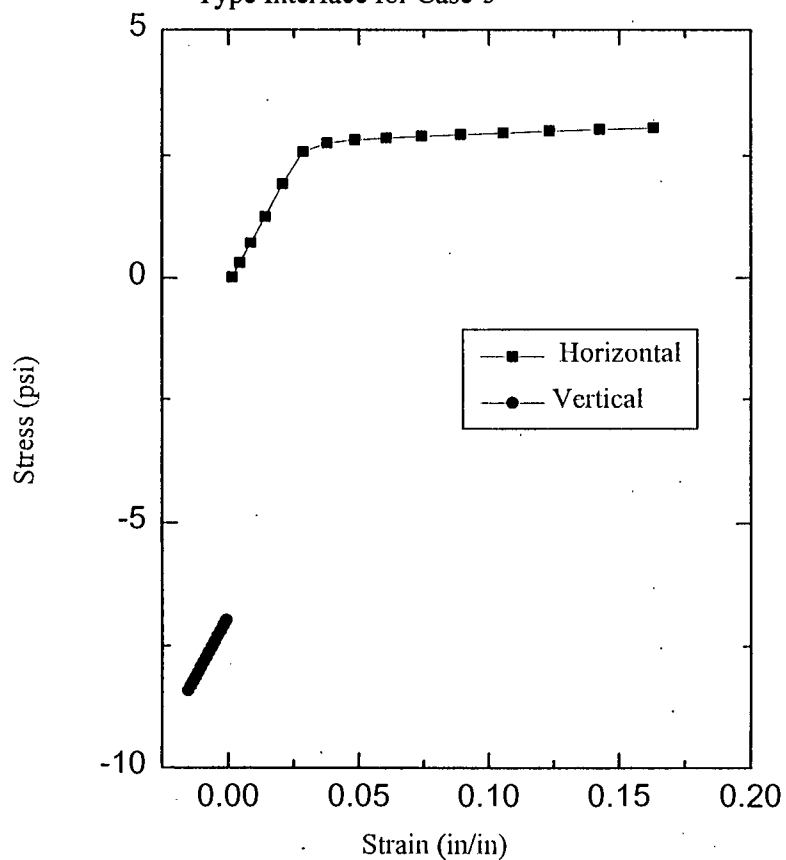
Figure 5-35(b): Stress vs Strain variation inside of Goodman Type Interface for Case-5.

179
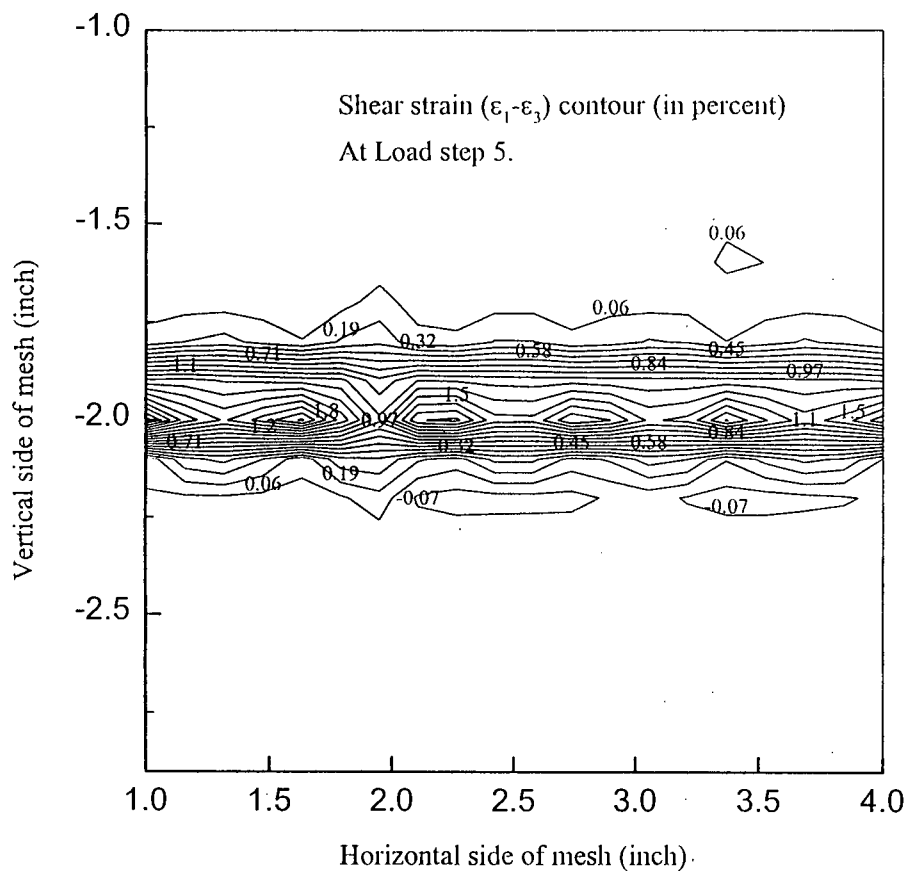
Figure 5-36(a): Shear strain contour for Case-5 of Goodman Type Interface at load step-5.
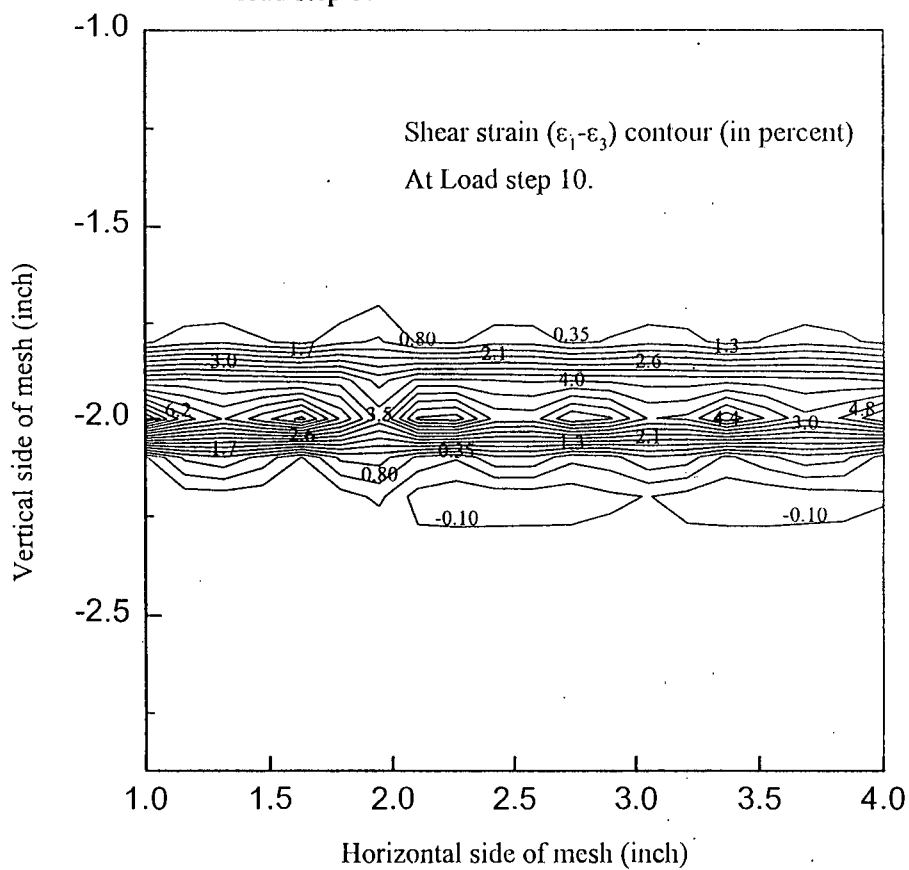
Figure 5-36(b): Shear strain contour for Case-5 of Goodman Type Interface at load step-10.
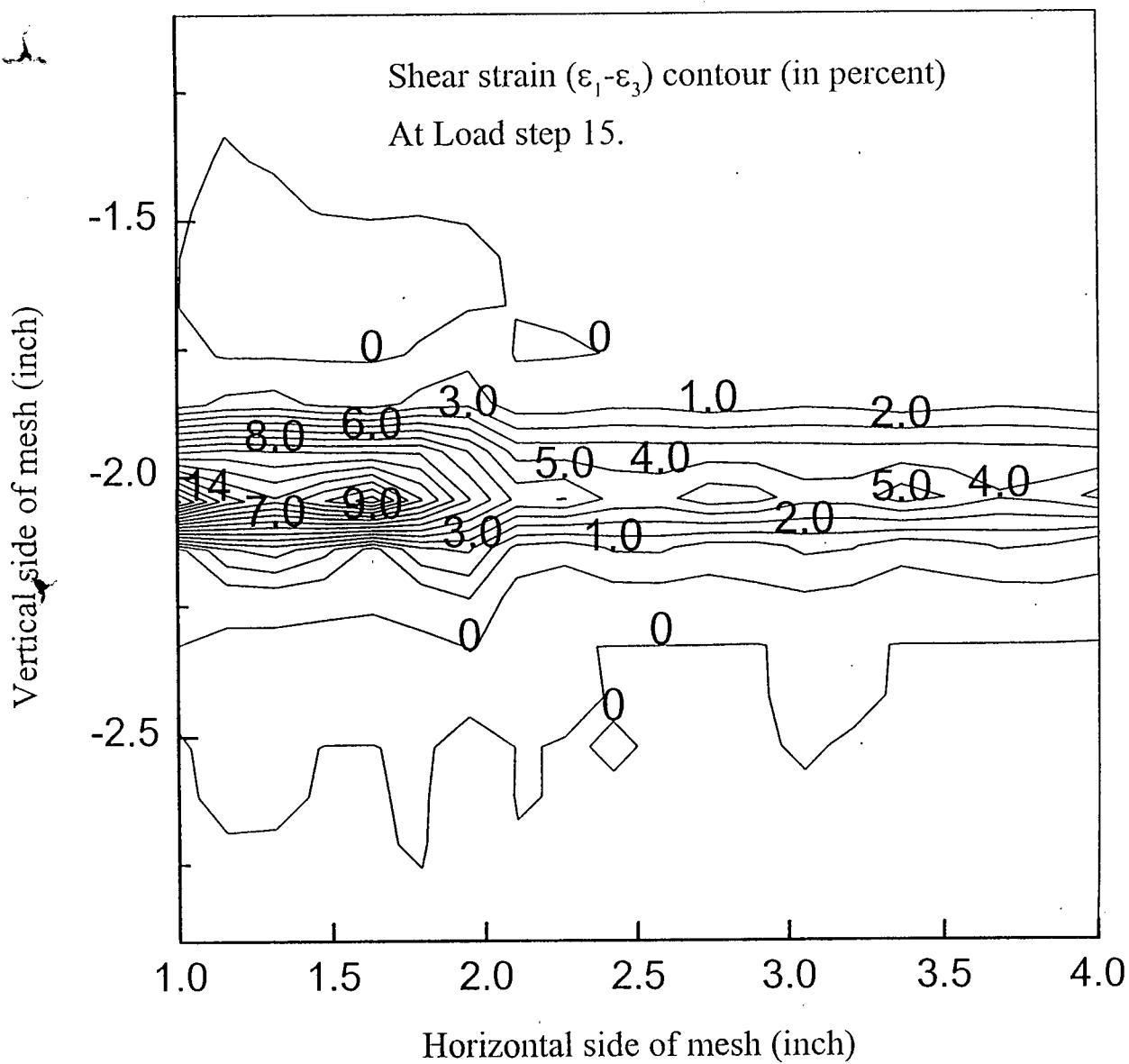
Figure 5-36(c):   Shear strain contour for Case-5 of Goodman Type Interface at load step-15.
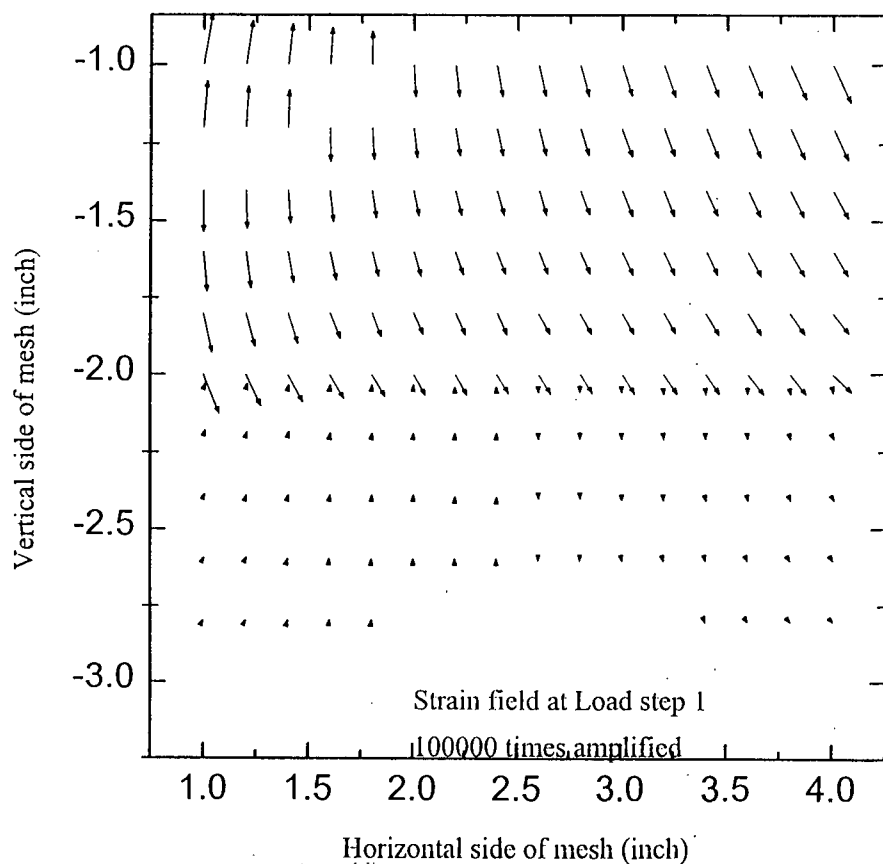
Figure 5-37(a): Displacement field for Case-5 of Goodman Type Interface at load step-1.
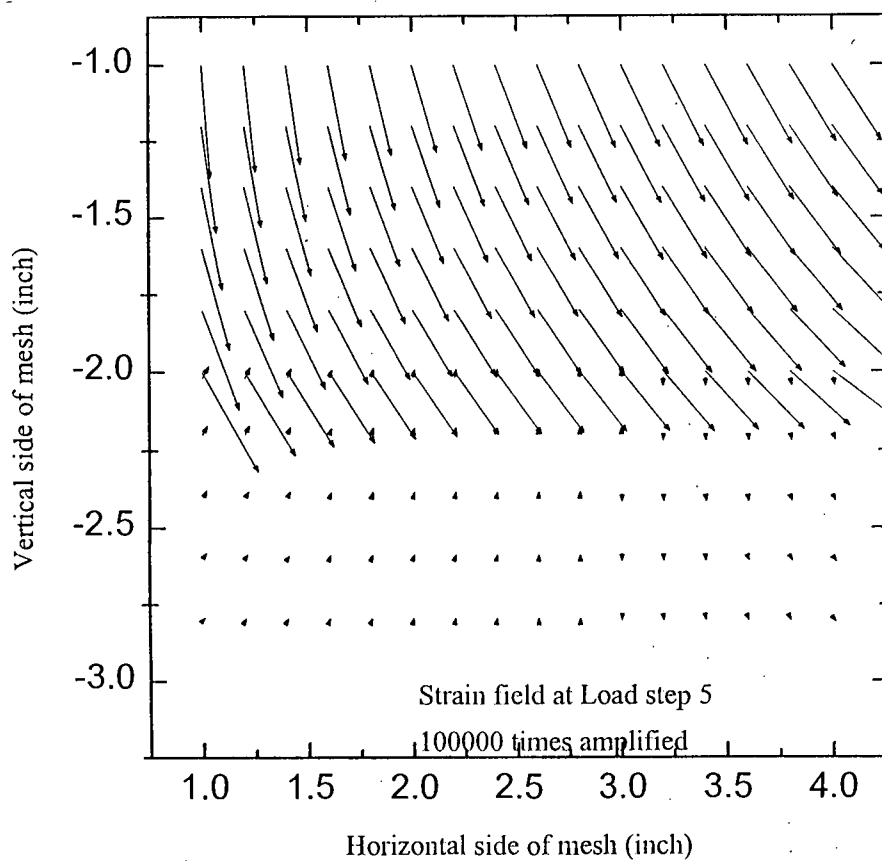
Figure 5-37(b): Displacement field for Case-5 of Goodman Type Interface at load step-5.

182
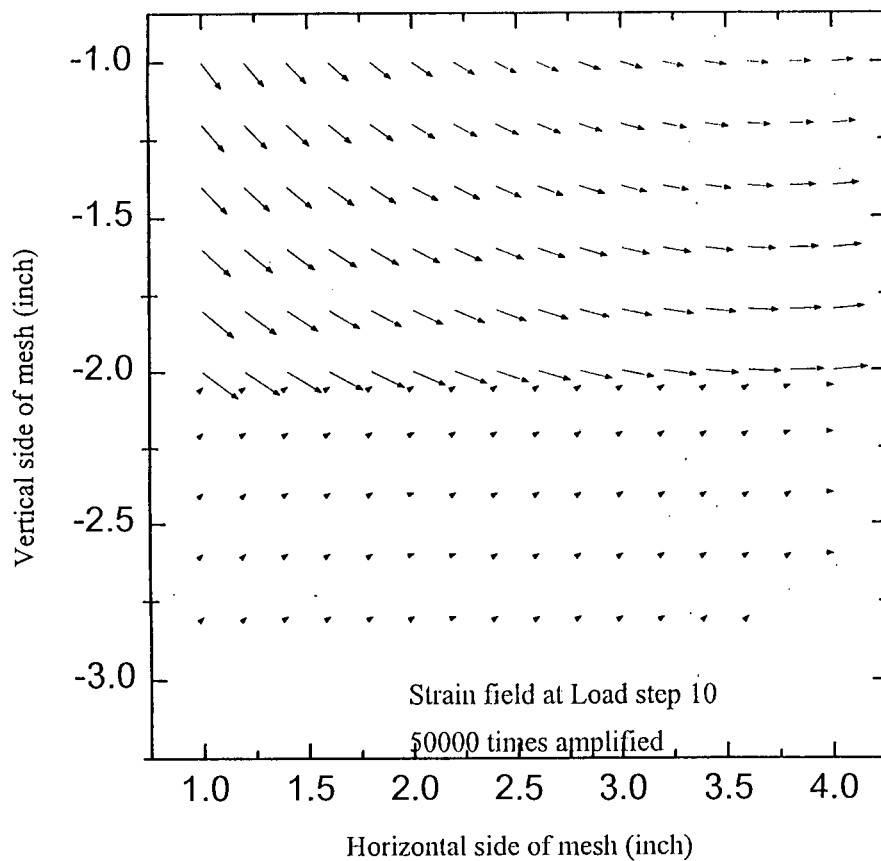
Figure 5-37(c):   Displacement field for Case-5 of Goodman Type Interface at
load step-10.
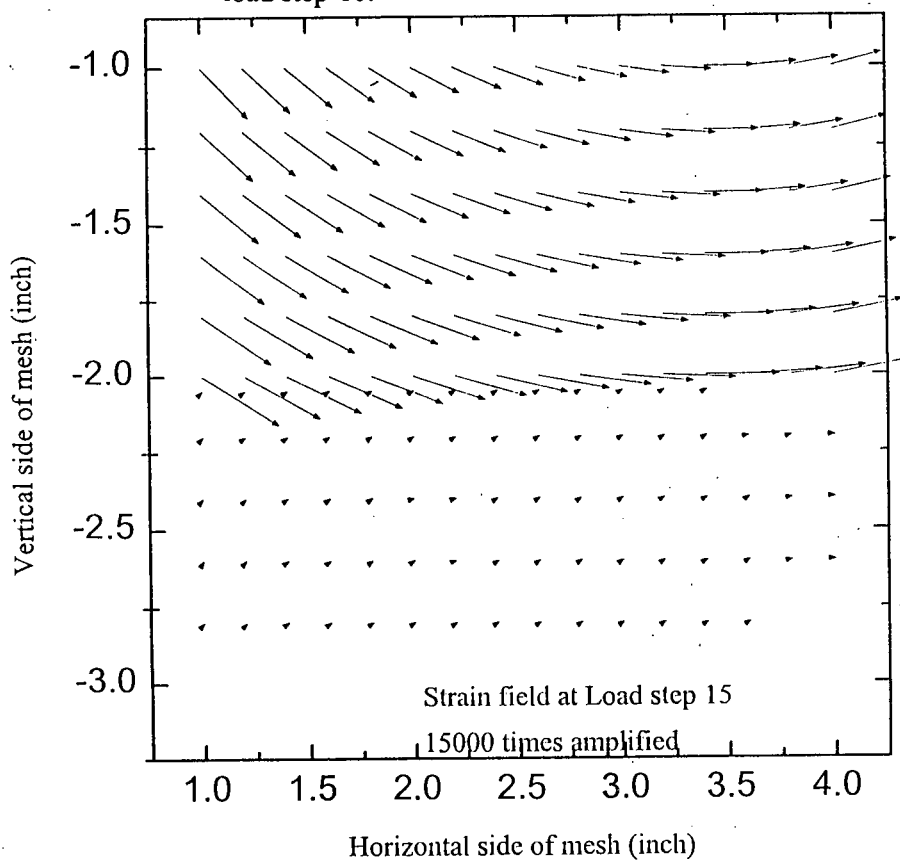
Figure 5-37(d):   Displacement field for Case-5 of Goodman Type Interface at
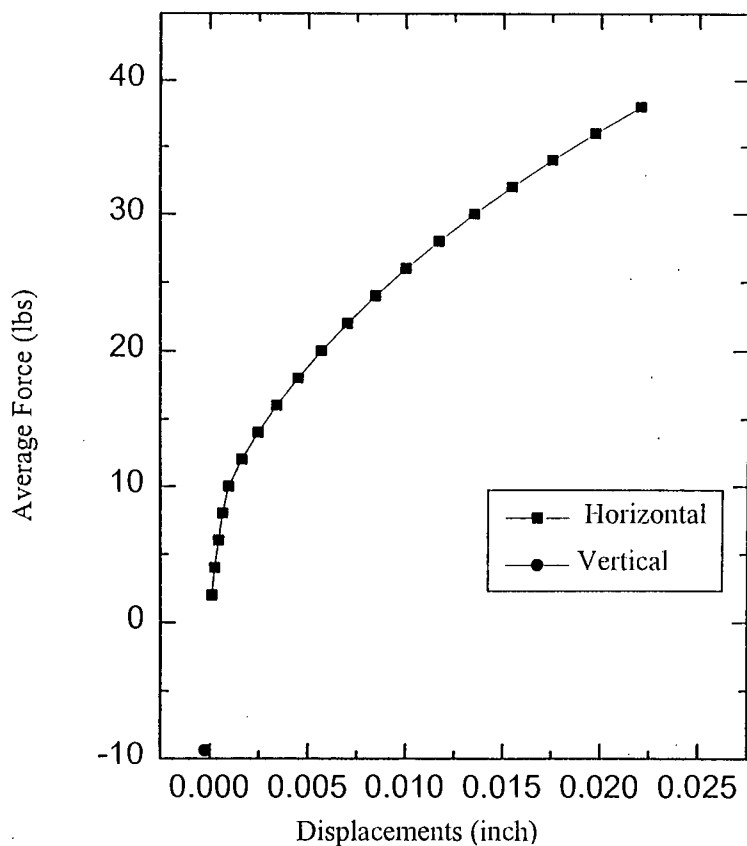load step-15.

183
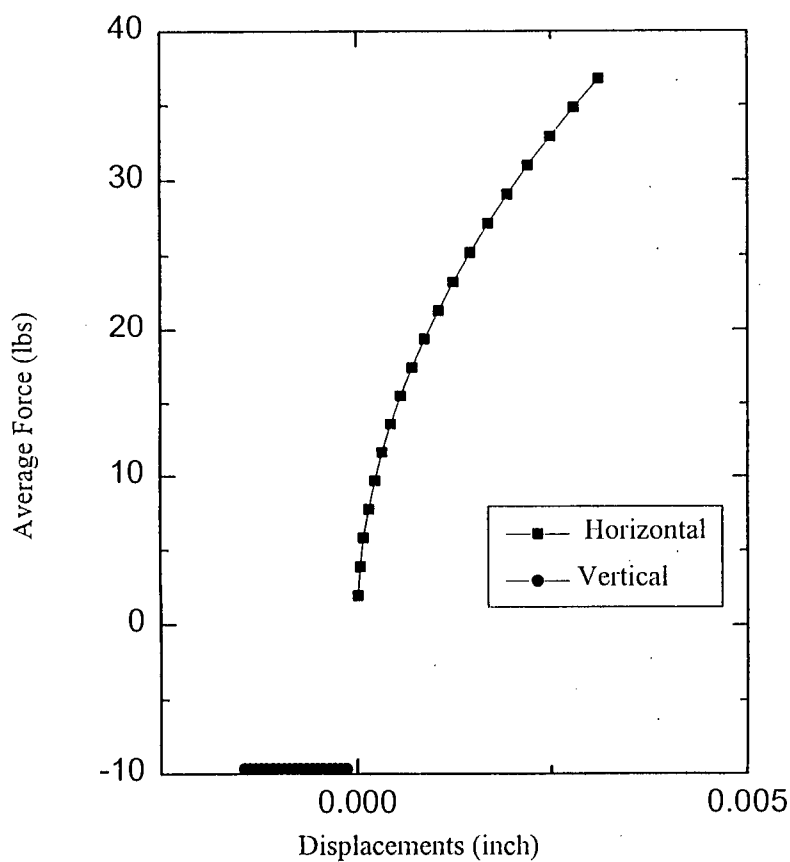
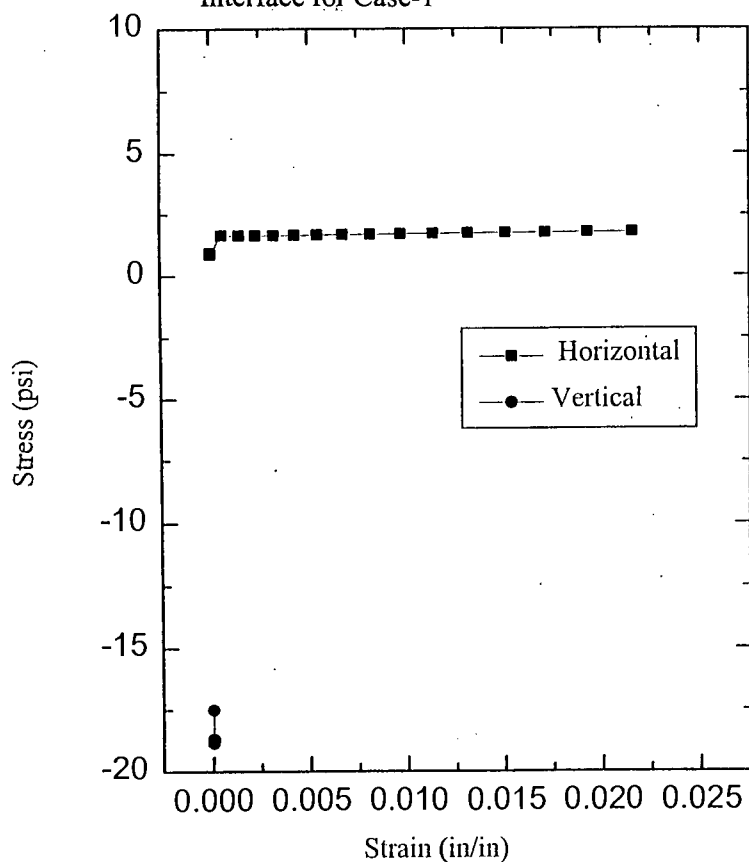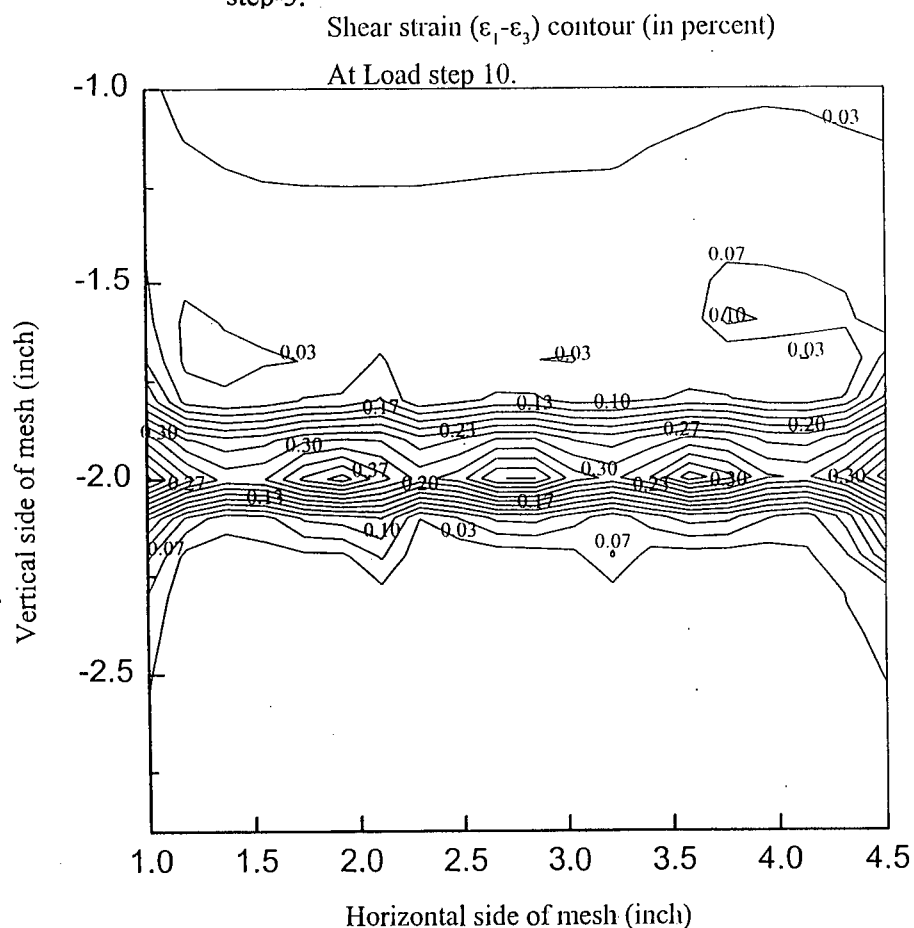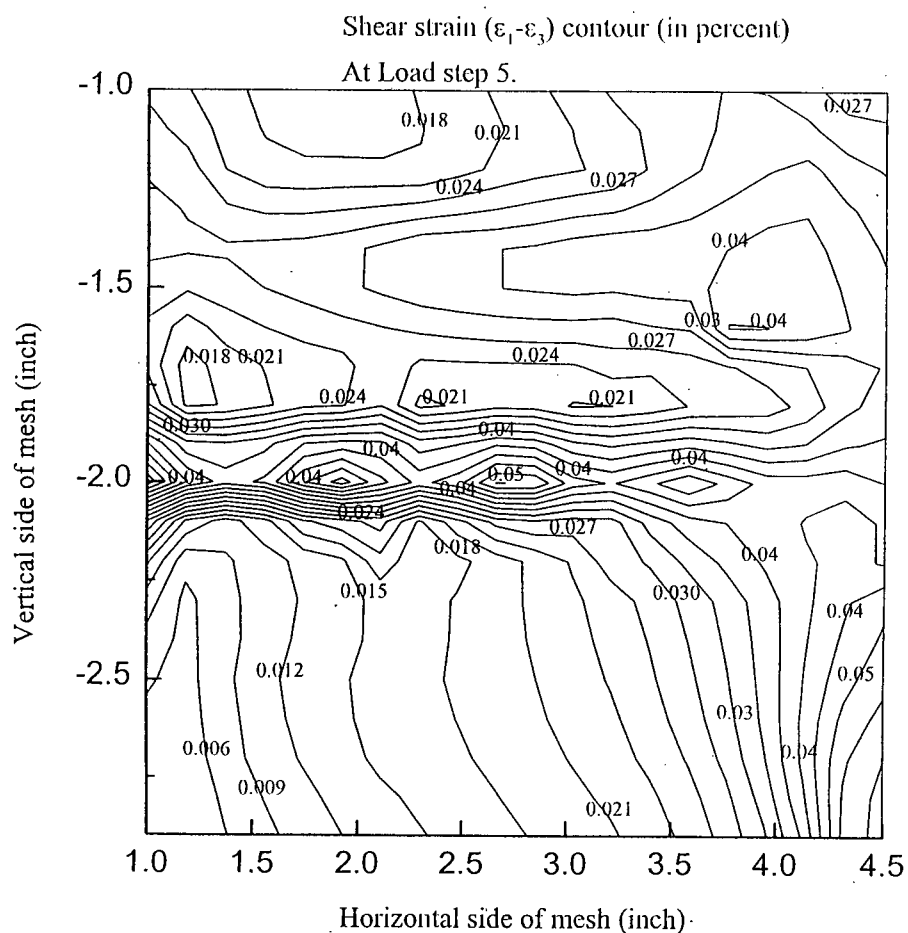Figure 5-38(a): Average Force vs Displacement variation inside of Goodman Type Interface for Case-6

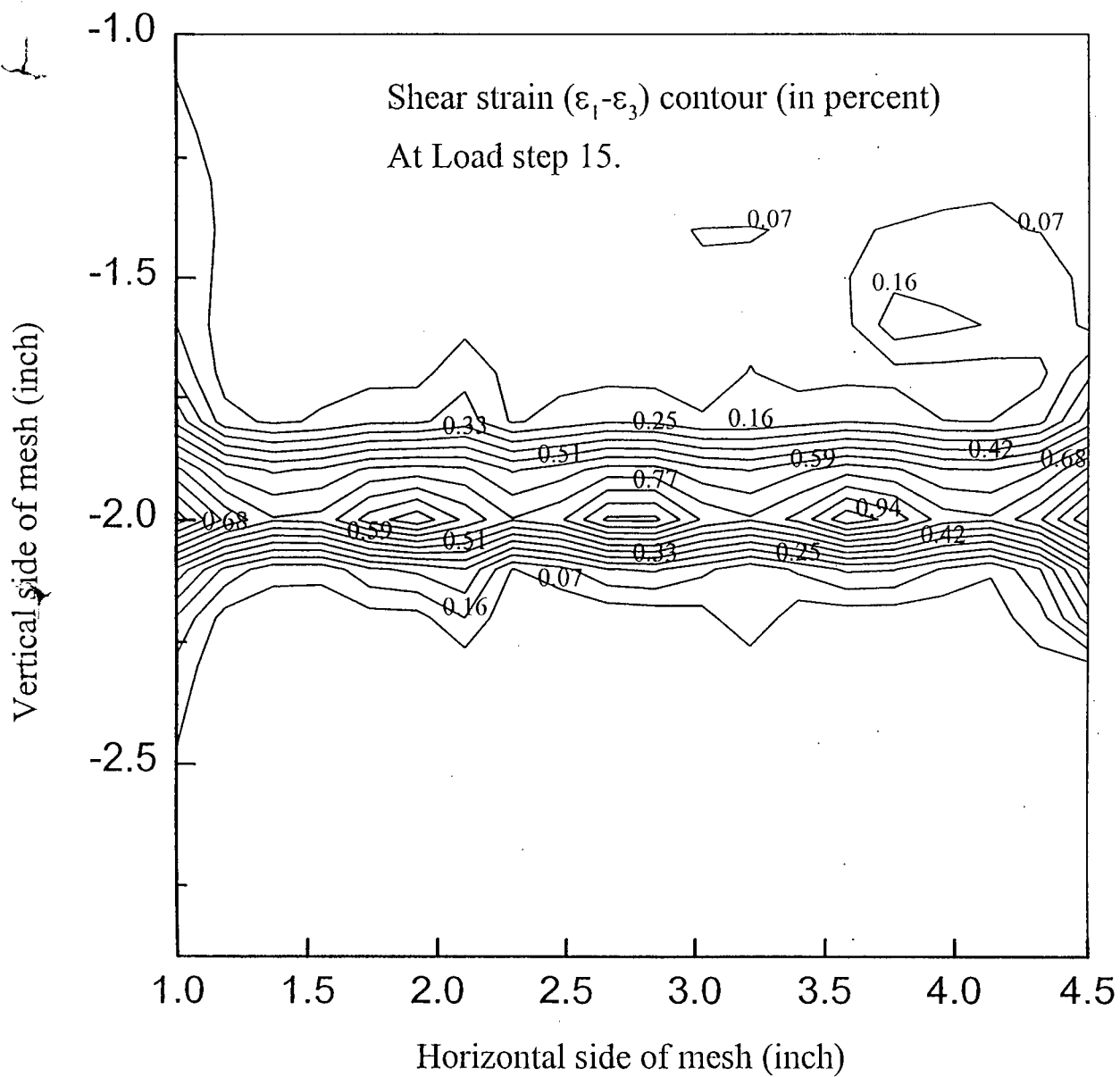Figure 5-38(b): Stress vs Strain variation inside of Goodman Type Interface for Case-6.
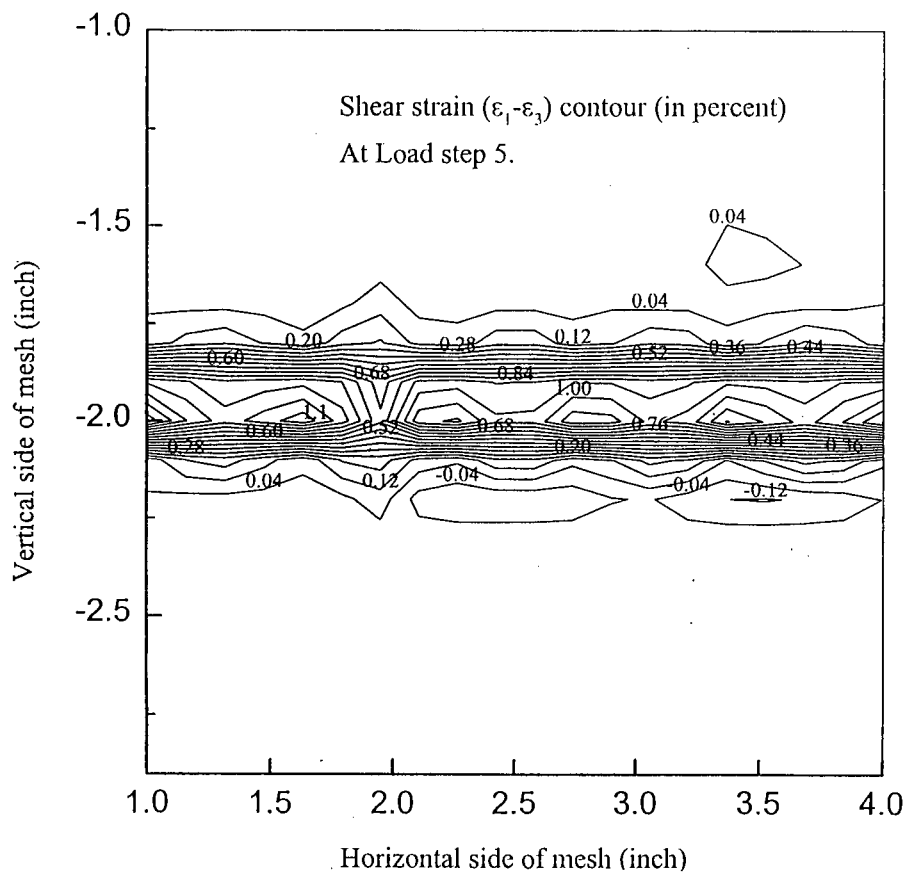
Figure 5-39(a): Shear strain contour for Case-6 of Goodman Type Interface at load step-5.
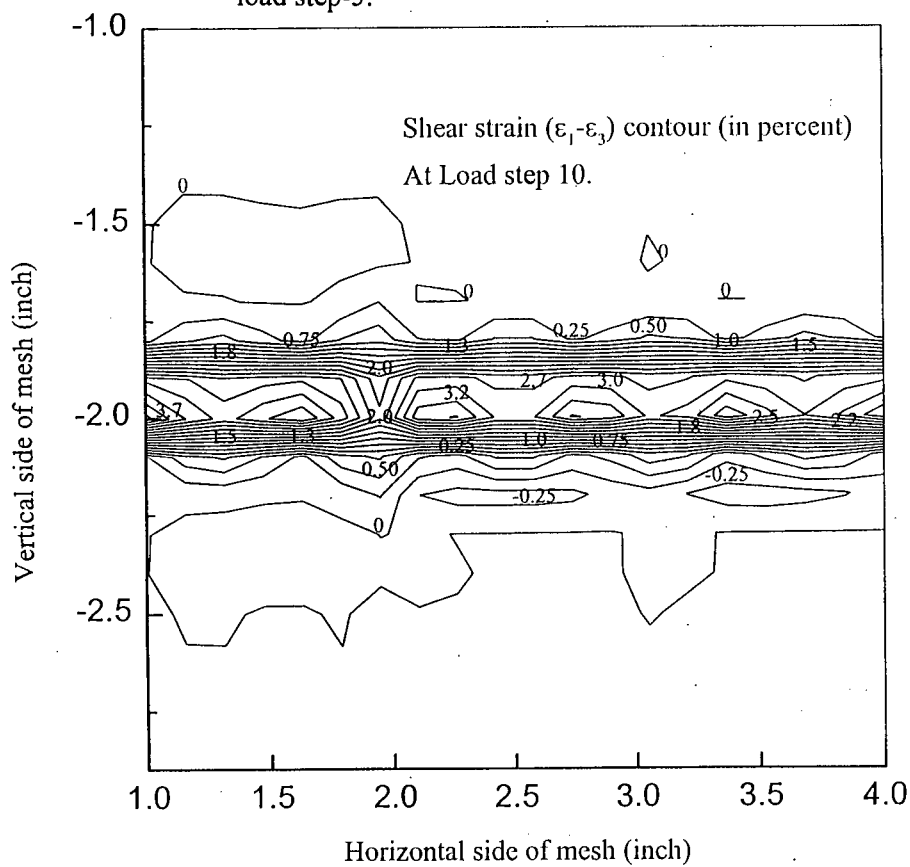
Figure 5-39(b): Shear strain contour for Case-6 of Goodman Type Interface at load step-10.

185
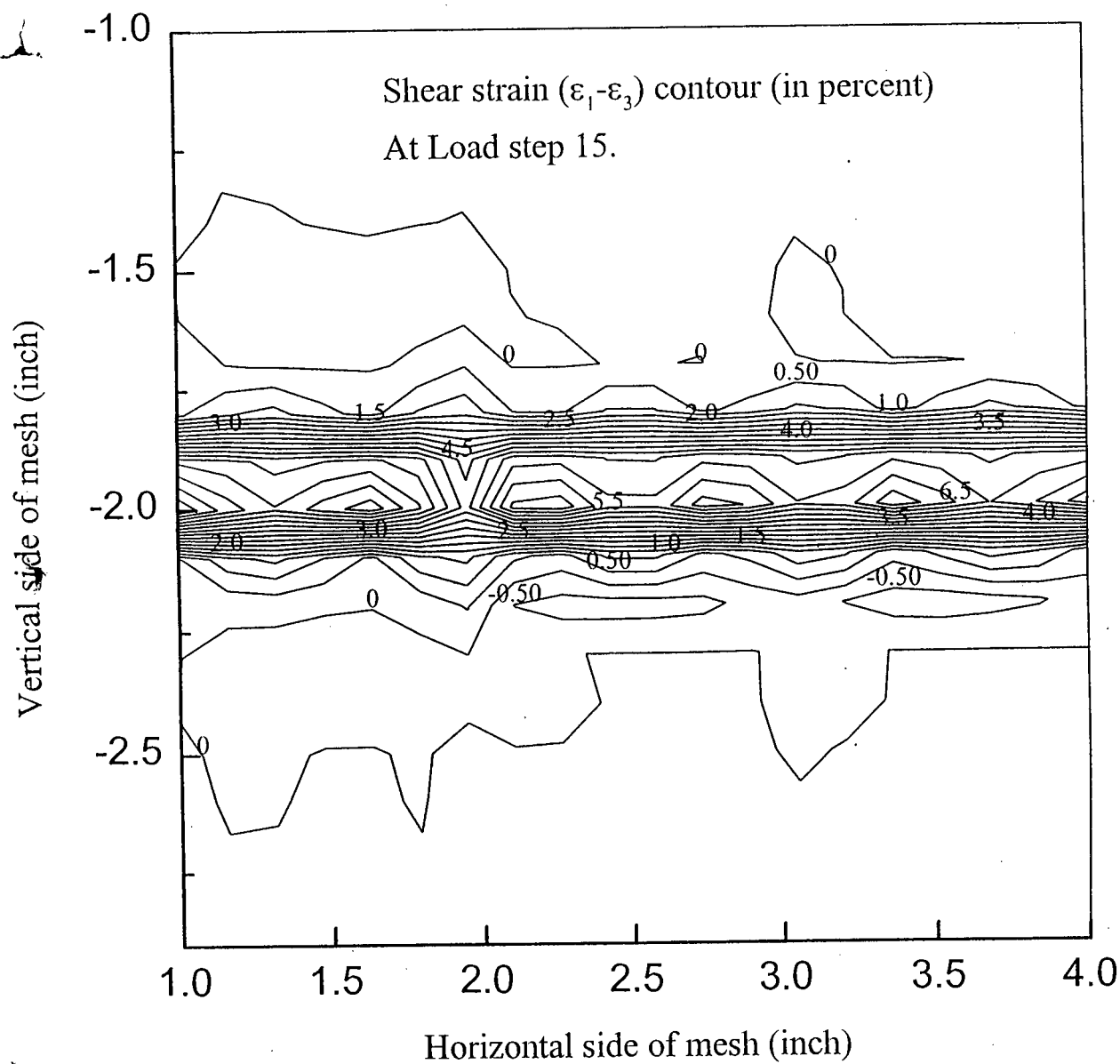
Figure 5-39(c): Shear strain contour for Case-6 of Goodman Type Interface at load step-15.
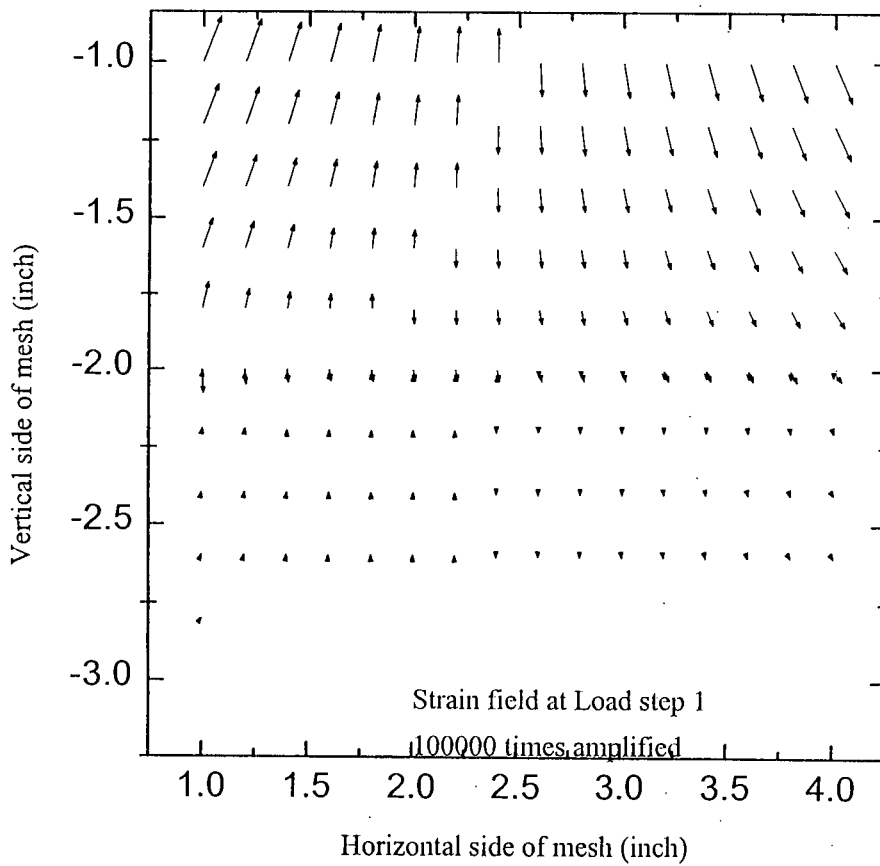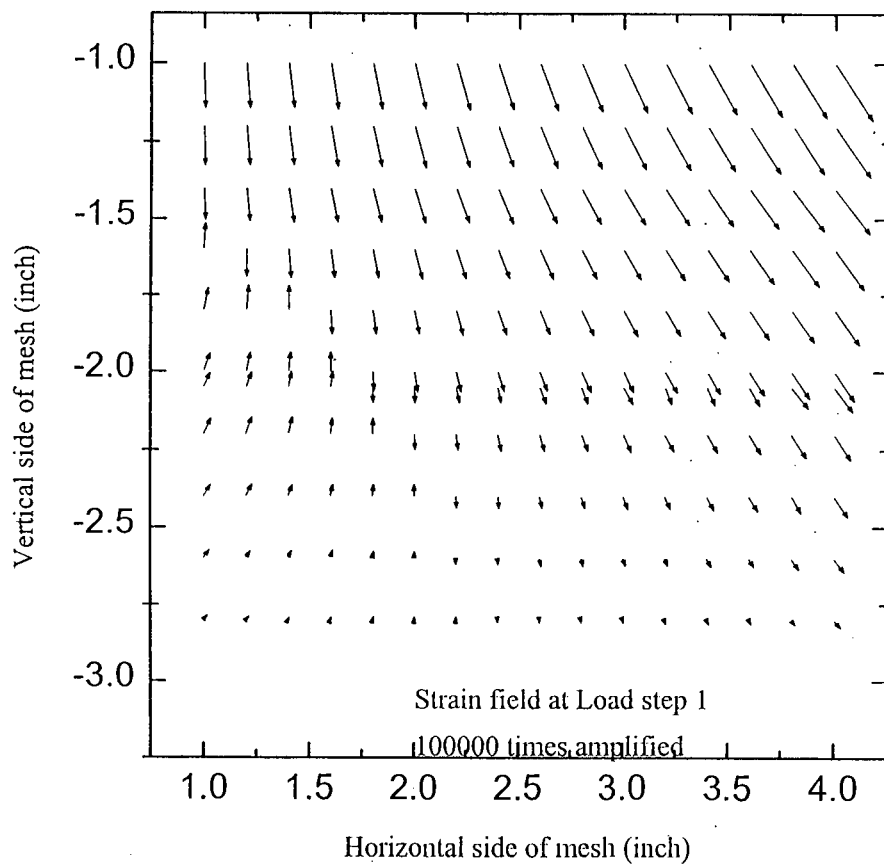
Figure 5-40(a): Displacement field for Case-6 of Goodman Type Interface at load step-1.
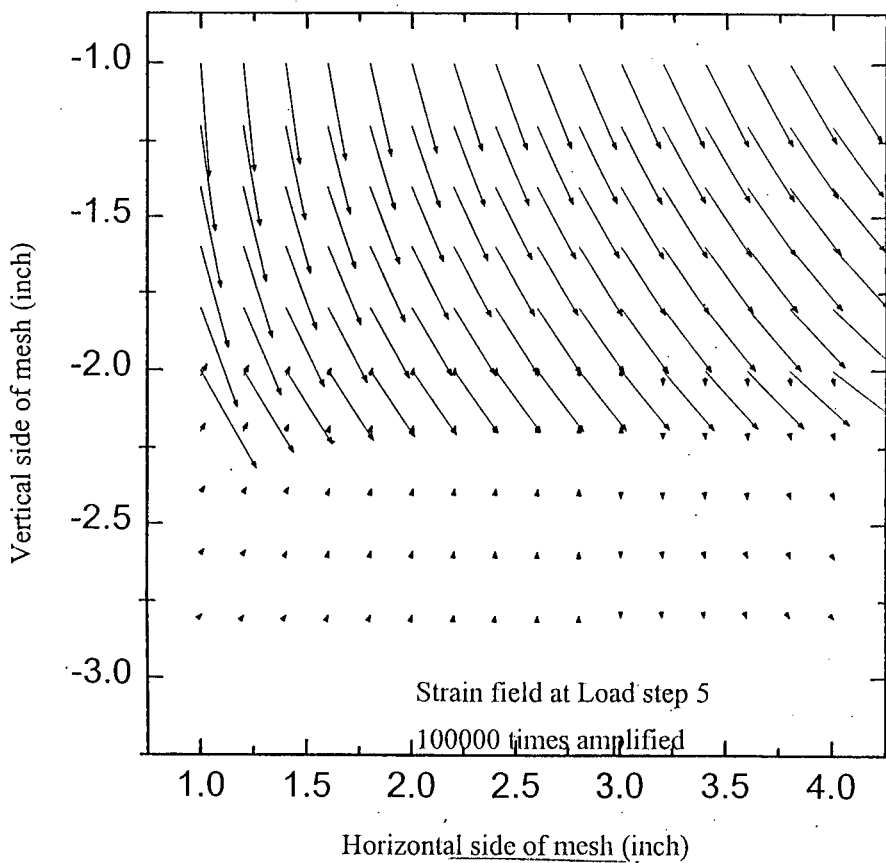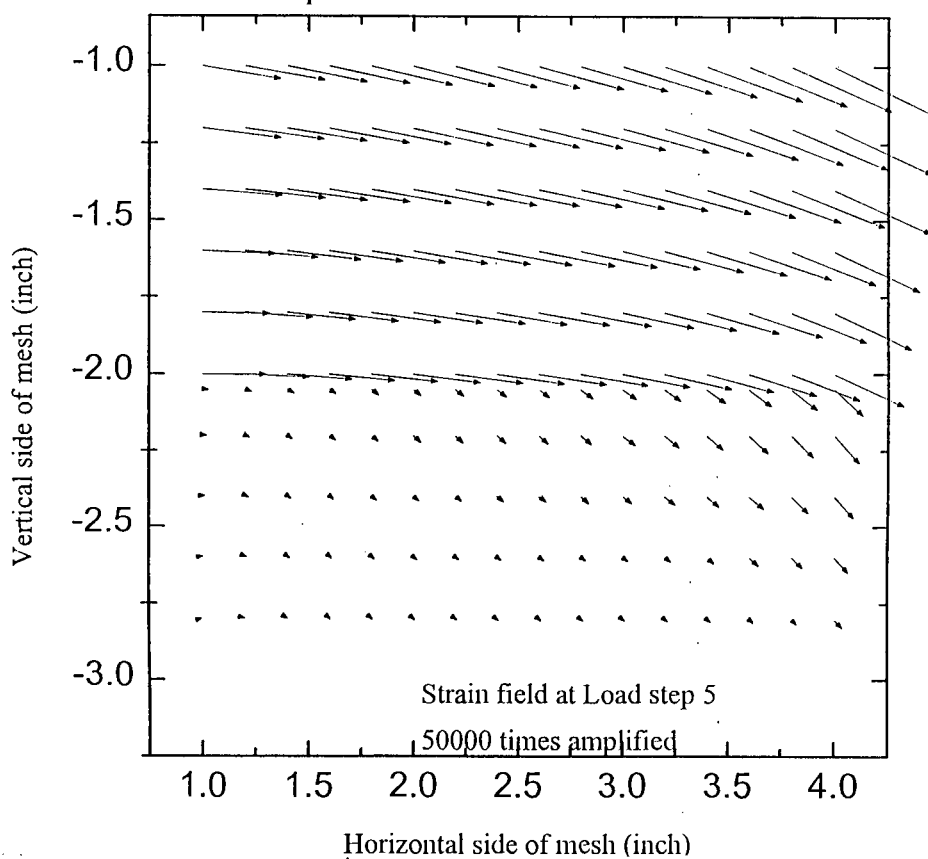

Figure 5-40(b): Displacement field for Case-6 of Goodman Type Interface at load step-5.
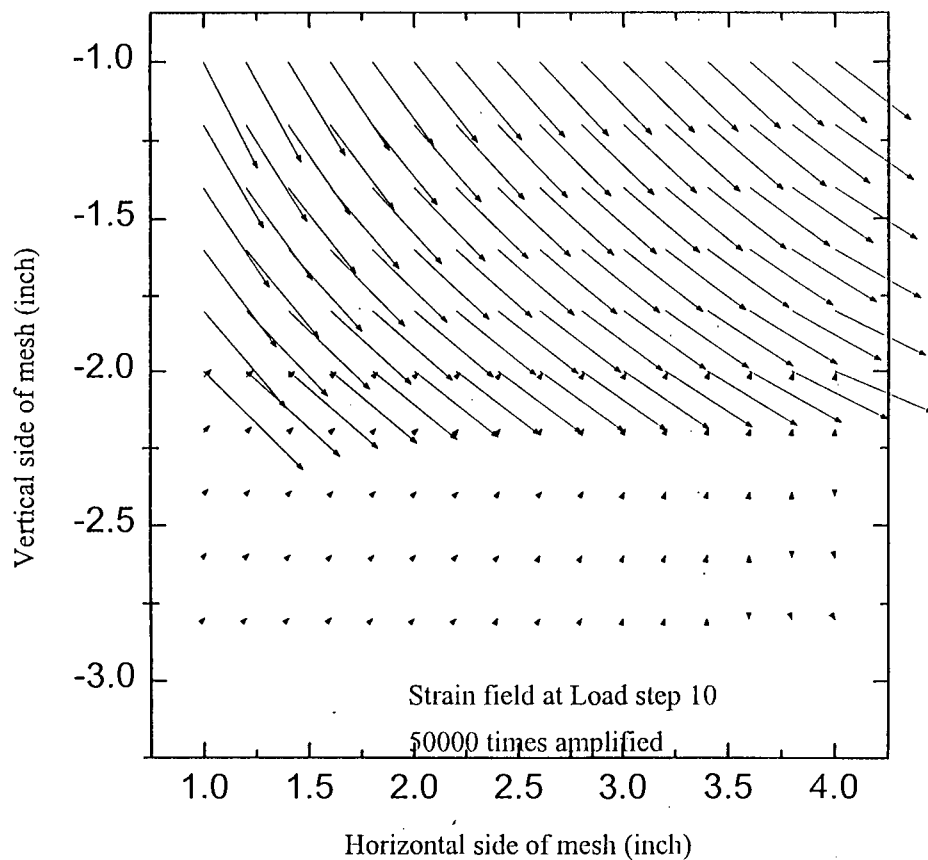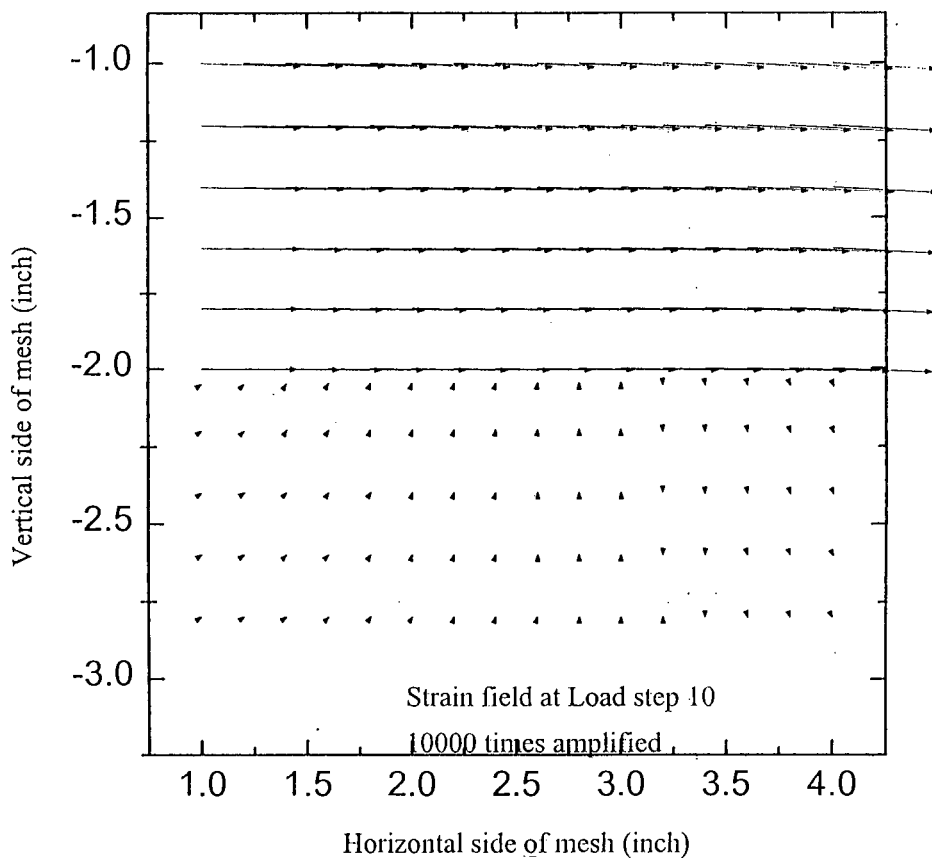
Figure 5-40(c): Displacement field for Case-6 of Goodman Type Interface at load step-10.
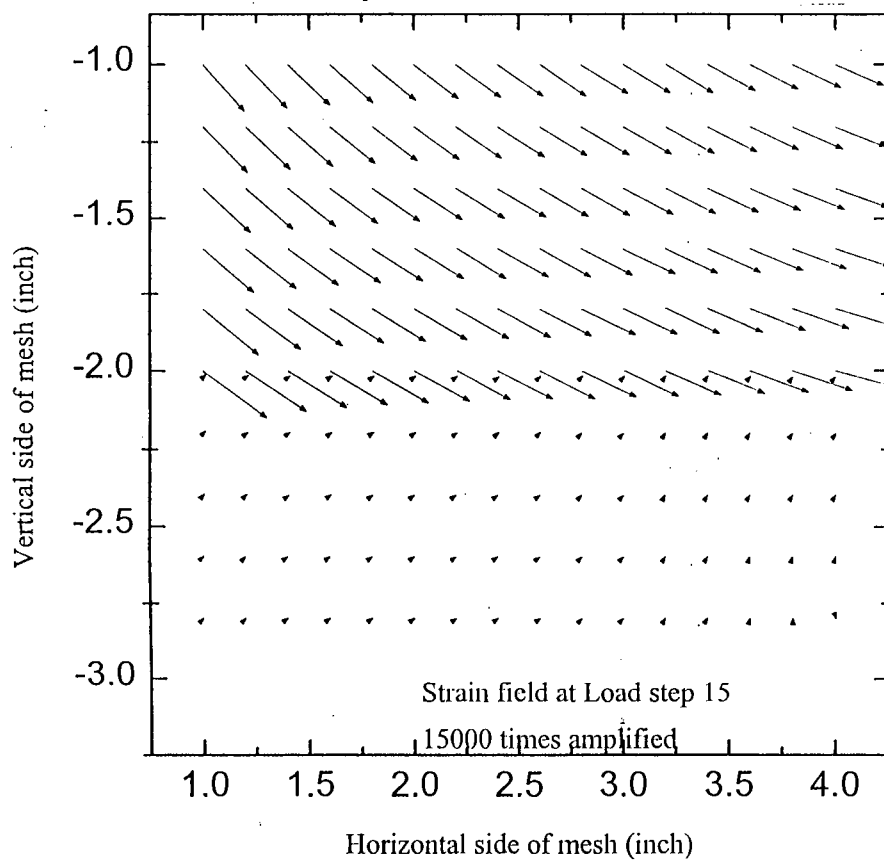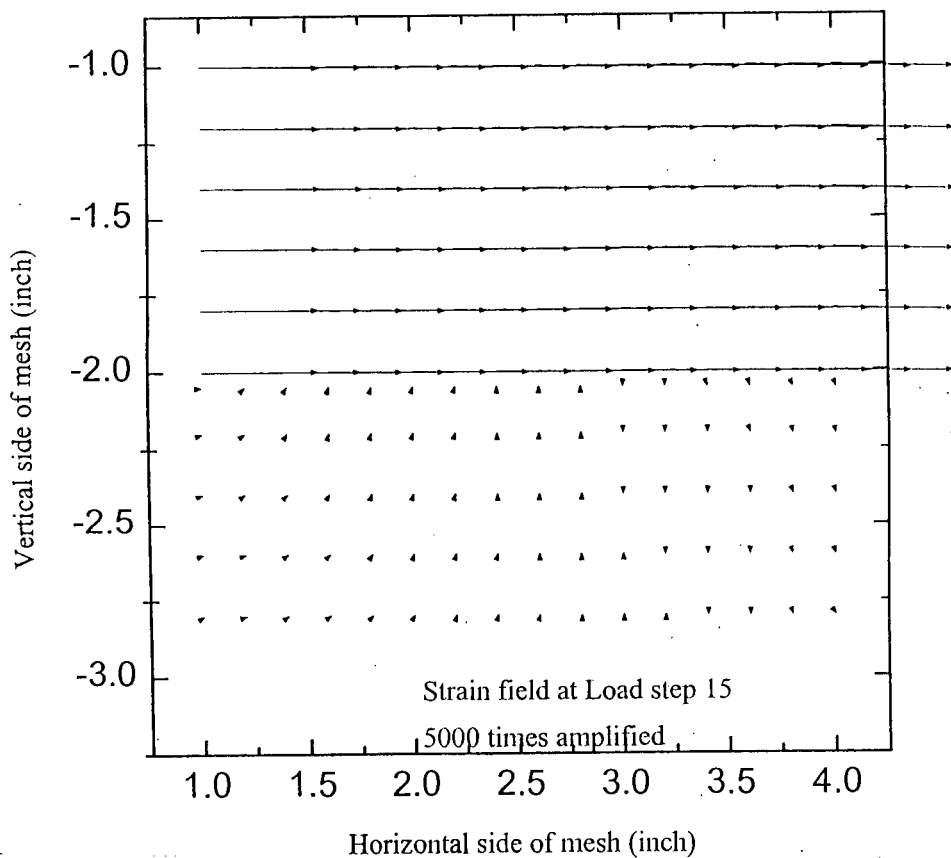

Figure 5-40(d): Displacement field for Case-6 of Goodman Type Interface at load step-15.
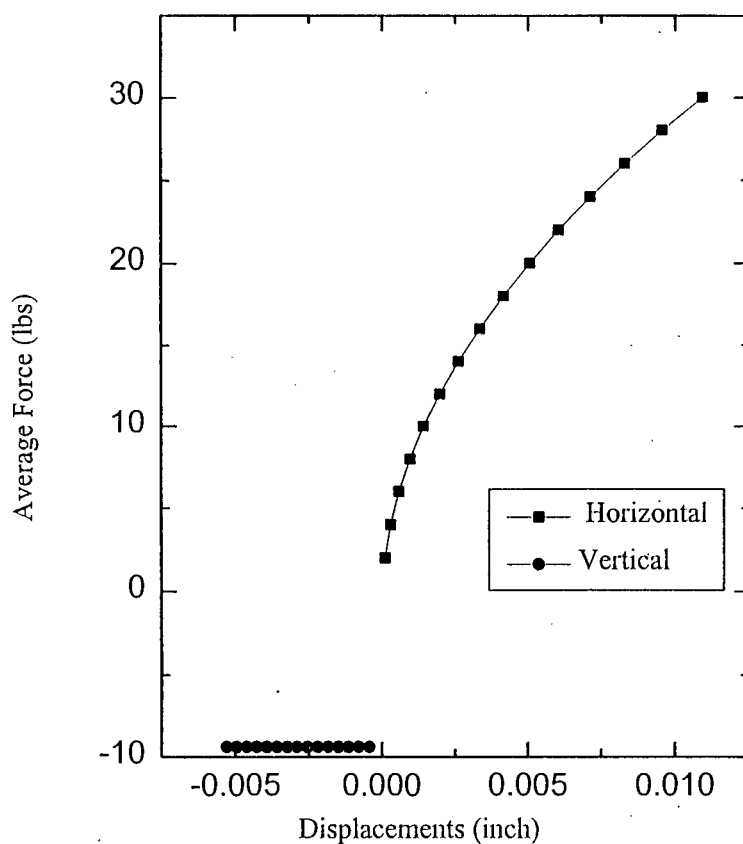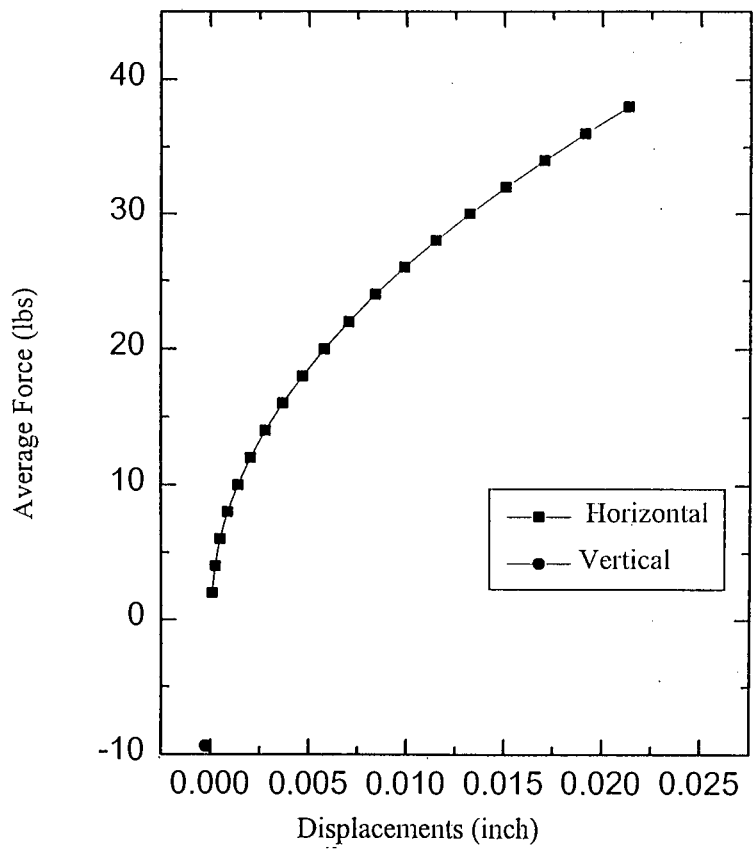
Figure 5-41(a): Average Force vs Displacement variation inside of Goodman
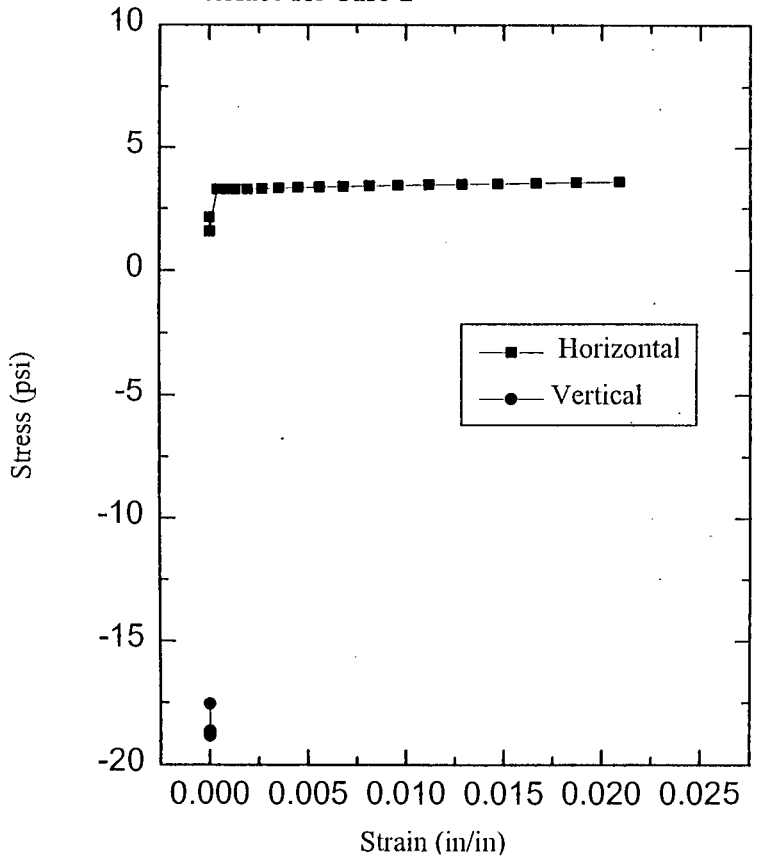Type Interface for Case-7

Figure 5-41(b): Stress vs Strain variation inside of Goodman Type Interface for
Case-7.
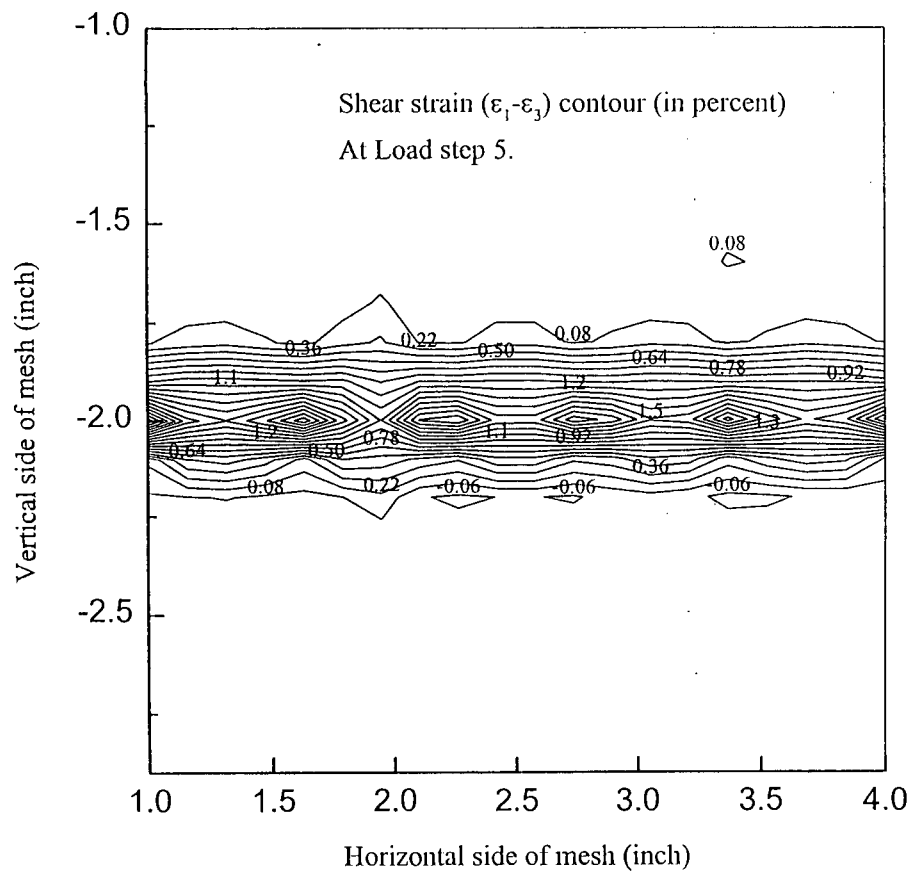
Figure 5-42(a): Shear strain contour for Case-7 of Goodman Type Interface at load step-5.

Figure 5-42(b): Shear strain contour for Case-7 of Goodman Type Interface at load step-10.

Figure 5-42(c): Shear strain contour for Case-7 of Goodman Type Interface at load step-15.

Figure 5-43(a):   Displacement field for Case-7 of Goodman Type Interface at
load step-1.

Figure 5-43(b):   Displacement field for Case-7 of Goodman Type Interface at
load step-5.

192

Strain field at Load step 10

50000 times amplified

Horizontal side of mesh (inch)

Figure 5-43(c): Displacement field for Case-7 of Goodman Type Interface at load step-10.

Strain field at Load step 15

15000 times amplified

Horizontal side of mesh (inch)

Figure 5-43(d): Displacement field for Case-7 of Goodman Type Interface at load step-15.

193

Figure 5-44(a): Average Force vs Displacement variation inside of Goodman
Type Interface for Case-8

Figure 5-44(b): Stress vs Strain variation inside of Goodman Type Interface for
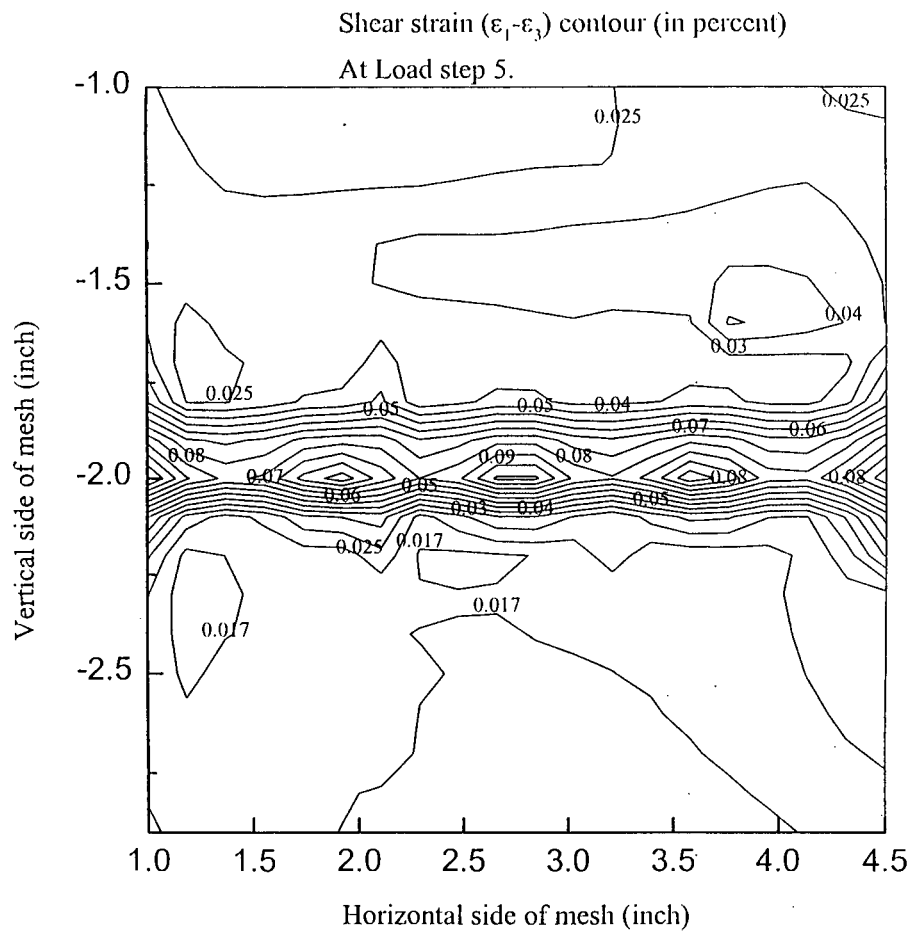Case-8.
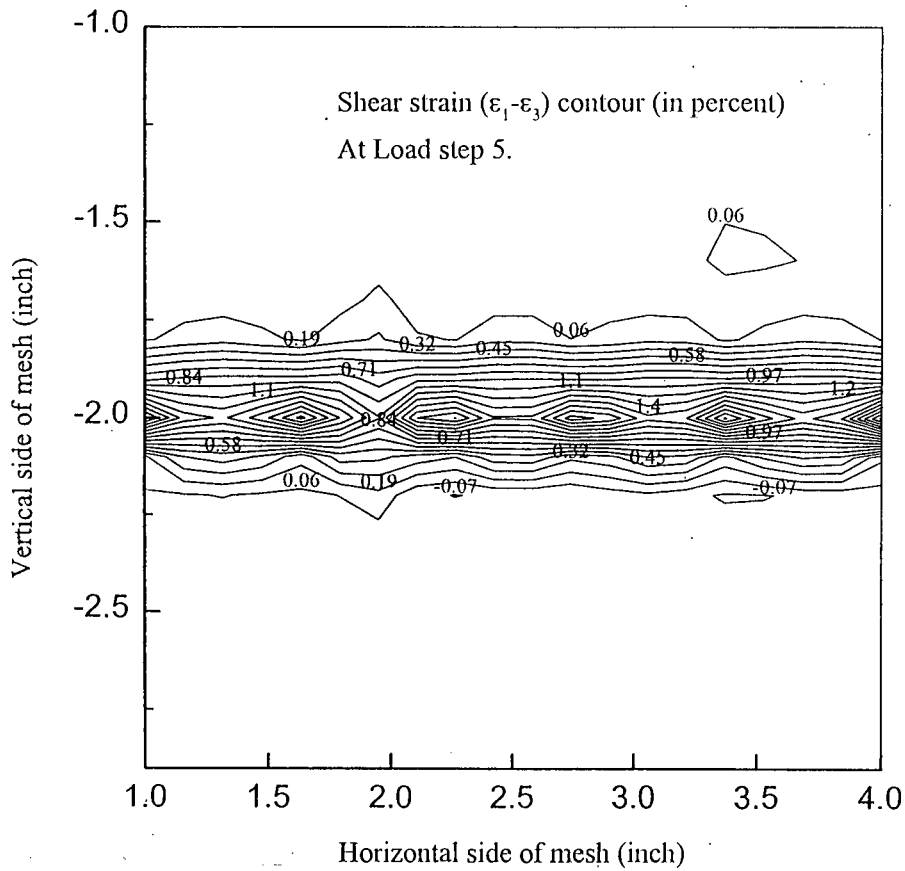
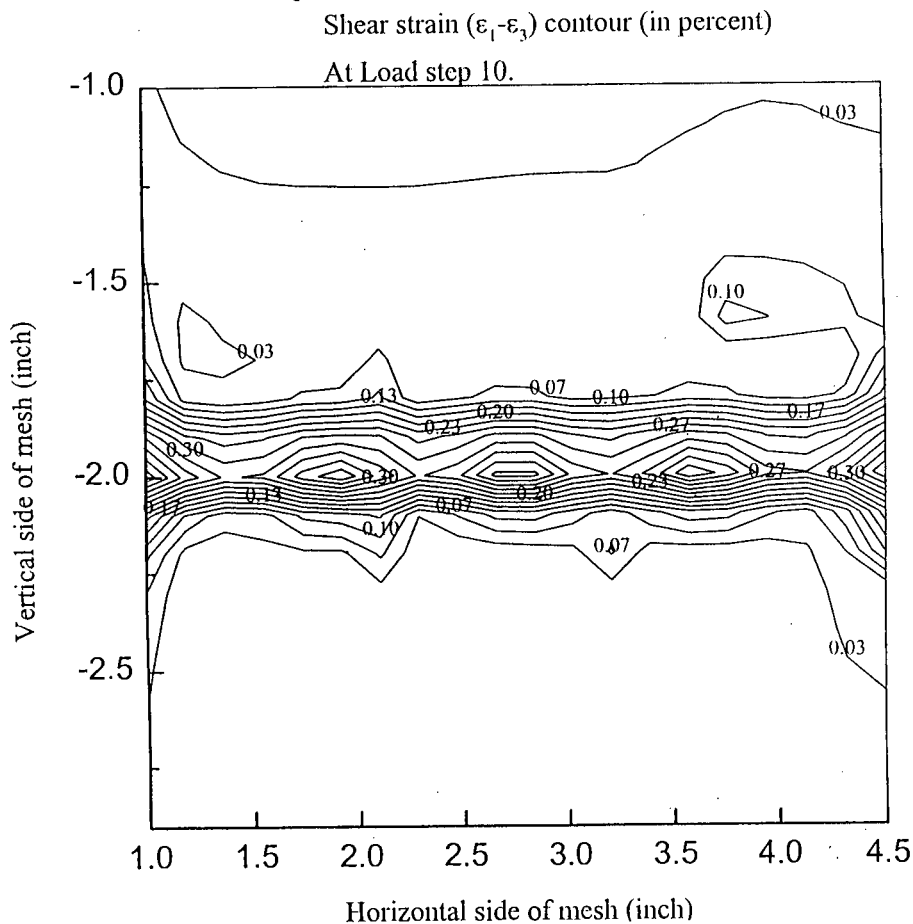Figure 5-45(a): Shear strain contour for Case-8 of Goodman Type Interface at load step-5.

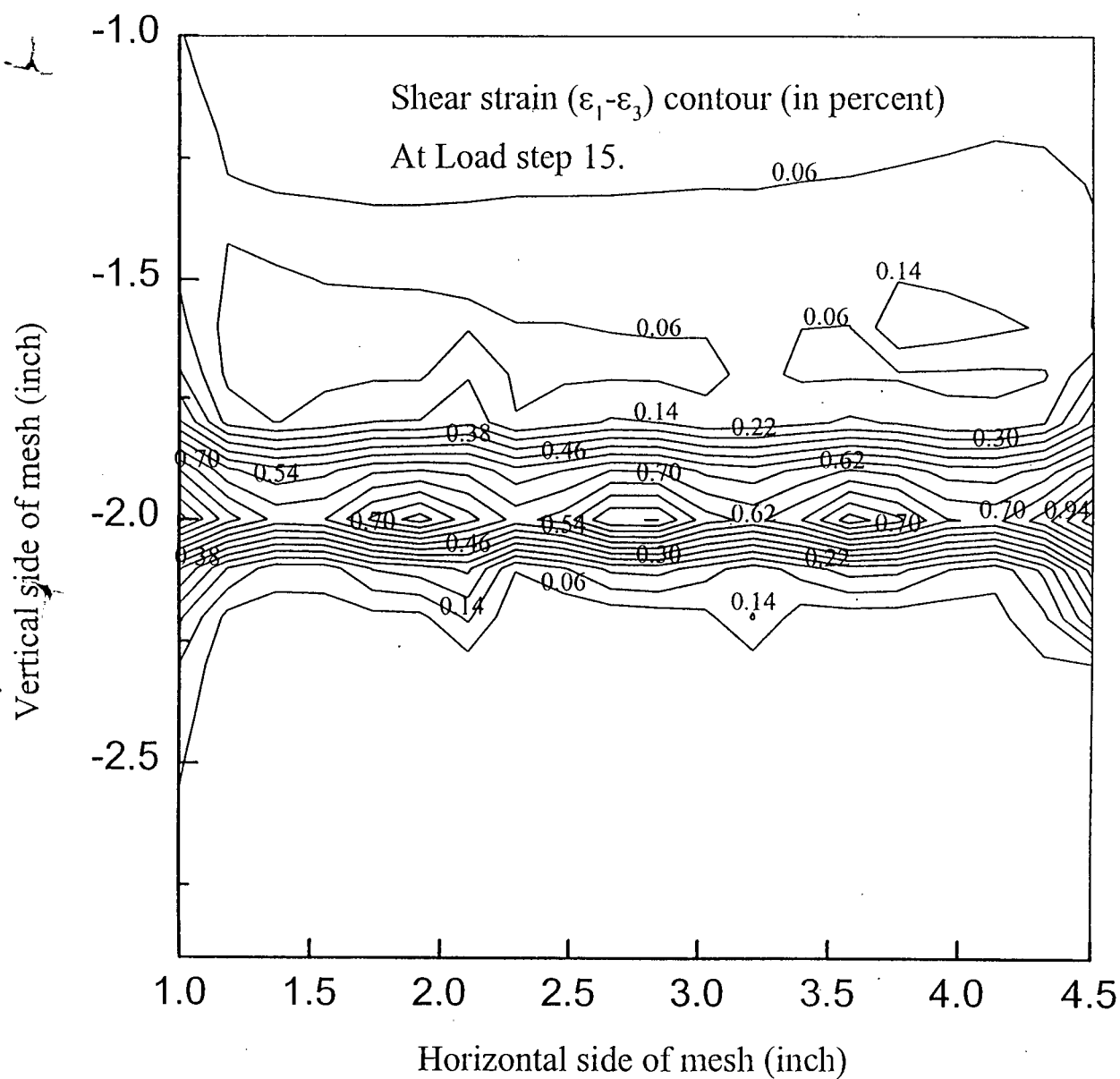Figure 5-45(b): Shear strain contour for Case-8 of Goodman Type Interface at load step-10.

Figure 5-45(c): Shear strain contour for Case-8 of Goodman Type Interface at load step-15.
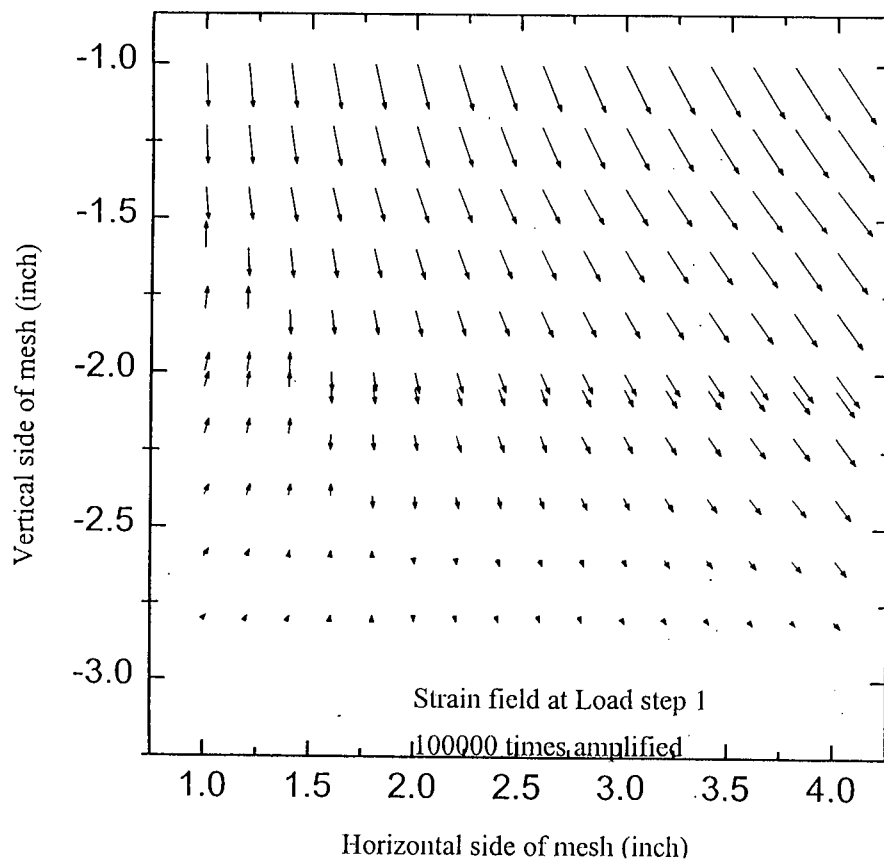
Figure 5-46(a):   Displacement field for Case-8 of Goodman Type Interface at load step-1.
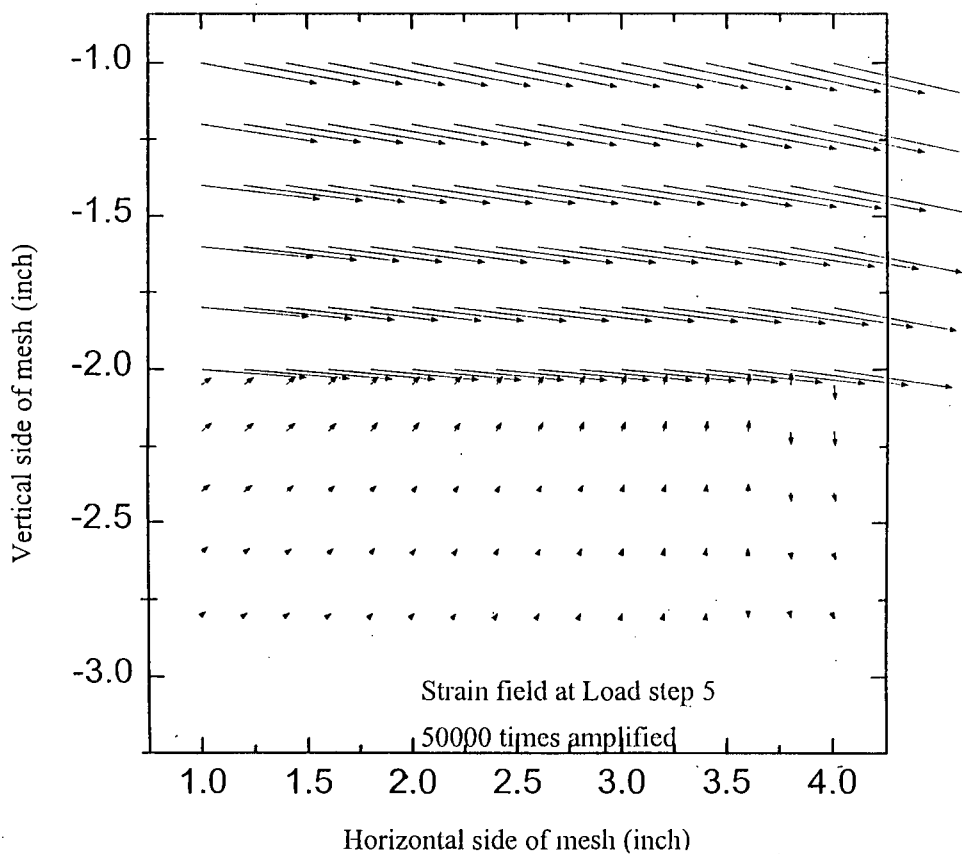

Figure 5-46(b):   Displacement field for Case-8 of Goodman Type Interface at load step-5.
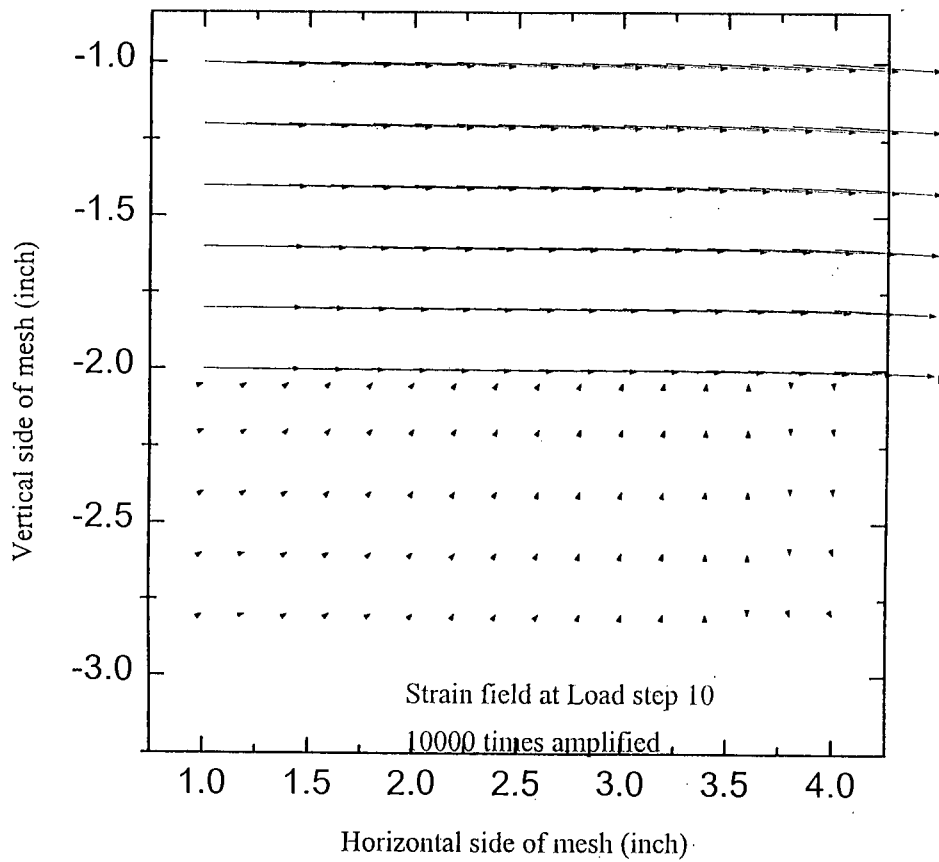
197

Figure 5-46(c):   Displacement field for Case-8 of Goodman Type Interface at load step-10.
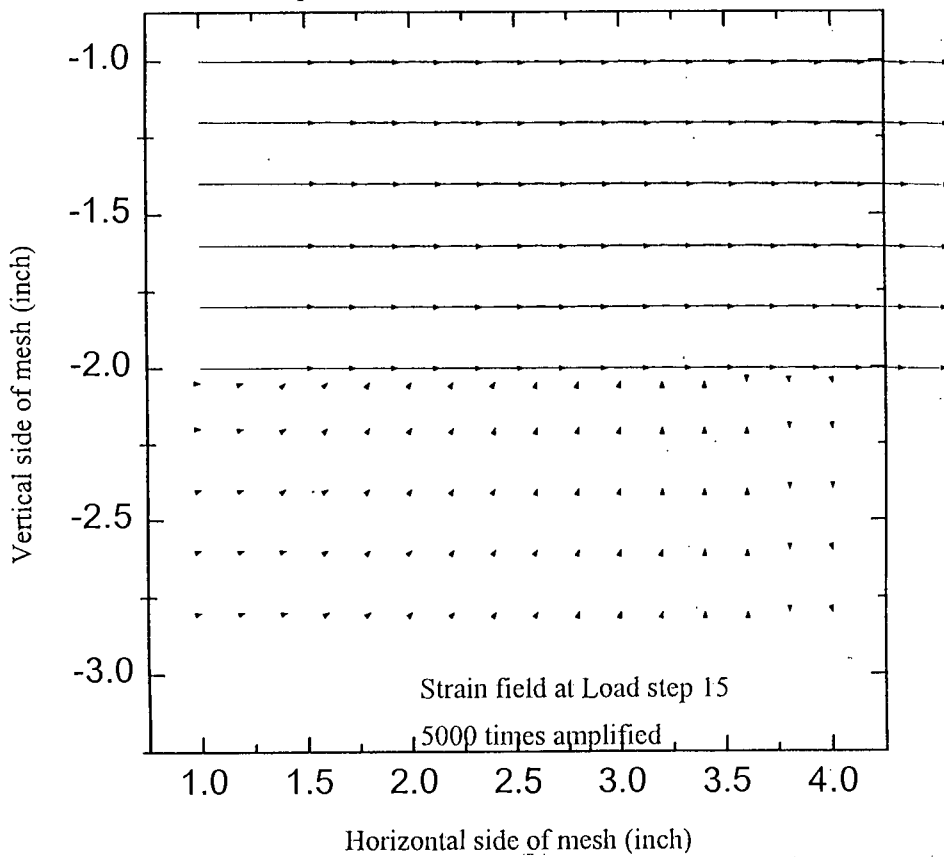

Figure 5-46(d):   Displacement field for Case-8 of Goodman Type Interface at load step-15.
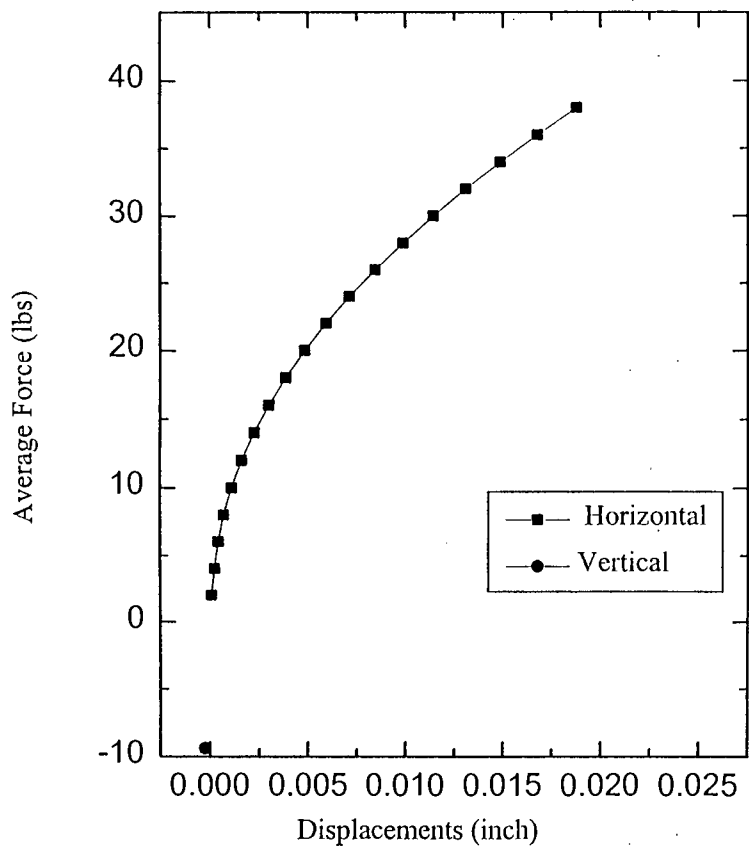
198

Figure 5-47(a): Average Force vs Displacement variation inside of Katona Type Interface for Case-1
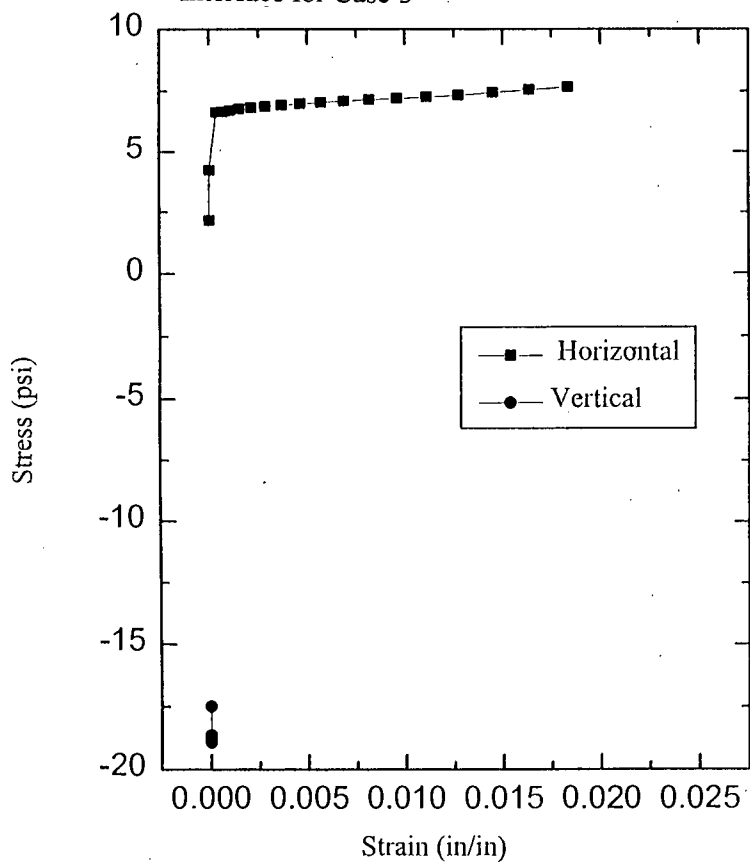

Figure 5-47(b): Stress vs Strain variation inside of Katona Type Interface for Case-1.

Shear strain (ε_1-ε_3) contour (in percent)

At Load step 5.

Horizontal side of mesh (inch)

Figure 5-48(a):   Shear strain contour for Case-1 of Katona Type Interface at load step-5.

Shear strain (ε_1-ε_3) contour (in percent)
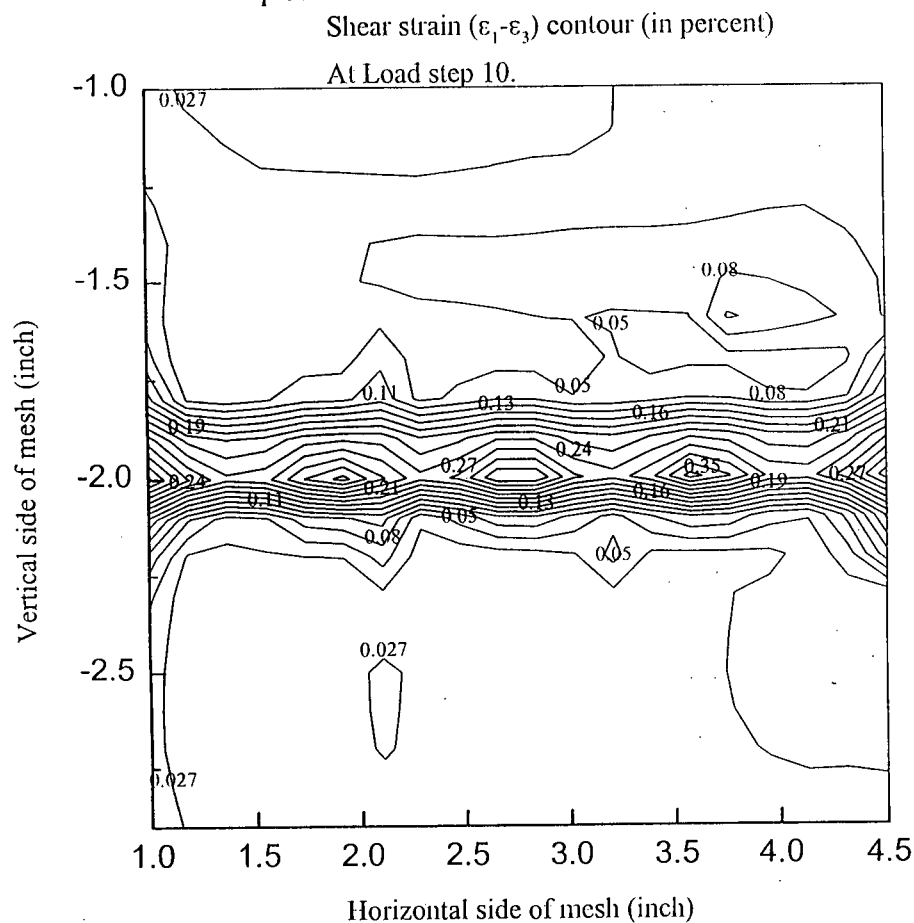
At Load step 10.

Horizontal side of mesh (inch)

Figure 5-48(b):   Shear strain contour for Case-1 of Katona Type Interface at load step-10.
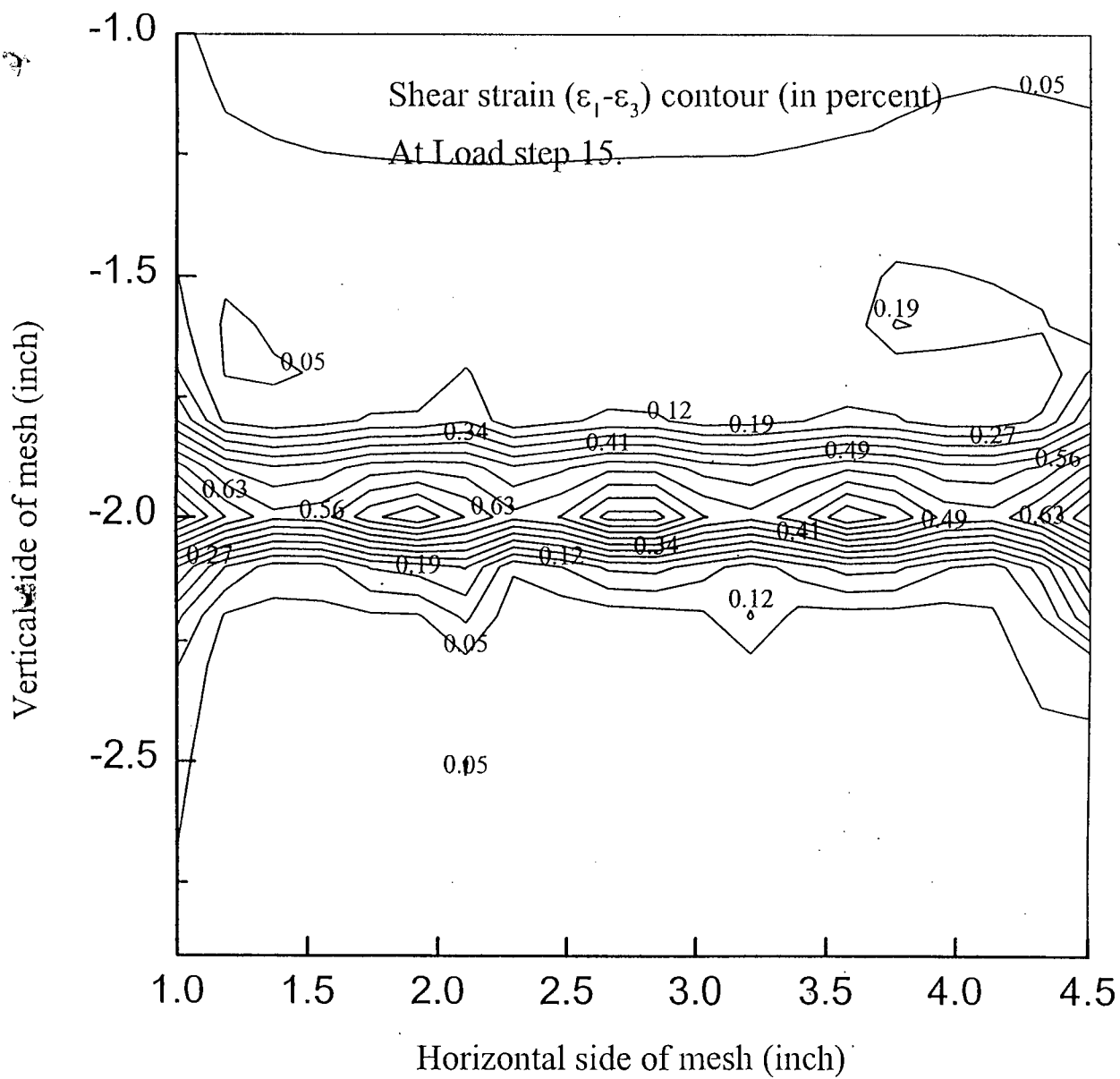
200

Figure 5-48(c): Shear strain contour for Case-1 of Katona Type Interface at load step-15.
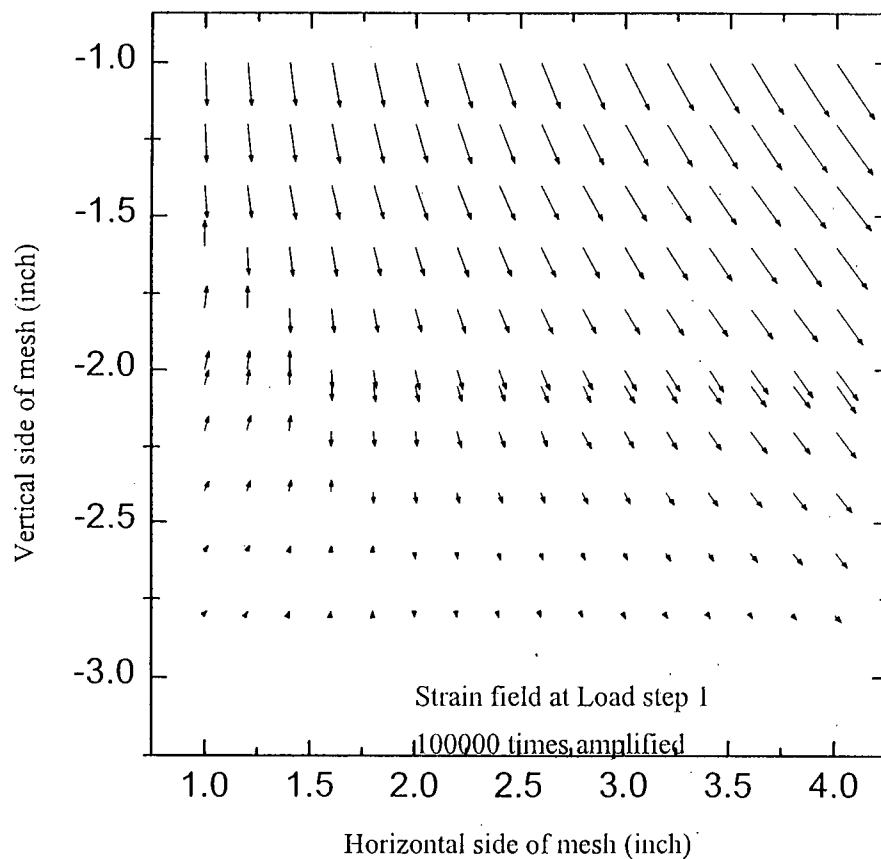
201

Figure 5-49(a):   Displacement field for Case-1 of Katona Type Interface at load step-1.

Figure 5-49(b):   Displacement field for Case-1 of Katona Type Interface at load step-5.

Strain field at Load step 10

10000 times amplified

Figure 5-49(c): Displacement field for Case-1 of Katona Type Interface at load step-10.

Strain field at Load step 15

5000 times amplified

Figure 5-49(d): Displacement field for Case-1 of Katona Type Interface at load step-15.

Figure 5-50(a): Average Force vs Displacement variation inside of Katona Type
Interface for Case-2

Figure 5-50(b):   Stress vs Strain variation inside of Katona Type Interface for
Case-2.

Shear strain (ε_1-ε_3) contour (in percent)
At Load step 5.

Horizontal side of mesh (inch)

Figure 5-51(a): Shear strain contour for Case-2 of Katona Type Interface at load step-5.

Shear strain (ε_1-ε_3) contour (in percent)
At Load step 10.

Horizontal side of mesh (inch)

Figure 5-51(b): Shear strain contour for Case-2 of Katona Type Interface at load step-10.

Figure 5-51(c):   Shear strain contour for Case-2 of Katona Type Interface at load step-15.

206

Figure 5-52(a): Displacement field for Case-2 of Katona Type Interface at load step-1.

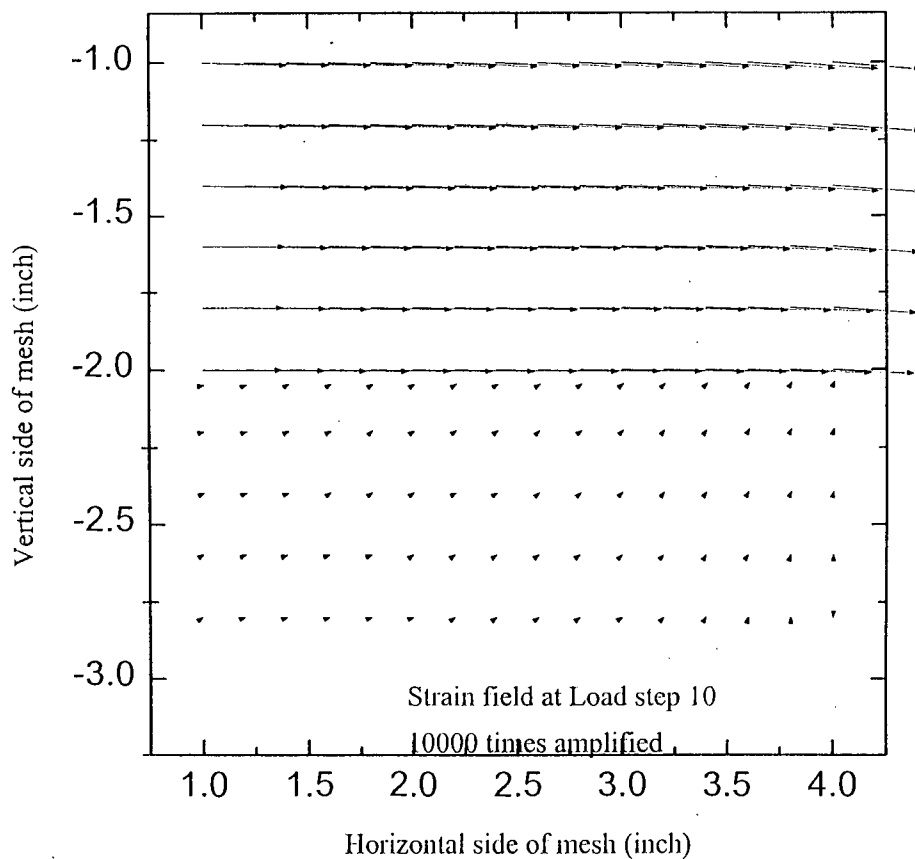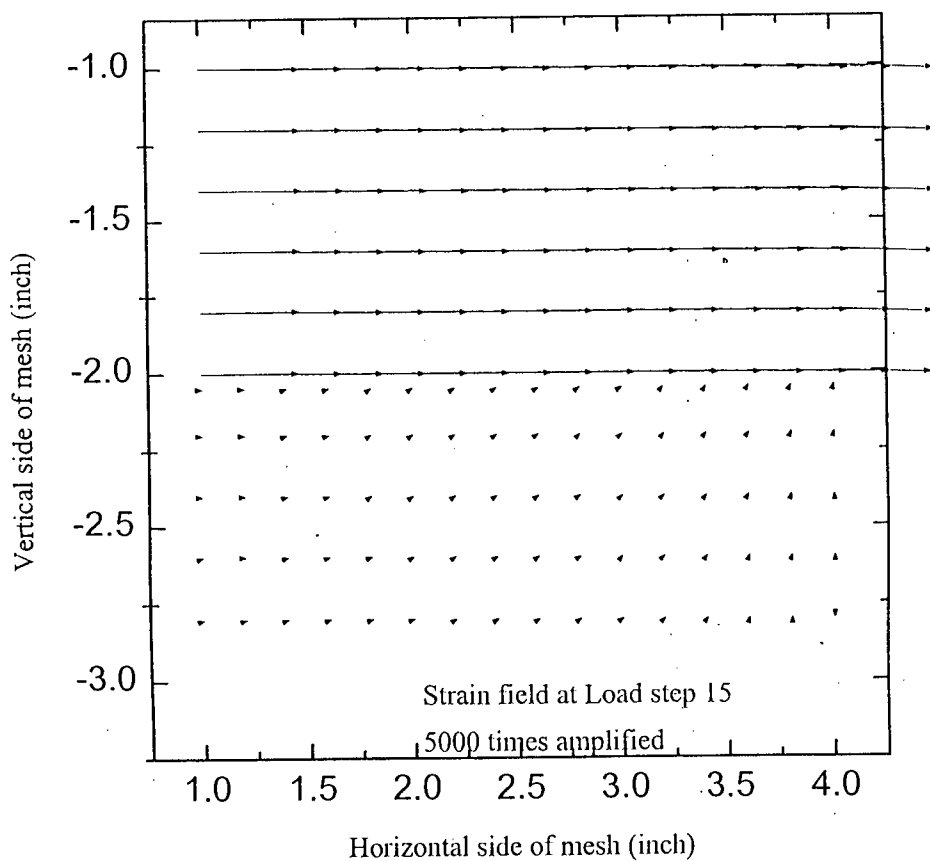Figure 5-52(b): Displacement field for Case-2 of Katona Type Interface at load step-5.

207

Strain field at Load step 10

10000 times amplified

Figure 5-52(c): Displacement field for Case-2 of Katona Type Interface at load
step-10.

Strain field at Load step 15

5000 times amplified

Figure 5-52(d): Displacement field for Case-2 of Katona Type Interface at load
step-15.

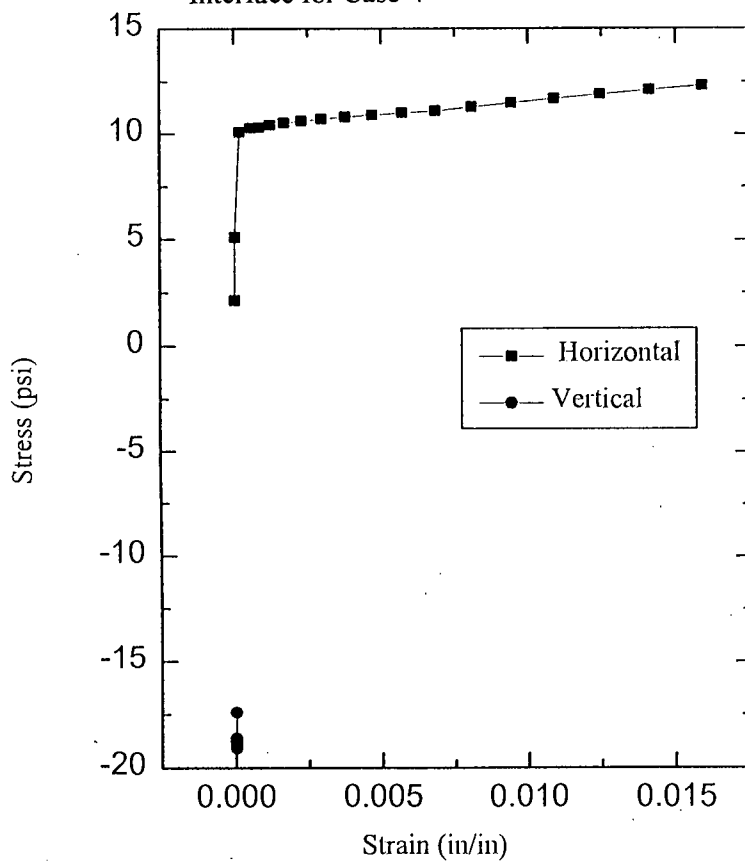Figure 5-53(a): Average Force vs Displacement variation inside of Katona Type Interface for Case-3

Figure 5-53(b): Stress vs Strain variation inside of Katona Type Interface for Case-3.
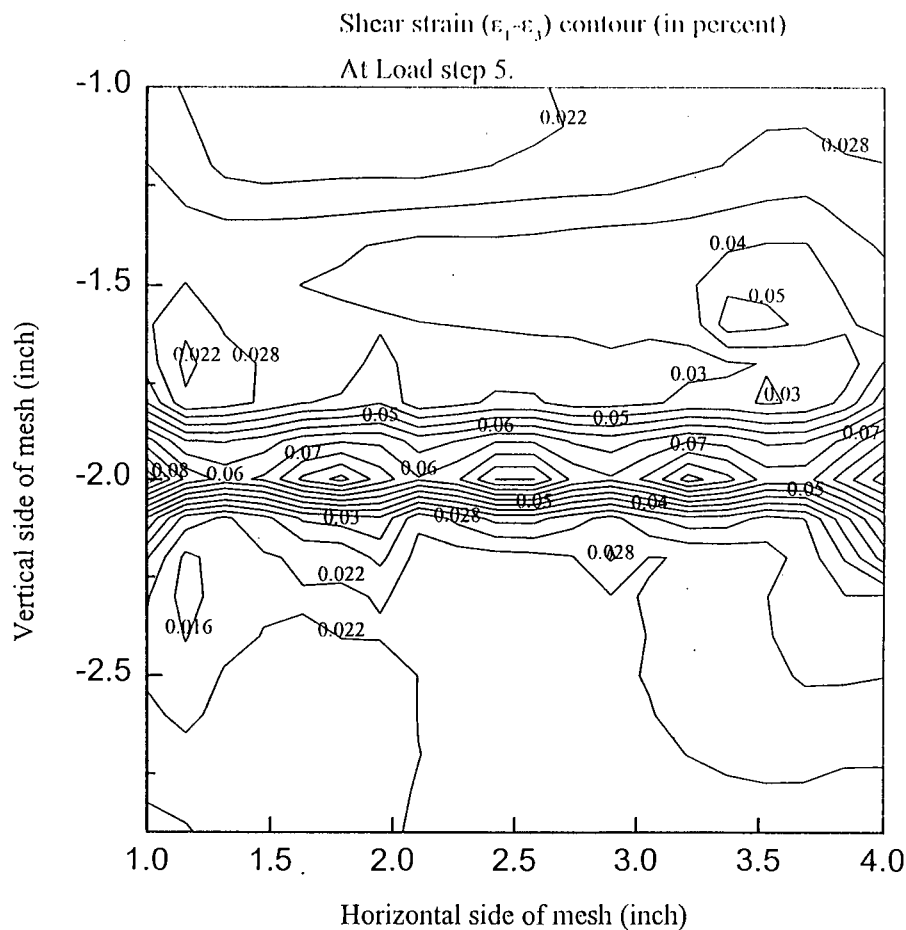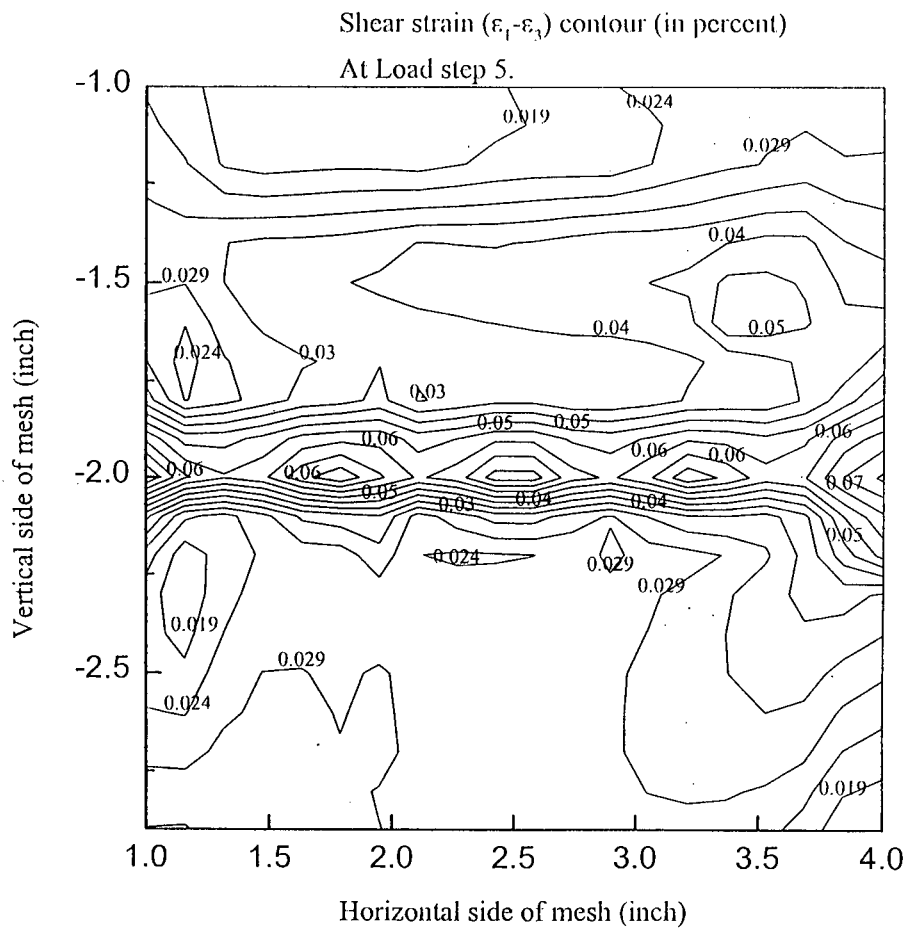
At Load step 5.

Figure 5-54(a): Shear strain contour for Case-3 of Katona Type Interface at load
step-5.

Shear strain (ε_1-ε_3) contour (in percent)
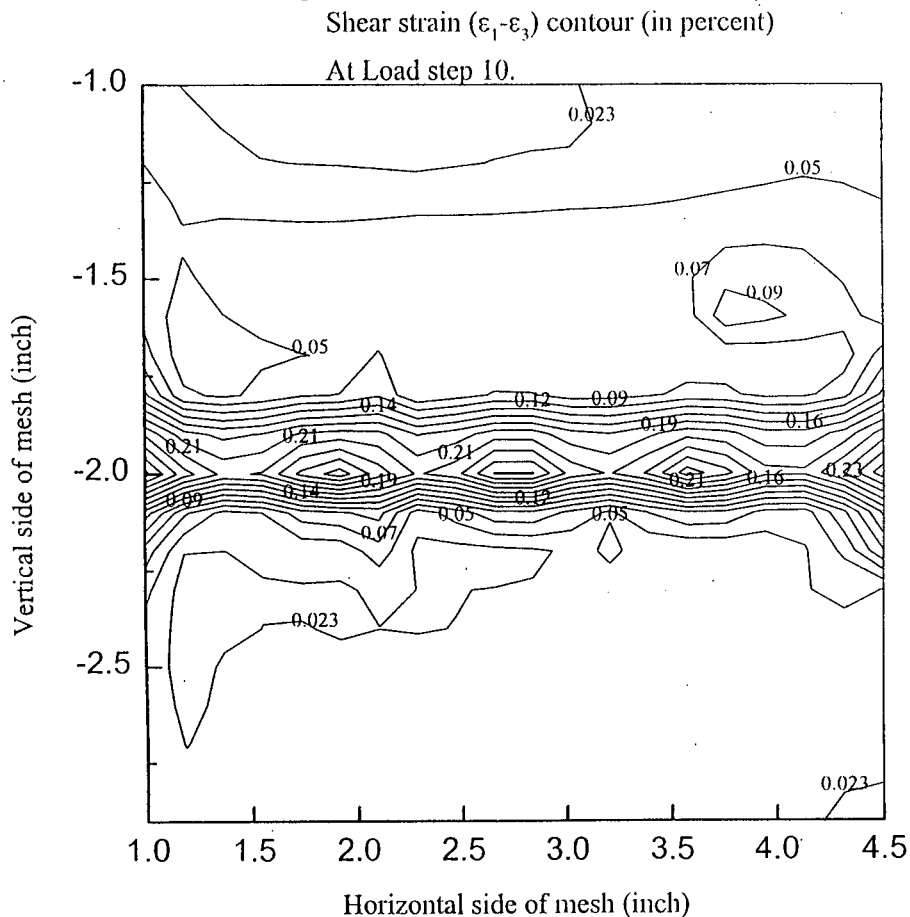
At Load step 10.

Figure 5-54(b): Shear strain contour for Case-3 of Katona Type Interface at load
step-10.

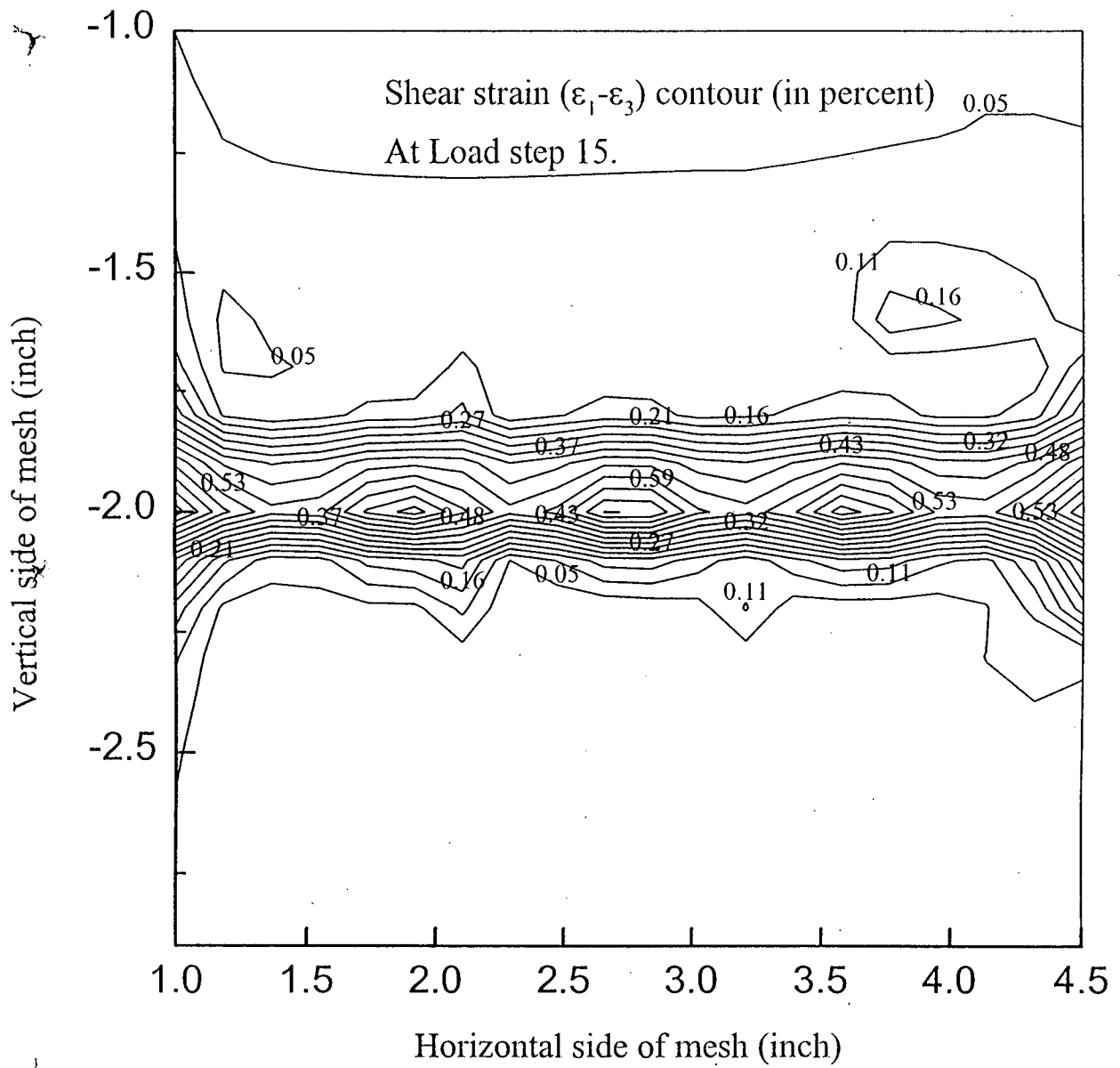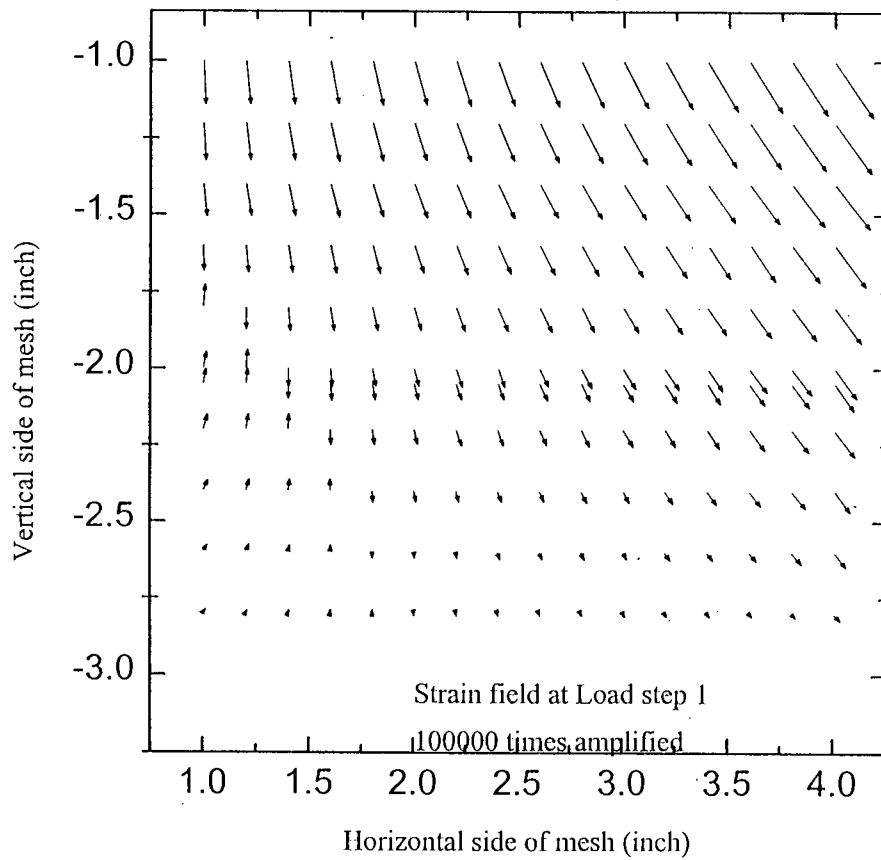Figure 5-54(c): Shear strain contour for Case-3 of Katona Type Interface at load step-15.

211

Figure 5-55(a):   Displacement field for Case-3 of Katona Type Interface at load step-1.
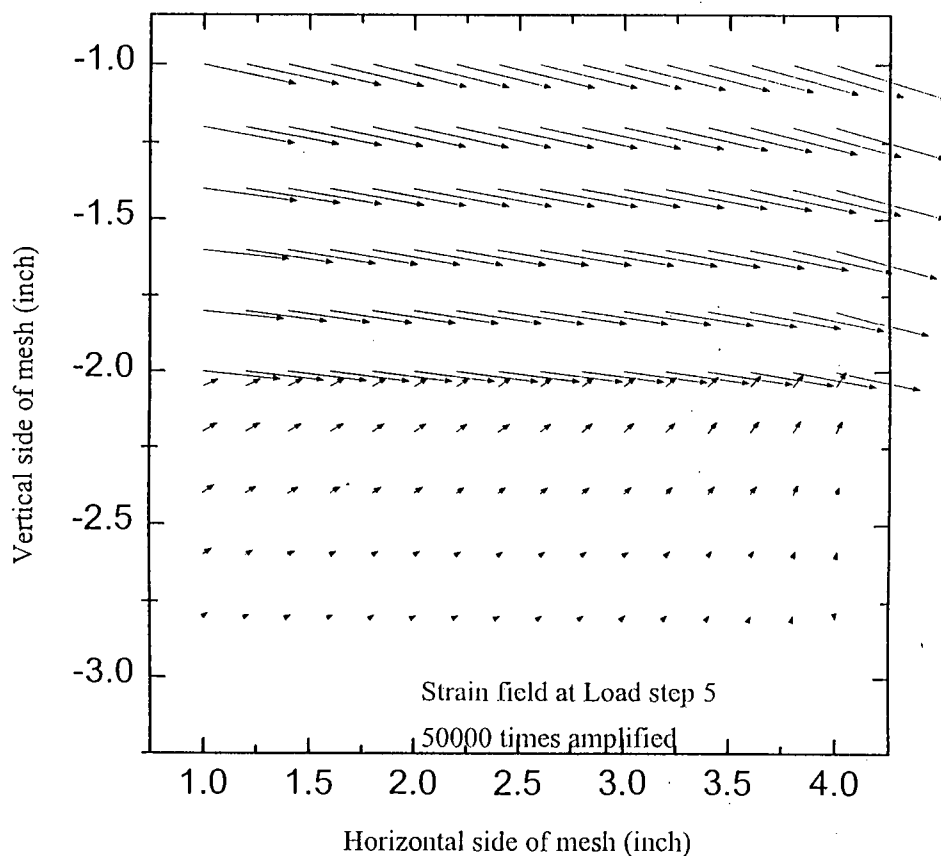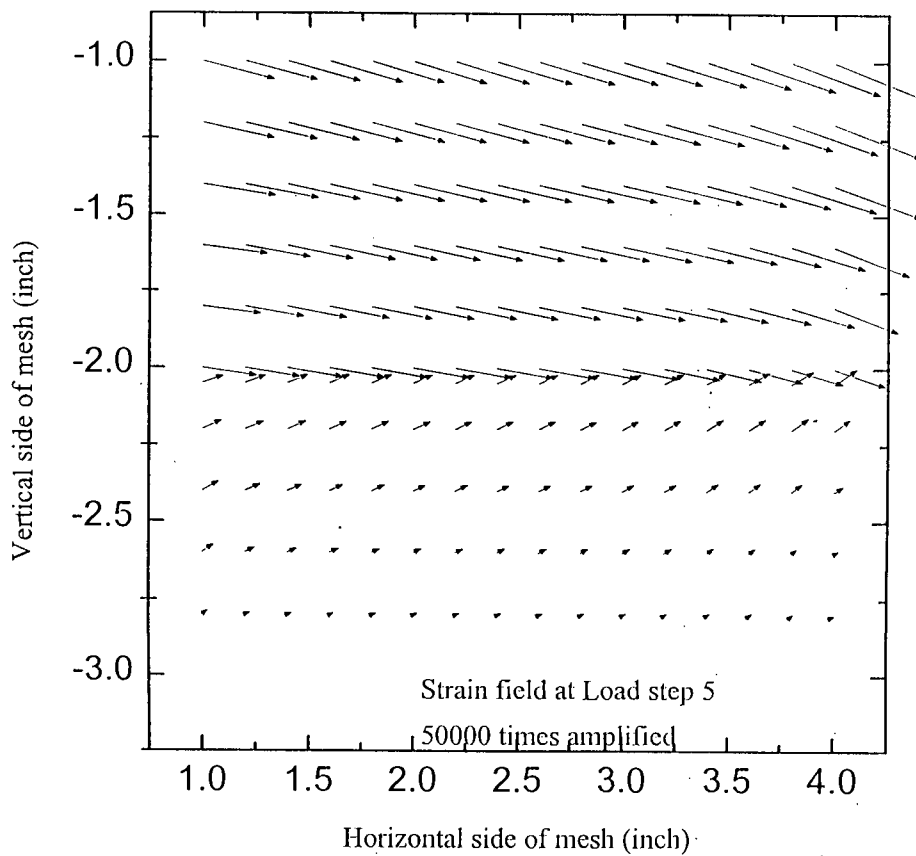

Figure 5-55(b):   Displacement field for Case-3 of Katona Type Interface at load step-5.
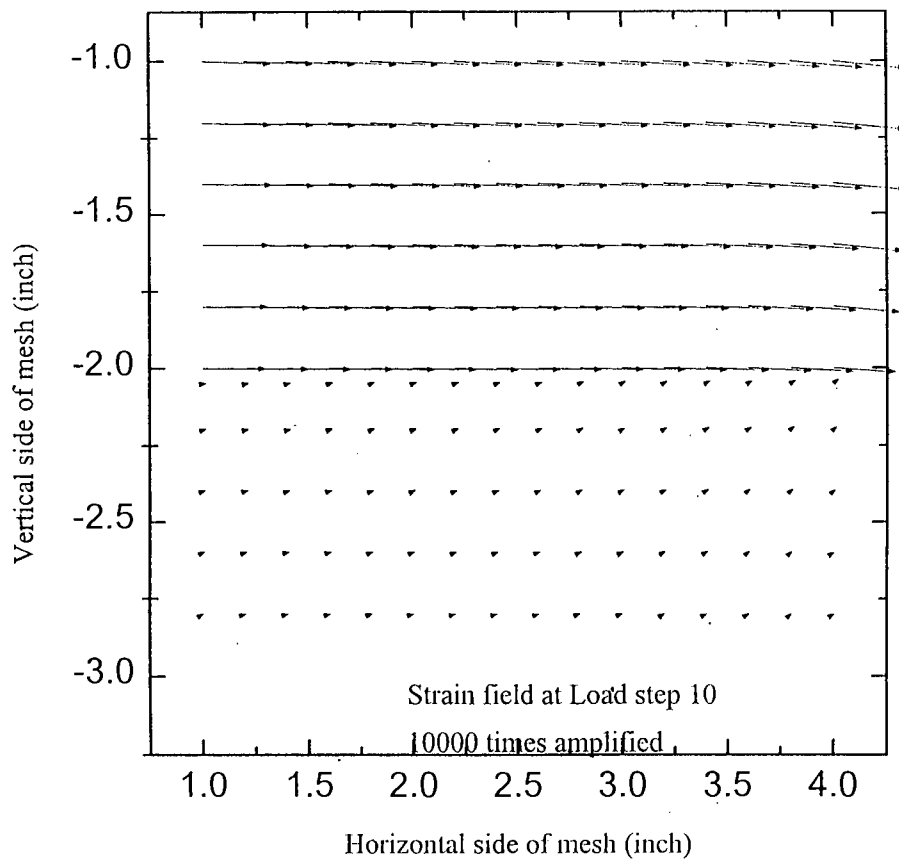
Figure 5-55(c): Displacement field for Case-3 of Katona Type Interface at load step-10.
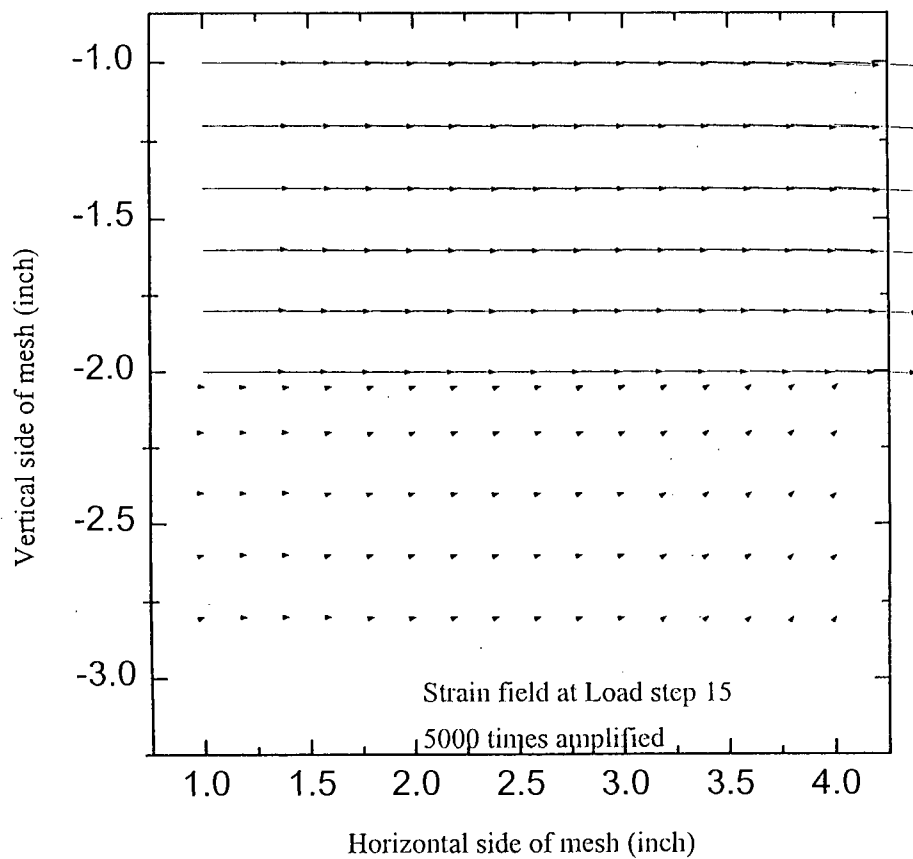

Figure 5-55(d): Displacement field for Case-3 of Katona Type Interface at load step-15.
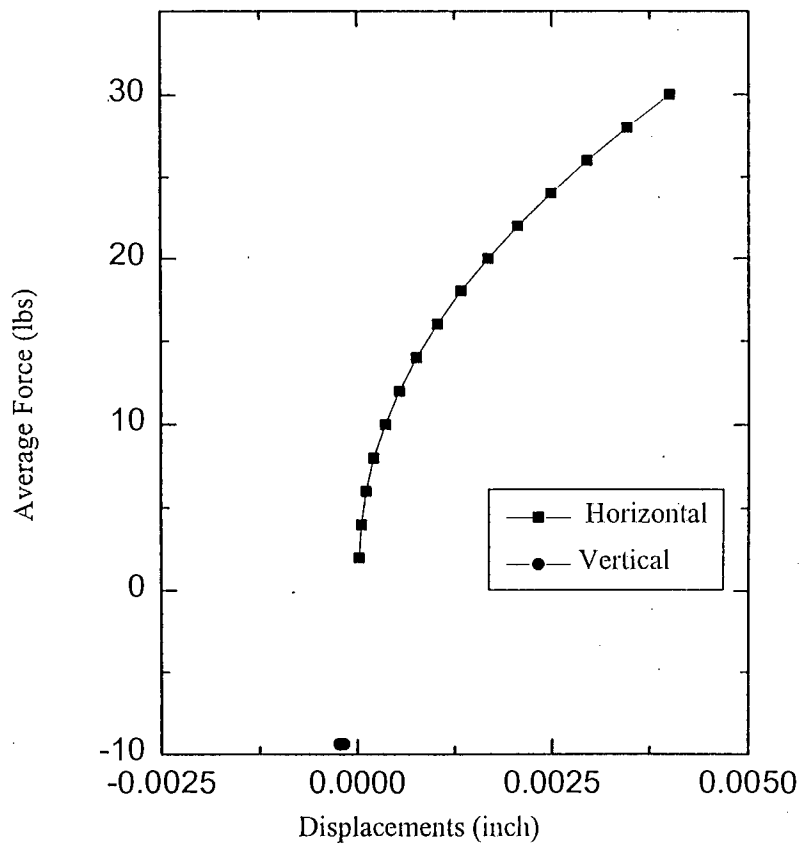
213
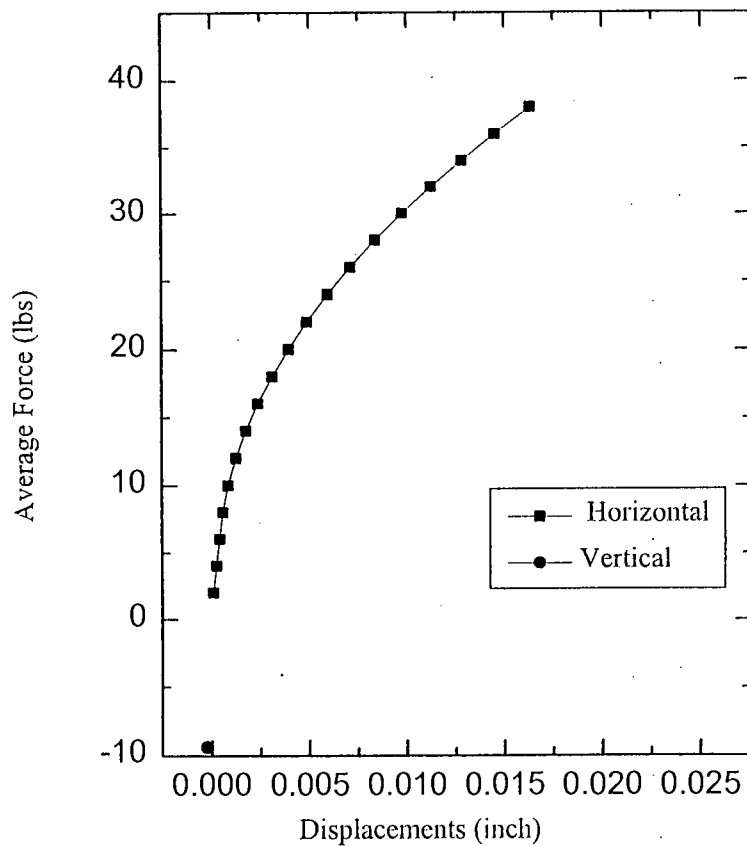
Figure 5-56(a): Average Force vs Displacement variation inside of Katona Type Interface for Case-4
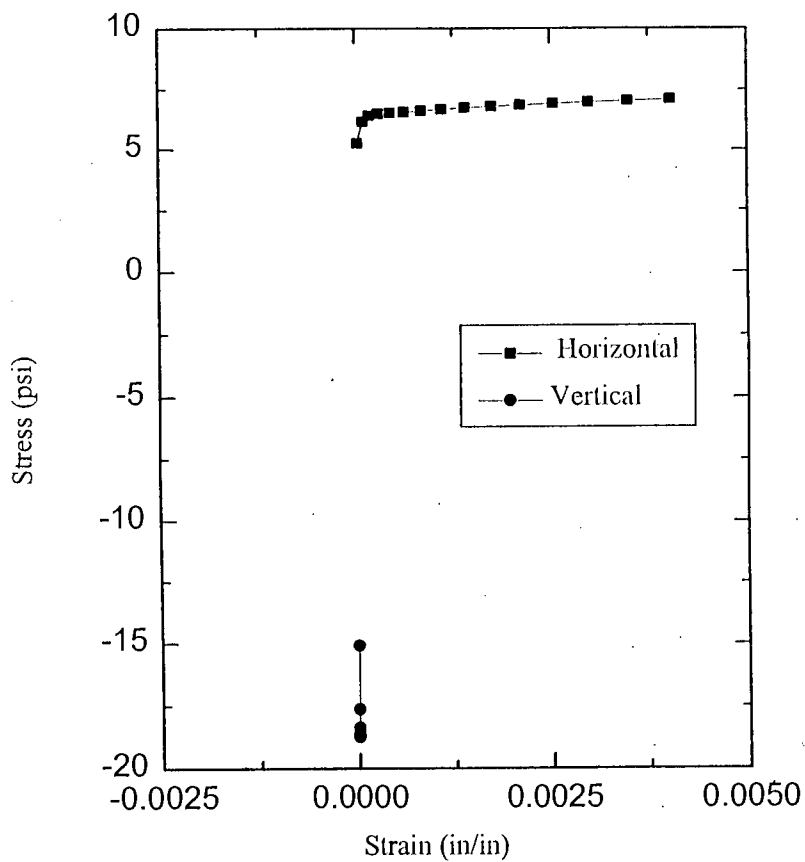

Figure 5-56(b): Stress vs Strain variation inside of Katona Type Interface for Case-4.

Shear strain (ε_1-ε_3) contour (in percent)
At Load step 5.

Figure 5-57(a):   Shear strain contour for Case-4 of Katona Type Interface at load step-5.

Shear strain (ε_1-ε_3) contour (in percent)
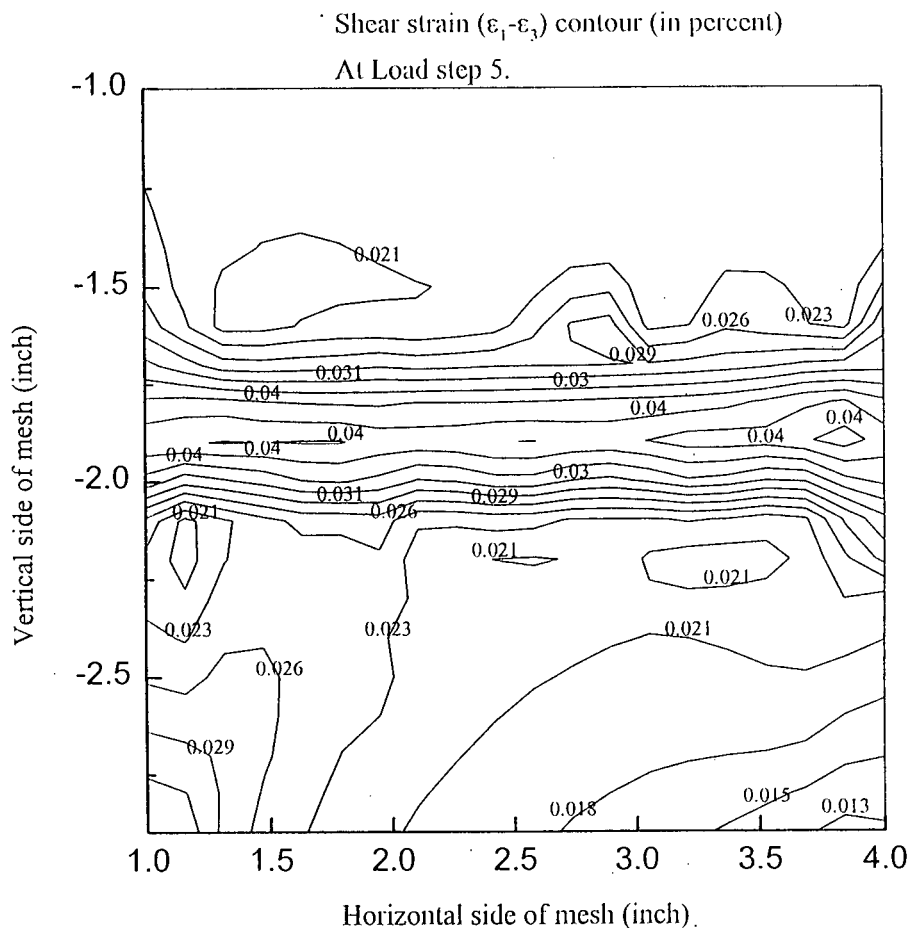At Load step 10.

Figure 5-57(b):   Shear strain contour for Case-4 of Katona Type Interface at load step-10.

215

Figure 5-57(c):   Shear strain contour for Case-4 of Katona Type Interface at load step-15.

Figure 5-58(a): Displacement field for Case-4 of Katona Type Interface at load step-1.

Figure 5-58(b): Displacement field for Case-4 of Katona Type Interface at load step-5.

217

Figure 5-58(c): Displacement field for Case-4 of Katona Type Interface at load step-10.

Figure 5-58(d): Displacement field for Case-4 of Katona Type Interface at load step-15.

218

Figure 5-59(a): Average Force vs Displacement variation inside of Katona Type
Interface for Case-5

Figure 5-59(b): Stress vs Strain variation inside of Katona Type Interface for
Case-5.

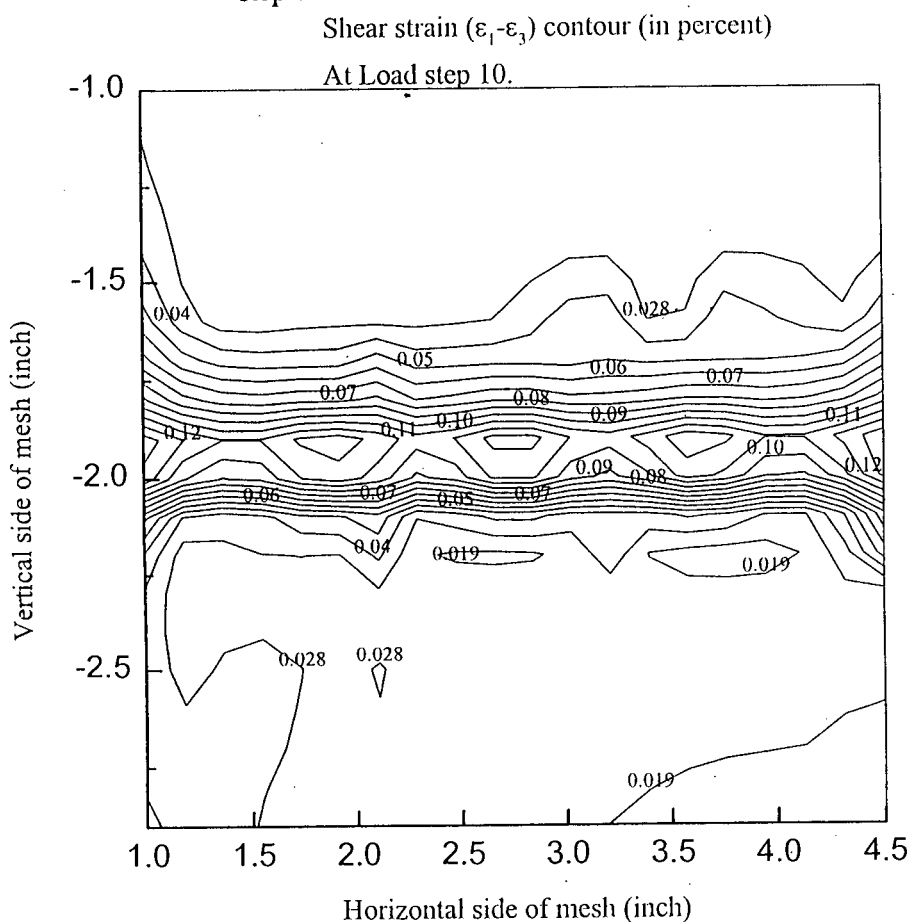Figure 5-60(a): Shear strain contour for Case-5 of Katona Type Interface at load step-5.

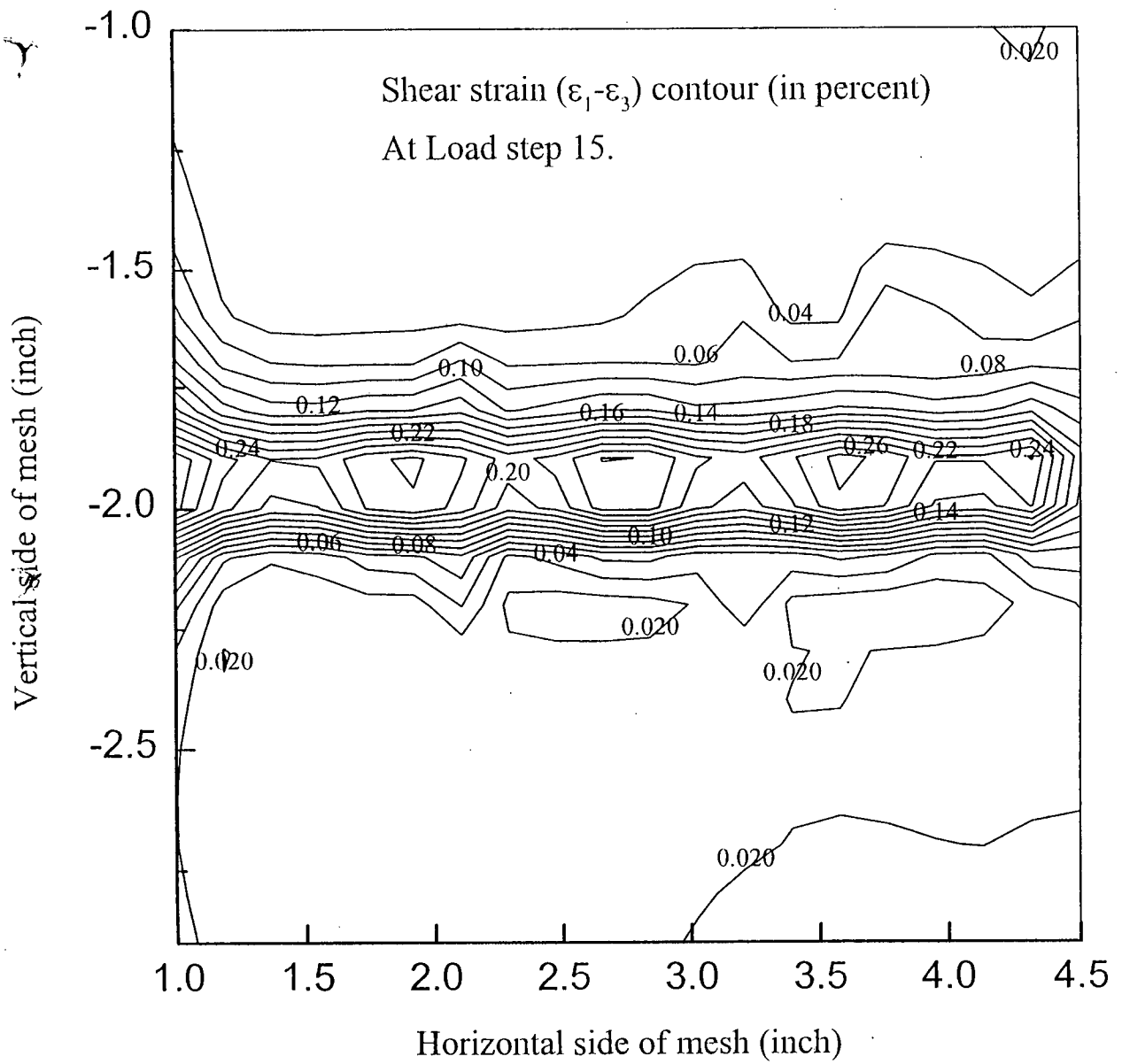Figure 5-60(b): Shear strain contour for Case-5 of Katona Type Interface at load step-10.

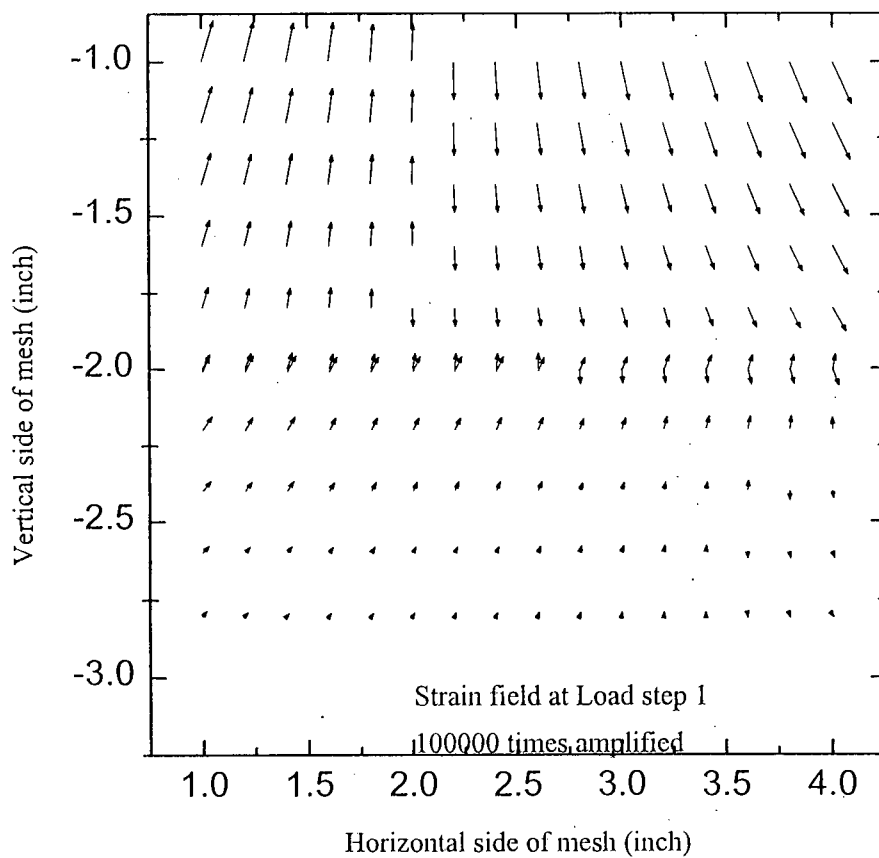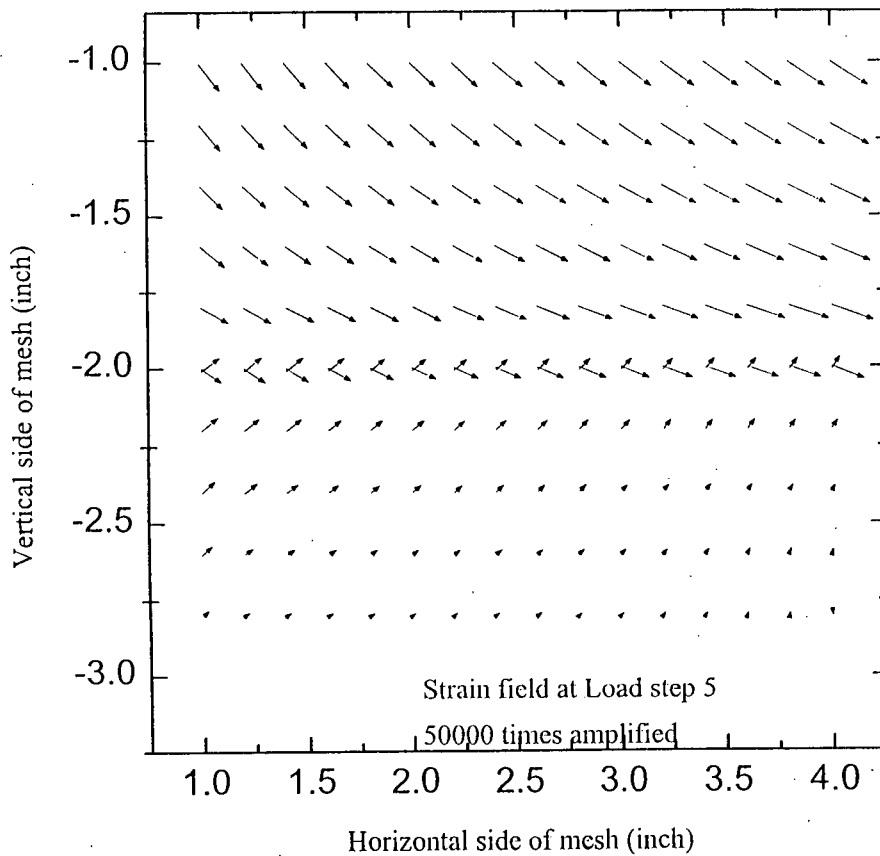Figure 5-60(c): Shear strain contour for Case-5 of Katona Type Interface at load step-15.

Strain field at Load step 1
100000 times amplified

Horizontal side of mesh (inch)

Figure 5-61(a):   Displacement field for Case-5 of Katona Type Interface at load
                   step-1.

Strain field at Load step 5
50000 times amplified

Horizontal side of mesh (inch)

Figure 5-61(b):   Displacement field for Case-5 of Katona Type Interface at load
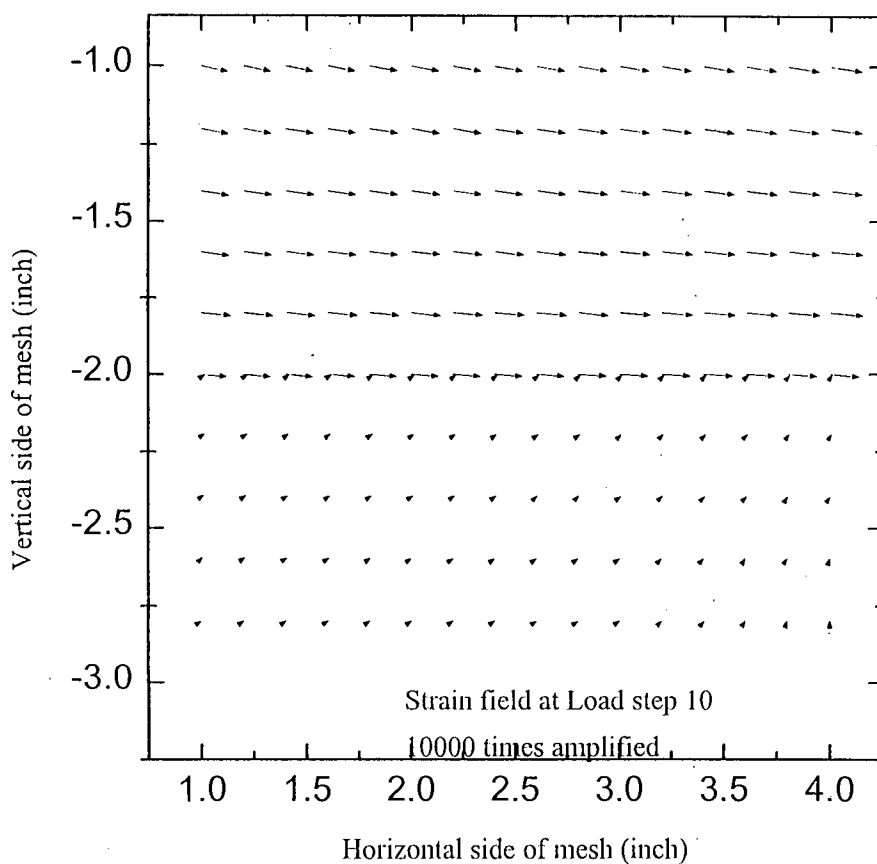   step-5.

Figure 5-61(c):   Displacement field for Case-5 of Katona Type Interface at load
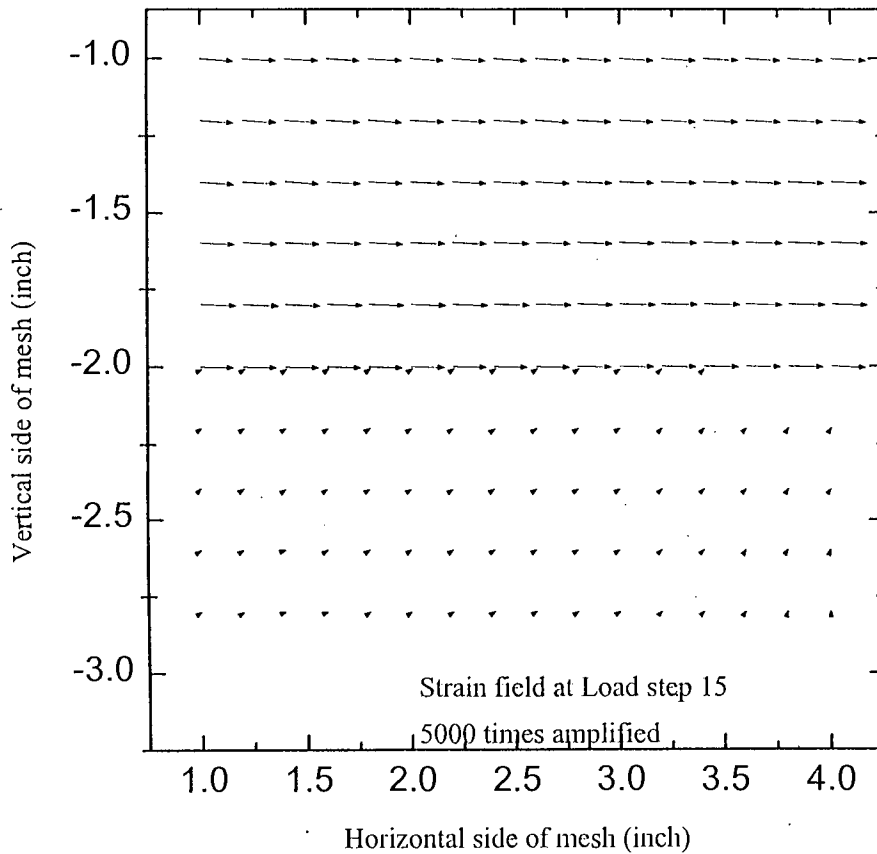step-10.

Figure 5-61(d):   Displacement field for Case-5 of Katona Type Interface at load
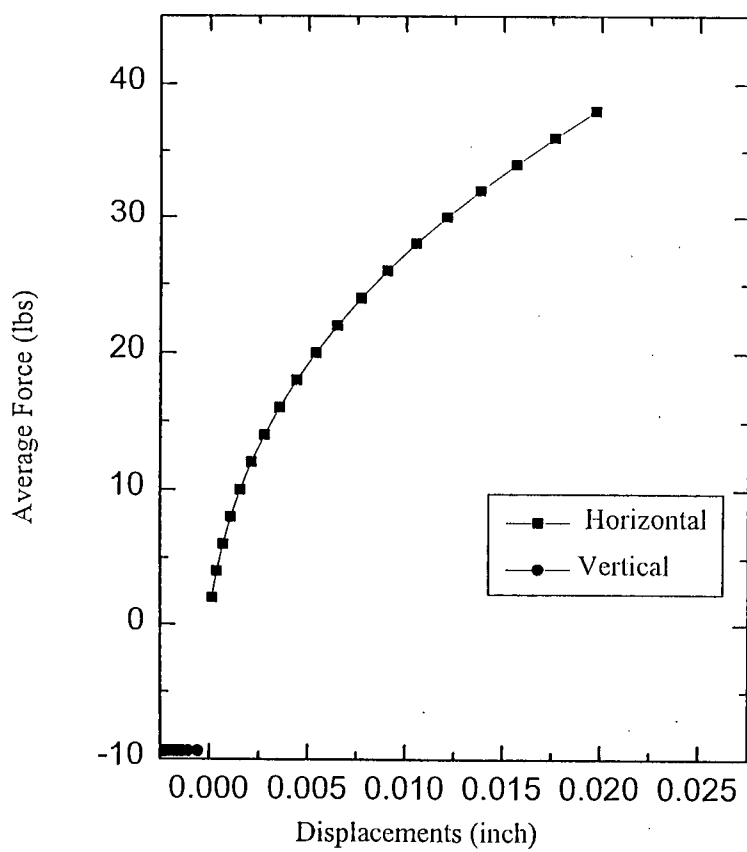step-15.

Figure 5-62(a): Average Force vs Displacement variation inside of Desai Type Interface for Case-1
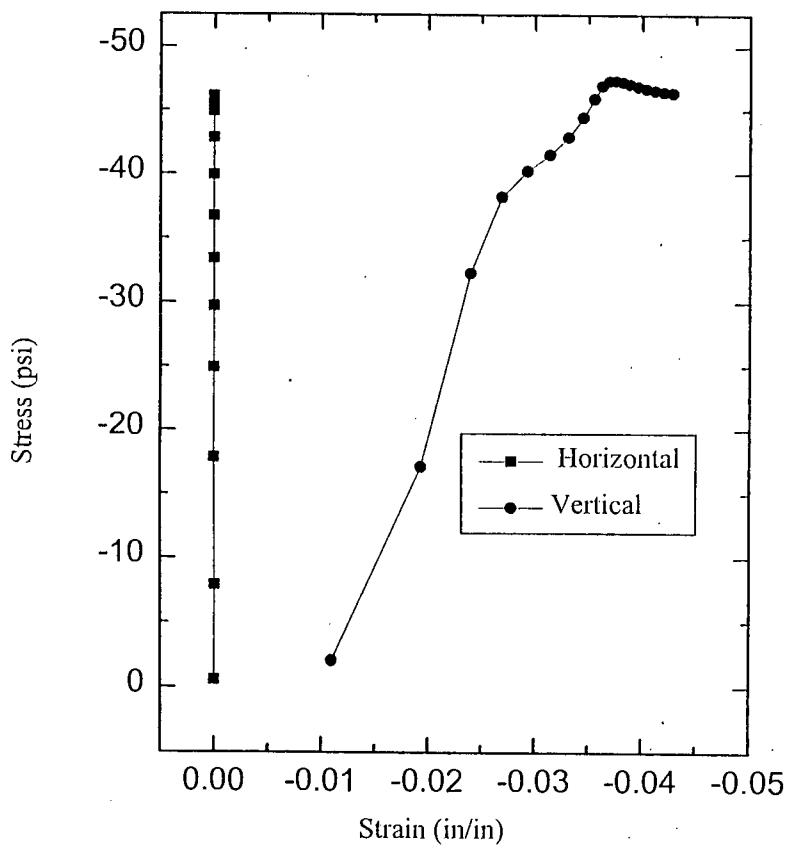

Figure 5-62(b): Stress vs Strain variation inside of Desai Type Interface for Case-1.
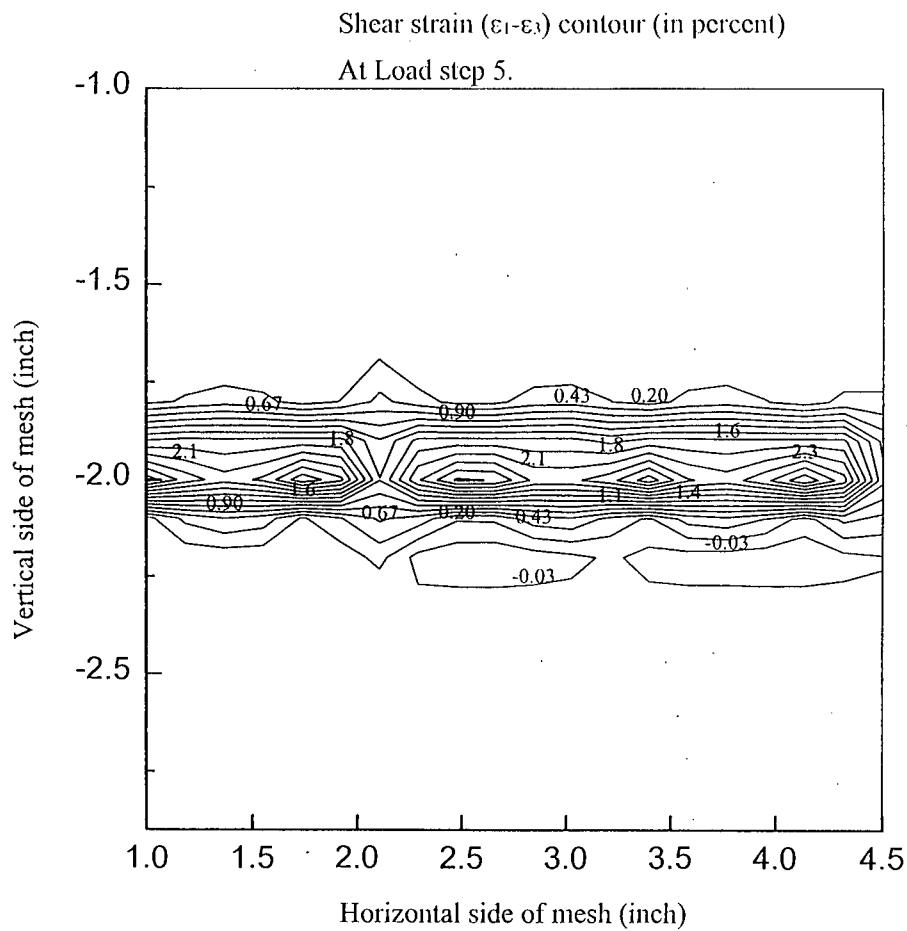
Figure 5-63(a):   Shear strain contour for Case-1 of Desai Type Interface at load step-5.
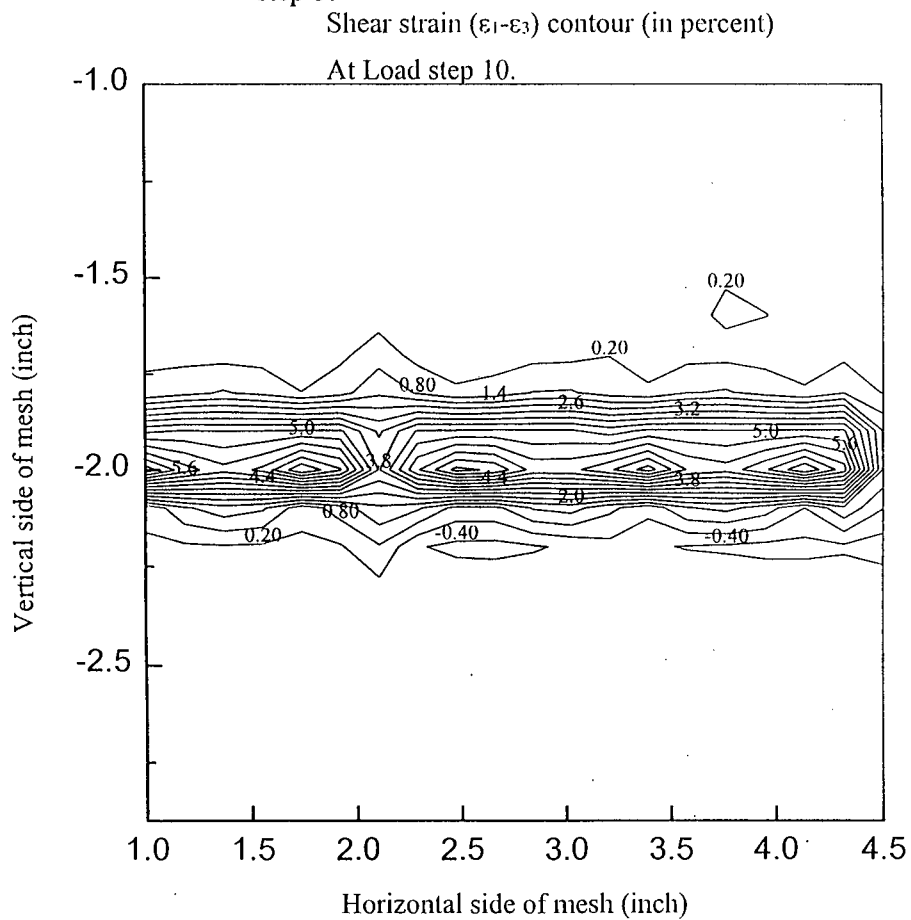
Figure 5-63(b):   Shear strain contour for Case-1 of Desai Type Interface at load step-10.
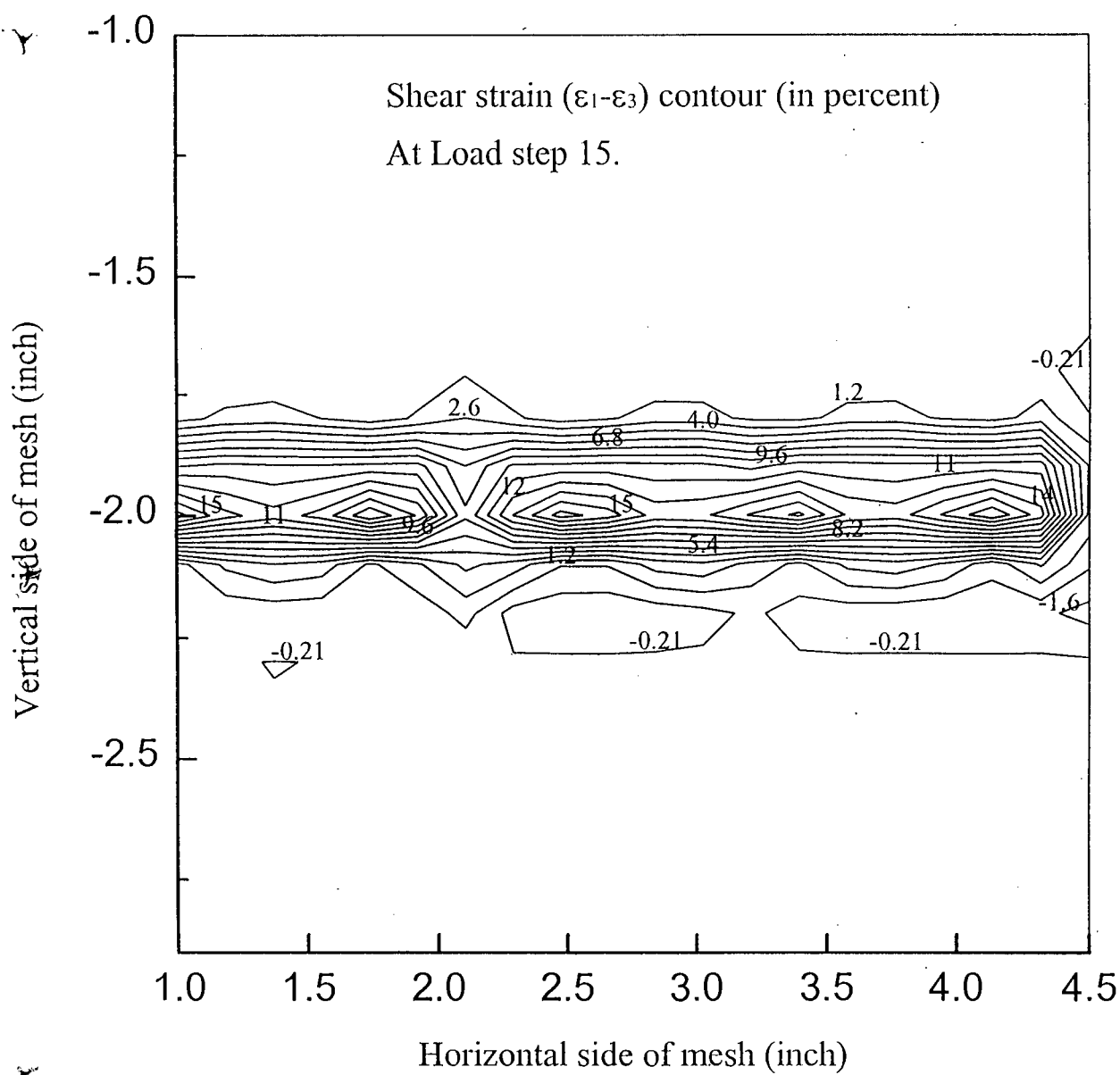
Figure 5-63(c): Shear strain contour for Case-1 of Desai Type Interface at load step-15.
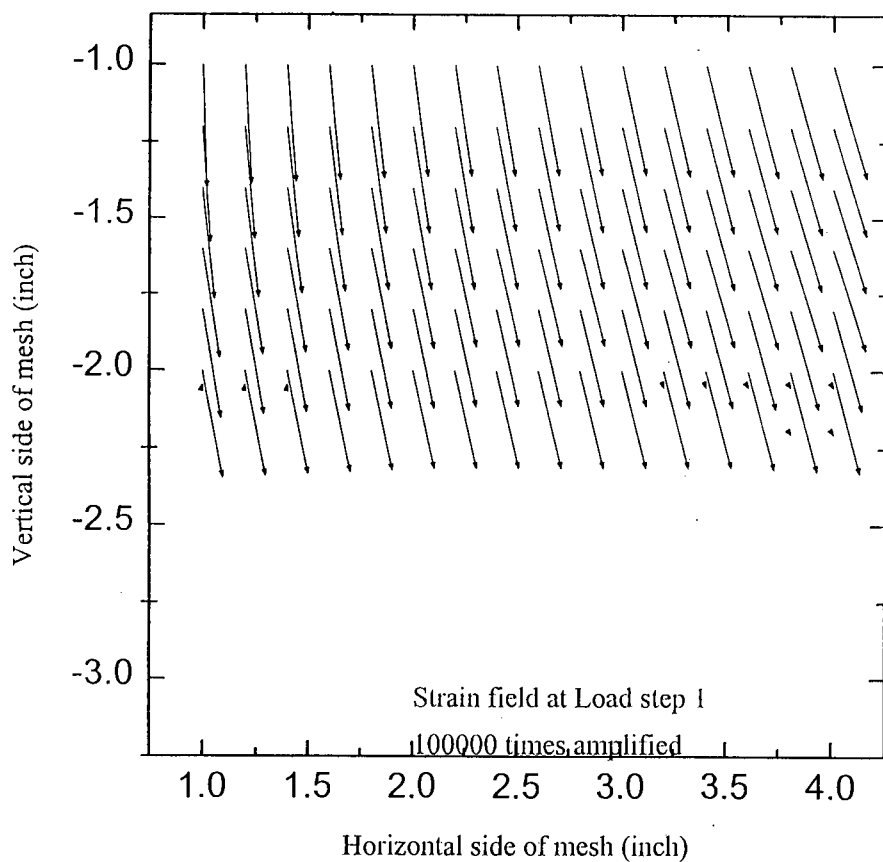
Figure 5-64(a): Displacement field for Case-1 of Desai Type Interface at load step-1.
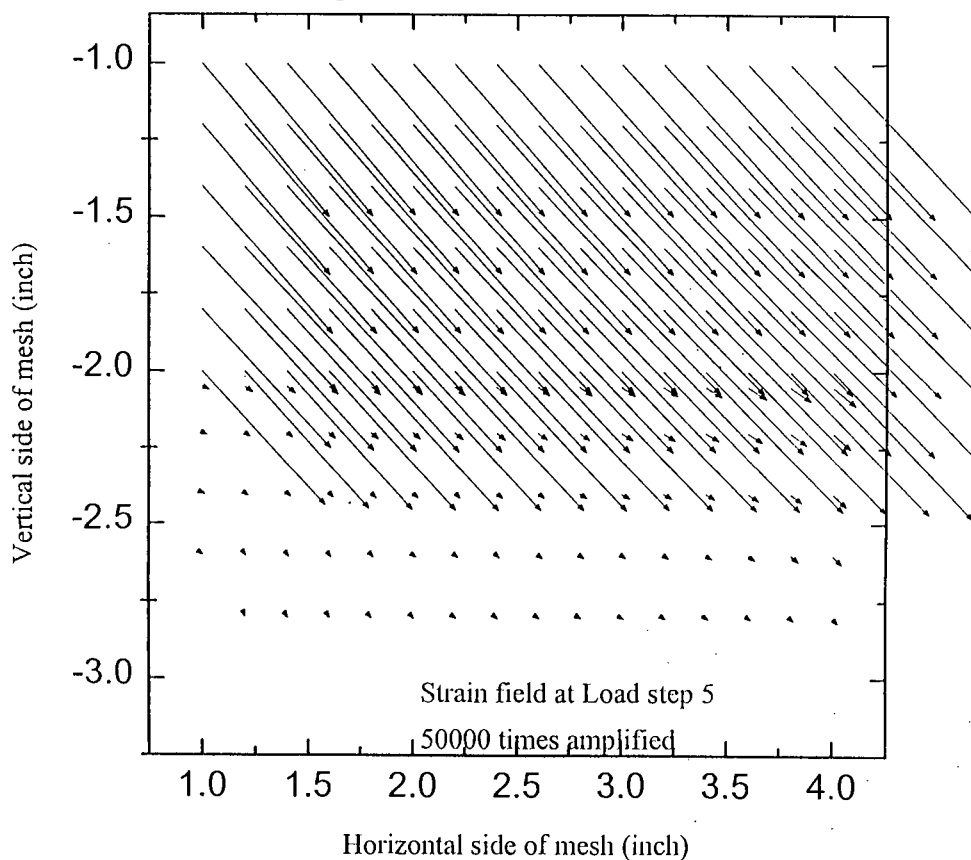

Figure 5-64(b): Displacement field for Case-1 of Desai Type Interface at load step-5.

Figure 5-64(c): Displacement field for Case-1 of Desai Type Interface at load
step-10.

Figure 5-64(d): Displacement field for Case-1 of Desai Type Interface at load
step-15.

Figure 5-65(a): Average Force vs Displacement variation inside of Desai Type Interface for Case-2

Figure 5-65(b): Stress vs Strain variation inside of Desai Type Interface for Case-2.

Shear strain ($\varepsilon_1-\varepsilon_3$) contour (in percent)
At Load step 5.

Figure 5-66(a): Shear strain contour for Case-2 of Desai Type Interface at load step-5.

Shear strain ($\varepsilon_1-\varepsilon_3$) contour (in percent)
At Load step 10.

Figure 5-66(b): Shear strain contour for Case-2 of Desai Type Interface at load step-10.

Figure 5-66(c): Shear strain contour for Case-2 of Desai Type Interface at load step-15.

Figure 5-67(a): Displacement field for Case-2 of Desai Type Interface at load step-1.

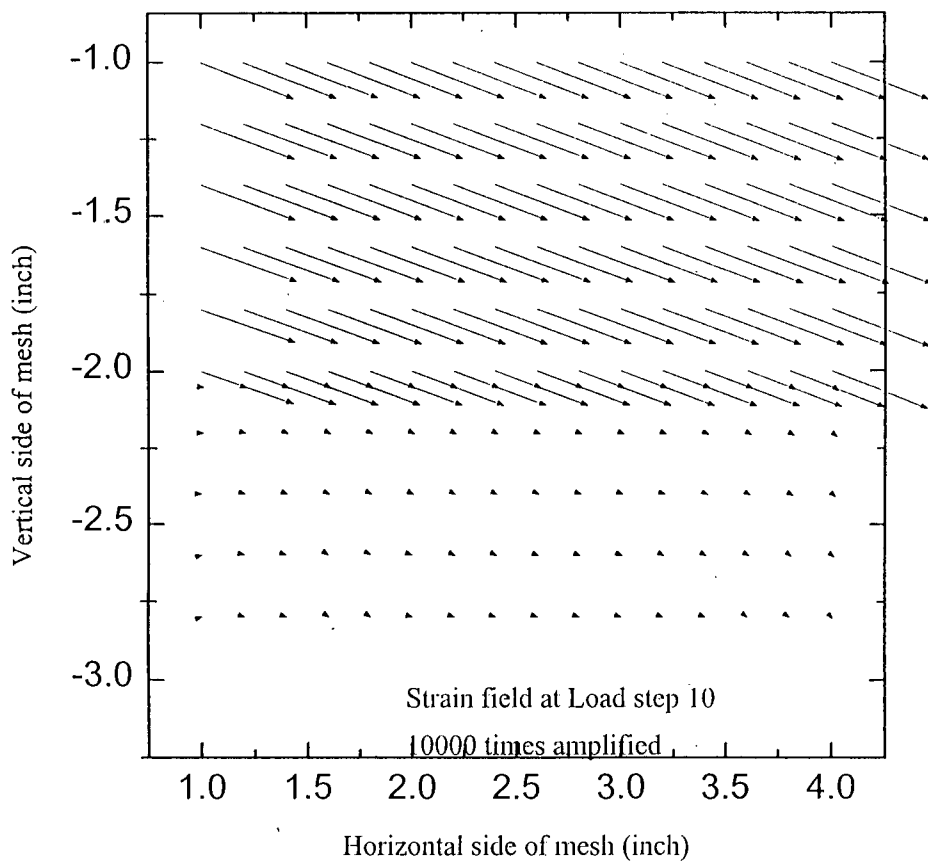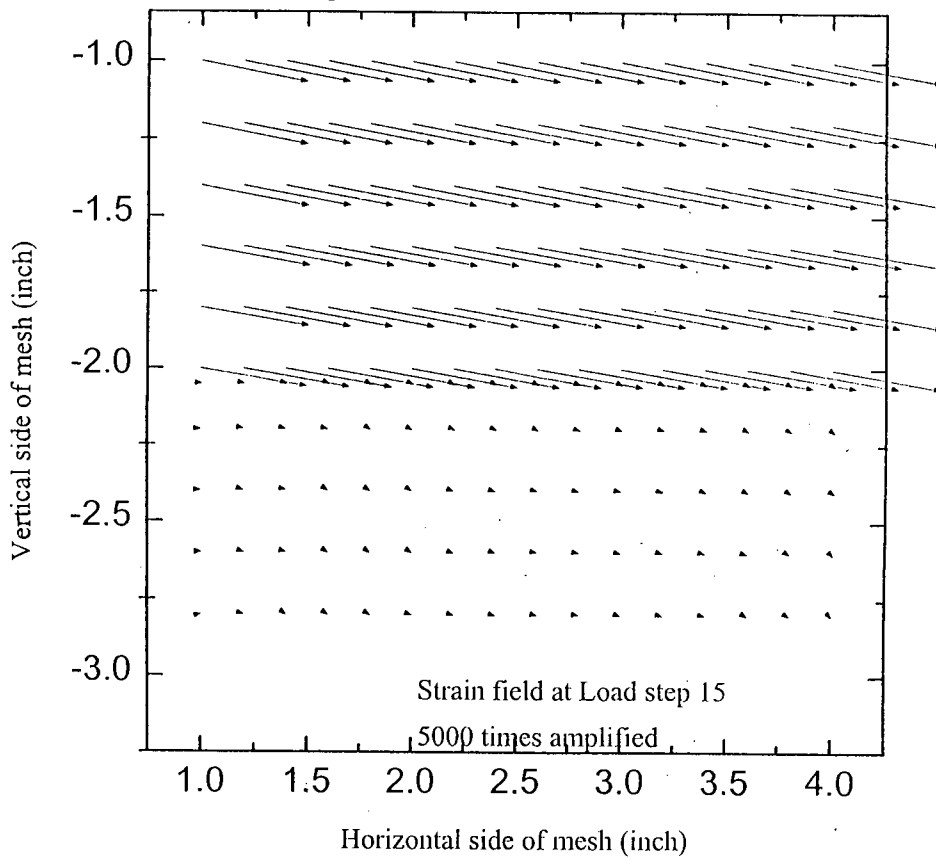Figure 5-67(b): Displacement field for Case-2 of Desai Type Interface at load step-5.

232

Figure 5-67(c): Displacement field for Case-2 of Desai Type Interface at load step-10.

Figure 5-67(d): Displacement field for Case-2 of Desai Type Interface at load step-15.
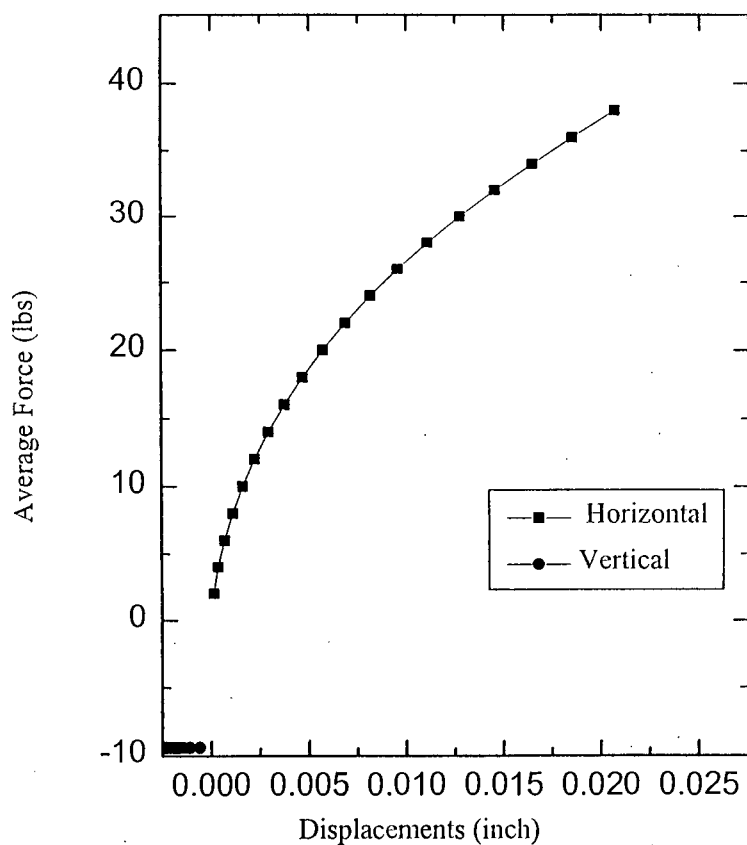
233

Figure 5-68(a): Average Force vs Displacement variation inside of Desai Type
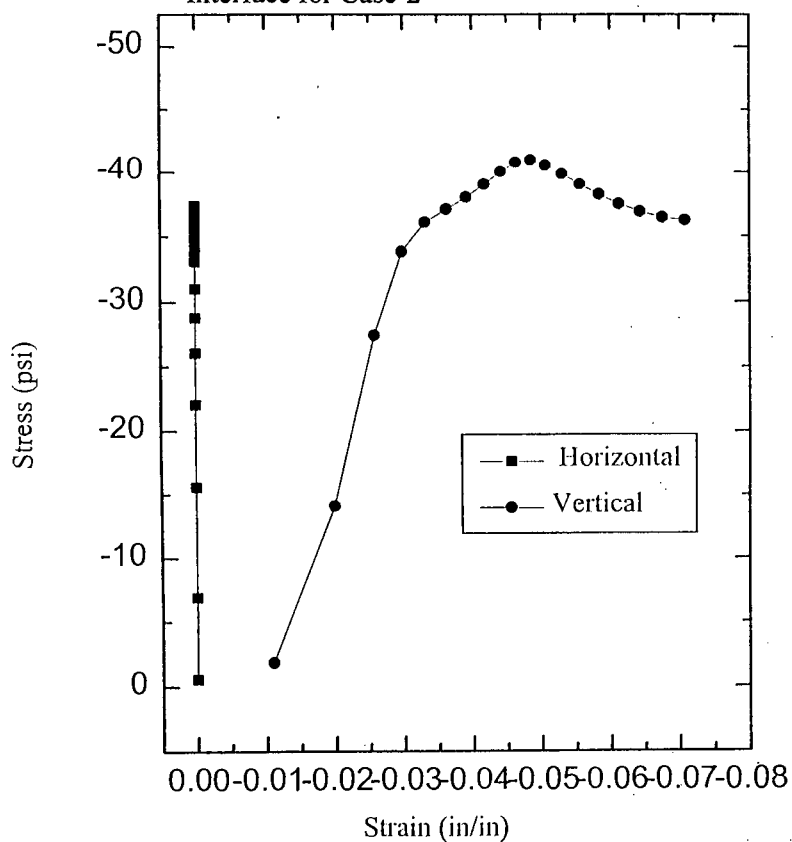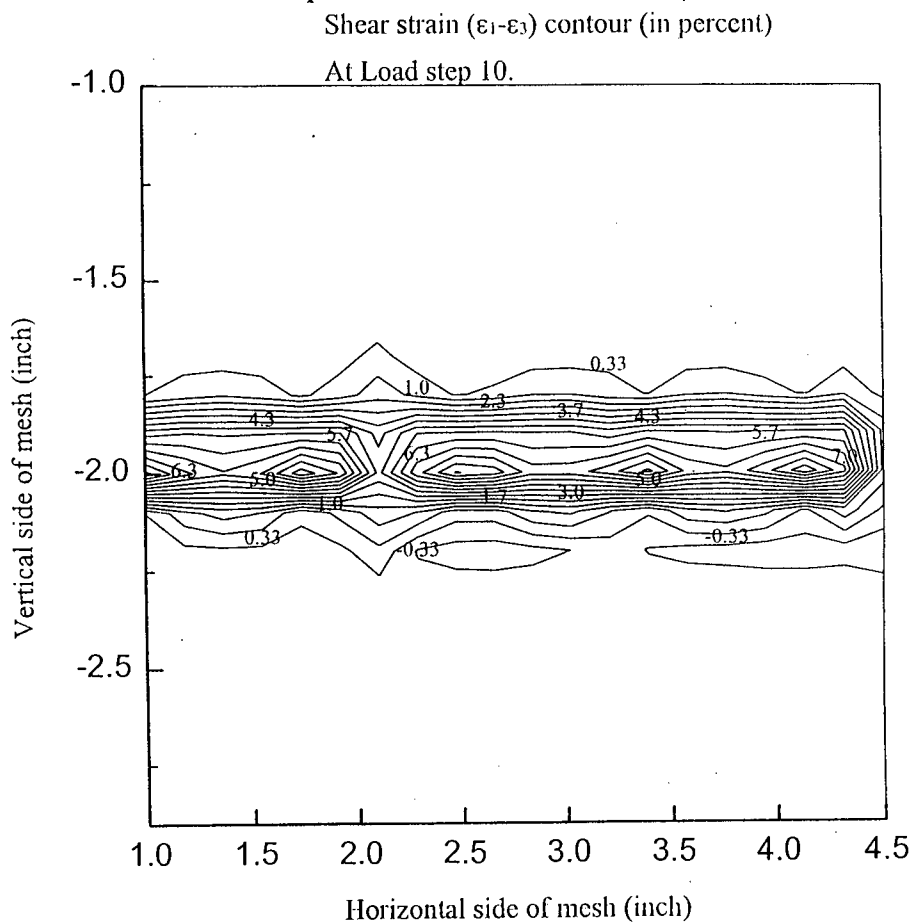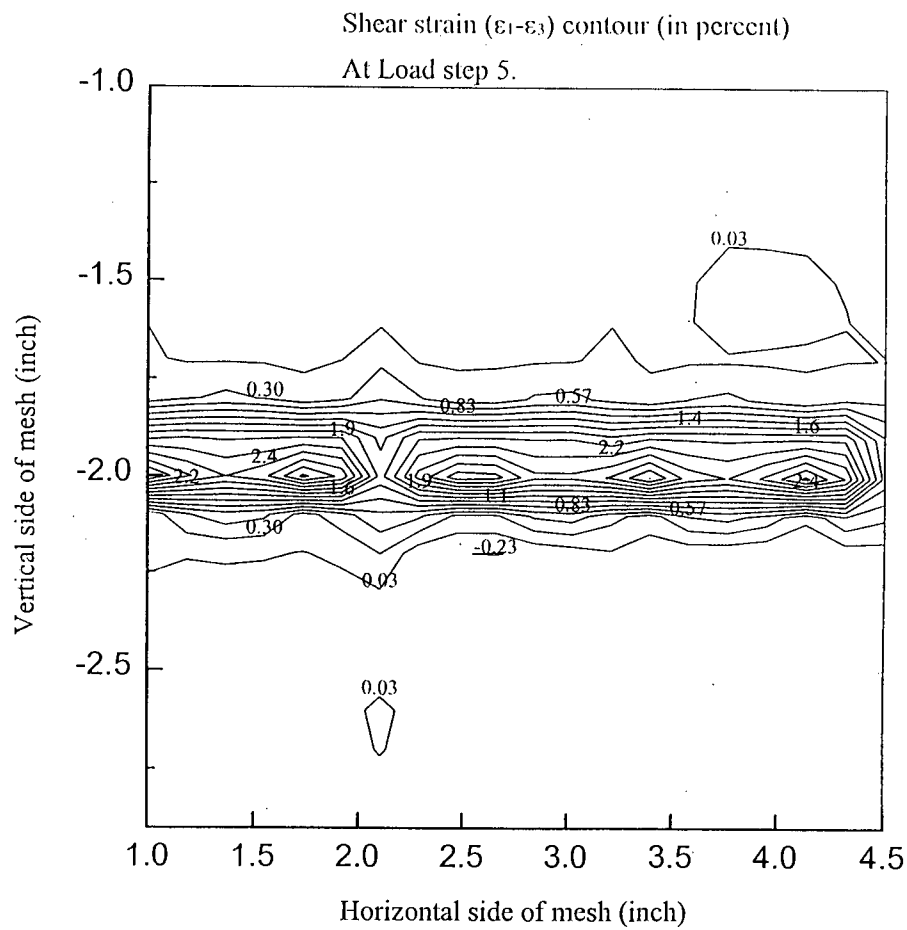Interface for Case-3
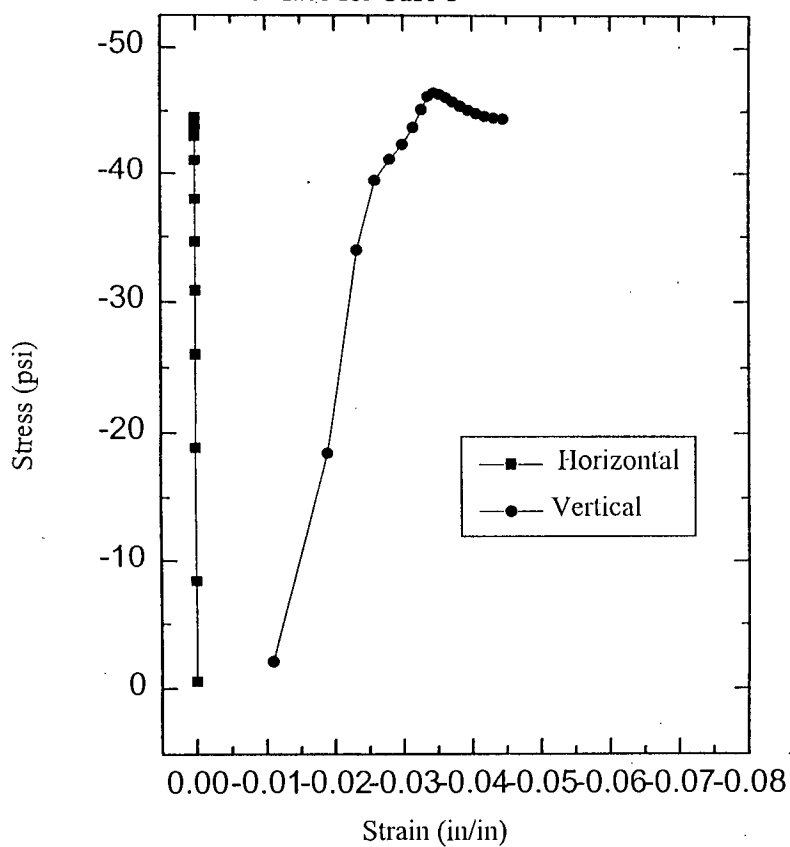
Figure 5-68(b): Stress vs Strain variation inside of Desai Type Interface for
Case-3.

234

Figure 5-69(a): Shear strain contour for Case-3 of Desai Type Interface at load step-5.

Figure 5-69(b): Shear strain contour for Case-3 of Desai Type Interface at load step-10.
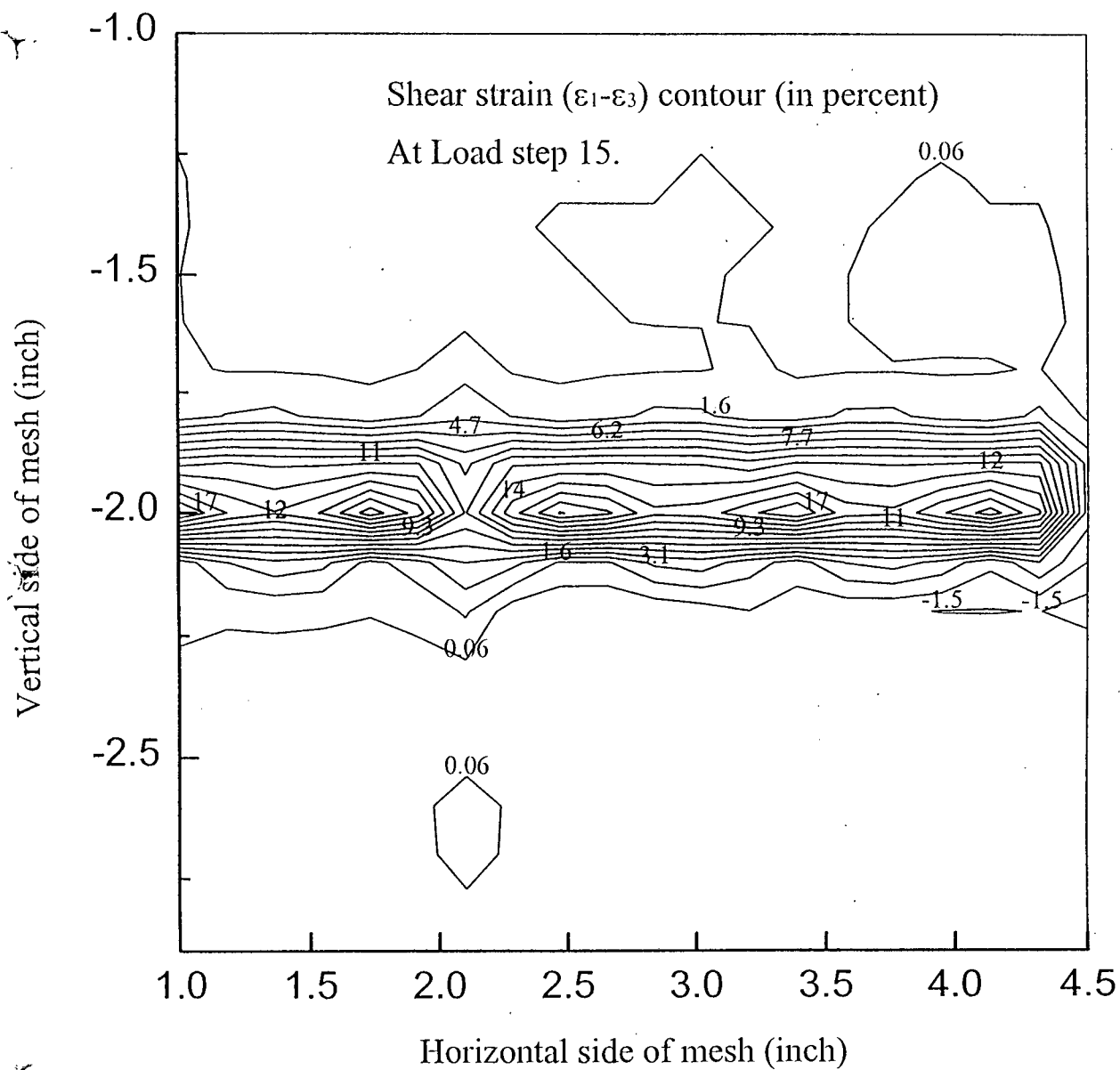
235

Figure 5-69(c): Shear strain contour for Case-3 of Desai Type Interface at load step-15.
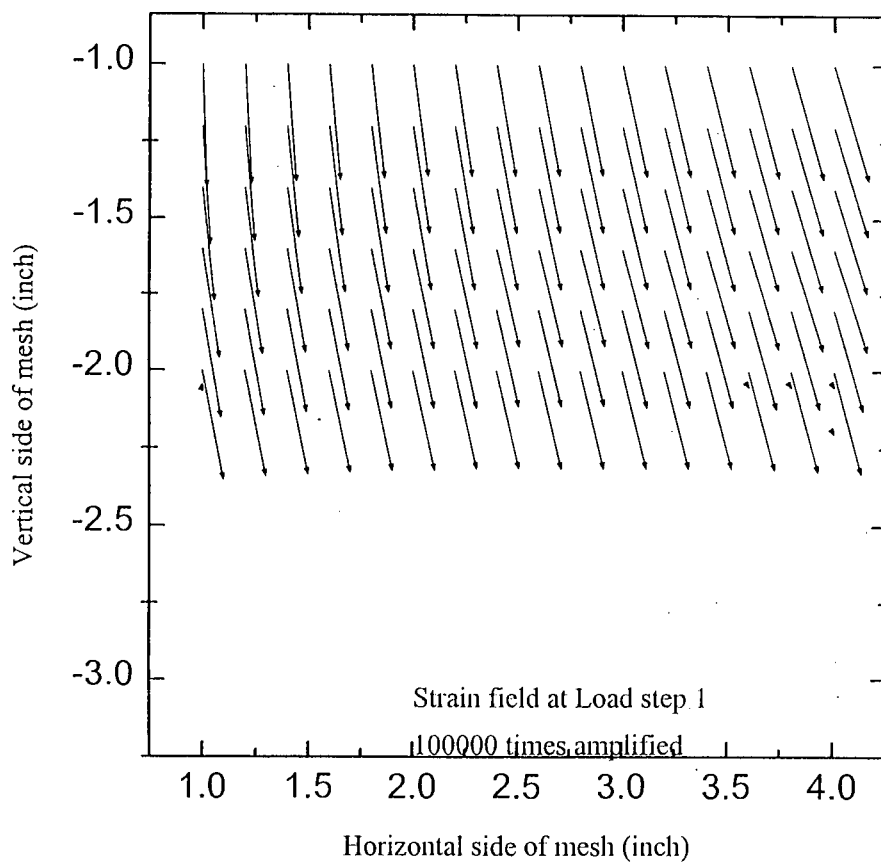
Figure 5-70(a): Displacement field for Case-3 of Desai Type Interface at load step-1.
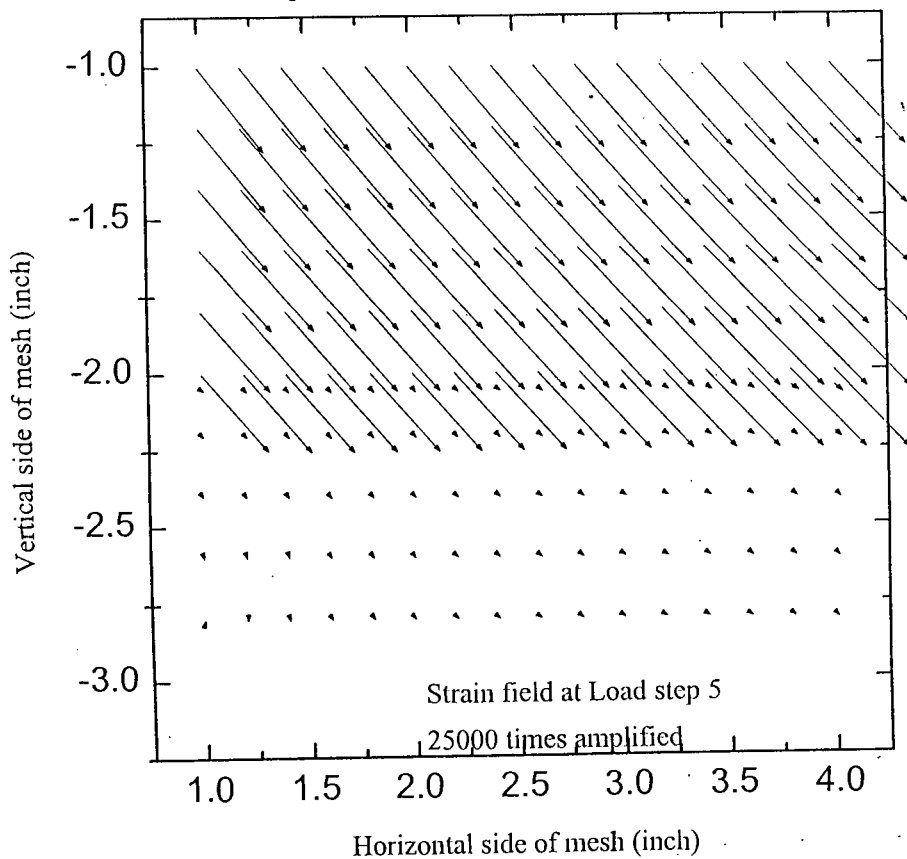

Figure 5-70(b): Displacement field for Case-3 of Desai Type Interface at load step-5.
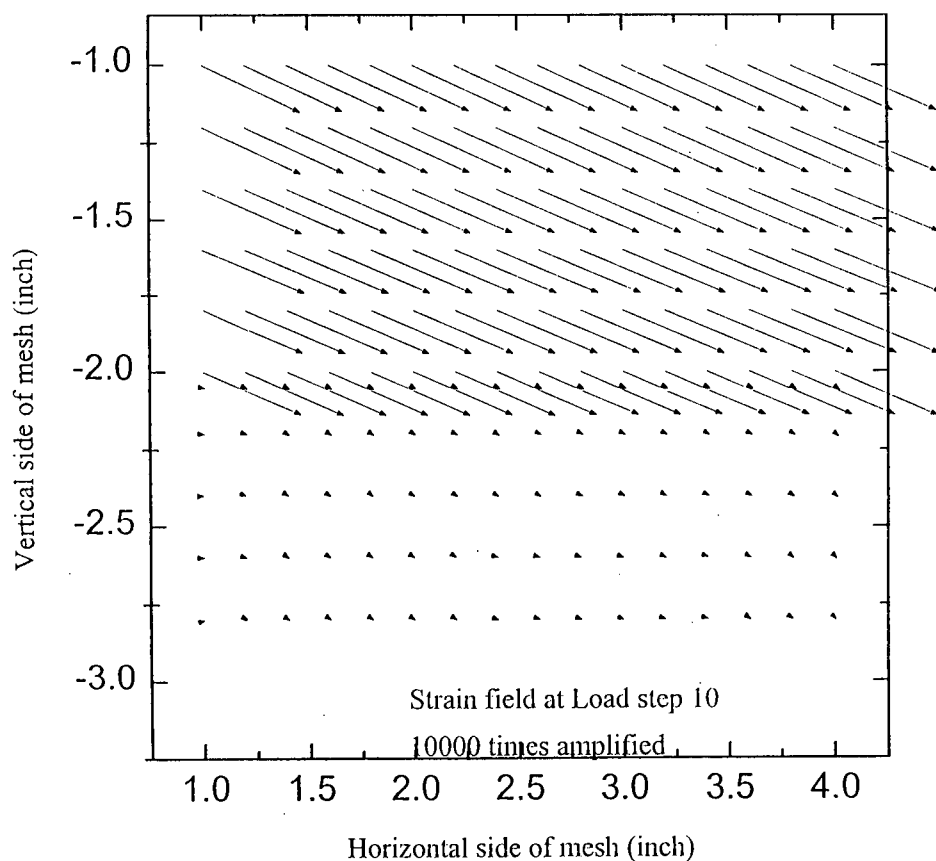
237

Figure 5-70(c): Displacement field for Case-3 of Desai Type Interface at load step-10.
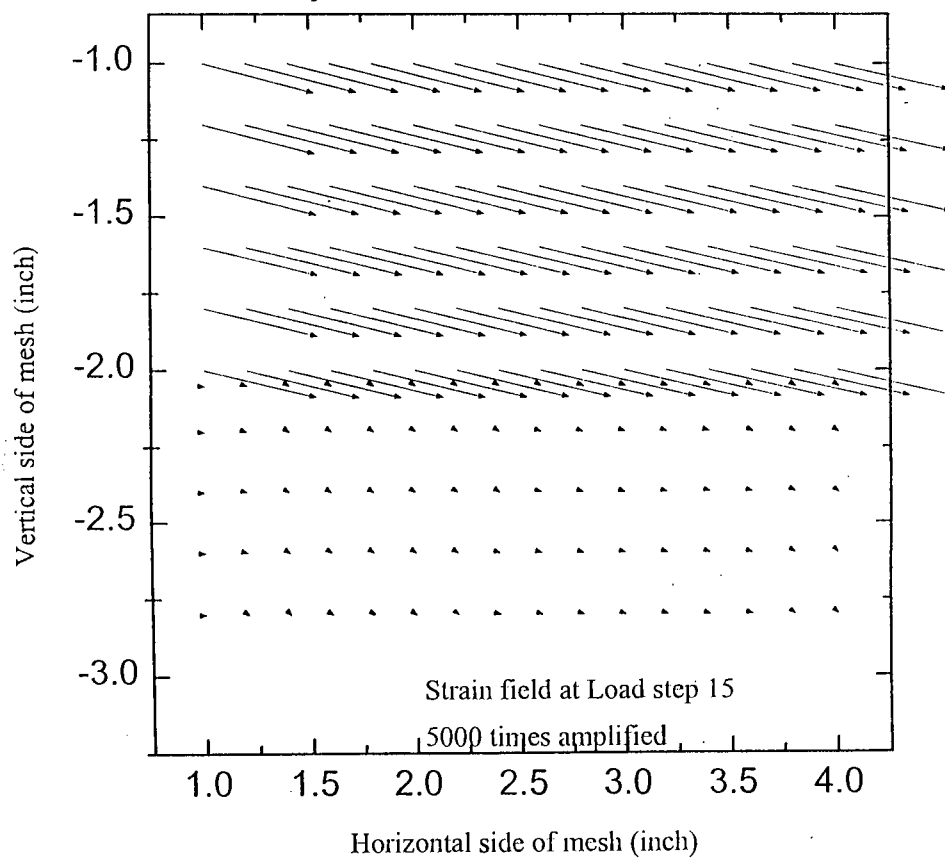

Figure 5-70(d): Displacement field for Case-3 of Desai Type Interface at load step-15.
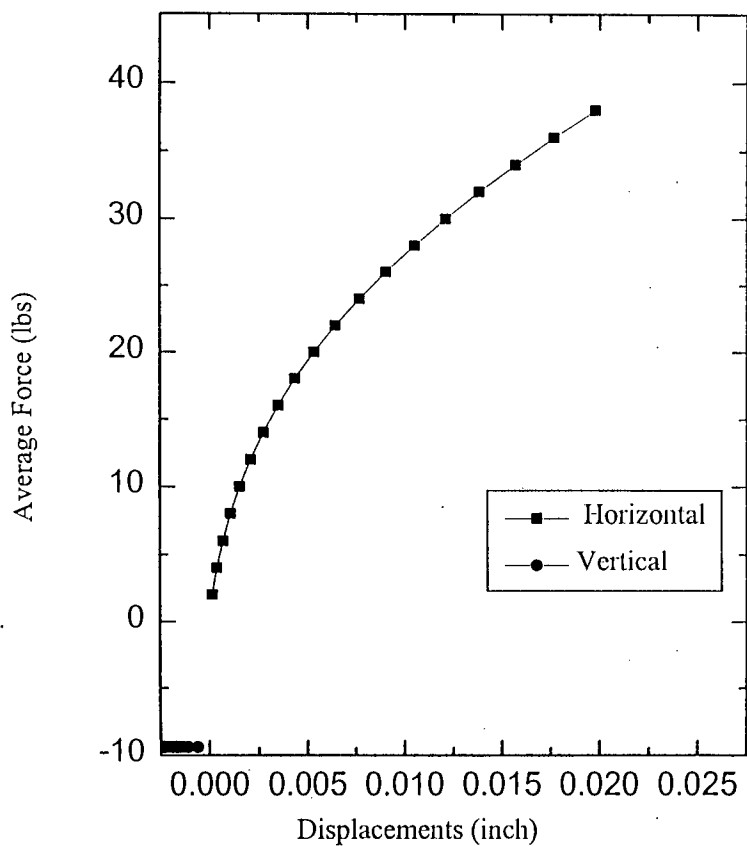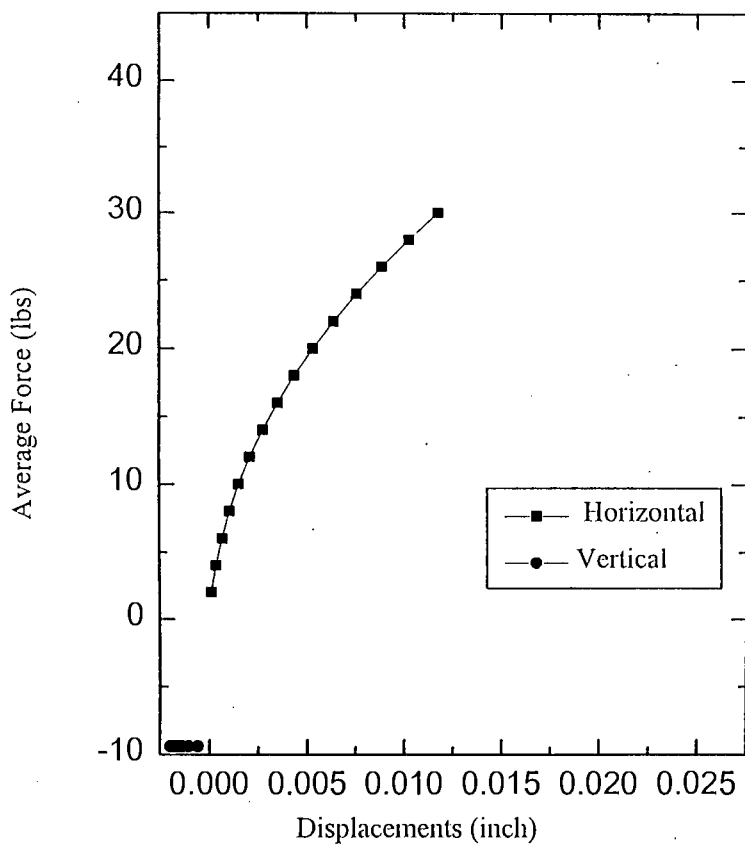
Figure 5-71(a): Average Force vs Displacement variation inside of Desai Type Interface for Case-4
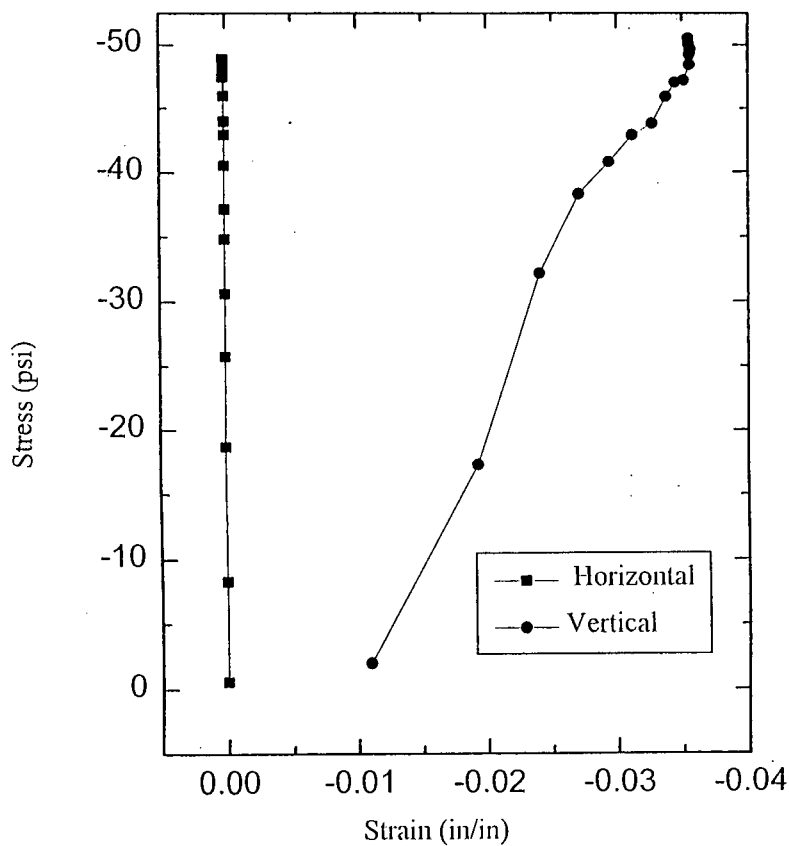
Figure 5-71(b): Stress vs Strain variation inside of Desai Type Interface for Case-4.

Shear strain (ε_1-ε_3) contour (in percent)
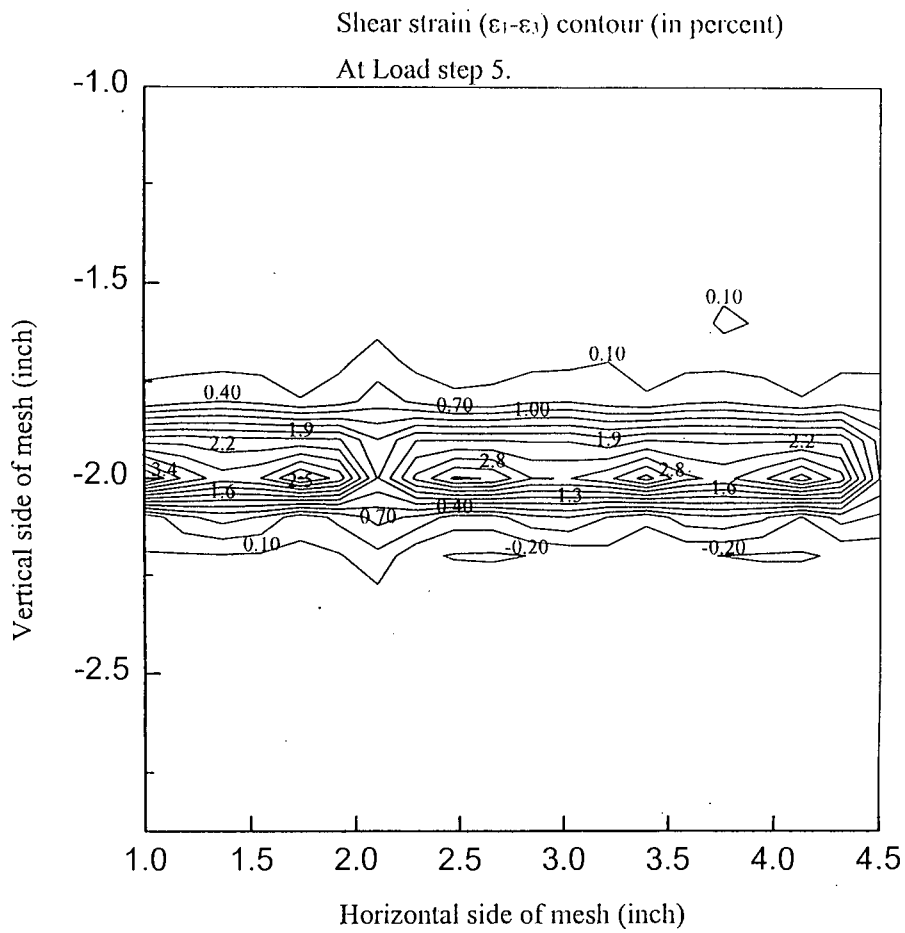
At Load step 5.

Figure 5-72(a): Shear strain contour for Case-4 of Desai Type Interface at load step-5.

Shear strain (ε_1-ε_3) contour (in percent)
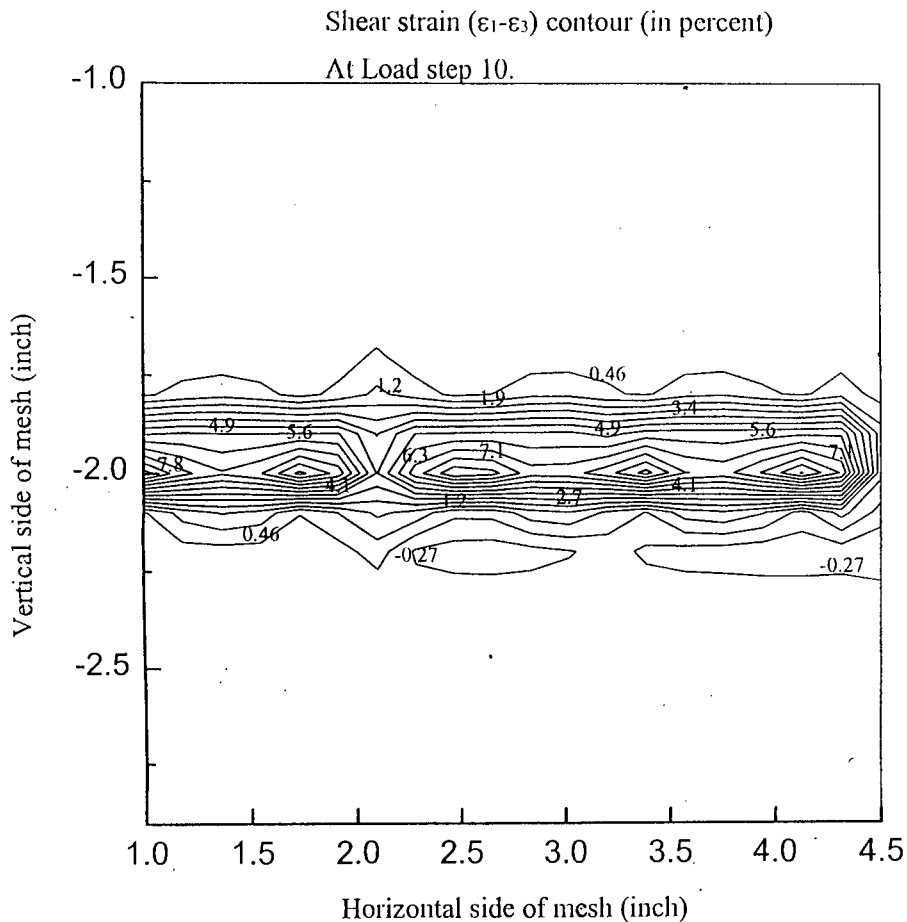
At Load step 10.

Figure 5-72(b): Shear strain contour for Case-4 of Desai Type Interface at load step-10.

240
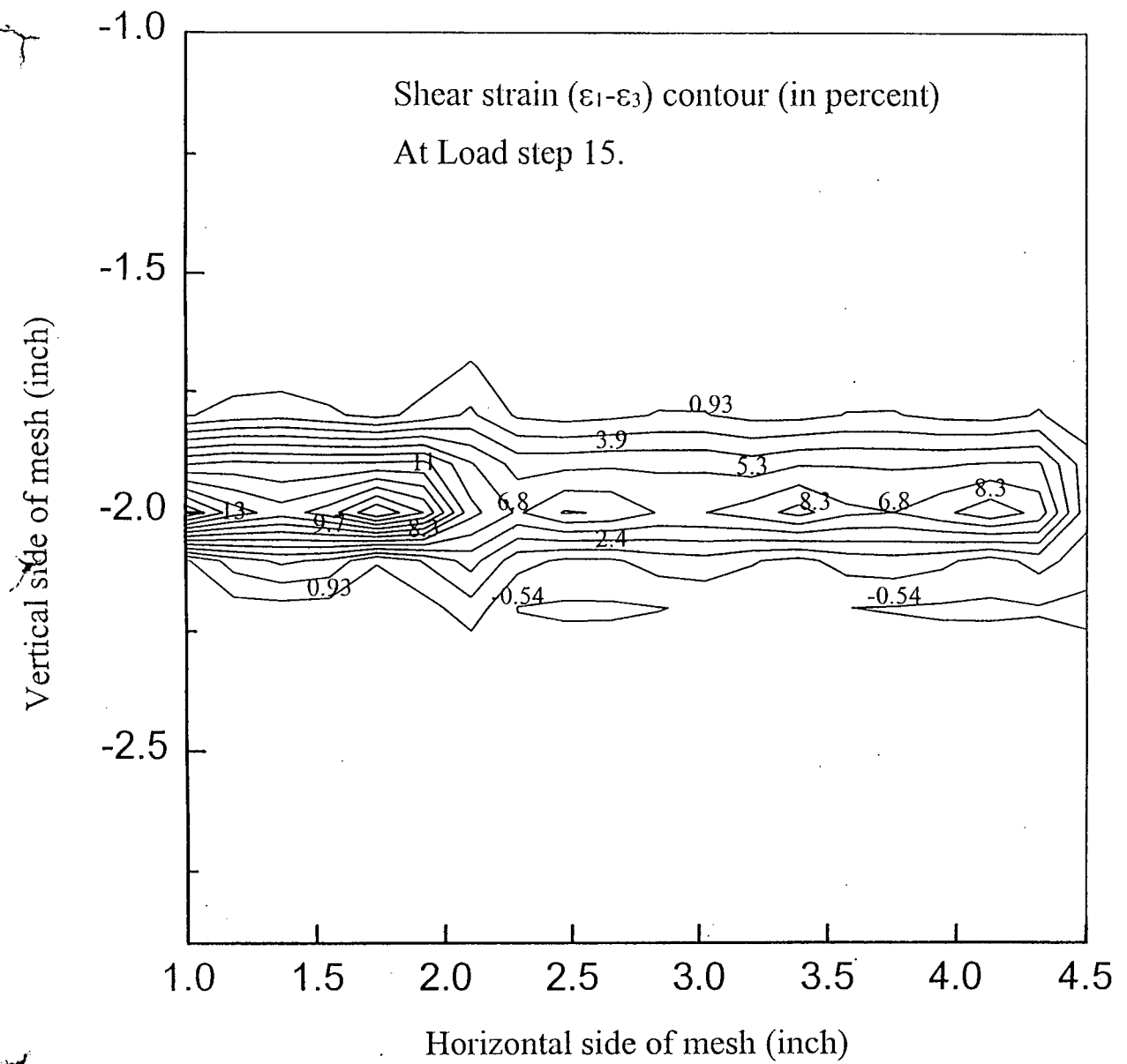
Figure 5-72(c):   Shear strain contour for Case-4 of Desai Type Interface at load step-15.
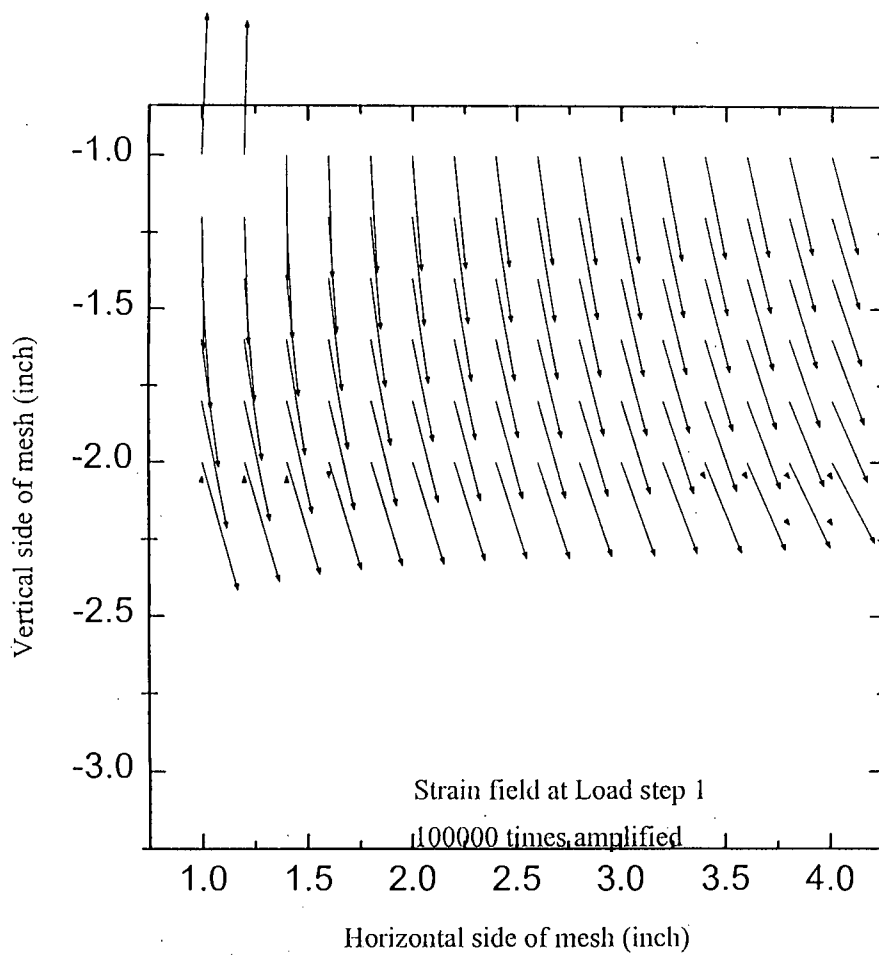
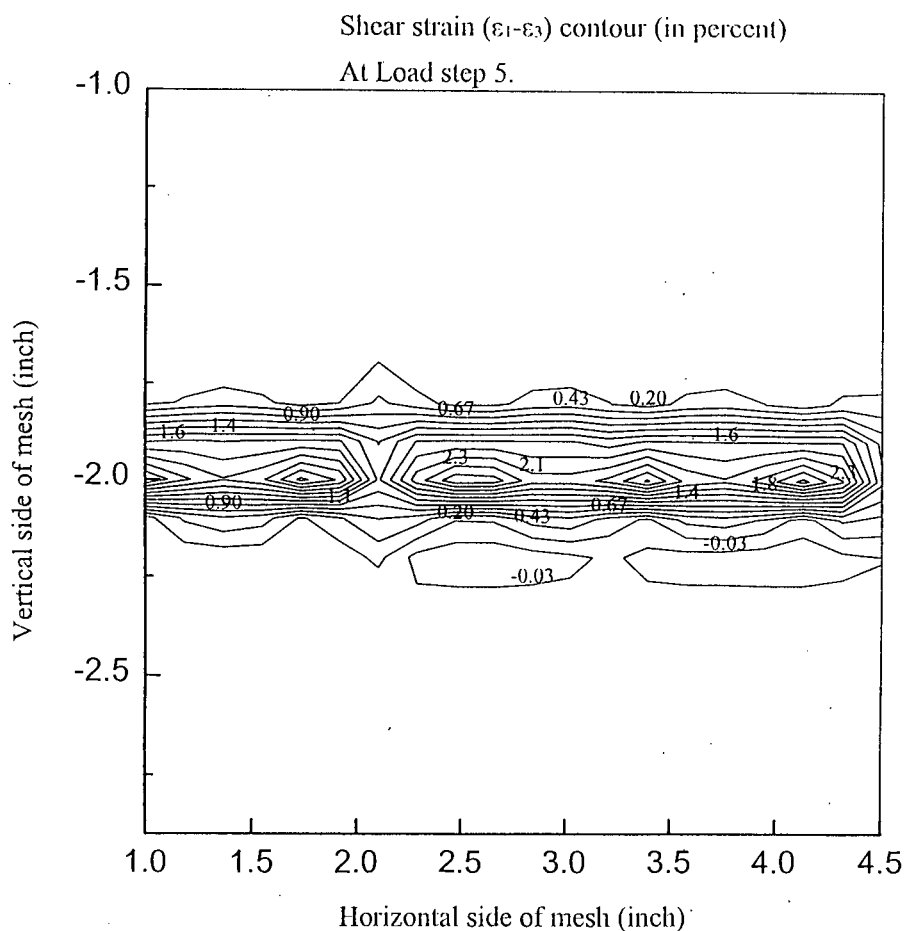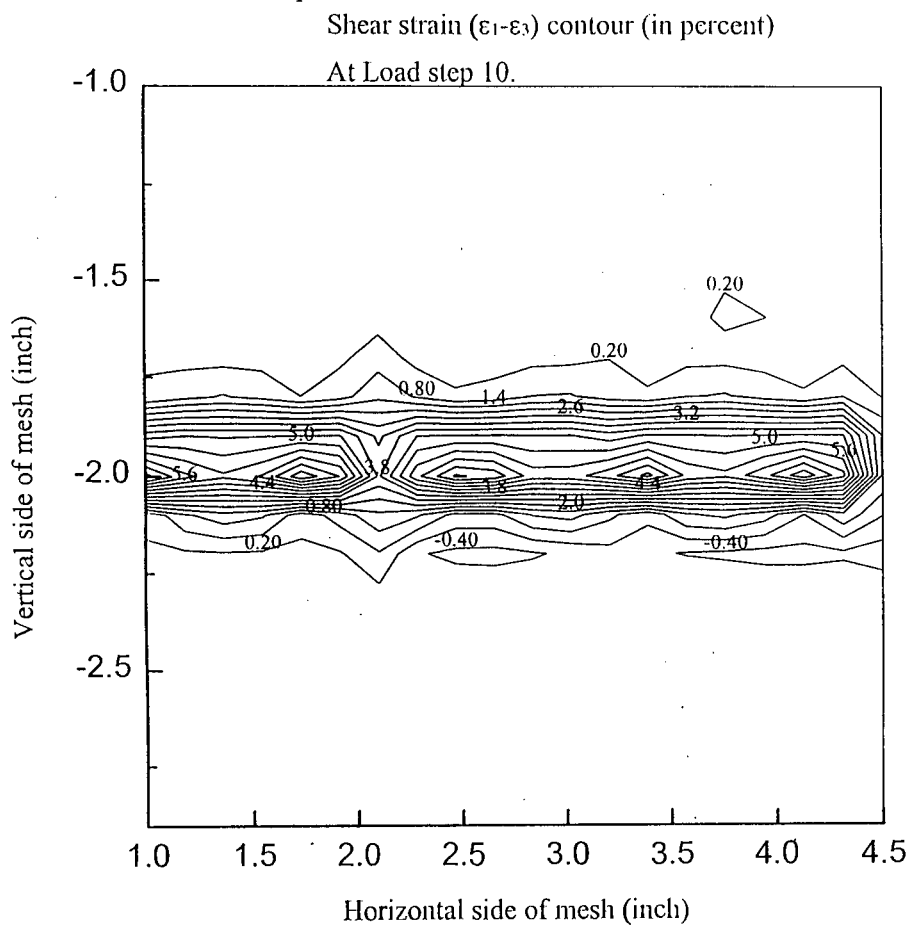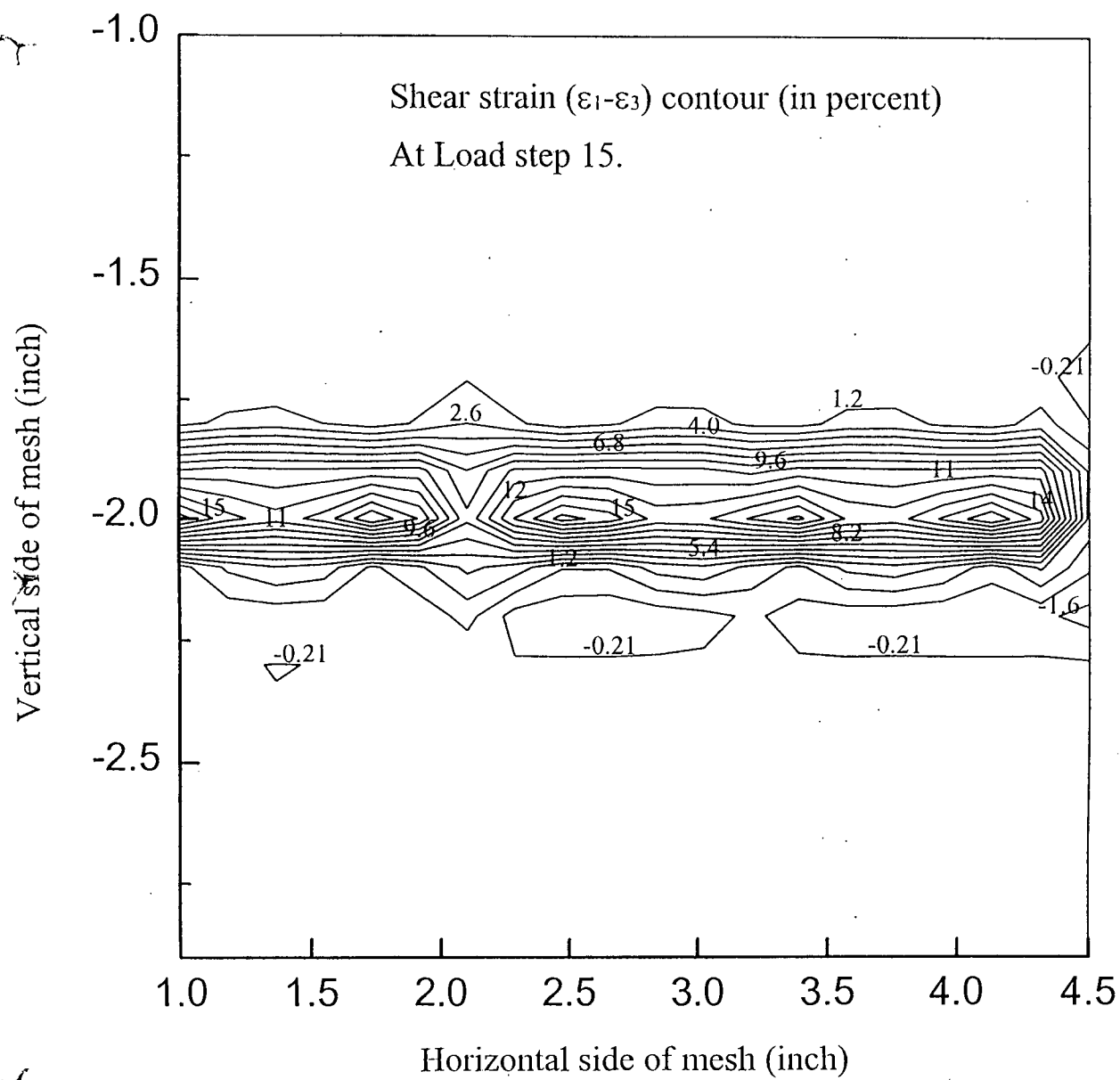Figure 5-73(a): Displacement field for Case-4 of Desai Type Interface at load step-1.
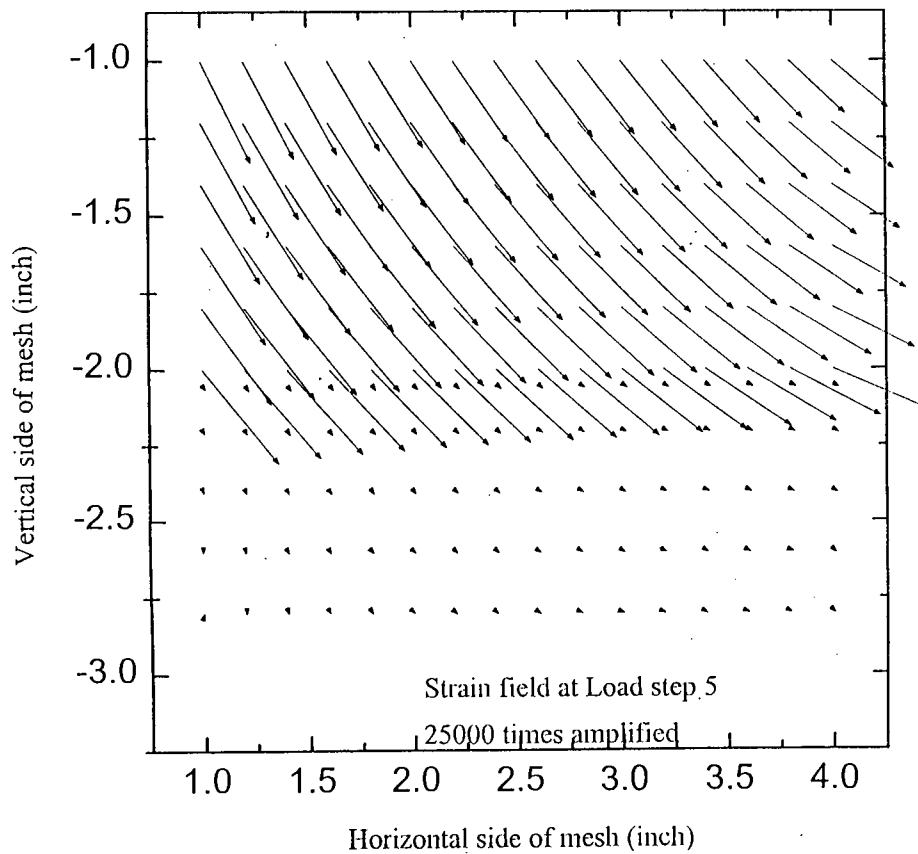
Figure 5-73(b): Displacement field for Case-4 of Desai Type Interface at load step-5.

Strain field at Load step 10
10000 times amplified

Horizontal side of mesh (inch)
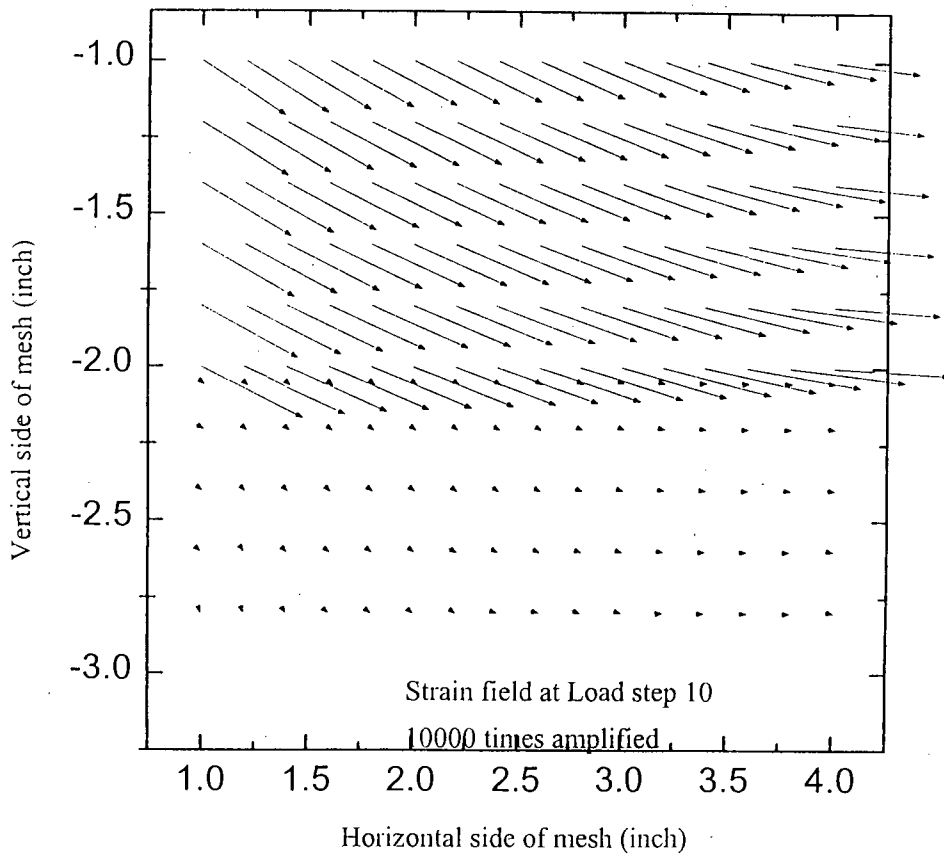
Figure 5-73(c):   Displacement field for Case-4 of Desai Type Interface at load step-10.

Strain field at Load step 15
5000 times amplified

Horizontal side of mesh (inch)

Figure 5-73(d):   Displacement field for Case-4 of Desai Type Interface at load step-15.

243
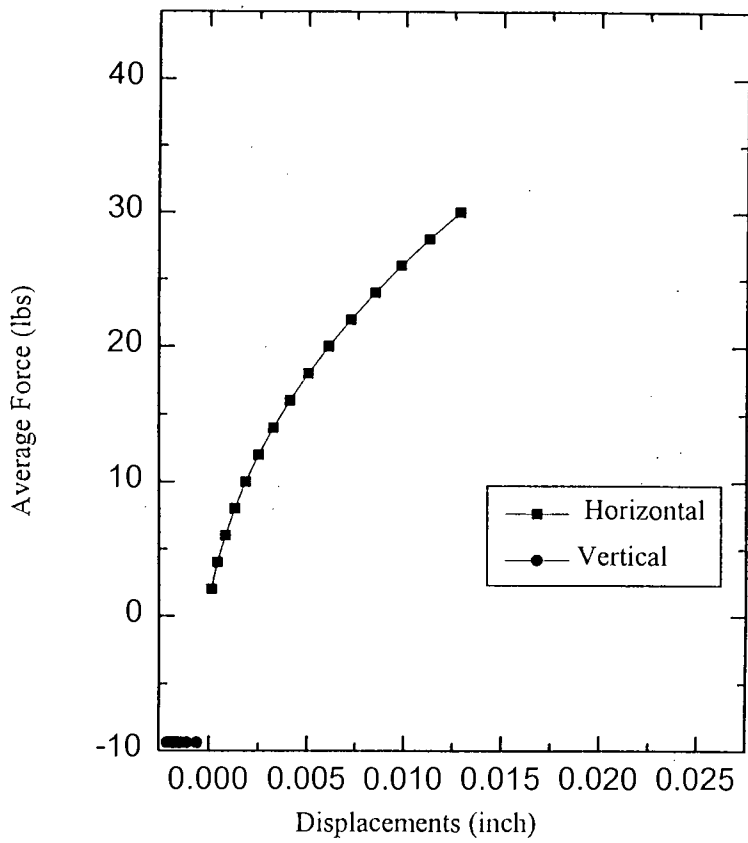
Figure 5-74(a): Average Force vs Displacement variation inside of Desai Type Interface for Case-5
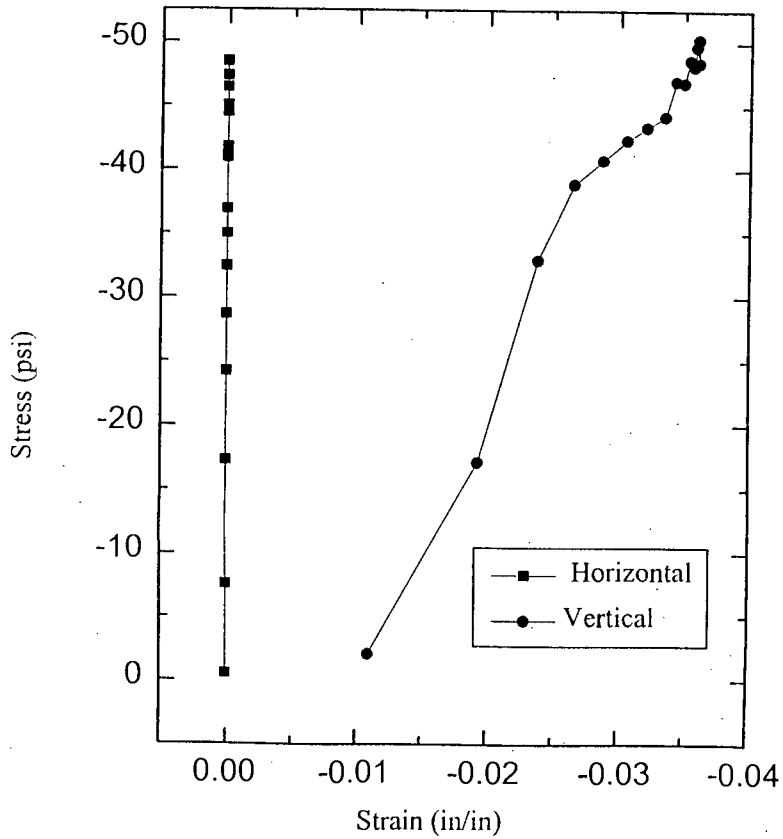
Figure 5-74(b): Stress vs Strain variation inside of Desai Type Interface for Case-5.

244

Shear strain (ε₁-ε₃) contour (in percent)
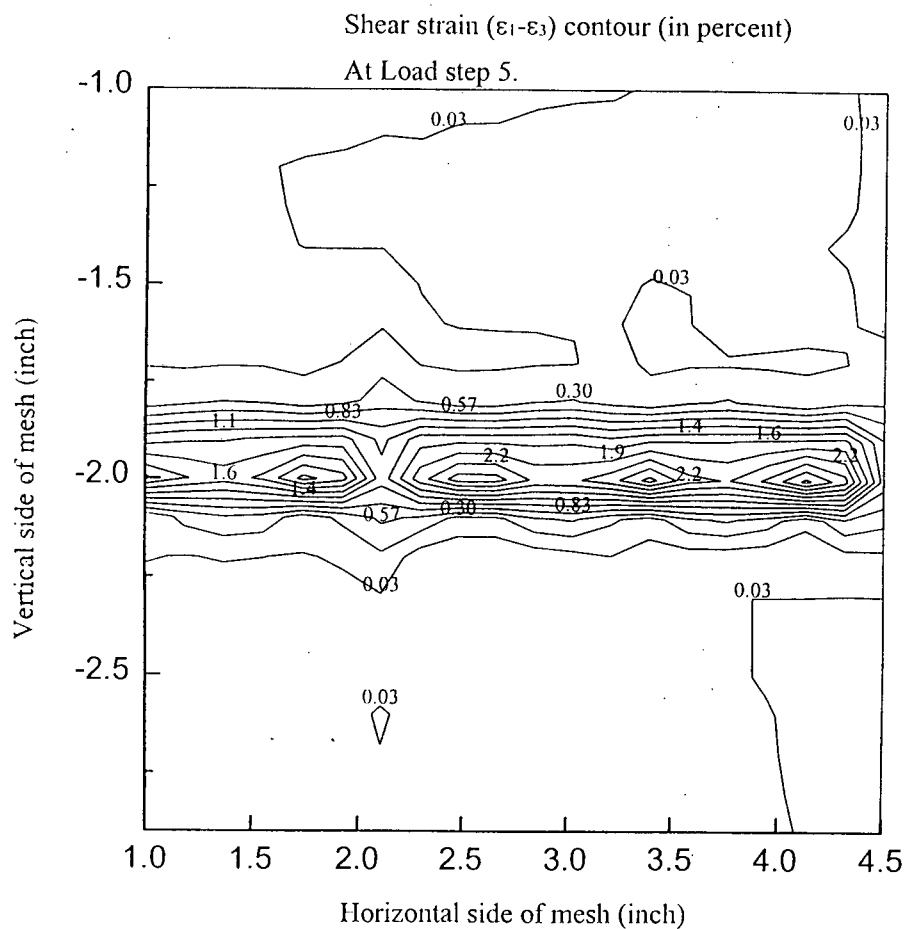
At Load step 5.

Figure 5-75(a): Shear strain contour for Case-5 of Desai Type Interface at load step-5.

Shear strain (ε₁-ε₃) contour (in percent)
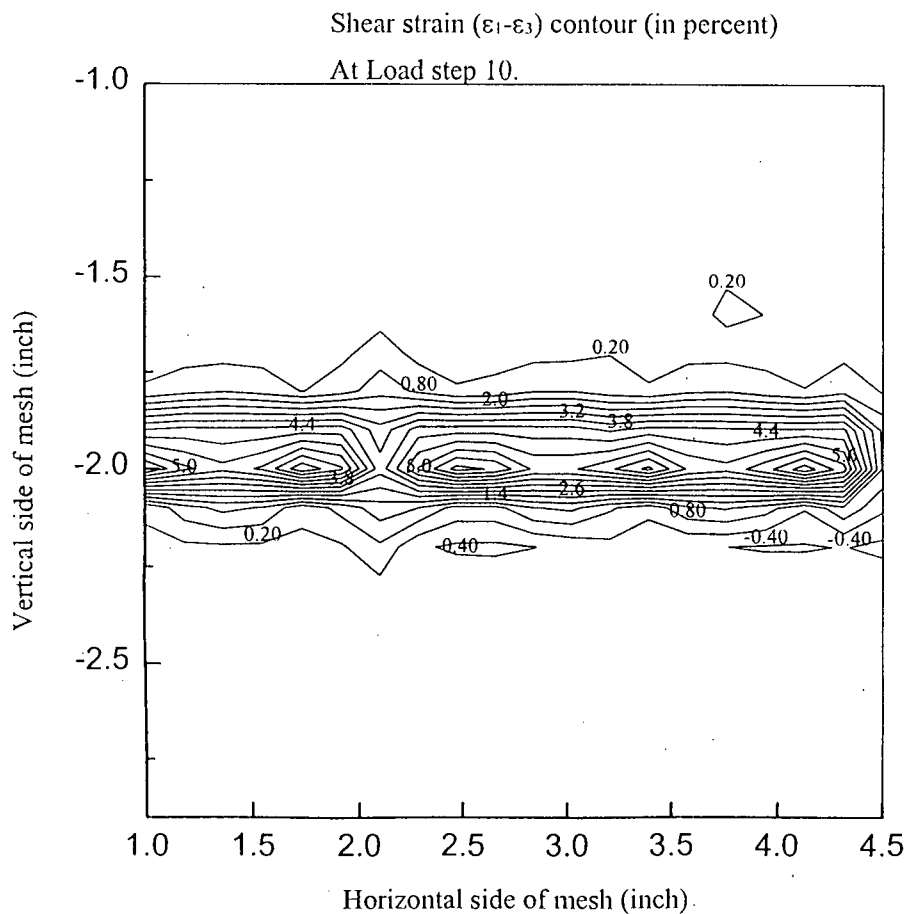
At Load step 10.

Figure 5-75(b): Shear strain contour for Case-5 of Desai Type Interface at load step-10.
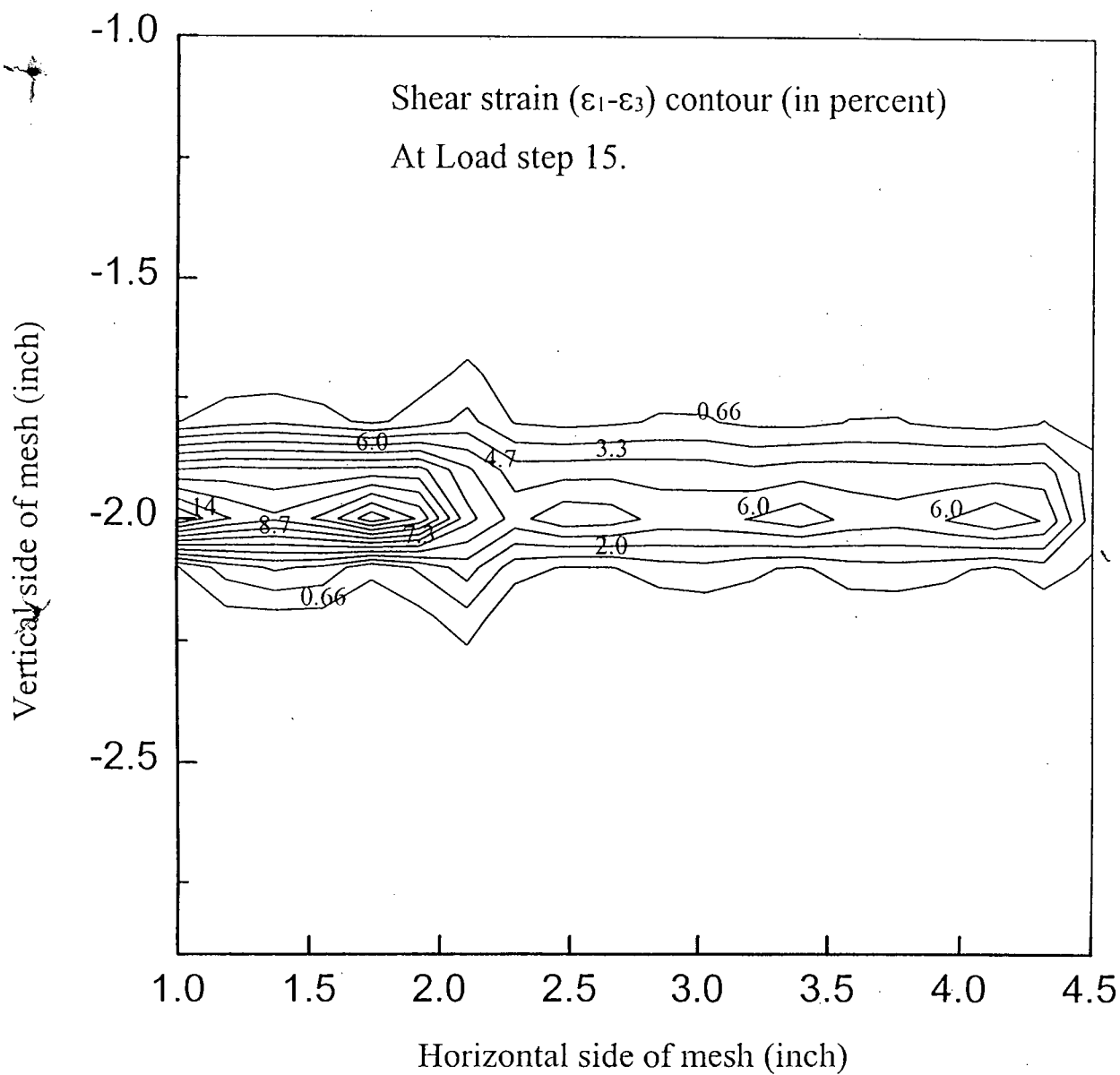
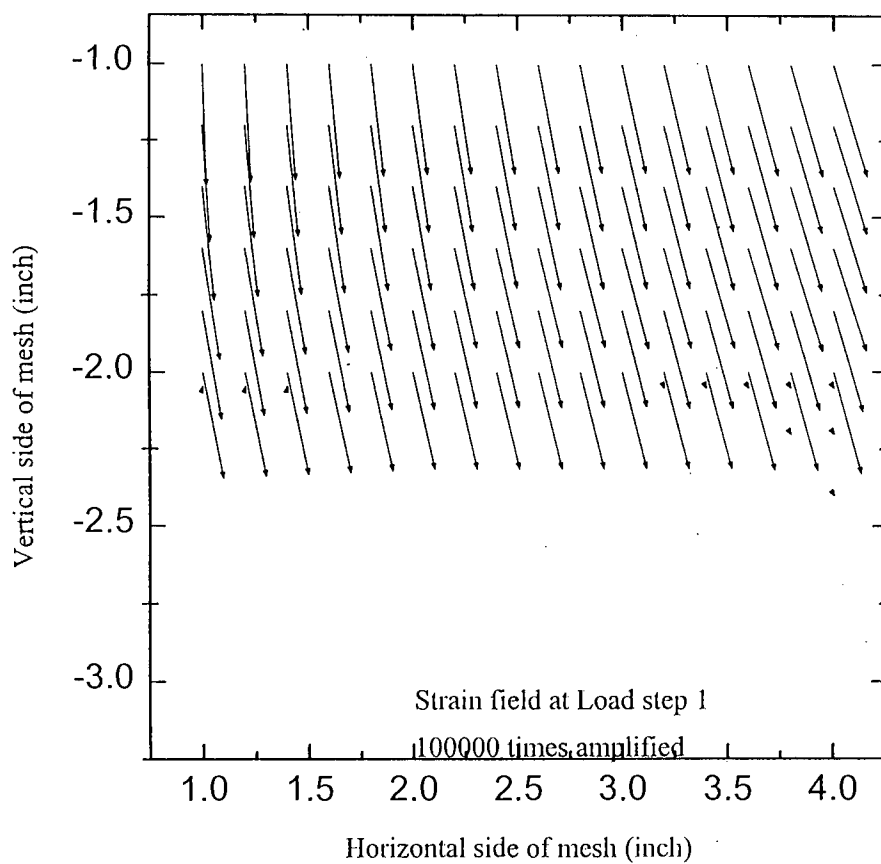Figure 5-75(c): Shear strain contour for Case-5 of Desai Type Interface at load step-15.
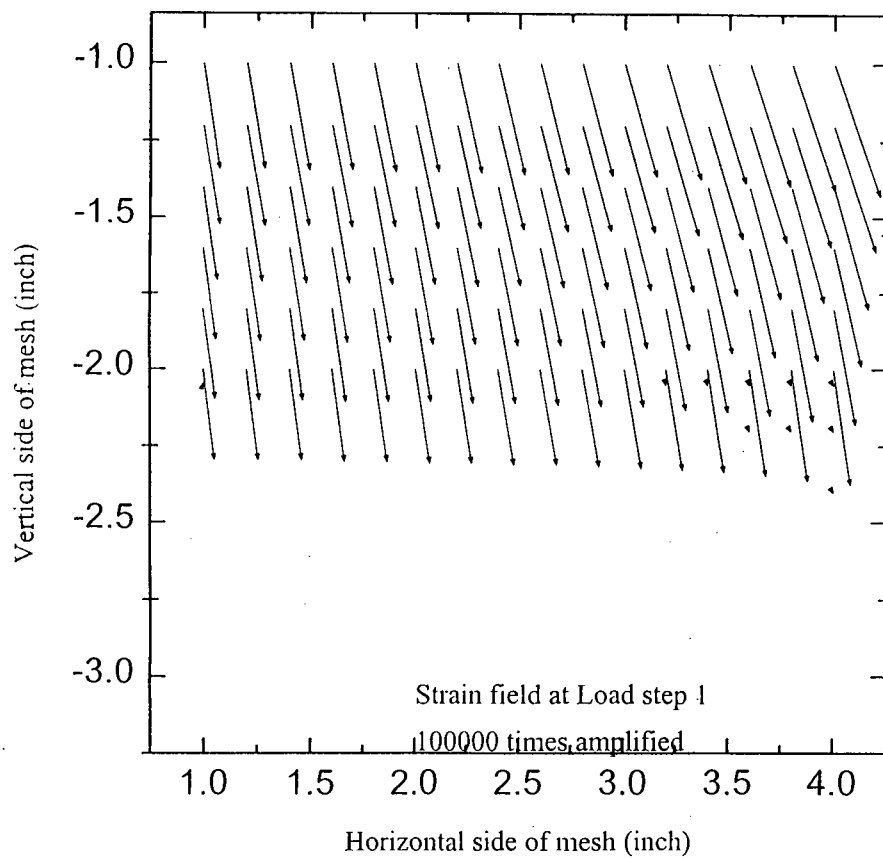
Figure 5-76(a): Displacement field for Case-5 of Desai Type Interface at load step-1.
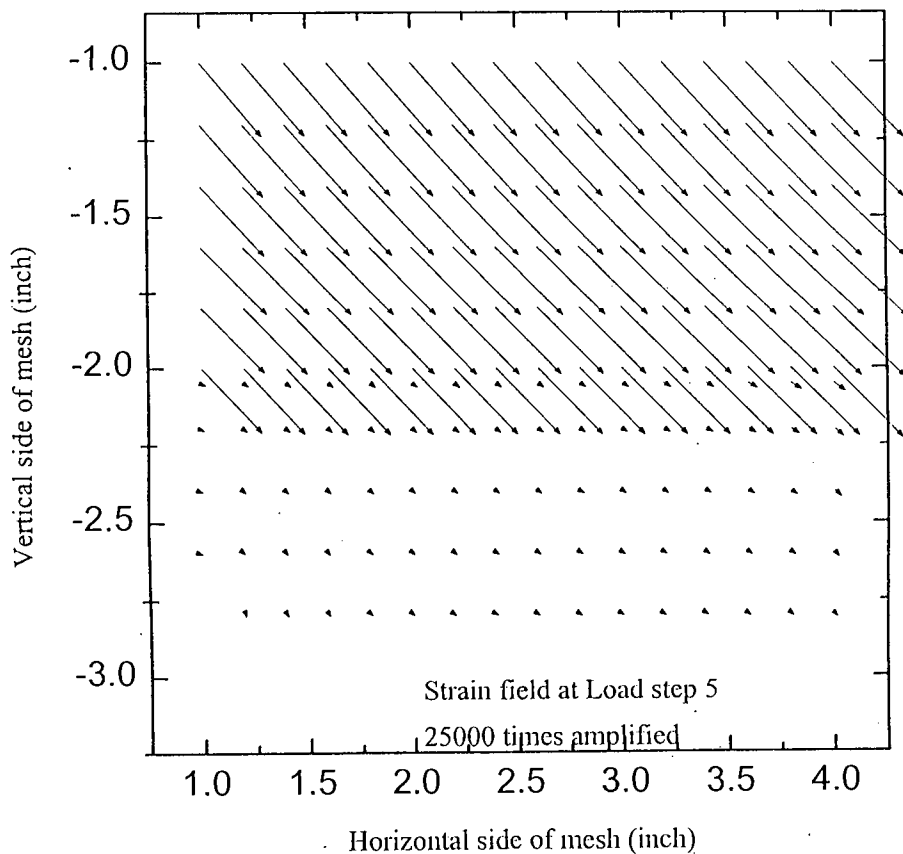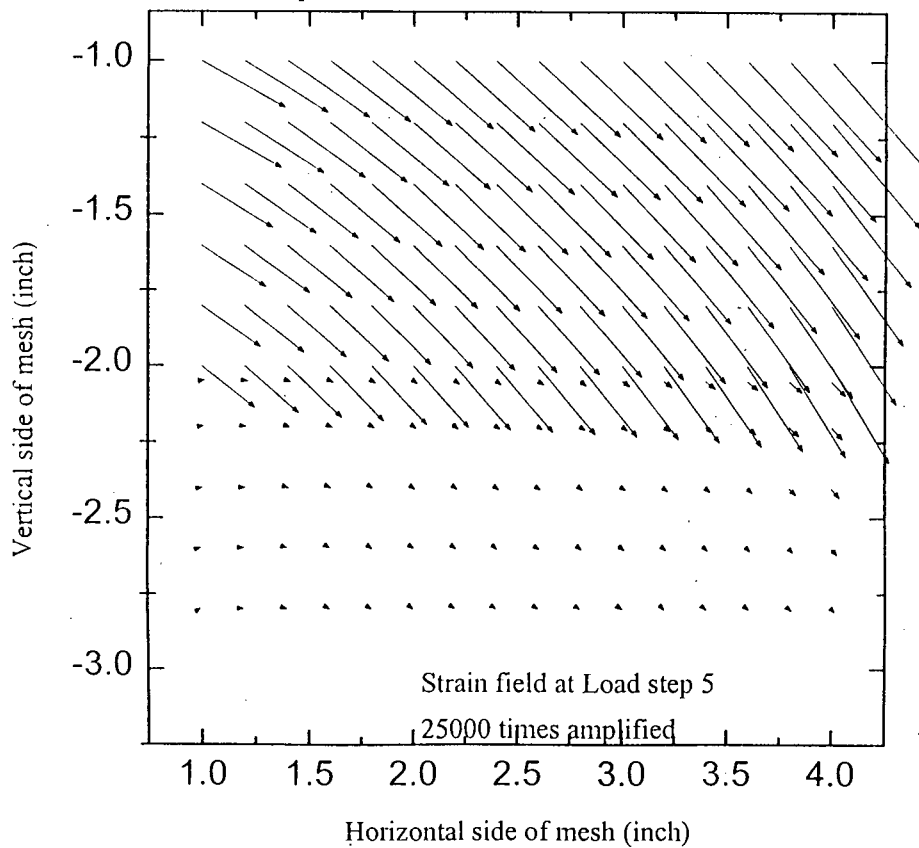

Figure 5-76(b): Displacement field for Case-5 of Desai Type Interface at load step-5.
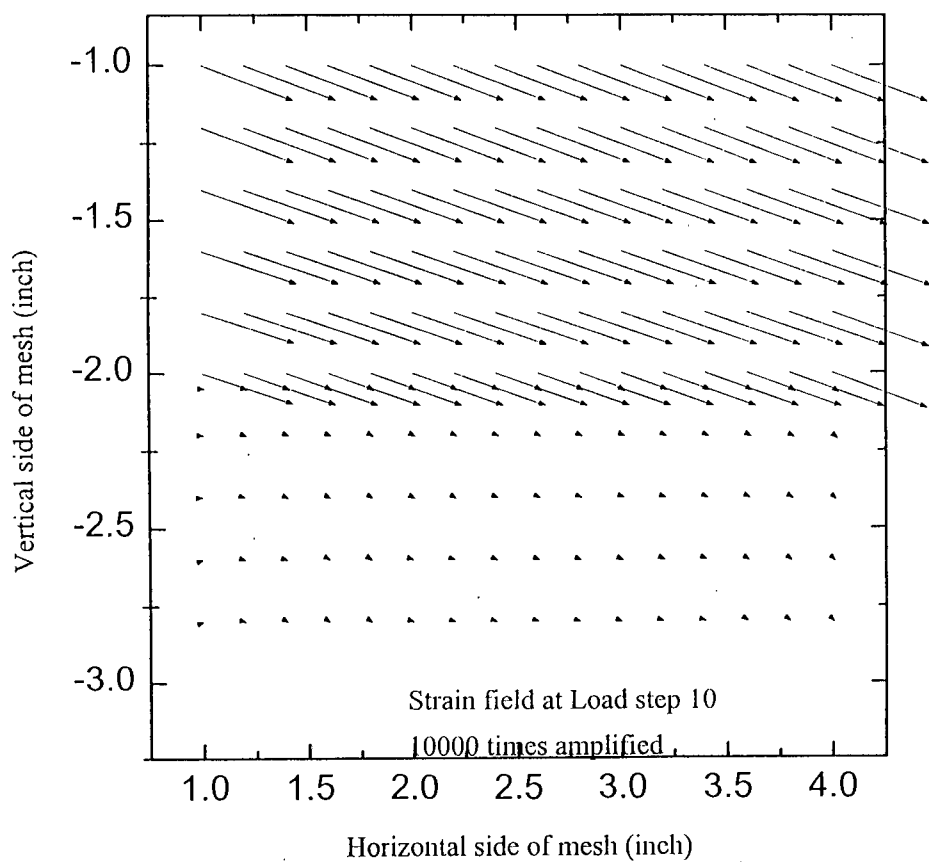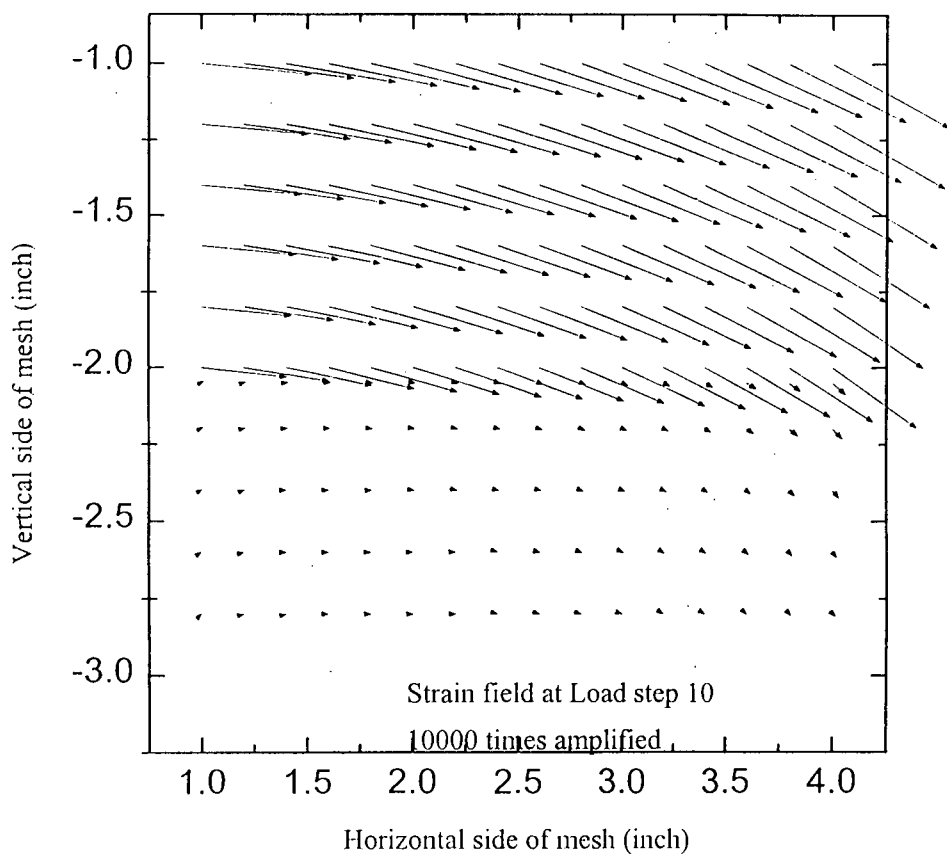
Figure 5-76(c): Displacement field for Case-5 of Desai Type Interface at load step-10.
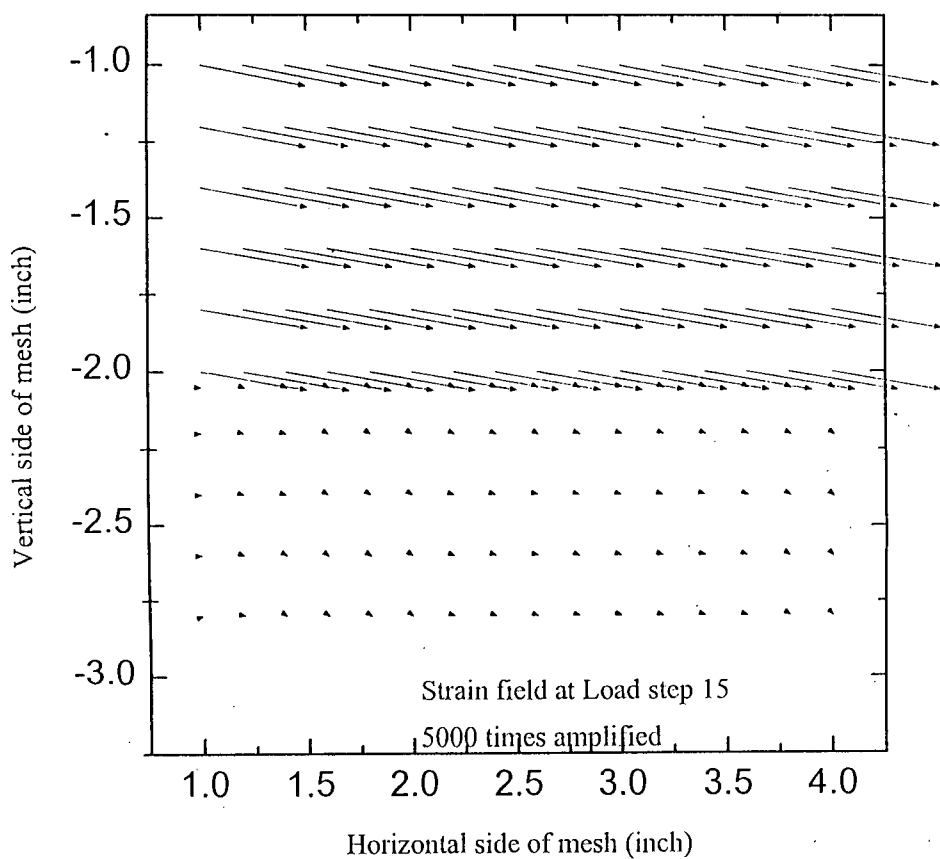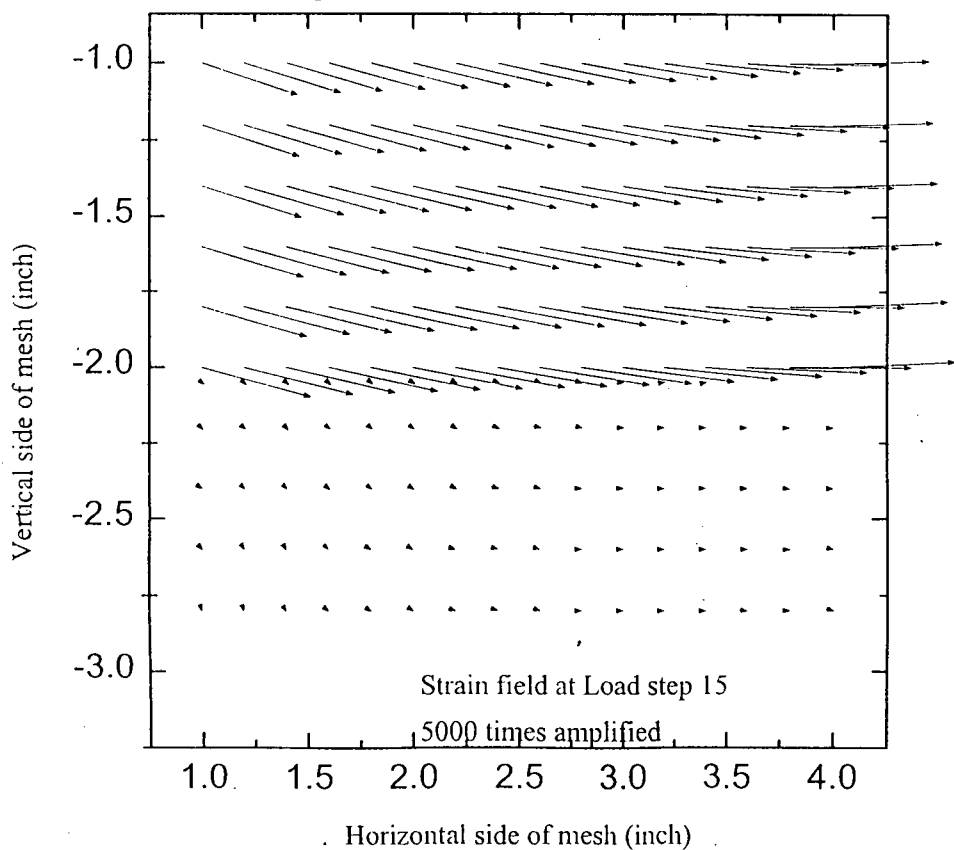

Figure 5-76(d): Displacement field for Case-5 of Desai Type Interface at load step-15.
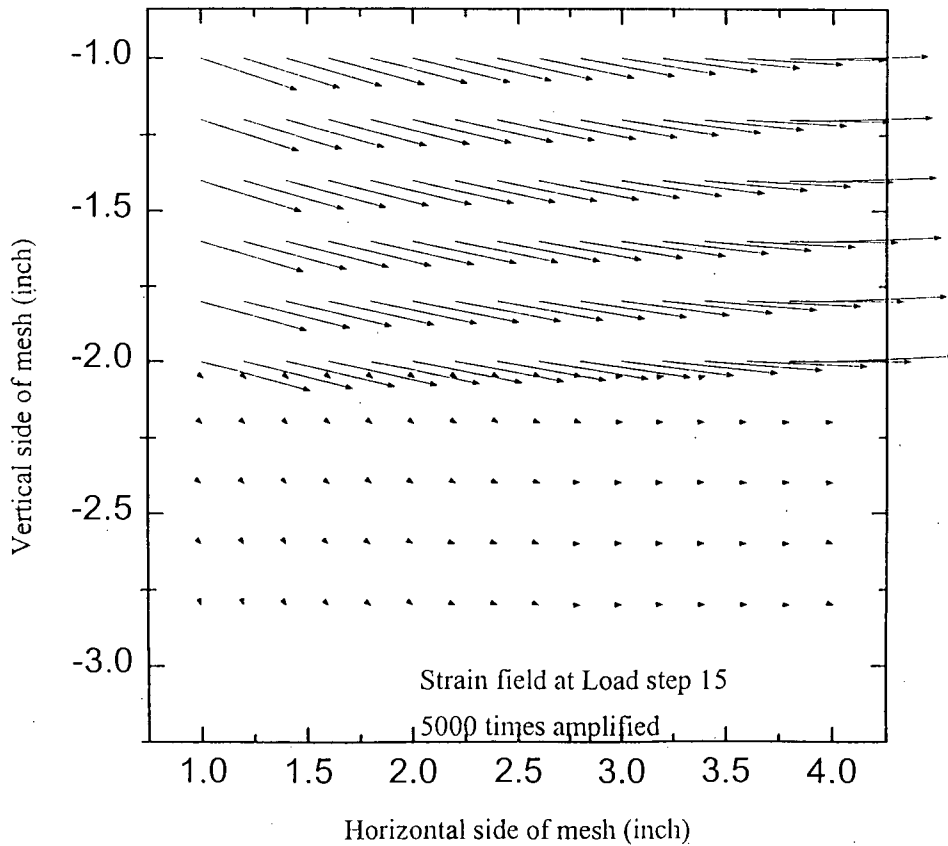
CHAPTER 6

6 CONCLUSION

6.1 GENERAL

The three types of interface elements have been reformulated and parameters are critically examined. A detail parametric study has been conducted to evaluate the performance of the elements. Due to the limitation of time and cost of analysis only the most critical parameters are studied to each type of interface. Following conclusions can be drawn from the analysis:

- Goodman Type of interface element is easy to formulate and implement in any nonlinear incremental iterative FEM code. On the other hand Katona type of interface is rather difficult to implement in an incremental iterative framework. Desai type of interface requires the details of material model.

- Goodman type of interface is susceptible to mesh penetration. In a number of cases mesh penetration occurred. On the other hand Katona and Desai type of interface have no such problem. Although Desai type of interface has a tendency of penetration but with the reduction of interface thickness it disappears.

- From the observation of the displacement fields of all three interface element type analysis, it has been found that Katona interface shows smooth horizontal flow of the upper part of the shear box, but other interfaces had variety of movements.

- Goodman and Katona type of interface followed the Mohr-Coulomb friction laws strictly. But Desai type of element followed more natural and practical material law, which in this case is generalized Mohr-Coulomb type yield function.

- From the view point of accuracy of solution Desai type of interface provides more realistic solution for this specific test simulation compared to those of Goodman or Katona solutions.

249

- The cost of any numerical analysis depends on its convergence properties. Hence, Desai type of interface elements showed quickest convergence behavior compared to Goodman or Katona elements.

- In case of Katona formulation, there is actually no element involved in it. It is the constrained equation, which play major role in its implementation. This creates major problem in its implementation in ordinary FEM code.

6.2 RECOMMENDATIONS FOR FUTURE RESEARCH

Three types of interface elements have been examined in this study, embedding them in a direct shear test simulation for a fixed normal load. The analyses are carried out in a limited manner in order to accommodate the study within the scope of time and resource limit. This study can be further extended in the following manner:

- The soil model used in the study was linear elastic. Any type of generalized strain hardening-softening elasto-plastic soil model can be used.
- The interface elements can be tested in a pullout/ pile load test simulation
- The interface elements can be reformulated in 3D and tested in application of 3D problems.

REFERENCES

AISI (1975), Steel Pile Load Test Data, American Iron and Steel Institute, Washington, D.C., 84.

Ameen, F. (1985), Geotechnical Characteristics of Dhaka Clay, M.Sc. Engg. Thesis, Department of Civil Engineering, Bangladesh University of Engineering and Technology, Dhaka.

Bari Md. Shafiqul (1996), Development of a Realistic Soil-structure Interaction System, M.Sc. Engg. Thesis, Department of Civil Engineering, Bangladesh University of Engineering and Technology, Dhaka.

Borst R. de and Vermeer P.A. (1984), Possibilities and Limitations of Finite Elements for Limit Analysis, Geotechnique, 34: 199 – 210.

Batoz J.L. and Dhatt G. (1979), Incremental Displacement Algorithms for Nonlinear Problems, International Journal of Numerical Methods in Engineering, 14: 1262 – 1267.

Berezantzev, V. G., Khristoforov, V., and Golubkov, V. (1961), Load Bearing Capacity and Deformation of Piled Foundations, Proc. 5th Int. Conf. S. M. & F. E., vol.2, 11-15.

Boulon M., Garnica P. and Vermeer P.A. (1995), Soil-structure Interaction: FEM computations

Bowles, J.E. (1989), Foundation Analysis and Design, McGraw-Hill International Book Company, Fourth Edition, New York.

Britto, A. M. and Gunn, M. J. (1987), Critical State Soil Mechanics Via. Finite Elements,John Wiley & Sons Limited, New York.

Burland, J.B. (1973), Shaft Friction of Piles in Clay – A Simple Fundamental Approach, Ground Engg., vol. 6, no. 3, May; 30-42.

Carter J.P. and Booker J.R. and Davis E.H. (1977), Finite Deformation of an Elasto-plastic Soil, International Journal of Numerical Analysis Methods in Geomechanics, 1: 25 – 43.

Cassel A.C. and Hobbs R.E. (1976), Numerical Stability of Dynamic Relaxation Analysis of Nonlinear Structures, International Journal of Numerical Methods in Engineering, 10: 1407-1410.

Chen W.F. and Mizuno E. (1990), Nonlinear Analysis in Soil Mechanics, Elsevier, Amsterdam.

Clough, G.W. and Duncan, J.M (1969), Finite Element Analysis of Port Allen and Old River Locks, Report No. TE-69-13, Univ. of California, Berkeley.

Coyle, H.M. and Reese, L.C. (1966), Load Transfer for Axially Loaded Piles in Clay, J.S.M.F.P., ASCE, vol. 92, SM2; 1-26.

Crawford, C.B. and Burn, K.N. (1962), Settlement Studies on the Mt. Sinai Hospital, Engineering Journal of Canada, Ottawa, vol. 45, No.12, December.

Crisfield M.A. (1981), A Fast Incremental/Iterative Procedure That Handles Snap-through, Computers and Structures, 13: 55 – 62.

Day R.A. and Potts D.M. (1994), Zero Thickness Interface Element-Numerical Stability and Application, Intl. Jnl. For Numetical and Analytical Methods in Geomechnics, vol. 18, 689-708.

D'Appolonia, D.J. et al. (1970), Closure: Settlement of Spread Footings on Sand, JSMFD, ASCE, vol. 96, SM2; 754-762.

Desai, C.S., Zaman M.M., Lightner, J.G. and Siriwardane, H.J. (1984), Thin-layer Elements for Interfaces and Joints, Int. Jnl. For Numerical and Analytical Methods in Geomechanics, V.8; 19-43.

Dewaikar, D.M. and Prajapati, A.H. (1992), Geomechanics Today, Proc. Indian Geotechnical Conf., Calcutta, 18-20; 133-136.

Ghaboussi, J., Wilson, E.L. and Isenberg, J. (1973), Finite Element for Rock Joints and Interfaces, J. Struct. Eng. Div. Proc. ASCE, V.99, SM10.

Golder, H.Q. (1957), A Note on-Piles in Sensitive Clays, Geot., vol.7; 192-195.

Golder, H.Q., and Leonard, M.W. (1954), Some Tests on Bored piles in London Clay, Geot.. vol.4, 32-41.

Goodman, R.E., Taylor, R.L. and Brekke T.L. (1968), A Model for Mechanics of Jointed Rock., J. Struct. Eng. Div. Proc ASCE, V.94, SM3.

Goodman, R.E.,Taylor R.L. (1968), A Model for Mechanics of Jointed Rock, J. Struct. Engg. Div. Proc. ASCE, V.94, SM3

Herrmann, L.R. (1978), Finite Element Analysis of Contact Problems, J.Eng. Mech. Div., Proc. ASCE, V.104, EM5.

Iwasaki, T and Tatsuoka, F. (1977), Effects of Grain Size and Grading on Dynamic Shear Modulus of Sands, Soils and Foundations, J.S.M.F.E., vol. 17, no. 3; 20-35.

Janbu, N. (1976), Static Bearing Capacity of Friction Piles, Proc. 6th European Conf. On SMFE, vol. 1.2; 479-488.

Jeyatheran, K. (1996), Application of CRISP in Embankments, Excavations and Piles, Presented at a Short Course on Numerical Analysis in Geotechnical Engineering, Held at AIT, 12-16 February, 1996.

Kaliakin, V.N. and Li. J. (1995), Insight into Deficiencies Associated with Commonly used Zero-thickness Interface Elements, Comp. And Geomech., vol. 17; 225-252.

Kamal Uddin, M. (1990), Compressibility and Shear Strength of Remolded Dhaka Clay.

Karim, M. R. (1985), An investigation of the behavior of Soil-steel Structure, M. Sc. Engg. Thesis, Department of Civil Engineering, Bangladesh University of Engineering and Technology, Dhaka.

Katona, M.G., Smith, J.M., Odello, R.S. and Allgood, J.R. (1976), CANDE-A Modern Approach for Structural Design and Analysis of Buried Culverts, Report No. FHWA-RD-77-5, Naval Civil Engineering Laboratory.

Katona, M.G. (1981), A Simple Contact Friction Interface Element with Applications to Buried Culvert, Proc. Symp. on Impl. of Computer Procedure and Stress-strain Laws in Geotechnical Engineering, Chicago, Illinois,V.1.

Katona, M.G. (1983), A Simple Contact-friction Interface Element with Applications to Buried Culvert, Intl. Jnl. For Numerical and Analytical Methods in Geomechanics, vol. 7, 371-384.

Krieg R.D. and Krieg D.B. (1977), Accuracies of Numerical Solution Methods for Elastic-Perfectly Plastic Model, ASME Journal of Pressure Vessel Technology, 99: 510-515.
McClelland, B. (1972), Design and Performance of Deep Foundations, Proc. Spec. Conf. on Perf. of Earth and Earth-supp. Struc., ASCE, vol. 2; 111.

McClelland, B. (1974), Design of Deep Penetraition Piles for Ocean Structures, Jnl. Geot. Eng. div., ASCE, vol. 100, no. GT7; 704-747.

Meyorhof, G.G. (1959), Compaction of Sands and Bearing Capacity of Piles, J.S.M.F.D., ASCE, vol. 85: SM6; 1-29.

Meyorhof, G.G. (1976), Bearing Capacity and Settlement of Pile Foundations, Jnl.Geot. Eng. div. ASCE, vol. 102, no. GT3; 195-228.

Meyerhof, G.G. and Murdock L.J. (1953), An Investigation of the Bearing Capacity of Some Bored and Driven Piles in London Clay, Geot, vol.3; 267.

Mohan, D. and Chandra, S. (1961), Frictional Resistance of Bored Piles in Expansive Clays, Geot., vol.11; 291.

Morshed, J. (1991), Prediction of Load Deformation Behavior of Axially Loaded Piles in Sand, M.Sc. Engg. Thesis, Department of Civil Engineering, Bangladesh University of Engineering and Technology, Dhaka.

Naylor, D.J. (1975), Non-linear Finite Element Models for Soil, PhD Thesis, University College of Swansea.

Potyondy, J.G. (1961), Skin Friction between Various Soils and Construction Materials, Geotechnique, vol. 11, 339-353.

Poulos, H.G. and Davis, E.H. (1980), Pile Foundation Analysis and Design, The Univ. of Sydney, John Wiley & Sons, Inc. Toranto, Canada.

Reese, L.C., Touma, F.T. and O'Neill, M.W. (1976), Behavior of Drilled Piers under Axial Loading, Inl. Geot. Eng. div. ASCE, vol. 102, GT5; 493-510.

Siddiquee, M.S.A, (1994), FEM Simulations of Deformation and Failure of Stiff Geomaterials Based on Element Test Results, PhD Thesis, University of Tokyo, Japan.

Schreyer H.L., Kulak R.F. and Kramer M.M. (1979), Accuracy of Numerical Solutions for Elastic-Plastic Models, ASME Journal of Pressure Vessel Technology, 10: 226 – 234.

Seraj, S.M. (1986), Structure-soil Interaction in Buried Rigid Culvert, M.Sc. Engg. Thesis, Department of Civil Engineering, Bangladesh University of Engineering and Technology, Dhaka.

Sowers, G.B. and Sowers, G.F. (1970), Introductory Soil Mechanics and Foundations, 3rd ed. New York, Macmillan.

Terzaghi, K. (1943), Theoretical Soil Mechanics, John Wiley & Sons, Inc., New York.

Tomlinson, M.J. (1957), The Adhesion of Piles Driven in Clay Soils, Proc. 4th Int. Conf. S.M. & F.E. vol. 2; 66-71.

Tomlinson, M.J. (1970), Some Effects of Pile Driving on Skin Friction, Conf. on Beh. of Piles, Inst. Civ. Engrs., London; 59-66.

Vesic, A.S. (1967), A Study of Bearing Capacity of Deep Foundations, Final Rep., Proj. B-189, School of Civil Eng., Georgia Inst. of Tech. Atlanta, Ga.

Whitaker, T. and Cooke, R.W. (1966), An Investigation of the Shaft and Base Resistance of Large Bored Piles in London Clay, Proc. Symp. On Large Bores Piles; 7-49.

Wong, K.S. (1977), SSTIP-Soil Structure Interaction Program with Interface Elements, Univ. of Clifornia, Berkeley.

Wroth, C.P. (1975), In-situ Measurement of Initial Stresses and Deformation Characteristics, Proc. of the Specialty Conf. in In-situ Measurement of Soil Properties, ASCE, Rayleigh, North Carolina, June; 181-230.

Zienkiewicz, O.C. (1977), The Finite Element Method, 3rd ed., McGraw-Hill Book Company, New York; 787.

Zienkiewicz, O.C., Valliappan, S., Dullage, C. and Stagg, K.G. (1970), Analysis of Non-linear Problems in Rock mechanics with Particular Reference to Jointed Rock System, Proc. of 2nd Conf. of Intl. Soc. For Rock Mech., Belgrade.